### Title

The Interplay of Design and Materials in Orthopedics: Evaluating the Impact of Notch Geometry on Fatigue Failure of UHMWPE Joint Replacements

### Author

Ansari, Farzana

### Publication Date

2015

Peer reviewed|Thesis/dissertation

# The Interplay of Design and Materials in Orthopedics: Evaluating the Impact of Notch Geometry on Fatigue Failure of UHMWPE Joint Replacements

By

Farzana Ansari

A dissertation submitted in partial satisfaction of the

requirements for the degree of

Doctor of Philosophy

in

Engineering – Mechanical Engineering

in the

Graduate Division

of the

University of California, Berkeley

Committee in charge:

Professor Lisa A. Pruitt, Chair
Professor Robert O. Ritchie
Professor Ronald Gronsky

Spring 2015

The Interplay of Design and Materials in Orthopedics: Evaluating the Impact of Notch Geometry on Fatigue Failure of UHMWPE Joint Replacements

by Farzana Ansari

# Abstract

## The Interplay of Design and Materials in Orthopedics: Evaluating the Impact of Notch Geometry on Fatigue Failure of UHMWPE Joint Replacements

by

Farzana Ansari

Doctor of Philosophy in Engineering-Mechanical Engineering

University of California, Berkeley

Professor Lisa A. Pruitt, Chair

Each year, roughly 750,000 patients in the US receive a total joint replacement (TJR), or a synthetic medical device that serves to replace the natural joint to restore function and relieve pain. TJRs have had a long history of use in the hip, knee and shoulder, yet still retain the same standard design of a hard-on-soft bearing coupling. Today, those bearings are primarily composed of hard cobalt chrome (CoCr) surface articulating against ultrahigh molecular weight polyethylene (UHMWPE), a polymer with notable mechanical toughness and biocompatibility that have driven its 50-plus years of use *in vivo*. TJRs have seen tremendous success for older patient cohorts for whom these devices were designed. However, increasing demand from younger patients has motivated the need for more durable materials that can sustain higher, more variable loading for a longer time. UHMWPE has become central to this mission, with limitations in its long-term wear resistance, oxidative stability and fracture/fatigue properties coming under the limelight in recent years.

Explanted devices that have been retrieved from patients following failure have provided significant insight into the vulnerabilities of different UHMWPE formulations currently in the market, especially with respect to component fracture. Three cases examined in this work describe fracture failures of UHMWPE components seen in the knee, hip and shoulder to demonstrate existing tradeoffs in material sterilization and processing. Irradiation crosslinked blends, initially introduced to the orthopedic market to improve wear resistance, exhibits reduced resistance to both oxidation and fatigue crack propagation. Such tradeoffs are shown to contribute to the failure of two fractured knee tibial inserts, a single fractured hip acetabular cup, and a series of severely fractured glenoid components used in the shoulder. The former two cases exhibit an additional precursor to fracture that has been recognized but largely ignored in the fatigue characterization of crosslinked UHMWPE: the existence of stress concentrations (notches).

Incidences of component fracture like the three reviewed in this work have motivated significant study of UHMWPE's mechanical deformation as a function of microstructural changes. In addition, computational studies have sought to establish how changes in design may reduce local stresses in UHMWPE components to mitigate failure. Material and design influences have thus predominantly been studied in isolation. The latter half of this work demonstrates how previous methodologies using linear elastic fracture mechanics (LEFM) and theoretical approaches to notch fatigue can been merged to elucidate the influence that notch geometry (notch-root radius) has on crack behavior in UHMWPE formulations. A robust computational analysis of existing theories regarding LEFM notch stress intensity and notch plasticity is presented, lending credibility to the use of the Dowling (1979) approach in characterizing the crack driving force in the vicinity of the notch. Standard compact tension (CT) specimens were modified to include one of five notch geometries: a sharp (0.13 mm) radius (control specimen), two crack-like radii (0.75 and 1 mm) and two blunt keyhole-type radii (2 and 3 mm). All radii were chosen to reflect geometries seen in modern TJR features, such as a tibial post in the knee or a liner locking mechanism in a hip. Cracks from 0.1 to 1 mm in length were created at each notch root using a sharp razor blade. Cyclic tensile loading (stress ratio, R = 0.1) was applied to impose an increasing cyclic stress intensity ($\Delta K$), and crack growth was monitored optically.

The fatigue crack propagation (FCP) behavior was mapped using the Paris law to compare the relative crack speeds at a given applied $\Delta K$ for each notch geometry and material formulation. Crack growth ahead of each notch was found to overlap with sharp crack data, further supporting the use of the Dowling approach in characterizing near-notch crack growth. This overlap in data implied that mechanisms of crack growth near the notch were similar to those further away from the notch (outside the "notch-affected zone", as calculated for each notch radius using the Dowling approach). The congruency of all notch-emanating crack data also revealed microstructure-driven trends between each material cohort that have been noted in previous sharp crack studies. Highly crosslinked and remelted UHMWPE (RXLPE) was found to display the least resistance to FCP, while highly crosslinked and Vitamin E blended (VXLPE) formulations demonstrated a notable improvement. Virgin UHMWPE consistently demonstrated the best resistance to FCP. The reduction in FCP resistance seen in highly crosslinked materials was associated with reduced local plasticity in amorphous regions that otherwise serves to mitigate crack advance. Above-melt annealing ("remelting") in RXLPE has been shown to minimize oxidation and subsequent embrittlement *in vivo* through free radical elimination, but can result in reduced percent crystallinity and lamellae quality that can further diminish FCP resistance. Blending Vitamin E similarly serves to reduce oxidation for VXLPE, but retains the crystalline quality and quantity of virgin UHMWPE. However, blended Vitamin E also diminishes crosslinking efficiency, thereby improving VXLPE's resistance to FCP relative to RXLPE but with a tradeoff in optimal wear resistance.

This study demonstrated that fatigue crack growth in UHMWPE primarily defers to microstructural influences, even when considering varying notch geometries within the vicinity of a crack. This work demonstrates that this methodology of investigating notch effects on crack behavior can be leveraged for polymeric materials, despite its primary origin from crystalline

metals. Furthermore, by mimicking previous specimen types, sample dimensions and loading conditions, the methodology used in this work is easily translatable to orthopedic manufactures or research groups seeking to evaluate notch effects in novel UHMWPE formulations. Results shown here reveal that blunter notches do serve to mitigate catastrophic failure by reducing local driving forces (lower $\Delta K$) within a larger notch-affected zone than sharp notches. However, this reduction may not offset the tradeoff in fatigue properties exhibited by highly crosslinked UHMWPE and a focus on optimizing the microstructure of this polymer may be more prudent for increasing its durability *in vivo*.

# Table of Contents

## Acknowledgements

Upon graduating from my undergraduate institution, I had never imagined pursuing a PhD, let alone one in Mechanical Engineering at UC Berkeley. Six years later, I am somehow finishing up final touches on this dissertation and am continually reminded of the *many* people who have got me to this point. First and foremost, I must thank my advisor, Lisa Pruitt. If it were not for Lisa, I would not even be at UC Berkeley. Lisa convinced me to join the program here, provided me with exceptional mentorship that brought me into her lab, and created a "home" for me in the Medical Polymer Group (MPG) that I could not bear to leave after only a Masters degree. Lisa, I am indebted to you for your guidance and encouragement, for your continual reminder of maintaining balance between my research and personal goals, and helping me decide what were the rocks, pebbles and sand in my life. I came to Cal to find a graduate advisor, and I am leaving with a lifelong friend.

The folks in MPG were a daily part of my experience at UC Berkeley and were integral to the completion of this body of work. In particular, I am grateful to have worked with many phenomenal undergraduates in my lab, especially: Gio and Connor, for their endless patience and commitment to learning FEA, performing hundreds of analyses under a time crunch, and helping me with the tedious task of measuring crack growth (and never complaining); Robin, for her diligent work ethic and perseverance on projects ranging from the retrievals database to learning FEA from scratch (and for laughing at my jokes); Jen, for being our go-to SEM technician and providing substantial data for the tibial post failure analysis (and being a joy to work with); Taylor for assisting me with the glenoid fracture map (and learning some new Photoshop skills along the way); and Suzanne for her fractography efforts for the hip liner rip failure (and for keeping my Masters work going with creativity and enthusiasm). And thank you to the many other undergraduate students who contributed to several other projects that I have had the pleasure working on at MPG. You kept me motivated to come into lab each day and reminded me how exciting our work can be, even when progress was slow.

To Louis, Noah and Hannah: After a few lonely intermediate years in the lab, I was so grateful to have a team to work with at the end – a team that I am confident will provide admirable leadership for MPG in the coming years. Thank you for your insight and comradery, and for tolerating my thesis-related grumbling during this past year.

I also am so grateful to Eli Patten, who I had the pleasure of sitting next to and working with for my first two years as a graduate student. Eli's light-hearted demeanor, approachability and mentorship made me feel at ease during what was a very confusing time at Cal. Eli, thank you for creating an open and dynamic lab space focused on teaching and mentoring, training us younglings on how to use everything from Elvis to Instron, and challenging me to Nerf gun battles when the research became particularly stressful!

I am also grateful to the many collaborators who provided me with guidance and resources throughout my Masters and PhD research. I thank Professor Ritchie for getting me hooked on fracture mechanics, and providing me with substantial assistance in choosing an appropriate methodology for assessing notch fatigue in UHMWPE. I also would have been at a loss dealing with our Instron system without the patience and advice of Bernd Gludovatz. Bernd, I am happy I was introduced to you during my time at Cal, and greatly appreciate every early morning coffee (or even after-work beer) arguing over fatigue plots, stress intensity equations and theoretical papers to help me extract sound and reasonable conclusions. With you, there were never any "stupid" questions – I truly appreciate your willingness to dig through my data and help me fill in the gaps.

I also want to thank Professor Douglas Van Citters at Dartmouth University, and Drs. Melinda Harman and Estefi Alvarez for their collaborations on retrievals work during my early years as a graduate student here. Several Skype meetings, phone calls and conference rendezvous led to an impressive body of work that actually made me *enjoy* research – something I never imagined as an undergraduate!

I also would like to acknowledge the entire Department of Mechanical Engineering staff for making Etcheverry Hall a home-away-from-home for me for the past five years. Thank you to Yawo, for always smiling and bringing up everyone's spirits even while we were filing paperwork; to Shareena, for all the diversity work you do and the many efforts we collaborated on to improve our department climate; to Dennis in the ME shop, for making hundreds of samples for my experiments in his "free" time, and always with a smile; to the rest of the ME shop guys (Mick, Gordon, Jesse, and Scott) and the Hesse staff (Alex, Mike and Pete) for the endless help with my research and equipment and for being an absolute joy to work with; to Sheila for going above-and-beyond to help fund my extracurricular travels while going to conferences; and finally to Donna, for *always* having your door open (and tissues ready!) when the stress of grad school was sometimes too much to bear.

Last but not least, I could not have gotten this far without my friends and family. To the friends I made in graduate school to even those who have I have known me since 9th grade, I thank you for sticking by me all these years. To my parents, I thank you for your continual encouragement, for calming me when the stress was overwhelming, and never pushing me too hard – my academic achievements would be incomplete without your continual love and support. To Alisha, thank you for bearing with me during the tough times, suffering as my roommate for a few years and for commiserating with me on everything, from life to school – I am very proud of you and hope I can provide you with a fraction of the support you have provided me. And finally to Will, for being my rock through the best and the worst of times; for being silly and supportive; for allaying my worries and encouraging my excitement; for being there for every day of "good data" and "bad data"; and for rock climbing with me, going to concerts with me, traveling with me, bearing through soccer games with me, camping with me and even being lazy with me. I am excited to see where we go next!

# Chapter 1 – The Evolution of Total Joint Replacements and UHMWPE

## 1.1 The Total Joint Replacement System

There are hundreds of joints in the human body that enable articulation and stability of our musculoskeletal system. The most well-known – and perhaps the most studied – are the synovial joints. These joints include ball-and-socket hips and shoulders, as well as bicondylar knees. Synovial joints are characterized by one or more articulating surfaces that are encapsulated by a fibrous sac that contains a viscous synovial fluid (**Figure 1.1**). The bone surfaces are coated with cartilage tissue whose high water content (60-80 weight %) in combination with an elastic collagen matrix provides a deformable yet recoverable medium for force absorption (Pruitt & Chakravartula 2011; Dumbleton 1981; Bartel et al. 2006). Cartilage's behavior is enabled by the presence of a viscous, healthy synovial fluid that not only softens impact, but also provides nutrients to the avascular cartilage tissues.

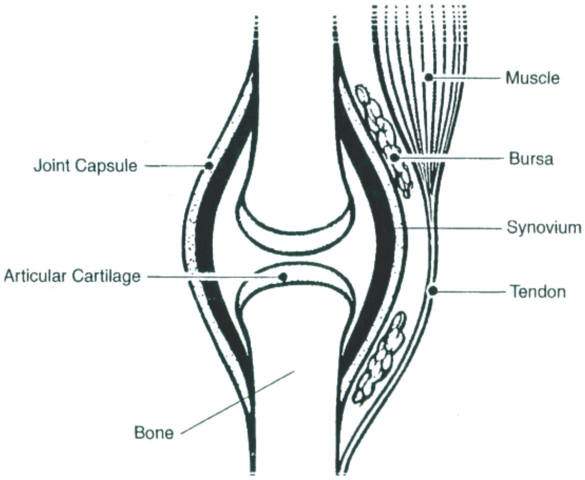

**Figure 1.1 |** Synovial joints consist of two cartilaginous-covered bone surfaces that articulate in a lubricious synovial fluid-filled medium, contained with a joint capsule (Bartel et al. 2006).

Damage to the cartilaginous surface can result in joint pain. Such damage can be associated with the direct breakdown of cartilage, either through osteoarthritis or trauma, or malnourishment through the decay of synovial fluid as in rheumatoid arthritis (Pruitt & Chakravartula 2011). Cartilage is not innervated, and thus does not elicit a pain response during loading. However, once worn away due to joint disease or trauma, exposure of the underlying innervated bone can result in often debilitating pain during cyclic loading. Currently, the best treatment for this pain is the total joint replacement (TJR), in which the entire joint is replaced with a synthetic bearing coupling system. The growing use of TJR to treat joint degeneration has largely derived from its success: over 90% of hip and knee replacements survive beyond 10 years (Kurtz et al. 2005; Pruitt & Chakravartula 2011). This success has led to higher expectations for joint prosthetic performance, with many orthopedic companies targeting a standard 20 year lifetime with novel material and design development.

The achievement of TJR is further exemplified when considering the fundamental design requirements of the synovial joint. Our natural joints are continually under high demand, bearing loads several times body weight on an area as small as 500 mm$^2$ (Dumbleton 1981). These loads are dynamic in nature: limbs can abduct, adduct, flex, extend and even rotate during our daily activities. Synovial joints are designed to retain a very low coefficient of friction through multiple degrees of freedom to minimize wear and tear to the cartilage surface. Natural hip and knee joints, for example, can achieve coefficients of friction as low as 0.01 and 0.005, respectively – orders of magnitude lower than what is seen with most engineered biomaterials (Bartel et al. 2006; Unsworth 1991). The tribological environment in joint systems has been characterized within the elastohydrodynamic to fluid film lubrication regimes, highlighting the dynamic “cushioning” behavior that cartilage serves within a viscous synovial fluid environment (Unsworth 1991; Fisher et al. 1994; Bartel et al. 2006). What natural “healthy” joints are designed to do for up to 100 years, synthetic joints can achieve for around 20, with the added challenges of a corrosive and biologically active environment and an already diseased system that likely experiences suboptimal loading and wear.

Much of the success of TJR has been associated with bearing materials that have persisted for the past 60 years (Kurtz 2009). The coupled bearing typically pairs a polymeric component, made from ultrahigh molecular weight polyethylene (UHMWPE), with a metallic (cobalt chrome) or ceramic counter-bearing (**Figure 1.2**). This metal-on-polymer design has demonstrated notable success in hip, knee, shoulder, elbow and wrist joints, with over one million patients in the US receiving devices annually (Kurtz et al. 2005). The introduction of an UHMWPE bearing articulating against a metal head is attributed to Sir John Charnley, who published his findings in 1961 on the coupling’s low coefficient of friction, high degree of toughness, and reduced incidence of biological attack compared to predecessors (Charnley 1961). Since then, other bearing couplings have grown in popularity – including metal-on-metal, ceramic-on-ceramic and ceramic-on-polymer – but the forgiveness of UHMWPE has allowed this material to dominate the market for over six decades.

The past twenty years in particular have seen a dramatic spike in use that some authors refer to ask the “epidemic” of joint arthroplasty. From 1990 to 2002, the rate of total hip replacement (THR) procedures in the US increased by 46% and total knee replacement (TKR) rates almost tripled to account for 193,000 and 381,000 implanted devices, respectively, in 2002 (Kurtz et al. 2005). During a similar time period, total shoulder replacement (TSR) rates outpaced that of hips and knees with a 319% increase and total elbow replacement (TER) rates followed closely behind with a 214% increase (Day et al. 2010). This surge in joint arthroplasty far outpaced the growth of the US population within the same decade, reflecting an increased recognition of successful outcomes for joint prostheses and wider usage for not only older (>65) but also younger (45-65) patient cohorts (Kurtz et al. 2005; Kurtz et al. 2009). Interestingly, while the increase in arthroplasty frequency was gaining speed over the 10-13 year period, the overall revision rate remained fairly consistent (**Figure 1.3 A**), with an average 17.5% of THA, 8.2% of TKA, and 14% of upper extremity devices being revised within a 5 to 20 year lifetime (Day et al. 2010; Kurtz et al. 2005).

**Figure 1.2** | Metal-on-polymer bearing couplings for a hip, knee and shoulder joint. This material coupling of cobalt-chrome on UHMWPE has dominated the total joint replacement market for 60 years (healthbase.com, thewomensjournal.com, springerimages.com).

The "epidemic" of arthroplasty, however, is not stagnant: it is predicted that current growth rates will effectively quadruple the number of TJR procedures seen today to greater than 4 million arthroplasties annually within the next two decades. The upswing in primary procedures could result in twice the number of THR and TKR revision procedures provided the current revision burden remains unchanged (**Figure 1.3 B**). Not only do revision procedures come at a higher burden to patients, but these procedures have greater financial consequences than primary arthroplasties, accounting for over 20% of Medicare costs in the late 1990s (Kurtz et al. 2007). And this projected rise in revisions at the current rate may be conservative. It is expected that more than half of patients undergoing joint replacement in the next two decades will be between 45-65 years of age (Kurtz et al. 2007). Historically, younger patients have been documented as an even higher risk for revision due to persistent high activity levels and therefore high demands on their devices. The resurge of metal-on-metal couplings, resurfacing treatments and ceramic-on-ceramic devices have attempted to restore function under greater loads, but have recently succumbed to pathological challenges through metal debris toxicity and more benign issues of squeaking (Jarrett et al. 2009; Doorn et al. 1996).

Reasons for revision for each device, despite variations in design and kinematic loading, demonstrate remarkable consistency across the TJR landscape. Common causes include, in average decreasing frequency: instability, mechanical or aseptic loosening, infection, implant failure or breakage, dislocation (THR), bearing surface wear, periprosthetic fracture (Bozic et al. 2009; Bozic et al. 2010; Alberton et al. 2002; K. I. Bohsali et al. 2006). Loosening has remained a persistent challenge over metal-on-polymer device history, prompting not only the initial transition to UHMWPE, but also the radiation, thermal and processing treatments that have marked its growth since. In particular, wear resistance of UHMWPE has remained a driving force behind the polymer's evolution, given the well-established link between submicron-size wear debris and osteolysis, or bone loss, that leads to prosthetic loosening (Dumbleton 2002; Willert & Semlitsch 1977).

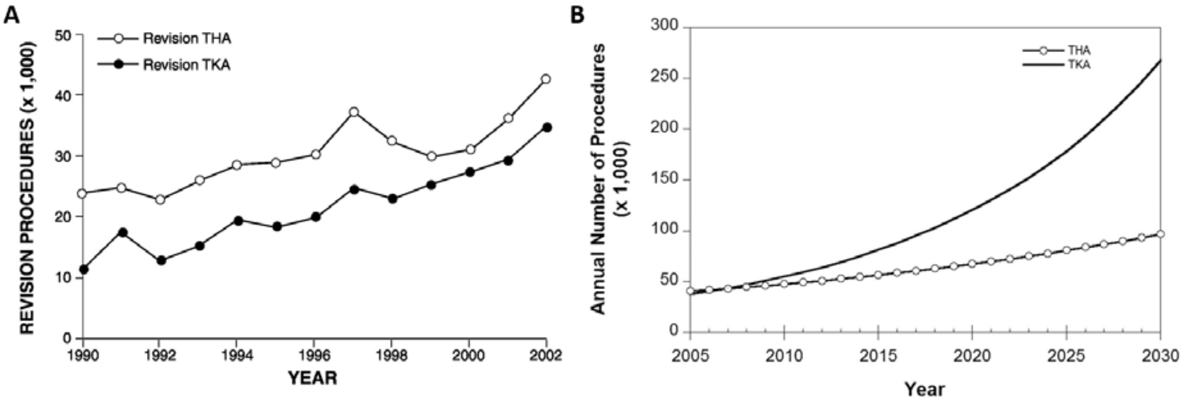

**Figure 1.3** | (**A**) Number of reported revision procedures in the US from 1990-2002 (Kurtz et al. 2005). (**B**) Projected number of revision procedures in the US from 2005 to 2030 (Kurtz et al. 2007).

## 1.2 Ultrahigh Molecular Weight Polyethylene (UHMWPE)

*Structure, Properties and Mechanical Behavior of UHMWPE*

UHMWPE is biocompatible linear homopolymer and member of the polyethylene family. It contains a repeating $[C_2H_4]_n$ monomer unit with a degree of polymerization ***n***. The International Standards Organization (ISO 11542) requires a minimum molecular weight of 1 million g/mol (***n*** ~ 36,000), but typical orthopedic manufacturers use UHMWPE with a ***n*** from 71,000 to 214,000, equating to a molecular weight from 2-6 million g/mol (Kurtz 2009; Sobieraj & Rimnac 2009). For comparison, the next highest molecular weight in the polyethylene family is high density polyethylene (HDPE), with a molecular weight of 200,000 g/mol. Celanese, formerly known as Ticona, is the current manufacturer for most orthopedic grade UHMWPE, and produces two resins, GUR® 1020 (3.5 million g/mol) and GUR ® 1050 (5.5-6 million g/mol). These resins are most often used by TJR manufacturers around the world, and can be compression molded or ram extruded. Final implants can then be machined into their final form, sometimes from a direct molded part (Kurtz 2009).

The chains of UHMWPE are organized in a semi-crystalline structure, with both sheet-like crystalline lamellae and spaghetti-like amorphous regions (**Figure 1.4**). Most UHMWPE blends exhibit roughly 45 – 50% crystallinity (Pruitt 2005). Lamellae are spaced approximately 50 nm apart, with a thickness from 10-50 nm and approximately 10-50 µm in length (Kurtz 2009). These lamellae provide UHMWPE with added impact strength, in addition to enhanced ductility as they unravel at high strains. This morphology is sensitive to temperature ($T_g$ = –120°C, $T_{melt}$ = 137°C), sterilization treatments, and post-sterilization processing (Atwood et al. 2011; Gerrits & Tervoort 1992; Kurtz et al. 2002; Kurtz 2009). Moreover, such changes in the number, size and quality of lamellae can directly impact tensile and fatigue properties ( a Gomoll et al. 2002;

Atwood et al. 2011; Medel et al. 2007). Some mechanical properties of untreated GUR 1050 UHMWPE at room temperature and body temperature are shown in **Table 1.1**.

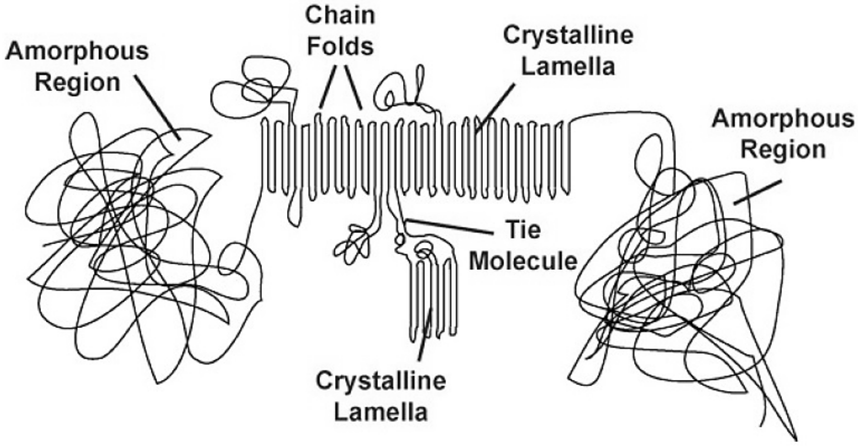

**Figure 1.4** | Morphology of UHMWPE, containing both crystalline phases and amorphous regions (Kurtz 2009).

**Table 1.1 | Properties of GUR 1050 UHMWPE**

| | |
|---|---|
| Molecular Weight | 3-6 million g/mol |
| Crystallinity | 45-50% |
| Density | 0.93 – 0.935 |
| Glass Transition Temperature ($T_g$) | -120 **°C** |
| Melt Temperature ($T_{melt}$) | 135 **°C** |
| Poisson’s Ratio | 0.46 |
| Ultimate Tensile Strength (20-21°C) | 42 – 52.2 MPa |
| True Ultimate Strength (20°C) | 262 MPa |
| Ultimate Tensile Strength (37°C) | 35 MPa |
| Yield Strength (21°C) | 20 – 23 MPa |
| True Yield Strength (20°C) | 26.9 MPa |
| Yield Strength (37°C) | 21 MPa |
| Elastic Modulus (21°C) | 1.0 – 1.39 GPa |
| Elastic Modulus (37°C) | 0.67 GPa |
| Elongation at Break (21°C) | 330% |
| Elongation at Break (37°C) | 375% |
| Shore D Hardness (21°C) | 60 – 65 |
| Fracture Toughness | 3.5 – 4.0 MPa√m |

Adapted from: Pruitt 2005; Li & Burstein 1994; Kurtz et al. 2002; Gencur 2003; Kurtz 2009

### *Deformation under Uniaxial Loading*

UHMWPE’s suitability for TJR application is largely attributed to its toughness as a polymeric biomaterial. The high molecular weight and semicrystalline structure greatly contributes to this toughness, as demonstrated through studies of uniaxial deformation of the polymer. Reorientation of polymer chains and lamellae, in particular, have been shown to contribute to

UHMWPE's strength and ductility. **Figure 1.5** illustrates a typical stress-strain curve of semicrystalline materials, outlining three broad stages of deformation: alignment, chain extension, and unraveling.

While chain alignment in the draw direction tends to occur at low true strains around 0.12, locking of lamellae structures at an angle to the applied force enables resistance to deformation at low draw ratios (**Figure 1.6A**) (Gerrits & Tervoort 1992; Steven M. Kurtz et al. 1998). Coarse slip is primary associated with the unlocking and rotation of these larger lamellae structures, which inevitably align with the applied force at true strains around 0.35 or higher (**Figure 1.6B**) (Steven M. Kurtz et al. 1998). While primary slip systems leading to such depends on fold structure, higher draw ratios of 3 or more tend to be dominated by a (100) [001] single-crystal-like texture (Gerrits & Tervoort 1992). Upon lamellae alignment, unraveling of the crystalline structures promotes a great degree of ductility under plastic loading, achieving impressive elongation values listed in **Table 1.1**. Final fracture derives from microvoid formation and coalescence in amorphous regions (**Figure 1.6B**), followed by fibrillation due to chain extension and eventual backbone failure.

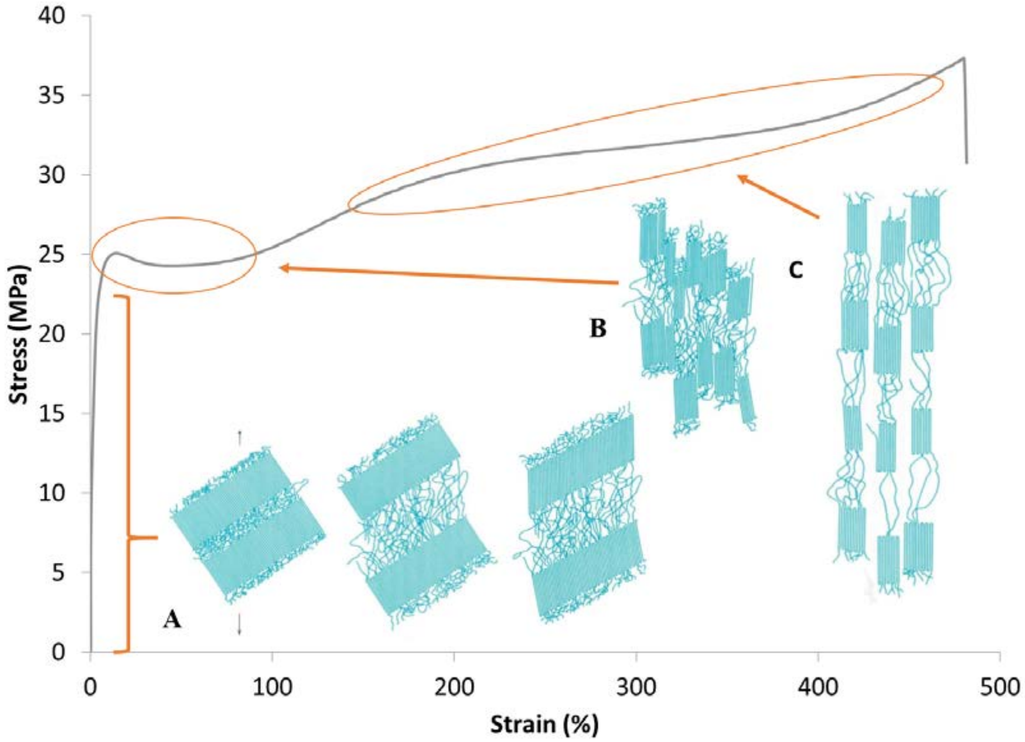

**Figure 1.5 |** Representative engineering stress-strain curve for UHMWPE deformation illustrating microstructural events that define macroscopic deformation. (**A**) Elastic deformation is primarily dominated by extension of amorphous regions, especially tie molecules that link crystalline phases. Extension results in chain alignment at low strains, but lamellae structure remained "locked" at an angle to the pull axis. (**B**) Yielding and permanent deformation correlate with lamellae slip, and alignment of the crystalline regions occurs under sustained force. (**C**) Large plastic strains before break see unraveling of crystalline and amorphous regions, in which much of the tensile force is resisted by covalent bonds in the polymer backbone (Kurtz et al. 2002; Kurtz et al. 1998; Gerrits & Tervoort 1992; *Images adapted from:* Callister 2003).

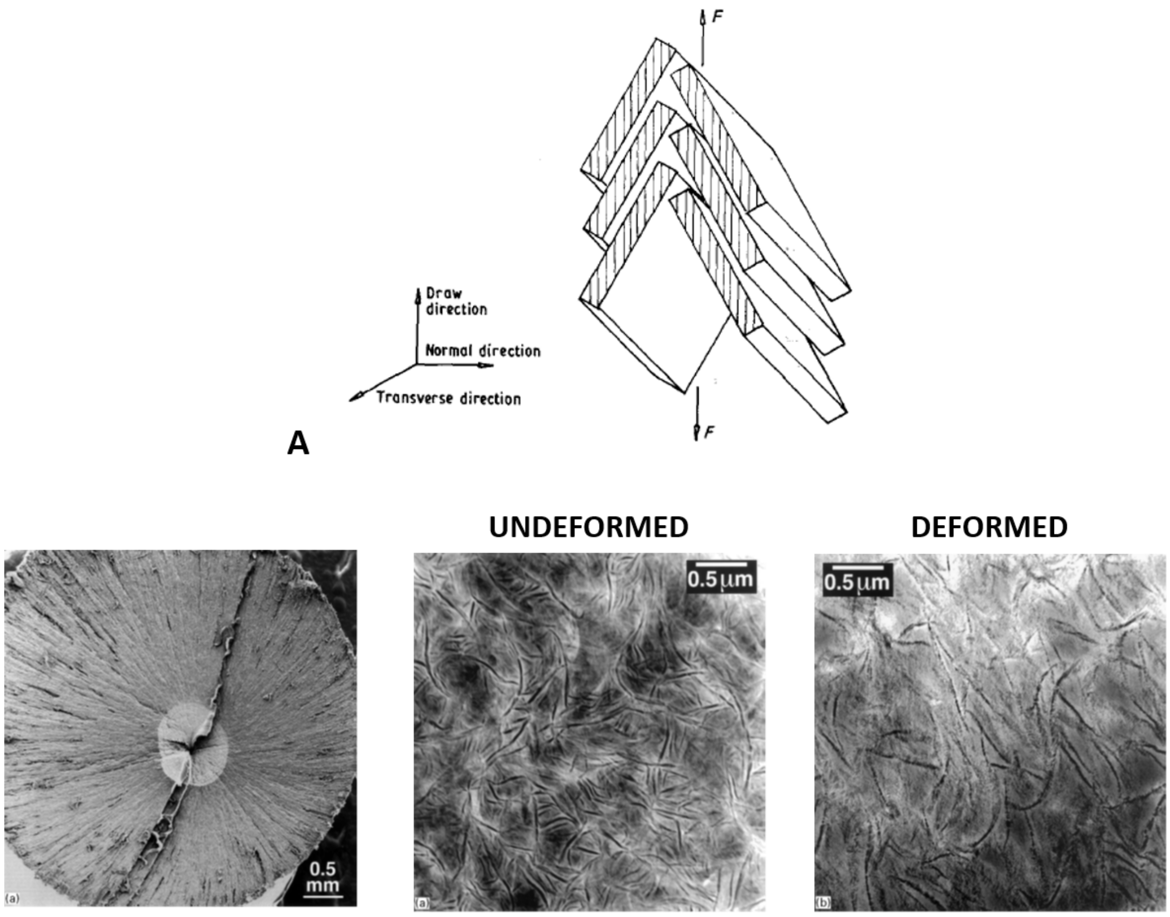

**Figure 1.6** | (**A**) Illustration of lamellar locking that occurs during initialization of plastic flow of UHMWPE (Gerrits & Tervoort 1992). (**B**) Optical micrograph of fracture surface of UHMWPE dogbone, showing crack initiation at an internal microvoid (LEFT), as well as TEM imagery of lamellae structures random orientation in an undeformed sample (CENTER) and elongation and alignment after deformation (RIGHT) (Steven M. Kurtz et al. 1998).

### *Tribological Performance*

The issue of component wear has troubled device manufacturers as early as 1950s (Charnley 1961). UHMWPE has trumped most other biocompatible structural polymers – most notably polytetrafluoroethylene (PTFE, or Teflon) (Kurtz 2009) – in TJRs; however, wear of UHMWPE is still recognized as one of the primary reasons for device revision for hip, knee and shoulder replacements provided its role in osteolysis-induced implant instability (Sobieraj & Rimnac 2009a; K. I. Bohsali et al. 2006; Dumbleton et al. 2002).

UHMWPE wear debris can be generated by abrasive, adhesive and fatigue mechanisms, as demonstrated through analysis of retrieved devices (**Figure 1.7**) (McKellop 2007). Abrasive wear is primarily associated with hard, sharp asperities that plough into a softer UHMWPE surface. Such wear can derive from either third body cement or bone particles that traverse the articulating space or second body wear generated by a roughened counter-bearing surface, which can both scratch or gouge the surface in isolated or repetitive patterns. Adhesive wear can be generated by chemical interactions between asperities on both a hard (alloy or ceramic) bearing and soft polymer surface, which can result in the softer asperity sticking to the harder bearing and being pulled away. Cyclic contact stresses during articulation can also create shear stresses that peak just below the surface, resulting in crack initiation and propagation that can liberate debris, exemplary of fatigue wear. This can result in instances of subsurface cracking, pitting, delamination and fracture (**Figure 1.7C-E**). (Pruitt & Chakravartula 2011; McKellop 2007; Bartel et al. 2006)

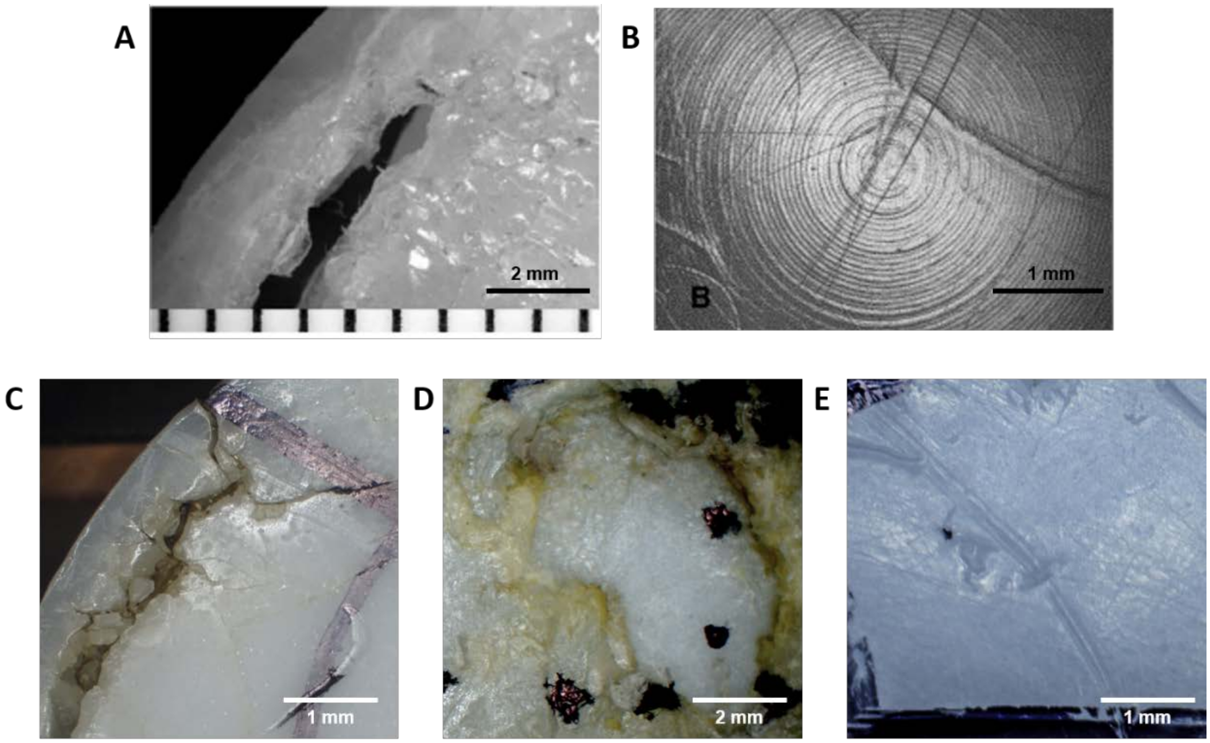

**Figure 2.7** | Damage seen on retrieved UHMWPE bearings, including: (**A**) fracture and subsurface cracking on a tibial insert of a TKR; (**B**) scratching across circumferentially-aligned machine marks on an acetabular liner of a THR; and TSR glenoids damaged by (**C**) cracking and fracture, (**D**) delamination and (**E**) pitting (Muratoglu et al. 2003; Harman et al. 2011; Farzana Ansari et al. 2014).

UHMWPE wear can be attributed to microstructural evolution under cyclic sliding and/or rolling motion. Simulator studies and retrieved implants have revealed plastic deformation at the subsurface layer of UHMWPE components in the form of lamellae alignment (**Figure 1.8**), similar to that seen in tensile testing shown in **Figure 1.6**) (Edidin et al. 1999; Kurtz et al. 2000). This "plasticity-induced" damage layer has been reproduced through unidirectional pin-on-disk testing (Klapperich et al. 1999). Such alignment presents a deviation from otherwise randomly oriented lamellae in the UHMWPE structure, and thus introduces anisotropy which can reduce strength and increase liberation of wear debris under multidirectional motion, especially considering abrasive conditions or cyclic loading (Wang et al. 1997; Patten et al. 2013; Patten et al. 2014).

As a result, crosslinking the backbone chains through gamma or e-beam radiation sources has been widely adopted to combat chain alignment and dramatically improve wear resistance (Muratoglu et al. 1999; Ries & Pruitt 2005; Kurtz 2009). However, crosslinked UHMWPE has been shown to generate smaller wear debris, which can have a greater potency with regard to osteolytic pathways (Williams et al. 2007). Furthermore, tradeoffs in oxidative and fatigue crack propagation resistance for highly crosslinked UHMWPE, as discussed in the following section, suggest greater potential for fatigue-based wear mechanisms that result in delamination, pitting and gross fracture seen in **Figure 1.8** (Atwood et al. 2011). Fatigue wear becomes especially concerning for non-conforming bearing couplings, such as knees and shoulders, or near design features with sharp corners or small radii, all of which can exhibit elevated stresses (Furmanski et al. 2009; Bartel et al. 1986).

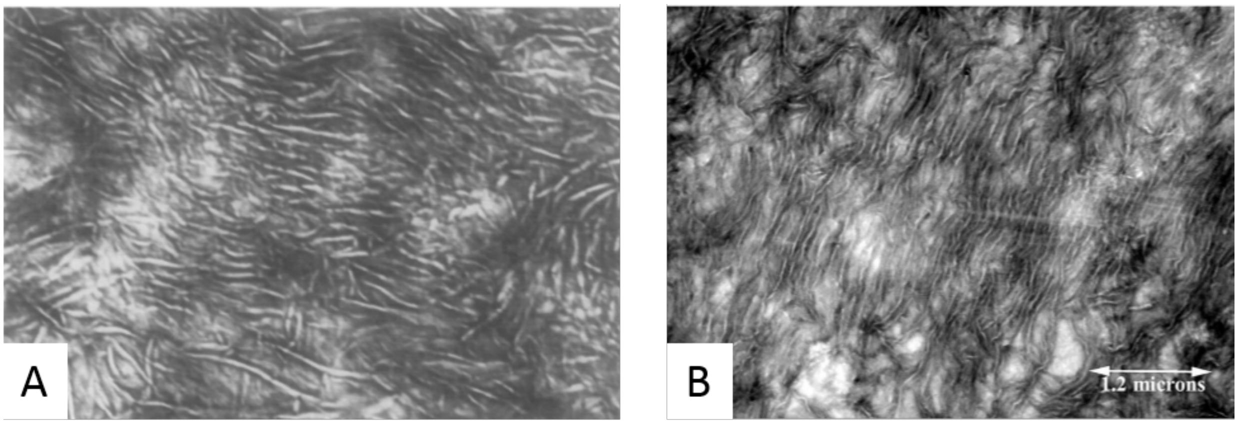

**Figure 1.8** | Evidence of a plasticity-induced damage layer (i.e. lamellae alignment due to articulation) in UHMWPE components as seen in (**A**) simulator studies and (**B**) retrievals (Edidin et al. 1999; Kurtz et al. 2000).

### *Cyclic Loading*

Cyclic loading on UHMWPE components can present itself through several mechanisms *in vivo*. Repeated sliding and/or rolling through articulation can result in alternating stresses at the surface. For example, contact stresses on tibial inserts for knee replacements have been shown to cycle from tension (15 MPa) to compression (-40 MPa) (Bartel et al. 1986). Contact stresses can be supplemented by bending forces that occur along the component rim, as seen with glenoids in the shoulder that experience eccentric loading (Anglin et al. 2000). Impingement or repeated dislocations can also introduce recurring loads, especially in the presence of stress concentrations (Furmanski et al. 2009; Ansari, Chang, et al. 2013). Furthermore, cyclic loading *in vivo* can be multiaxial, fully reversible (tension-compression), or even supplemented by singular overloads (e.g. falls). Implant damage resulting from these cyclic loads can range from submicron wear debris liberation to catastrophic fracture.

The degree of damage imparted by cyclic loading varies depending upon specific UHMWPE formulation, magnitude of loading and number of cycles (Krzypow & Rimnac 2000; Meyer & Pruitt 2001). Krzypow and Rimnac (2000) assessed fully-reversed cycling of GUR 4150

UHMWPE for clinically relevant alternating true strains up to ±0.12. All strain levels resulted in strain softening to roughly the same degree in tension and compression, and each sample reached a "steady-state" in less than 300 cycles. This steady-state region continued to exhibit hysteresis, however, which was attributed to viscous (non-recoverable) deformation seen at temperatures above $T_g$.

Meyer and Pruitt (2001) also evaluated cyclic loading effects on nonsterilized and sterilized GUR 4150 using zero-to-tension loading at higher alternating true strain values of ±0.12 to ±1. Their study also found cyclic strain softening that persisted through 100 cycles of testing, even at the lowest alternating strains levels. Furthermore, whitening of specimens reflecting build-up of microvoids and fibrillation during testing (**Figure 1.9**). Defect accumulation appeared to worsen with sterilized/aged samples compared to untreated UHMWPE, most likely due to oxidative chain scission events that weaken to amorphous regions of the polymer (Meyer & Pruitt 2001).

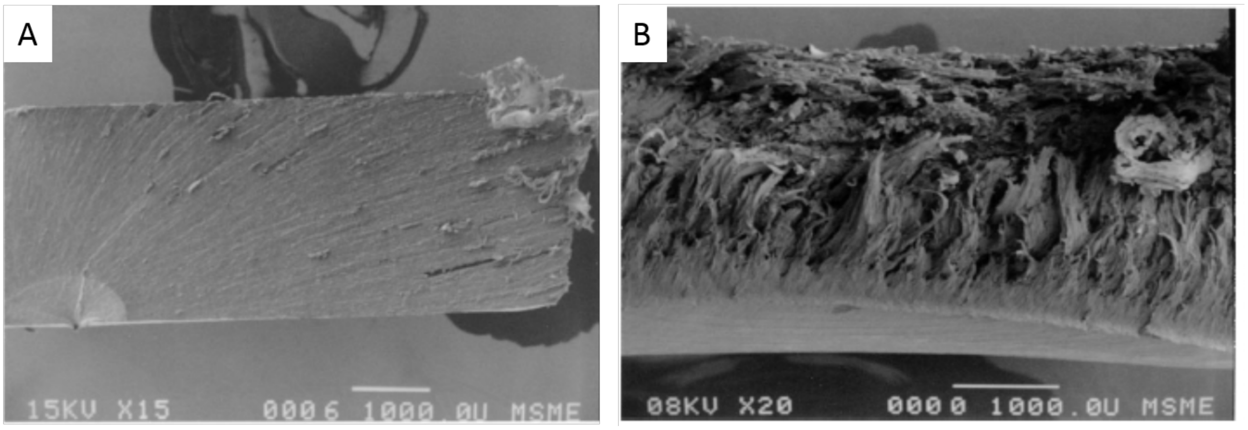

**Figure 1.9** | Scanning electron micrographs of (A) untreated UHMWPE and (B) sterilized UHMWPE fracture surfaces following cyclic loading. Sterilized UHMWPE shows significant fibrillation due to defect accumulation in the form of microvoids (Meyer & Pruitt 2001).

Persistence strain softening and hysteresis effects at low cycle fatigue reflect damage accumulation that can occur within a few days – if not hours – of an implant's life. Such initial defect nucleation and coalescence can contribute to propagation later at millions of cycles of use. High cycle fatigue analyses have demonstrated such damage accumulation at the nanometer scale. Baker et al. (2001) utilized small-angle X-ray scattering to reveal submicron crack accumulation while cycling sterilized UHMWPE dogbone specimens at 2 million cycles or less, or within roughly 2 years of clinical use. Further studies examining defect initiation and propagation for millions of cycles will be discussed in Chapter 4.

## 1.3 Evolution of UHMWPE in TJRs

The introduction of UHMWPE to TJR application traces back to the early 1960s, when Sir John Charnley first published his findings on the design of a functional hip replacement (Charnley 1961). Charney's designs initially utilized an acetabular cup made entirely from polytetrafluoroethylene (PTFE, more commonly known as Teflon), but dramatic wear-induced failures of the devices forced him to look to other options. Harry Craven, Charnley's technician at the time, had obtained UHMWPE from a traveling salesman, and after three weeks of testing on a primitive pin-on-disc wear tester in the Charnley home, demonstrated a significant reduction in wear. Charnley's further testing – while often unorthodox – convinced him to implant the material into patients as early as 1962 (Charnley 1963; Kurtz 2009). UHMWPE has remained a gold standard for bearing surfaces in TJRs since then.

UHMWPE's long history in the orthopedic domain has been associated with numerous processing changes that have significantly impacted implant performance and longevity *in vivo*. Medical grade UHMWPE is primarily polymerized by Celanese (formally known at Ticona, Hoeschst, and Ruhrchemie AG), which processes GUR (Grancular UHMWPE Ruhrchemie) resins. Early generations of GUR (GUR 1120 and 1150) originally included calcium stearate, an additive used to help remove residual catalyst components that had corrosive potential (Kurtz 2009). However, controversy surrounding the role of calcium stearate in fusion defects, as well as improved processing methods, led to its removal from Celenese's manufacturing line. Modern resins include GUR 1020 and 1050, which are consolidated by third parties, such as Orthoplastics, MediTECH, and Westlake Plastics, and then provided to device manufacturers (Kurtz 2009).

While GUR 1020 and 1050 are predominantly used today, numerous modifications to these UHMWPE resins during post-processing and sterilization have been utilized in joint replacements over the past few decades. The 1980s saw a joint Dupont-Depuy Orthopedics venture that led to the development of Hylamer$^{TM}$ Enhanced Bearing Polymer, an UHMWPE formula that is subjected to a high pressure, high temperature, and controlled cooling process (Rockwood & Wirth 2002; Li & Burstein 1994). This increased crystallinity of the polymer from 50% to up to 70%, without a change in molecular weight, but with improved yield strength, tensile modulus, creep resistance, impact resistance and fatigue crack propagation resistance – but all in an unsterilized form (Baker et al. 2000; Li & Burstein 1994; Rockwood & Wirth 2002; Kurtz 2009).

By the 1990s, Hylamer$^{TM}$ hip, knee and shoulder components were integrated into the predominant sterilization procedures of the time, a 25 kGy dose of gamma irradiation in an air environment, and packaged in air permeable packages (Rockwood & Wirth 2002; Kurtz 2009). Performance of Hylamer$^{TM}$ *in vivo* provided a dramatically different picture than *in vitro* tests predicted. Significant damage to the bearing surface was noted on retrieved implants, primarily associated with chemical embrittlement of the polymer (**Figure 1.10**). This rapid deterioration of implants motivated a surge of studies attempting to understand the role of gamma irradiation sterilization methods on polyethylene durability (Rockwood & Wirth 2002; Sutula et al. 1995; Rimnac et al. 1994; Livingston et al. 1997). The collective effort revealed two important consequences of radiation treatment on UHMWPE: first, crosslinking between the polymer backbone chains, and second, the presence of residual free radicals within the amorphous that fuel material breakdown via oxidation.

The issue of oxidative embrittlement took the front stage in the late 1990s. Free radicals that are generated during irradiation can remain in the UHMWPE bulk for years, eventually reacting with oxygen while sitting on the shelf or *in vivo* (Ries & Pruitt 2005). Such reactions lead to chain scission, generating oxidized products such as hydroperoxides ketones, acids, alcohols and esters (Kurtz 2009). As a result, the polymer suffers from a loss in molecular weight and build-up of large molecular byproducts that inhibit chain mobility, causing degradation in material properties including a loss of toughness, strength, ductility, stiffness, and durability (Sobieraj & Rimnac 2009a). This results in reduced resistance to wear and fatigue *in vitro* and *in vivo*, even resulting in failures seen in **Figure 1.10** (Bohl et al. 1999; Ries & Pruitt 2005; Ries et al. 1996). Such oxidation has been correlated with higher mechanical stresses through observation of retrievals, indicating a greater propensity for gross wear or catastrophic fracture (Eyerer et al. 1987; Jahan et al. 1991). The oxidative effect took a greater toll on Hylamer$^{TM}$ properties compared to conventional, leading to a transition to gamma-inert radiation methods to reduce free radical generation, gas plasma sterilization to avoid irradiation altogether, and eventually complete discontinuation of the formulation (Sutula et al. 1995; Rockwood & Wirth 2002).

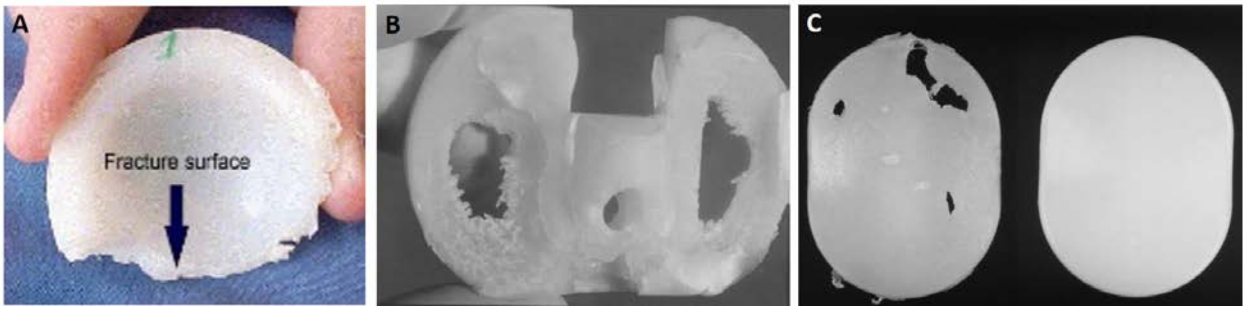

**Figure 1.10** | Oxidized, worn and fractured (**A**) hip, (**B**) knee and (**C**) shoulder components, all made from Hylamer$^{TM}$ and sterilized using gamma irradiation in an air environment (Burger et al. 2007; Rockwood & Wirth 2002; Kennedy et al. 2000).

Even with advances in resin generation and consolidation and a more robust gamma-inert sterilization process by the early 2000s, conventional UHMWPE component longevity still suffered from bearing surface wear during everyday articulation. UHMWPE represented a significant improvement over Charnley's initial PTFE designs in preventing gross deformation, but even relatively small volumes of wear debris were linked to periprosthetic osteolysis, or bone loss, that ultimately cause implant instability and a need for revision surgery (**Figure 1.11**) (Dumbleton et al. 2002; Willert & Semlitsch 1977; Kurtz 2009). This immunological response is associated with UHMWPE particles roughly 0.1-10 µm in size, which can be generated through abrasive, adhesive or fatigue wear mechanisms depending on joint design and kinematics (McKellop 2007). Improving UHMWPE wear resistance has long been a driving force behind material enhancement, and studies on the influence of gamma sterilization provided a significant breakthrough. Despite generation of free radicals, irradiation methods provided a side-benefit of crosslinking between UHMWPE backbones. Such crosslinking led to a drastic improvement in wear resistance, reducing wear volumes almost 50-80% *in vitro* for doses of 50-200 kGy and leading to a substantially lower risk of osteolysis (Muratoglu et al. 2001; Muratoglu et al. 1999;

McKellop, Shen, Lu, et al. 1999; McKellop, Shen, DiMaio, et al. 1999; Kurtz et al. 2011). This led to establishment of first generation highly crosslinked UHMWPE as the new “gold standard” for many manufacturers today (**Figure 1.12**).

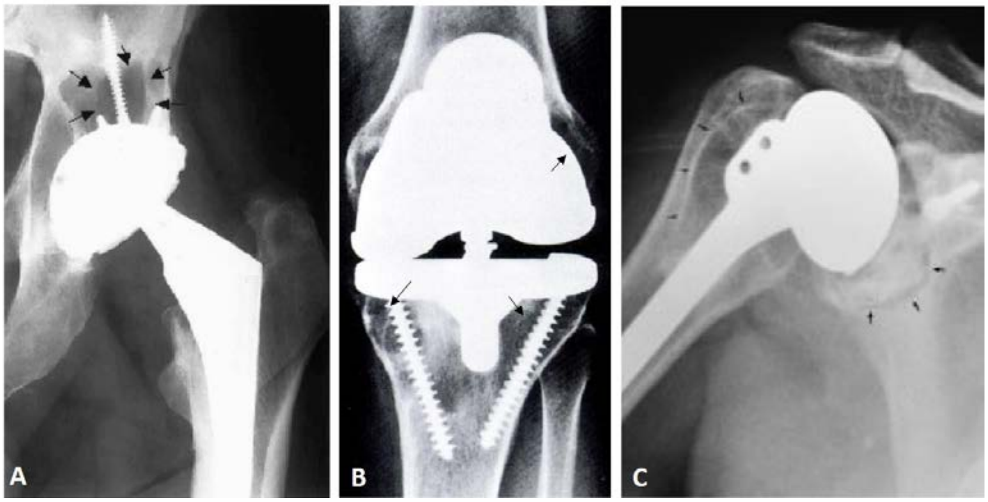

**Figure 1.11** | Radiographs demonstrating regions of bone loss (black arrows) associated with UHMWPE wear particle-induced osteolysis for a (**A**) hip, (**B**) knee and (**C**) shoulder.

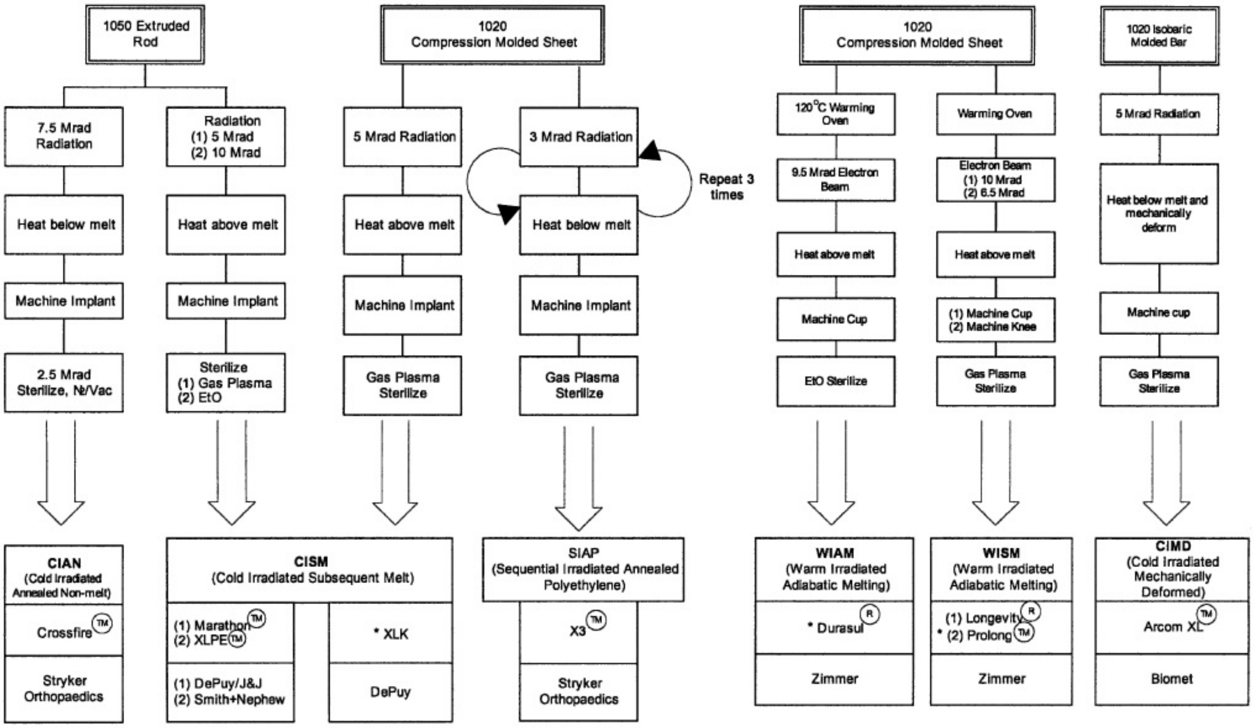

**Figure 1.12** | Flow chart of known manufacturing processes for UHMWPE formulations used by major orthopedic companies in the market as of 2005. Note that all listed formulations utilize moderate to high crosslinking doses, followed by a heat treatment either above or below the melt temperature (Ries & Pruitt 2005). *(*Available in Knees)*

Still, as with gamma irradiation sterilization, additional doses of irradiation only exacerbate the issue of free radical release and subsequent oxidation, especially *in vivo* (Reinitz et al. 2014). Moreover, increased radiation doses significantly reduce UHMWPE's resistance to fatigue crack propagation (Bradford et al. 2004; Atwood et al. 2011; Pruitt 2005; Baker et al. 1999a). Such tradeoffs have led to further modifications in materials processing, especially in an effort to reduce oxidation potential.

Most manufacturers today have introduced post-irradiation treatments to reduce or completely annihilate free radicals in the polymer bulk. Post-irradiation heat treatments that have been popularly adopted include annealing below and remelting above the UHMWPE melt temperature. While remelting results in complete neutralization of free radicals, it also results in melting of crystalline regions, which are not fully restored after cooling to room temperature (Atwood et al. 2011; Ries & Pruitt 2005). This contributes to reduced tensile and fatigue properties compared to conventional UHMWPE (Atwood et al. 2011). Annealing below the melt temperature allows not only preservation of crystalline structure, but even enhanced crystallinity; however, this comes at the cost of residual free radicals in the system which can eventually oxidize *in vivo* (Medel, Kurtz, Parvizi, et al. 2011).

While post-irradiation heat treatments serves to address the oxidation issue, still unresolved is the issue of highly crosslinked UHMWPE's reduced resistance to fatigue crack growth. **Figure 1.13** compares crack growth under cyclic loading for the several formulations of UHMWPE used in TJRs today. Highly crosslinked and subsequently remelted materials demonstrate the least resistance to fatigue crack growth, but the highest resistance to oxidation. Annealing does not provide the full benefits of free radical elimination through a single treatment, but can improve resistance to fatigue crack growth relative to remelted materials.

The consequences of reduced resistance to crack growth have manifested themselves in catastrophic implant failures. **Figure 1.14** shows several hip and knee replacements in which fracture occurred *in vivo* within 3 months to 8 years – well under the predicted lifetime of 20 and 15 years, respectively (Pruitt & Chakravartula 2011). These implants were all crosslinked at doses ranging from 25 kGy to 100 kGy, with or without post-irradiation heat treatments (Pruitt et al. 2013; Ansari, Chang, et al. 2013; Ansari, Patten, et al. 2013; Furmanski et al. 2009). For each of these implants, fractures initiated at stress concentrations created by design features incorporated to improve stability, such as a liner locked mechanisms on acetabular components or a tibial post for knees. Such stress concentrations increase the propensity for crack initiation and propagation. The role and evolution of these design features will be discussed in the next section.

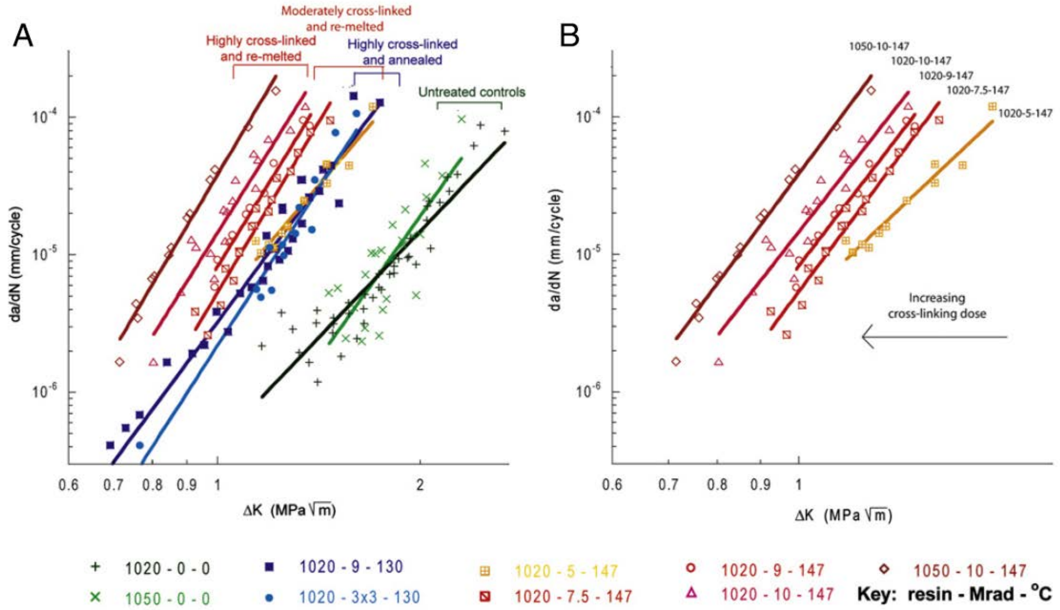

**Figure 1.13** | Fatigue crack propagation data for various formulations of UHMWPE, including highly crosslinked and remelted, moderately crosslinked and remelted, highly crosslinked and annealed and untreated samples. Data displays crack growth rates listed on the ordinate, while applied stress intensities driving crack growth are listed on the abscissa. Data shows a trend toward a decreased resistance to crack propagation with increasing crosslinking dose, as well as with the introduction of remelt post-irradiation processing compared with annealing below melt (Atwood et al. 2011).

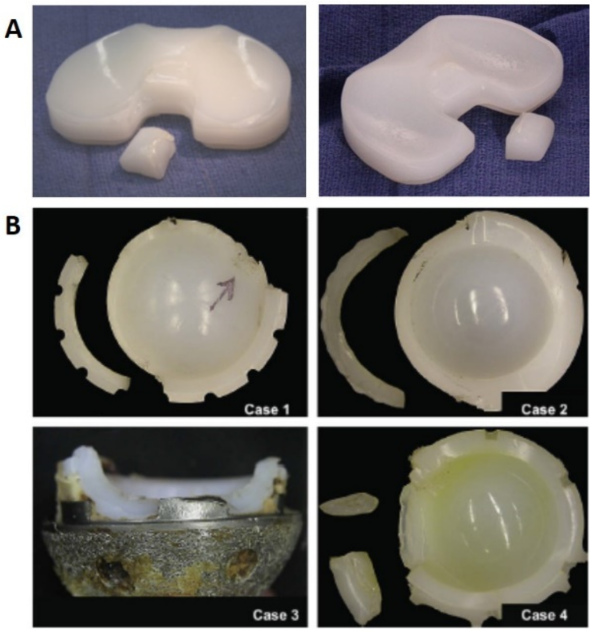

**Figure 1.14 |** Fractured crosslinked UHMWPE components. (**A**) Two light-to-moderately crosslinked (25-40 kGy) knee components that suffered fractures at the tibial post, used to improve kinematic stability for patients without sufficient ligament support. (**B**) Four moderately to highly crosslinked (50-100 kGy) and subsequently remelted acetabular liners in which fracture occurred along the component rim. (Pruitt et al. 2013; Ansari, Chang, et al. 2013; Ansari, Patten, et al. 2013; Furmanski et al. 2009)

Several second-generation UHMWPE have been developed since the advent of irradiated and remelted or annealed polymer formulations in the TJR market. To address the issue of *in vivo* oxidation, some manufacturers have moved towards crosslinked formulations of UHMWPE that have been infused with antioxidants. Most notable is the use of Vitamin E, which has shown improvement in wear, toughness, and fracture resistance; however, such properties show a high dependence on the method of incorporating the antioxidant into UHMWPE, as it can lead to diminished crosslinking and concomitant loss of wear resistance if blended into the resin (Oral, Godleski Beckos, et al. 2008). Other second-generation UHMWPEs have attempted to address the reduction in toughness that comes as a trade-off with wear resistance achieved with crosslinking. Manufacturers such as Stryker (Kalamazoo, Michigan) have recognized the improved fatigue resistance for annealedformulations of UHMWPE, and adopted a sequentially-annealed process that involves repeated radiation and annealing treatments to provide optimal wear and oxidation, without complete loss of fatigue resistance (Ries & Pruitt 2005; Sobieraj & Rimnac 2009a) (**Figure 1.12**). Biomet also produces ArCom XL, a highly crosslinked polyethylene that is mechanically deformed and reportedly more resistance to wear and fatigue (Kurtz et al. 2006; Sobieraj & Rimnac 2009b). Finally, high pressure high temperature materials are being explored due to their enhancement of crystallinity and thus improvement of tensile properties as well as improved resistance to fatigue crack propagation (Simis et al. 2006). Some of these formulations have already been introduced into patients today, but recently enough that little is known about their clinical performance.

The retrievals shown in **Figure 1.10** and **Figure 1.14**, in combination with radiographic evidence of osteolysis in **Figure 1.11**, demonstrate the known clinical consequences of tradeoffs exhibited by current formulations of highly crosslinked UHMWPE. These tradeoffs in material properties (**Table 1** and **Figure 1.15**) still provide significant challenges to improving device longevity today. Understanding how changes in material microstructure via sterilization and post-processing techniques provide a crucial step forward for second generation crosslinked formulations introduced in the future. Over 50 years of history with UHMWPE have resulted in failed attempts at improving mechanical properties (Hylamer$^{TM}$ with gamma-air sterilization), but also introduced novel microstructural changes in the form of crosslinking to greatly improve resistance to clinical osteolysis. As the orthopedics industry moves forward, careful attention should be paid to not only material compositional changes that may come with the introduction of antioxidants, but also the design-material interaction in implant performance, as this can result in elevated stresses resulting in catastrophic fracture.

**Table 1.1 | Effects of Crosslinking and Heat Treatments on UHMWPE Properties**

| Material Property | Untreated UHMWPE | Minimally Crosslinked (25-30 kGy) | Highly Crosslinked & Annealed (90-100 kGy, 110-130 °C) | Highly Crosslinked & Remelted (100 kGy, 147-150 °C) |
|---|---|---|---|---|
| Crystallinity | 50.4% | 51.3% | 60.8% | 45.7% |
| Elastic Modulus (MPa) | 453 | 433 | 548 | 407.5 |
| Yield Strength (MPa) | 23.5 | 24.1 | 24.8 | 21.4 |
| True Yield Strength (MPa) | 26.9 | 27.3 | 27.9 | 24.5 |
| Ultimate Strength (MPa) | 50.2 | 47.1 | 46.4 | 37.1 |
| True Ultimate Strength (MPa) | 262 | 223 | 162 | 123 |
| Fracture Toughness (MPa√m) | 4.0 | 4.5 | 2.8 | 3.0 |

Adapted from: Pruitt 2005; Gencur 2003; Kurtz et al. 2002; Atwood et al. 2011

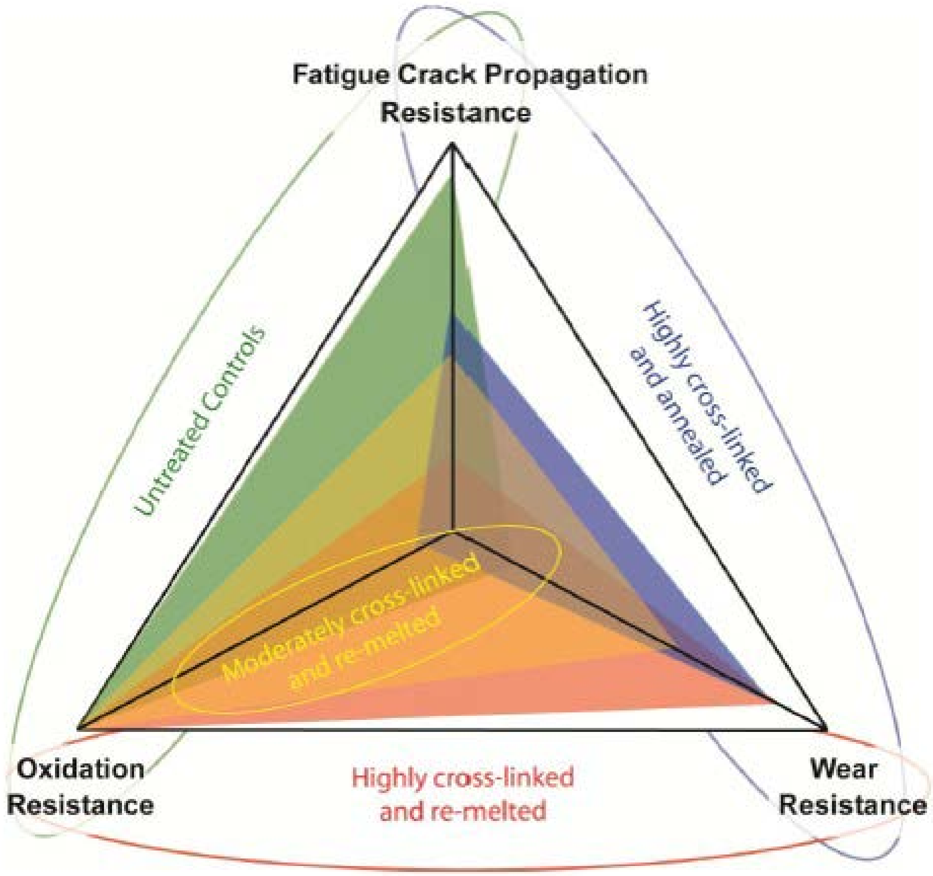

**Figure 1.15** | Tradeoffs in UHMWPE performance that face manufacturers today (Atwood et al. 2011).

# Chapter 2 – Clinical Fracture of UHMWPE used in Total Joint Replacements: Confluence of materials selection, component design and kinematics

## 2.1 Introduction

The evolution of UHMWPE has seen dramatic changes in the polymer's microstructure, with the primary goal of reducing wear-induced osteolysis and subsequent implant loosening (Kurtz 2009). This evolution has led us to a new generation of UHMWPE formulations in the past decade that are highly crosslinked (50-100 kGY) in nature with exceptional resistance to *in vivo* wear (Muratoglu et al. 1999). However, this modern material has come with significant tradeoffs in its resistance to oxidation and its resistance to fatigue crack propagation, leading to degradation of mechanical properties, device embrittlement and/or fracture (Atwood et al. 2011; Currier et al. 2013; Furmanski et al. 2009).

While these consequences have been soundly established through numerous experimental investigations in the past two decades (see **Chapter 3**), their initial discovery came only after implantation and subsequent retrieval of failed devices from patients. Explants have historically provided the most robust capture of a material's *in vivo* performance, especially for UHMWPE, which cannot be imaged using traditional radiographic techniques. Fracture of the polymer implant has primarily presented through two damage modalities on explants: fatigue wear and gross fracture. Fatigue wear occurs on the surface of retrieved bearings in the form of delamination, pitting or subsurface cracking, and initiates just below the UHMWPE surface due to cyclic sliding contact (McKellop 2007; Bartel et al. 1986). Gross fracture can also occur as a result of significant contact fatigue, or due to cyclic loading near a stress concentration that can initiate and propagate cracks. Oxidative embrittlement can contribute to and exacerbate both of these fracture damage modes (Ansari, Chang, et al. 2013; Williams et al. 1998; Reinitz et al. 2014; Pruitt et al. 2013; Rockwood & Wirth 2002).

Both fatigue wear and gross fracture are directly affected by device design. This dissertation primarily focuses on gross *in-vivo* fracture of implants and addresses the origin of this failure mechanism in various joint replacement designs. The following three sections outline how design features in current UHMWPE joint replacements can influence severe gross fracture events *in vivo*. A historical evolution of each design feature – the tibial post for the knee, the liner locking mechanism on a hip, and thickness/conformity tradeoffs for the shoulder – is presented, followed by a case study evaluating one or more fracture events for each of these clinical scenarios.

## 2.2 Knee Replacements: Posterior-Stabilized Tibial Inserts

The earliest known knee arthroplasty devices were introduced in the late 18th century, in the form of a fully-constrained hinge joint (Kurtz 2009). Early failures led to abandonment of this device;

resurgence of TKR devices came nearly a century later in the 1970s with the incorporation of UHMWPE on the tibial bearing surface (Ewald 1975). Implants used in the knee underwent several transformations including the introduction of unicondylar and bicondylar replacements, as well as patellar replacements (**Figure 2.1**).

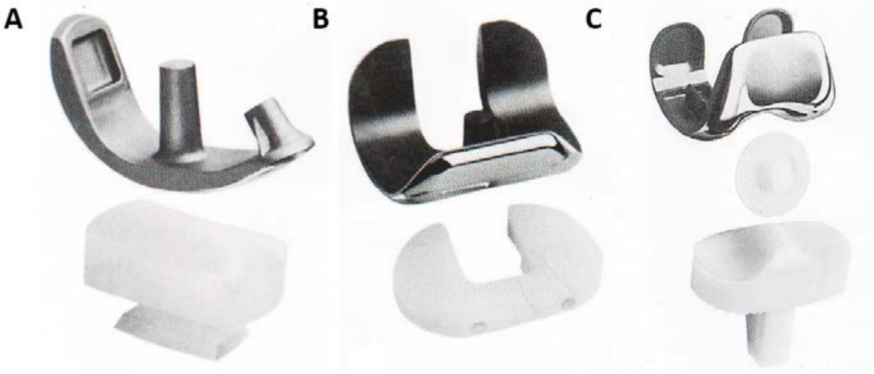

**Figure 2.1 |** Knee replacements from the 1970s, including (A) unicondylar, (B) cruciate-sparing bicondylar, and (C) cruciate-sacrificing bicondylar devices with a patellar replacement (Kurtz 2009).

Bicondylar replacements were designed for both "cruciate-sparing" and "cruciate-sacrificing" installation, referring to the retention or removal of the posterior cruciate ligament (PCL), respectively. The introduction of the latter derived from non-optimal performance of the PCL after arthroplasty due to progression of disease or surgically-induced weakening of the ligament (Kurtz 2009). However, removal of the PCL also resulted in insufficient anterior-posterior stability, restricted joint flexion, and increased potential for posterior sublaxation (Insall et al. 1979; Insall et al. 1976). As a result, the "posterior-stabilized" (PS) Total Condylar Prosthesis was introduced with a post-cam system to replace the PCL and constrain flexion-extension events during stair-climbing and sitting movements (**Figure 2.2**). This led to a marked improvement in patient range of motion (Kurtz 2009; Rodriguez et al. 2001).

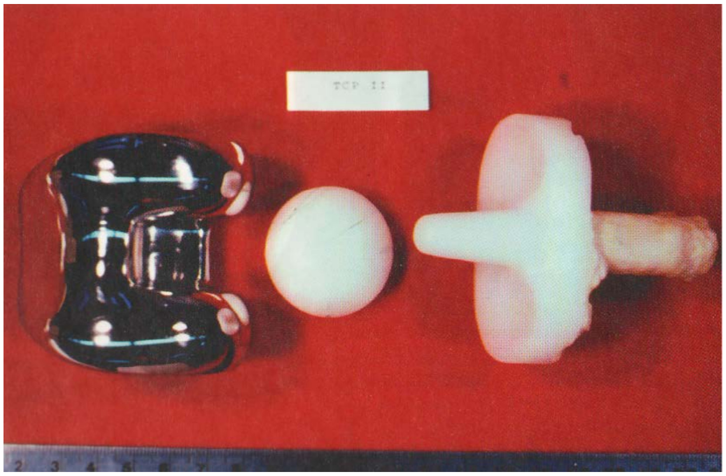

**Figure 2.2** | Posterior-stabilized Total Condylar Prosthesis, containing a vertical post on the tibial insert and a metal cam on the femoral component to stabilize flexion-extension during articulation (Kurtz, 2009).

The post-cam system success is primarily attributed to improving femoral rollback by pinning tibiofemoral contact more posteriorly, restraining relative motion of the two components during flexion (**Figure 2.3**) (Nakayama et al. 2005; Li et al. 2005; Hamai et al. 2008; Huang et al. 2007; Morra & Greenwald 2005). This effectively increases the amount of stable flexion that can be achieved by a patient, even enabling extreme movements such as kneeling or stair-climbing (Morra & Greenwald 2005). As a result, the posterior post sees repetitive shear loading while under flexion, which can result in peak contact stresses at the surface ranging from 22 to 34 MPa, near or above the yield strength of UHMWPE (Nakayama et al. 2005; Pruitt 2005). Contact stresses at the post-cam interface can also increase by 10-30 MPa when considering 1-10° of axial internal rotation between the two components (Li et al. 2004). Furthermore, with increased flexion, post-cam contact (and therefore the location of load) shifts superiorly along the post, creating a greater moment arm relative to the component base (Nakayama et al. 2005).

Post contact with the femoral component is not limited to the posterior side: anterior post contact with the intercondylar notch can occur during low flexion events or even neutral stance (Li et al. 2005; Stoller et al. 2011; Banks et al. 2002; Callaghan et al. 2002; Hamai et al. 2008). Such contact prevents anterior sliding of the tibial insert relative to the femoral condyles, effectively replacing the anterior cruciate ligament (ACL) (**Figure 2.3**). Removal of the ACL allows for more posterior contact of the tibiofemoral system, enhancing range of motion. Consequently, hyperextension of the two components can occur even with neutral skeletal alignment, influenced by surgical positioning of the implant such as the posterior slope (inclination) of the tibial insert and/or anterior femoral roll (Li et al. 2005; Stoller et al. 2011). Such positioning can lead to dynamic hyperextension during gait, resulting in high interfacial slip velocities as high at 20 cm/s during heel strike (Stoller et al. 2011).

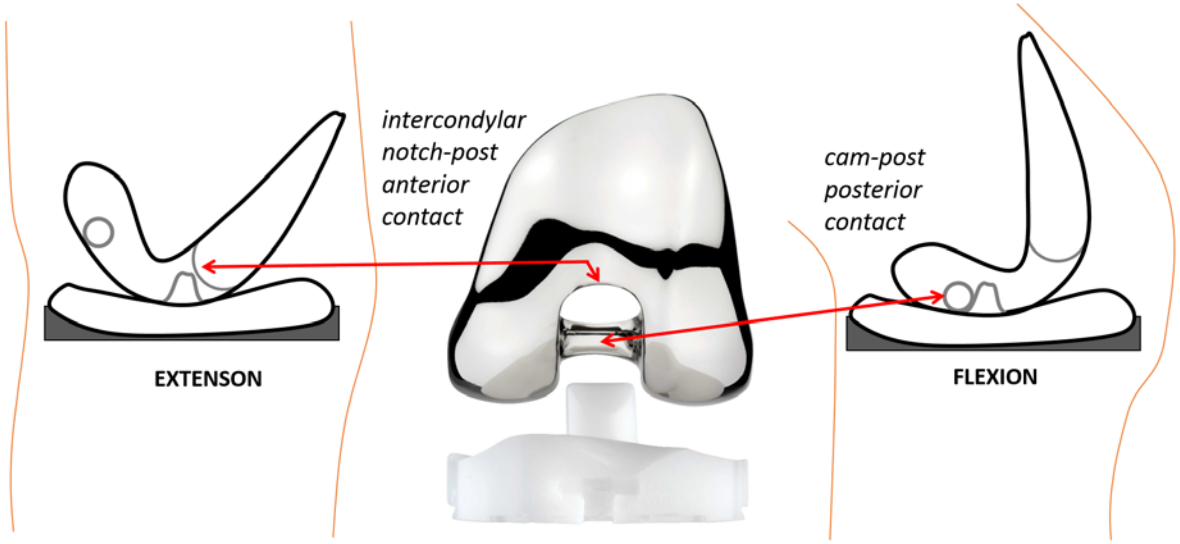

**Figure 2.3** | Illustration of contact during extension and flexion of the knee. Extension can generate anterior contact due to contact between the intercondylar notch and post. Stable flexion is achieved through posterior contact of the cam and post. Rotation about the post can also influence post contact depending on implant design.

Cyclic loading, high velocity impact, variable surgical positioning, and internal rotation provide a complex stress environment which, when combined with a stress riser such as the tibial post, has resulted in impingement, dislocation, severe delamination and pitting wear, or even fracture (Puloski et al. 2001; Mikulak et al. 2001; Mauerhan 2003; Callaghan et al. 2002; Nakayama et al. 2005; Li et al. 2005; Stoller et al. 2011; Lombardi et al. 1993; Banks et al. 2002).

The following case study takes a closer look at *in vivo* fracture of the tibial post in two PS tibial inserts that were gamma-sterilized (25-40 kGy) in an inert environment. This sterilization scheme delivers a moderate amount of crosslinking. The mechanisms of failure were determined through fractography, using both optical microscopy and scanning electron microscopy (SEM), as well as oxidative analysis using Fourier Transform Infra-Red (FTIR) spectroscopy.

### 2.2.1 Case Report: Fractured Tibial Posts in Moderately Crosslinked Zimmer Legacy Posterior-Stabilized (LPS) Tibial Plateaus

Two cases of tibial post fracture in two patients were investigated. Both patients received Legacy Posterior-Stabilized (LPS) Zimmer NexGen (Warsaw, Indiana) implants. Both were revised due to post fracture 8 years after surgery.

*Patient A* (*Implant A*), a 58 year-old man (215 pounds, BMI=32.7), had primary total knee replacement performed in 2002 for post-traumatic arthrosis. The patient led an active lifestyle as a college football coach and did well with no knee pain. After 8 years, he developed swelling, pain, and instability that began acutely after an episode of leg extension while performing leg curls with 90 pounds. His right knee had a large effusion (excess fluid accumulation) and a range of motion from a few degrees of hyperextension to 110 degrees of flexion. There was no obvious varus, valgus, or flexion instability. Post-operative x-rays indicated proper alignment of the TKR (**Figure 2.4**) without excessive posterior slope of the tibial component or significant flexion or extension of the femoral component.

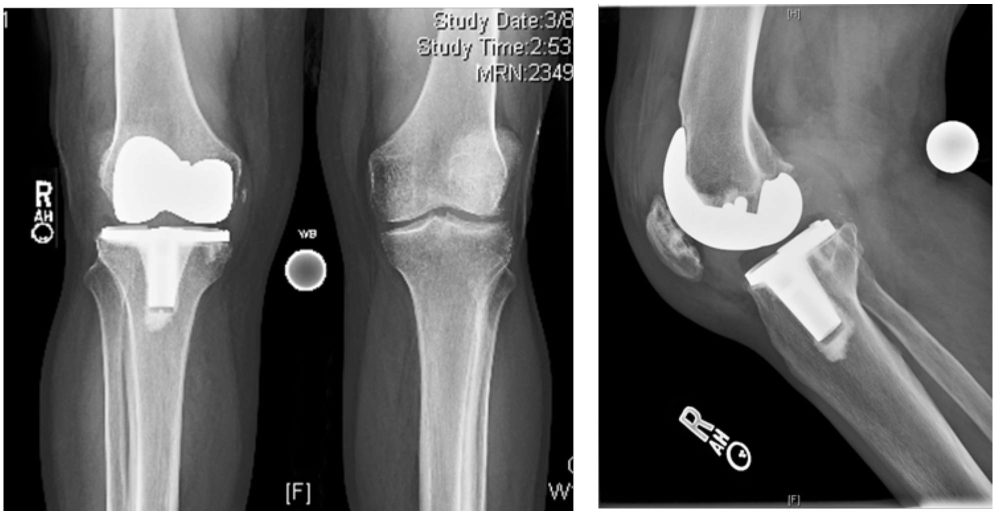

**Figure 2.4** | Postoperative anterior and lateral radiographs show proper implant alignment for *Patient A***.**

*Patient B* (*Implant B*), a 68 year-old woman (190 pounds, BMI=29.8), underwent primary left knee arthroplasty for osteoarthritis in 2001. The patient was relatively sedentary and her TKR functioned well with no pain or instability until eight years postoperatively, when she developed anterior knee pain and instability acutely after rising from a chair. Her left knee had a moderate effusion and range of motion from 5 degrees of hyperextension to 100 degrees of flexion. Post-operative x-rays indicated proper alignment of the TKR without excessive posterior slope of the tibial component or significant flexion or extension of the femoral component (**Figure 2.5**).

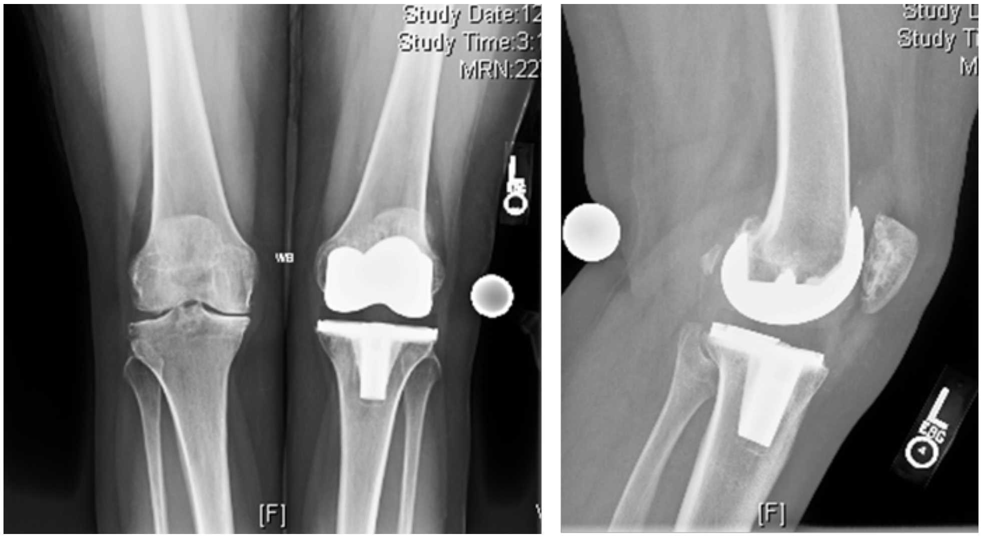

**Figure 2.5** | Postoperative anterior and lateral radiographs show proper implant alignment for *Patient B***.**

Both patients were treated with revision TKA. At surgery, fractured tibial posts were found. There was evidence of deformation and wear on the posts but no obvious oxidative damage. The implants were found to be well-fixed, well-sized, and well-aligned, but now showed instability. Zimmer moderately crosslinked inserts were used to replace the failed components.

### 2.2.2 Methods

Upon retrieval, the fracture surfaces of the retrieved tibial posts were examined using optical microscopy (Olympus BH-2) and SEM (Hitachi TM-1000, Pleasanton, CA) to study the fracture mechanisms involved in the failures. For oxidation analysis, the inserts were sectioned down the medial-lateral centerline and through the medial condyle in the sagittal plane using a band saw. Microtomed sections (~ 250 μm thick) were analyzed for oxidation using FTIR. Scans were taken every 100 μm at the anterior edge, the articular surface, the posterior edge, and through the anterior aspect of the fractured region. Scans were obtained from 2800 to 800 $cm^{-1}$ at intervals of 2 $cm^{-1}$, 32 scans per interval with a Thermo Nicolet iN 10 microscope. Scans were interrogated for oxidation, as identified through the ketone peak height (1713-1718 $cm^{-1}$) normalized to the 1368 $cm^{-1}$ peak height (1365-1371 $cm^{-1}$) (Currier et al. 2010; Currier et al. 2007).

### 2.2.3 Results

Optical images of the tibial post and the tibial plateau fracture surfaces for *Implant A* reveal striations and deformation that suggest crack propagation from both the anterior and posterior sides of the post (**Figure 2.6**). *Implant B* inspection shows great material loss on the anterior side as well as a white band on the posterior-lateral corner, suggesting an anterior-to-posterior direction of failure (**Figure 2.7**).

SEM analysis of the post fracture surface showed surface features that corroborated the macroscale analysis. For *Implant A*, the micrographs revealed clamshell markings at the anterior-medial corner, indicative of fatigue crack propagation moving in the anterior direction (**Figure 2.8**, *Region 4*). Furthermore, *Regions 1-3* of **Figure 2.8** show evidence of brittle fracture mechanisms – relatively flat surface, limited ductile "criss-cross" features common to UHMWPE – pointing in the direction of travel from posterior to anterior. On the other hand, surface striations seen in the optical microscope photos in **Figure 2.6** and in *Region 5* of **Figure 2.8** reveal evidence of localized ductile tearing along the direction of crack propagation in the anterior-to-posterior direction. This suggests the existence of two initiation sites, most likely at the anterior-medial and posterior-lateral corners (*Regions 1* and *4*), which met halfway through the tibial post before catastrophic failure. No regions of extensive ductility were observed on the surface which indicates the implant fractured in a brittle manner during a single overload event, most likely during the exercise routine of *Patient A* (described above).

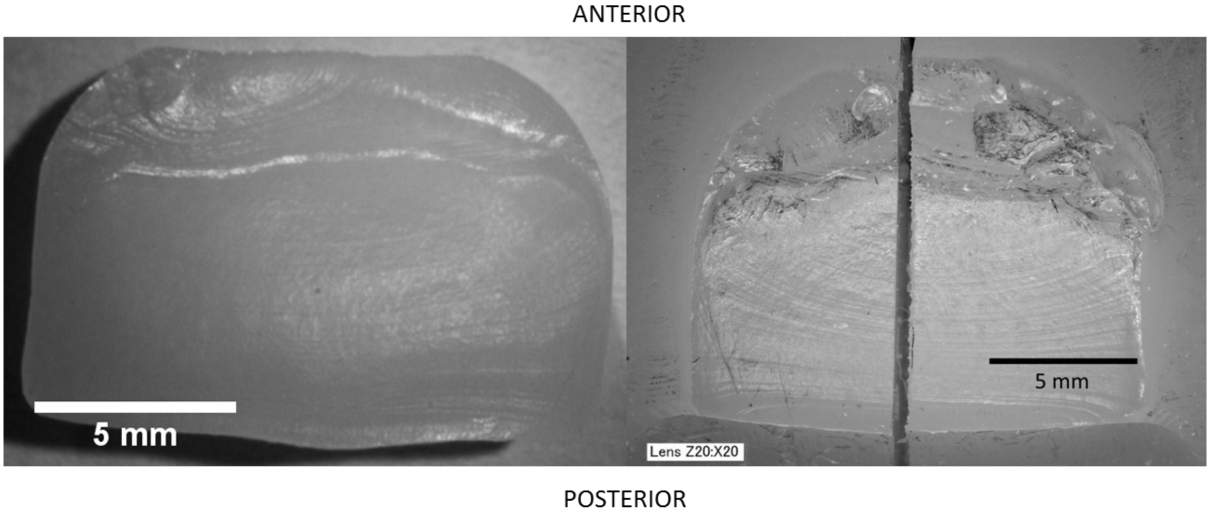

**Figure 2.6** | Optical micrographs of *Implant A* showing the fracture surface of the tibial post side (left) and tibial plateau side (right). The tibial plateau was sectioned down the center for later oxidation analysis. Anterior and posterior sides are noted.

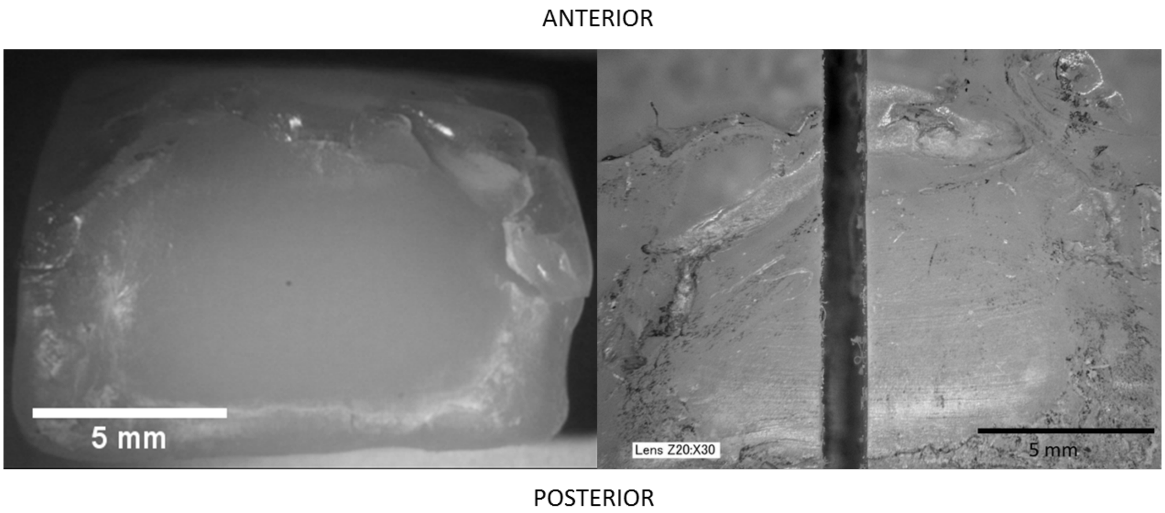

**Figure 2.7** | Optical micrographs of *Implant B* showing the fracture surface of the tibial post side (left) and tibial plateau side (right). The tibial plateau was sectioned down the center for later oxidation analysis. Anterior and posterior sides are noted.

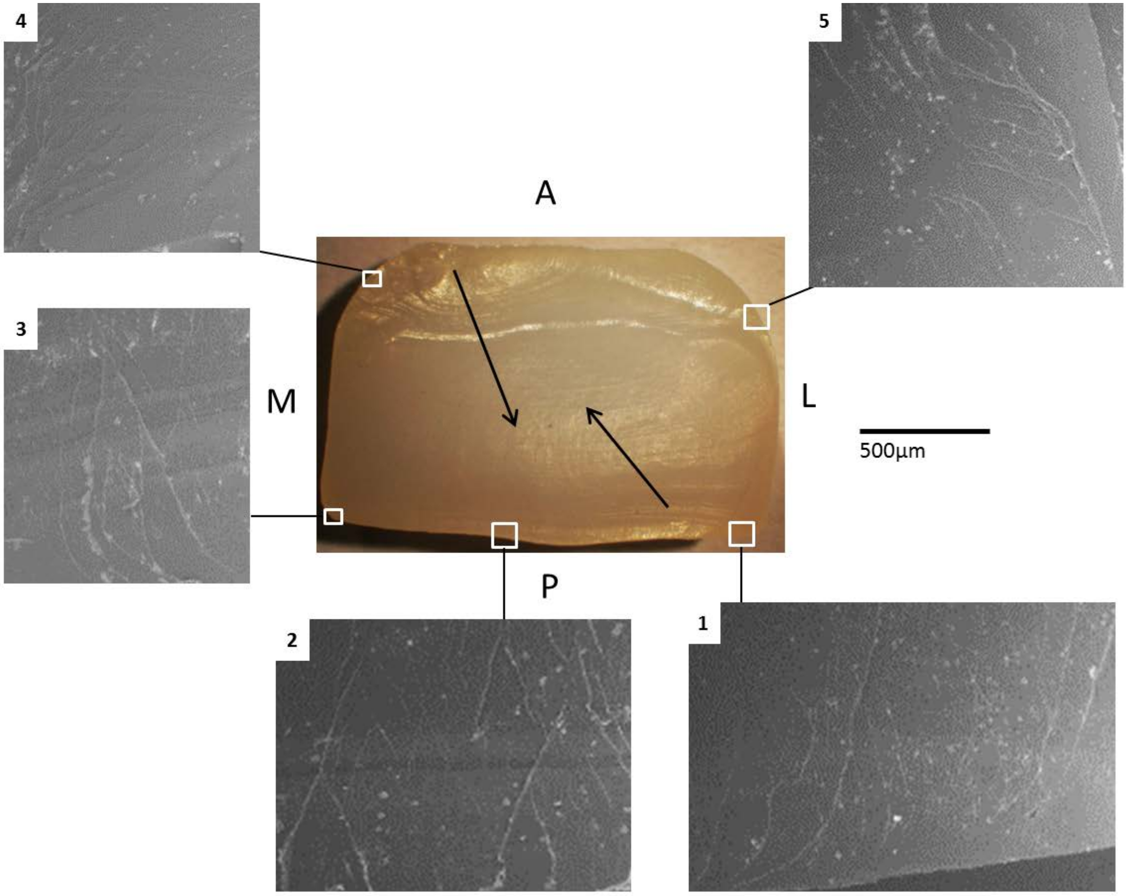

**Figure 2.8** | SEM map of the fractured tibial post belonging to *Patient A*. Scale bar applies to all SEM images. The arrows indicate direction of crack propagation. Fracture surfaces indicate fatigue crack propagation mechanisms as delineated by the classic “criss-cross” patterns and localized tearing associated with crack advance (Regions 1-5) in the UHMWPE tibial post. Anterior (A), posterior (P), medial (M) and lateral (L) sides of the implant are noted.

The fracture surface images of *Implant B* (**Figure 2.9**) suggest an oxidation embrittlement process rather than a classic fatigue crack propagation failure. In this explant, there is a white band that is typically associated with oxidative embrittlement processes along the posterior perimeter of the post (along Regions 6-10). In this case, the microcracks that develop within an oxidized region of the UHMWPE serve as the fracture initiation mechanism in the component.

**Figure 2.10** shows the difference in oxidation profiles between *Patient A* and *Patient B*. *Implant A* had a maximum oxidation index of below 0.8 near the anterior edge of the fracture. *Implant B* showed elevated oxidation above 1.5 near the anterior edge of the fracture. Indices above 1.25 are indicative of susceptibility to fracture due to oxidative embrittlement (Currier et al. 2007).

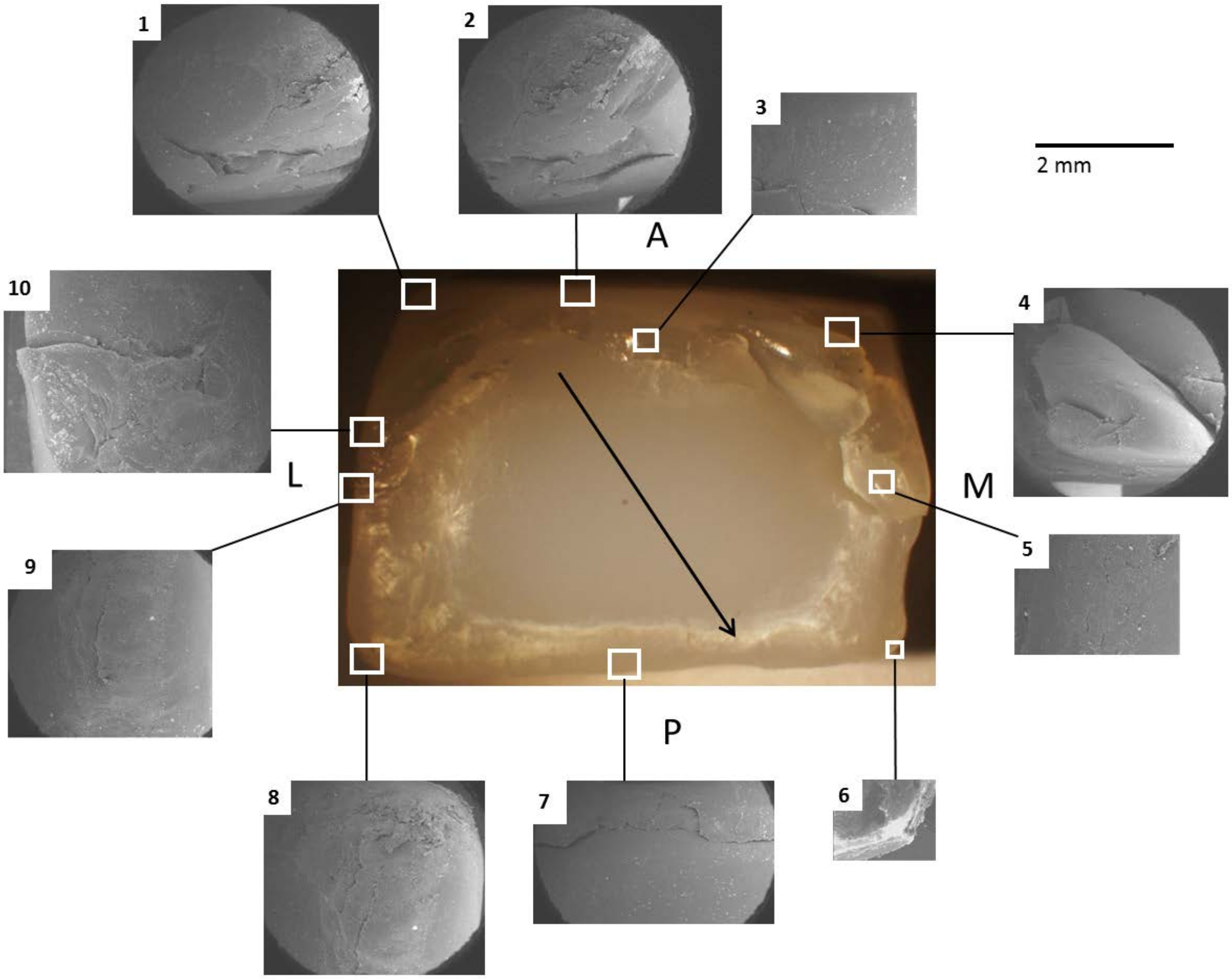

**Figure 2.9** | SEM map of the fractured tibial post belonging to *Patient B*. Scale bar applies to all SEM images. The arrow indicates the direction of crack propagation. Fracture surfaces indicate a highly oxidized region (white band) that circumnavigates the post and serves as fracture initiation sites in the UHMWPE. Brittle fracture modes are noted about the circumference of the oxidation band (Regions 1-10). Anterior (A), posterior (P), medial (M) and lateral (L) sides of the implant are noted.

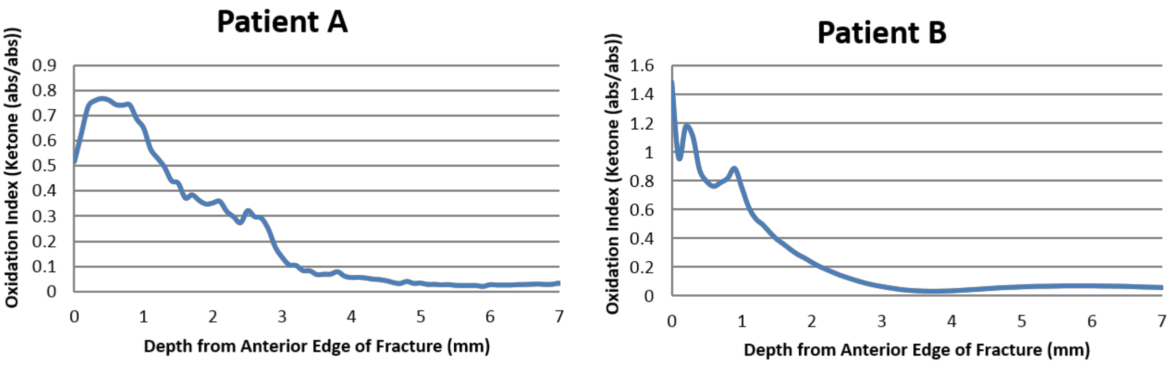

**Figure 2.10** | Oxidation profiles for *Patient A* (top) and *Patient B* (bottom). Note different ordinate scales and that the implant belonging to *Patient B* exceeds the 1.25 oxidation index indicative of susceptibility to fracture due to oxidative embrittlement (Currier et al. 2007).

### 2.2.4 Discussion

*Case Study Analysis*

*Implant A* shows a fatigue fracture process indicative of crack propagation through a less-tough (moderately crosslinked) form of UHMWPE, while *Implant B* shows an oxidation band and brittle fracture processes associated with oxidation embrittlement. FTIR analysis confirmed the presence of an oxidized region in *Implant B* and non-critical oxidation in *Implant A*. This indicates two distinct mechanisms for material embrittlement that have been associated with gamma sterilization: loss of fracture resistance owing to crosslinking and loss of mechanical toughness due to oxidation. For *Implant A*, dual crack initiation on opposite sides of the post reveals crack propagation and micromechanisms that are consistent with reduced ductility seen in bench testing of crosslinked UHMWPE (Baker et al. 2003; S. a Atwood et al. 2010). The implant belonging to *Patient B* demonstrated significant oxidation levels that exacerbated its embrittled state (Premnath et al. 1996).

Examination of the two retrievals in the above case study suggests that the immediate effect of gamma irradiation on mechanical properties and the later oxidation-induced decreases in toughness may compromise fatigue strength.  These decreases, when combined with stress concentrations such as the tibial post, can result in *in vivo* fracture.

*Tibial Post Fractures: Reported Cases*

Fracture of the tibial post for PS-TKR has been documented for a variety of implant designs, including the LPS NexGen (Zimmer) (Chiu et al. 2004; D’Angelo et al. 2010; Shih & Chou 2007; Lee et al. 2009), Insall-Burstein II (Zimmer) (Mestha et al. 2000; Hendel et al. 2003; Clarke et al. 2004), Foundation PS Total Knee System (Encore Orthopedics) (Mauerhan 2003;

Bal et al. 2008), Genesis Total Knee System (Smith & Nephew) (Mariconda et al. 2000), PFC Sigma Total Knee System (Depuy) (Sands & Silver 2005), AMK Total Knee (Depuy) (Ng & Chiu 2003) and Scorpio Knee System (Stryker Orthopedics) (Jung et al. 2008). The majority of these fractures occurred for well-aligned prostheses, and all implants failed in less than 9 years, with most only surviving for 3-4 years. Due to a lack of consistent fractography and oxidation analysis in these case studies, it is difficult to pin down the exact cause of failure. However, it is clear that both design and material composition have played a role.

Several of these case studies report fractures in tibial inserts composed of "conventional polyethylene", the majority of which received a relatively small dose of irradiation during sterilization, either in air or an inert environment. As a result, fracture may be attributed to oxidative embrittlement of UHMWPE, either on the shelf or *in vivo*; however, none of these reports confirm via FTIR analysis, as performed on *Implant B* in the case described in the previous section. It is possible that *Implant B*, a Zimmer LPS NexGen deice, may have been more susceptible to oxidative processes than other conventional UHMWPE implants due to exposure to more moderate doses of irradiation. Furthermore, moderate crosslinking without any evidence of oxidation can still lead to a reduced resistance to fatigue crack propagation and increased potential for fracture, as demonstrated with *Implant A* (Baker et al. 2003; S. a Atwood et al. 2010). Huot and colleagues reported on the relative contributions of oxidation and crosslinking to tibial post fractures, showing that oxidized tibial inserts and crosslinked tibial inserts can fail *in vitro* at similar numbers of cycles given the same load (Huot et al. 2010). Furthermore, in four reports of tibial post failure in NexGen devices, none cite oxidation of the implant, but do blame cam-post impingement (Chiu et al. 2004), non-traumatic fatigue (Lee et al. 2009), an overload event (Shih & Chou 2007), and a combination of fatigue and overloading resulting in a two-stage rupture (D'Angelo et al. 2010).

The clinical consequences of increased crosslinking with minimal oxidation is also seen in Jung et al.'s analysis of two tibial post fractures in Stryker's Scorpio Knee System (Jung et al. 2008). The inserts were composed of X3 HXLPE, a sequentially annealed highly crosslinked UHMWPE that receives a total of 90 kGy of radiation (Ries & Pruitt 2005). Both inserts failed in less than a year after implantation, even in as little as 8 weeks. The report, published in late 2008, notes that the authors' hospital recently switched to the X3 Scorpio system in January 2007. Before then, the hospital recorded 15,000 cases over 4 years of conventional UHMWPE Scorpio Knee Systems of which none had fractured. Jung et al.'s work suggests that simple substitution of conventional formulas with highly crosslinked UHMWPE into existing TJR designs may compromise the device's overall performance due to our lack of understanding of the material-notch interplay near stress risers such as the tibial post.

### *Loading of the Tibial Post*

The process of fatigue fracture can be broken down into two primary phases: the initiation of a flaw and the propagation of that flaw to failure. *In vivo* flaw initiation on the post of tibial inserts can be associated with contact stresses that are generated cyclically or during overloading events such as a patient fall. Cyclic bending stresses can also occur due to post-cam or post-intercondylar notch contact, resulting in fatigue loading that promotes crack growth, even with stresses within an elastic region for UHMWPE (Huang et al. 2007; Huang et al. 2006). Several studies have attempted to quantify the degree of cyclic loading during flexion and extension events expected during normal and extreme use using both experimental and computational methods (Nakayama et al. 2005; Huang et al. 2007; Morra & Greenwald 2005; Huang et al. 2006).

As illustrated in **Figure 2.3**, contact between the post and the femoral component occurs on both the posterior and anterior side during flexion and extension motion, respectively. Contact between bearing surfaces in conforming (hip) and nonconforming (knee) designs have demonstrated higher contact stresses in the UHMWPE component for the latter geometry, leading to damage morphologies such as delamination, pitting, subsurface cracking and fracture (Bartel et al. 1986; McKellop 2007; Hood et al. 1983). These morphologies have been documented on the anterior and posterior surfaces of tibial posts and ultimately create micrometer to millimeter-sized cracks that can ultimately propagate to failure (Puloski et al. 2001; Medel, Kurtz, Sharkey, et al. 2011; Furman et al. 2008; Skwara et al. 2008). Nakayama et al. (2005) provided an experimental assessment of contact stresses at the posterior post-cam junction. The authors found peak contact stresses just above UHMWPE yield strength at roughly 22 to 34 MPa. Contact stresses increased with higher flexion angles and, for square posts as used in Zimmer's NexGen LPS system, stresses as high as 56 MPa were recorded under a small degree of internal rotation. Nakayama et al. also highlighted that the point of application of stress on the post tended to shift superiorly along the post with increasing flexion. Superior repositioning combined with shear forces acting on the post in the anterior-posterior direction would lead to a greater moment arm, resulting in higher bending stresses at the base of the post.

The findings of Nakayama et al. were supported through computational studies performed by Morra et al. (2005) and Huang et al. (2006, 2007). Contact stresses above the UHMWPE yield strength offer direct evidence of *in vivo* mechanisms of damage accumulation, even under "normal" gait. The growth of cracks from these areas of high contact stresses can occur with continued cyclic loading through not only surface contact, but also bending stresses. Huang et al. (2006, 2007) used their computational model to evaluate the effects of flexion and extension on principal stresses in the post. Under simulated flexion events, maximum principal tensile stresses were recorded at the base of the post on the posterior aspect, reflecting the role of the post as a cantilever beam supporting a bending moment under anterior-posterior shear loading (**Figure 2.11**). Repeated flexion events ultimately result in cyclic tensile loading under bending, which can promote crack growth over time. Huang et al.'s follow up study found stresses on the anterior based of the tibial post to cycle between -13 MPa of compression under flexion to 16-30 MPa of tension during extension (**Figure 2.12**). Such compression-tension cyclic loading could lead to complex crack initiation and propagation behavior in UHMWPE, especially from varying notch geometries (Pruitt & Suresh 1993; Baker et al. 2000).

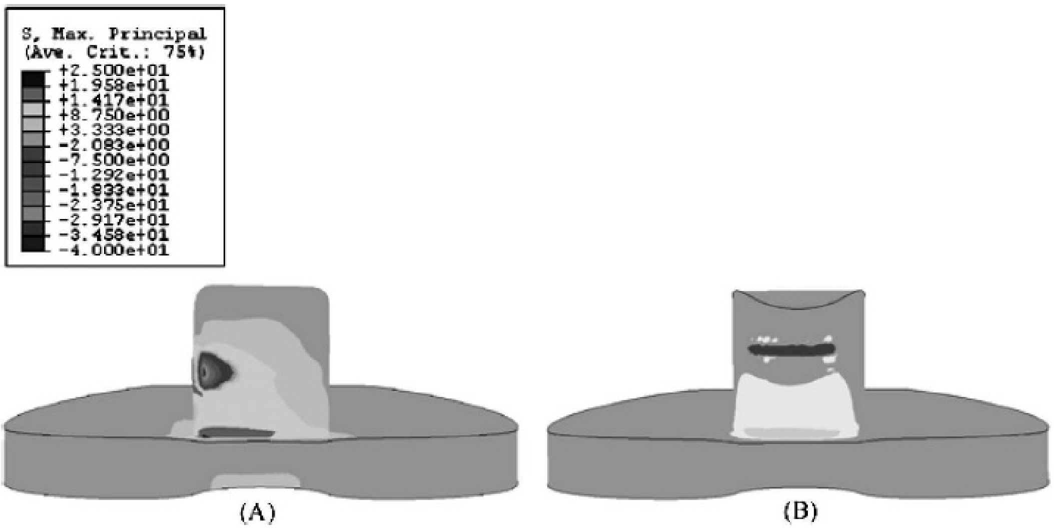

**Figure 2.11** | Finite element analysis of a (A) flat-on-flat post-cam design and (B) curved-on-curved design under flexion with internal rotation. Posterior post is shown. Peak tensile stresses appear at the base of the post on each design, with (A) showing clear edge loading associated with flat-on-flat designs. Contact near the center of the post is primarily in compression due to post-cam contact. (Huang et al. 2006)

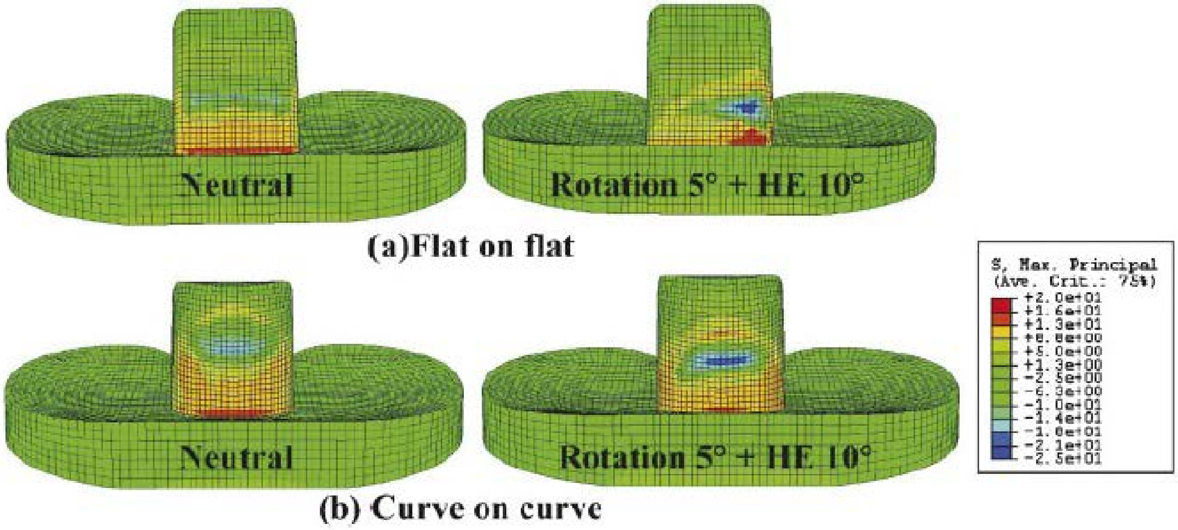

**Figure 2.12** | Finite element analysis of a (A) flat-on-flat post-cam design and (B) curved-on-curved design for eutral position (left) or hyperextension with internal rotation (right). Anterior post is shown. Peak tensile stresses appear at the base of the post on each design. Flat-on-flat demonstrates edge loading with added internal rotation. Compressive force near the center of the post are due to intercondylar notch-post contact. (Huang et al. 2007)

While these global stresses may be within the elastic limits of UHMWPE, the presence of a flaw as generated by wear damage or even an overload event can still lead to fracture, even for properly aligned implants. Due to the reduced resistance to fatigue crack propagation in crosslinked UHMWPE, such devices may suffer catastrophic failures earlier in their lifetime compared to conventional UHMWPE despite having the same design. Stoller et al. (2011) demonstrated an overall reduction in the number of fractures for highly crosslinked implants compared with untreated devices; however, the authors also noted a small change in component design for the highly crosslinked implants that provided for additional bending strength and thus reduced global stresses experienced by the post. Such design considerations may be the key to improving XLPE post performance without compromising wear resistance. Unfortunately, discussion in the literature of specific geometry changes has been limited in scope to post curvature in the transverse plane, aimed at minimizing edge loading during internal rotation (Huang et al. 2006; Nakayama et al. 2005; Hamai et al. 2008). Despite studies performed by Huang et al. that show peak stresses at the base of the post, and numerous reports of fracture emanating from this location, little investigation has been dedicated to notch geometries at the post-bearing surface junction.

## 2.3 Hip Replacements: The Liner Locking Mechanism

Hip replacements have undergone several modifications to reach today's 18-20 year expected lifetime (Pruitt & Chakravartula 2011; Melvin et al. 2014; Espehaug et al. 2009; Hailer et al. 2010). Its fundamental geometry still derives from Charnley's original design, which consisted of a much thicker cup to resist wear-through, but limited patients' range of motion (**Figure 2.13A**). When UHMWPE was introduced to TJRs in the 1960s, it was initially fixed to the pelvis using acrylic bone cement (Delaynay 2014; Kurtz 2009), but many manufacturers moved toward metal-backed acetabular liners around the 1970s (**Figure 2.13B**). Such modular components improved stress distribution at the component-bone interface, limited deformation and loosening, and significantly reduced the thickness of the UHMWPE liner, thereby greatly improving patients' range of motion (Ritter et al. 1990; Collier et al. 1990).

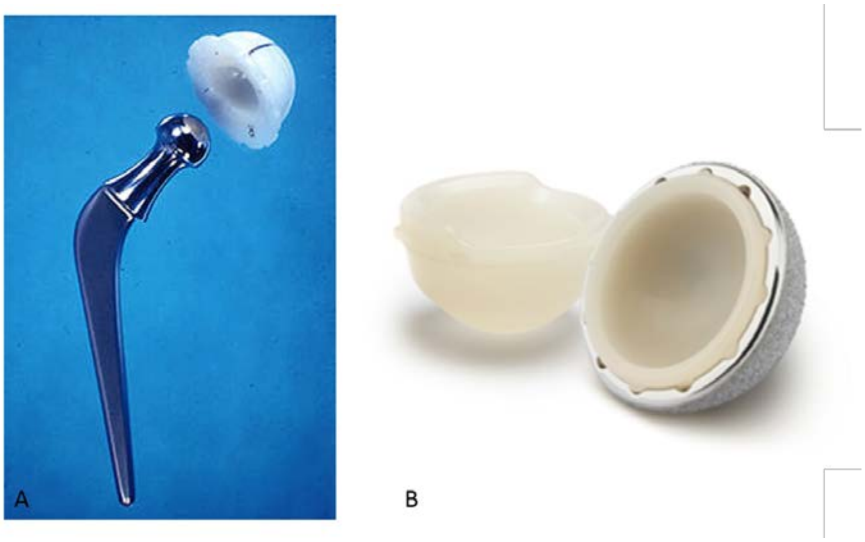

**Figure 2.13 |** (A) Low friction arthroplasty device originally designed by Charnley, featuring a thick UHMWPE liner that would interface with patient's bone using bone cement. (B) Modern-day modular implant with a UHMWPE liner and titanium acetabular shell. (Delaynay 2014; Zimmer 2014a)

The fixation of the metallic acetabular shells to the pelvis took center stage after the introduction of modularity, with the introduction of screw fixation into the bone and/or porous coatings to promote bone ingrowth (Bragdon et al. 2004; Harris & Jasty 1985). However, attention shifted to the securement of the UHMWPE liner within the metal shell after several reports of dissociation of the polymer component, particularly in Zimmer's Harris-Galante II acetabular design (Star et al. 1992; Brien et al. 1990; Mihalko & Papademetriou 2001; Werle et al. 2002; González della Valle et al. 2001; Parvizi et al. 2004). Such dissociation not only increased rates of revision, but also prompted concerns regarding backside UHMWPE wear due to nonconformity between the liner and shell, potentially further contributing to osteolysis (Fehring et al. 1999; Steven M Kurtz et al. 1998; Wasielewski et al. 2005).

Several manufacturers attempted to remedy the issue of dissociation through the development of liner locking mechanisms – intricate design features or "notches" along the UHMWPE rim that would allow stabilization of the component inside a titanium outer shell (**Figure 2.14**). Williams et al. (1997) evaluated the ability of six different locking mechanism designs utilized by manufacturers on backside wear, and found that limiting any rotational or axial motion of the polymer liner within the metal shell can greatly reduce overall wear. A finite element study by Kurtz et al. (1998) supported these findings, demonstrating that rotational and equatorial constraint can greatly diminish micromotion of the implant.

**Figure 2.14 |** A few of acetabular liners currently on the market. Each liner contains design features (notches) that enable liner fixation within a metal acetabular shell. These liner locking mechanisms have demonstrated enhanced fixation that reduce backside wear and liner dissociation; however, each mechanism includes notches that serve as stress risers where cracks can form and propagate. (Zimmer 2014a; Zimmer 2014b; Depuy 2013; Smith & Nephew 2014; Pierson 1995)

Locking mechanisms, however, create stress concentrations in hip devices that are susceptible to *in vivo* fracture. Several studies have reported increased incidence of cracking and fracture in modern devices, especially with the advent of crosslinked UHMWPE (Halley et al. 2004; Furmanski et al. 2009; Moore et al. 2008; Waewsawangwong & Goodman 2012; Schroder et al. 2011; Tower et al. 2007). The following case study examines a single case in which *in vivo* fracture initiated at this particular design feature in a highly crosslinked (100 kGy) and remelted acetabular liner. Mechanisms of failure were determined using optical microscopy, SEM and energy-dispersive X-ray spectroscopy (EDX).

### 2.3.1 Case Report: Fracture and Deformation of Rim in Zimmer Longevity Highly Crosslinked Acetabular Liner

A 60 year-old female suffered an acetabular hip fracture and dislocation in 2008 following a motor-vehicle accident (MVA). The patient underwent an Open Reduction and Internal Fixation (ORIF) surgery with a primary total hip arthroplasty. She received a 36mm XLPE Zimmer Longevity THR (Warsaw, Indiana) with a +3 mm Offset Liner, irradiated at 100 kGy and subsequently remelted. Within the first six months post-operation, the patient had two dislocations. There were no further problems with the implant until 2011 (after three years *in vivo*), when she had an irreducible hip dislocation. The patient underwent revision surgery to replace the device with a more constrained liner and a 28 mm femoral head.

### 2.3.2 Methods

The explant was documented using optical imaging (Sony NEX 3, Tokyo, Japan). A sharp razor blade was use to section the UHMWPE liner, taking care to avoid any damage to the fracture surface. SEM imaging (Hitachi S-2460N, Pleasanton, CA) was used to examine the exposed fracture surface between the liner rim and the locking mechanism. Initial observation of the cobalt chrome (CoCr) femoral head revealed severe scratching (**Figure 2.15**) and was further examined using EDX (Hitachi S-2460N with KEVEX, Pleasanton, CA) to search for material deposits.  Two regions were analyzed in order to compare the elemental composition between a "clean" region with no evidence of build up or failure modes and another surface with strong evidence of foreign particulates and scratching.

### 2.3.3 Results

Upon observation of the explant, it was apparent that the fracture initiated from the liner-locking mechanism, as the rim of the liner did not completely separate from the liner (**Figure 2.15**).  The rim deformed inward, most likely causing the irreducible dislocation. General observation of the liner bearing surface revealed mild pitting and scratching (Hood et al. 1983). The CoCr femoral head was covered in several wide scratches on one side, indicative of metal-on-metal contact (**Figure 2.15**).

**Figure 2.15** | Fractured highly crosslinked UHMWPE liner and CoCr femoral head. The left image shows mild pitting and scratching damage, highlighted using black ink, as well as the exposed surface of the fractured rim below. The middle image shows another perspective of the fracture. On the right, the CoCr femoral head exhibits several large scratches along the distal slope.

SEM micrographs revealed criss-cross or diamond patterns typical of UHMWPE fracture surfaces, particularly at the exterior of the locking mechanism moving inward toward the bearing surface (**Figure 2.16**, **Regions 1-6**) (Bradford et al. 2004; Baker et al. 2003; Connelly et al. 1984). The interior fracture surface demonstrates a greater degree of ductility (**Figure 2.16**, **Regions 7-9**), suggesting crack initiation at the exterior notch, propagation across the surface toward the interior, and ductile tearing toward the inner bearing surface. Tearing is also indicative near the corners of the fracture surface (**Figure 2.16**, **Regions 1&6**) where more texture is evident.

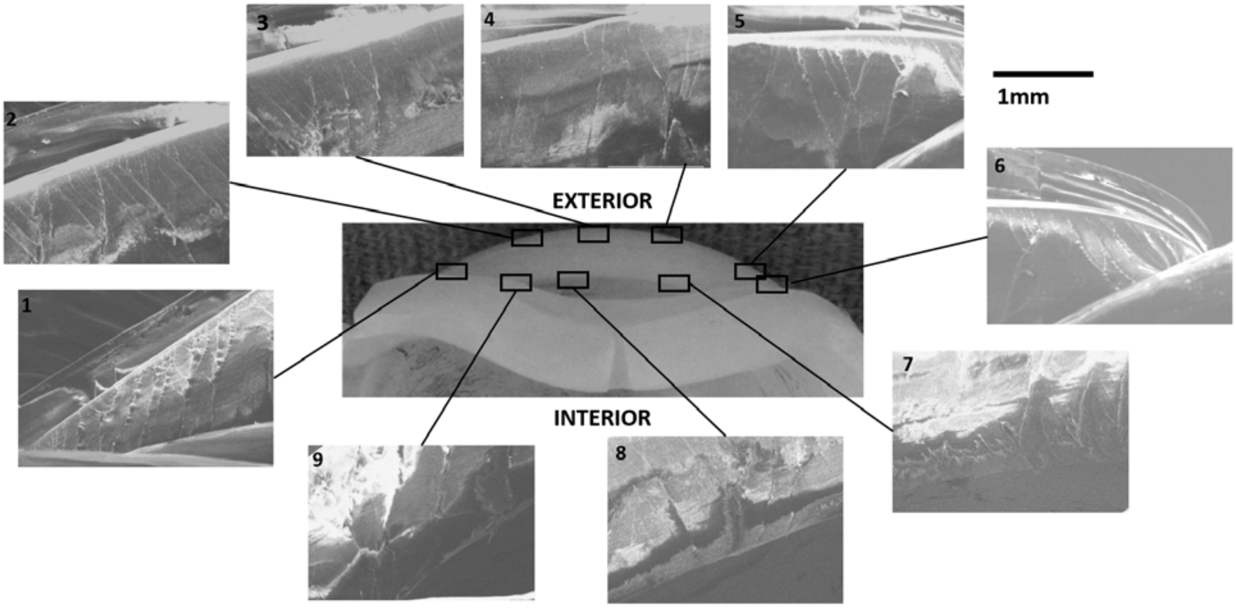

**Figure 2.16 |** SEM micrographs of fracture surface on fracture acetabular liner. The exterior fracture surface revealed criss-cross markings (**Regions 1-6**) typical of crack growth in UHMWPE. Ductile tearing (**Regions 7-9**) is evident near the interior surface, suggesting shear loading as a final loading event causing fracture across the thickness of the liner.

EDX analysis of the CoCr femoral head revealed 7.46 weight percent (2.89 atomic percent) of titanium at the observed damage (scratches), as well as expected contributions from cobalt and chrome. No titanium or other deposits were found on the clean surface of the retrieved head. Such titanium deposits most likely resulted from femoral head-stem contact following dislocation, causing severe scratching on the metallic surface.

### 2.3.4 Discussion

*Case Study Analysis*

While many studies have documented fracture of the acetabular liner *in vivo*, this particular case provides evidence that such failure modes can originate from stress concentrations in the device, particularly the liner locking mechanism. The criss-cross markings present on the fracture surface demonstrate similarity to those reported in bench fatigue studies of UHMWPE (Baker et al. 2003; Bradford et al. 2004) as well as previous retrieval studies, including the tibial posts in the previous section (**Figure 2.8**). This failure morphology has been associated with stable crack growth under both monotonic and cyclic loading (Connelly et al. 1984; Rimnac et al. 1988). Since this Zimmer Longevity implant underwent a post-irradiation remelting treatment, oxidation effects are thought to be minimal and thus any reduction in fracture resistance is primarily attributed to crosslinking of the polymer.

The size scale of these features are actually slightly larger and more defined than those seen on the tibial post in **Section 2.2**, despite having a higher dosage of crosslinking irradiation and presumably a higher degree of microstructural brittleness contributing to reduced fatigue strength (S. a Atwood et al. 2010; Baker et al. 2003). Furthermore, the direction of deformation of the rim toward the interior of the bearing surface, combined with the clinical history of two dislocation events preceding revision, suggest that recurrent dislocation and a subsequent attempt to reduce the hip may have resulted in repetitive shear loading on the exterior rim. Shear forces would contribute to a more ductile loading mechanism, resulting in a greater degree of fibrillation at the fracture surface compared to flat, brittle morphologies associated with tensile loading.

Fatigue striations are not evident on the fracture surface for this acetabular liner, suggesting a single overload event is most likely responsible for final fracture and rim deformation for this device. Still, the particular fracture location along the rim of a locking mechanism demonstrates increased susceptibility to flaw generation at stress concentrations included in the original design. Even small cracks are prone to growth under sustained cyclic loading, especially with a high dress of crosslinking.

### *Liner Locking Mechanism Fractures: Reported Cases*

*In vivo* fractures and cracking of THR acetabular liners are well-documented in the literature (Furmanski et al. 2009; Halley et al. 2004; Blumenfeld et al. 2011; Birman et al. 2005; Moore et al. 2008; Duffy et al. 2009; Waewsawangwong & Goodman 2012; Pruitt et al. 2013; Schroder et al. 2011; Tower et al. 2007; Furmanski, Kraay, et al. 2011) (**Figure 2.17**). Reasons for failure are associated with surgical factors, such as malpositioning (Moore et al. 2008; Halley et al. 2004; Tower et al. 2007), kinematic factors, including impingement and recurrent dislocation (Blumenfeld et al. 2011; Halley et al. 2004; Birman et al. 2005; Duffy et al. 2009; Pruitt et al. 2013), a thin UHMWPE liner (Moore et al. 2008; Waewsawangwong & Goodman 2012; Tower et al. 2007; Blumenfeld et al. 2011), and/or material property changes due to oxidation or reduction of fatigue resistance (Furmanski et al. 2009; Pruitt et al. 2013; Schroder et al. 2011; Moore et al. 2008; Duffy et al. 2009; Halley et al. 2004).

For all catastrophic fractures, cracks initiated at the liner rim and/or notches used in the locking mechanisms. Birman et al. (2005) examined 120 conventional UHMWPE liners to observe the incidence of cracking in correlation with oxidation and impingement damage. As seen in **Figure 2.18**, high crack density is primarily associated with impingement, but could also be exacerbated by oxidation of the polymer. While oxidation has been largely addressed with heat treatments such as remelting or annealing procedures, impingement has been reported for several implants, even those within proper alignment (Furmanski et al. 2009). Schroder et al. (2011) compared damage in both conventional and highly crosslinked Zimmer Trilogy liners, finding a greater degree of cracks and fracture in the latter cohort, revealing that modern devices are still susceptible to fracture. Cracks in Schroder and coworker’s studies were isolated to areas near the locking liner mechanism for devices that were implanted for several years. Furmanski et al. (2011) found similar cracking near notches in six highly crosslinked UHMWPE Zimmer Trilogy liners, some of which were removed in less than one year after implantation. These findings supplement the case study reviewed above regarding fracture and deformation of a highly crosslinked Zimmer liner, suggesting that this particular design may be more susceptible to crack initiation and growth due to notch geometry.

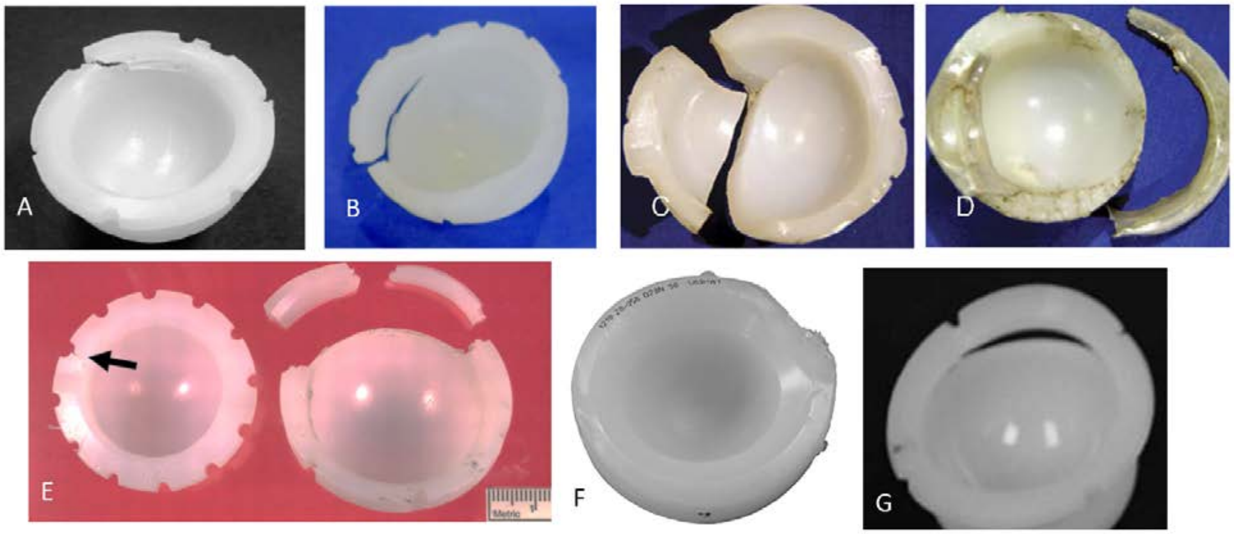

**Figure 2.17** | Fractured acetabular liners reported in the literature. All fractures emanated from notches included in the liner locking mechanisms of the liners. Included are highly crosslinked (75-100 kGy) and remelted (A, B), conventional (25 kGy) with no post-irradiation heat treatment (C, D, E) sequentially annealed highly crosslinked (F) and moderately crosslinked (50 kGy) and remelted components (G) (Schroder et al. 2011; Halley et al. 2004; Birman et al. 2005; Tower et al. 2007; Pruitt et al. 2013).

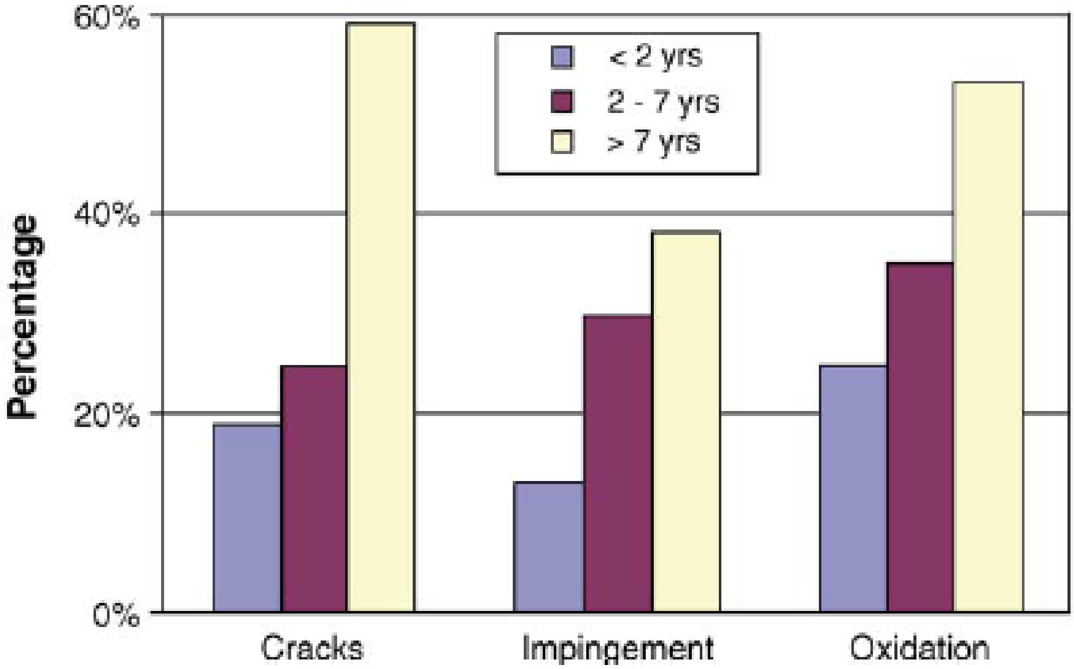

**Figure 2.18** | Incidence of cracking, impingement and oxidation in conventional UHMWPE liners. Percentage of liners are reported on the ordinance for each cohort of time *in vivo*. In general, implants with evidence of oxidation or impingement had higher density of cracking, especially near the locking mechanism (rim) (Birman et al. 2005).

### *Loading of the Linear Locking Mechanism*

Unlike the tibial post, few studies have been dedicated to assessing stresses at the liner locking mechanism. While some investigations have assessed overall stability of different locking mechanism designs against rotation and dissociation, few have provided a glimpse at stress distribution in the liner rim (Williams et al. 1997; Steven M Kurtz et al. 1998). The 1998 study by Kurtz et al. presented one of the first finite element analyses of load bearing in the locking mechanism, but was limited to only nodal rim constraints in the device model, as opposed to explicit notch designs. While non-specific in geometry, Kurtz et al. (1998) did reveal that a small degree of nonconformity can lead to the UHMWPE locking mechanisms carrying the majority of the load. Such nonconformity is likely during early stages of device lifetime due to different manufacturing tolerancing between the titanium shell and polymer lining, before creep and deformation promote better load distribution and load transfer to the metal shell. Thus, initial loading of the device can result in higher stresses along the locking mechanisms which can promote microscopic cracking along rim features, as seen in some retrievals as early as one month after implantation (Furmanski, Kraay, et al. 2011).

Limited knowledge on how each liner locking mechanism design bears loads is in part due to the recent surge in reports of fractured liners and concomitant incorporation of highly crosslinked UHMWPE into existing acetabular designs (Ast et al. 2014; Furmanski et al. 2009; Halley et al. 2004; Tower et al. 2007). Studies that have investigated load distribution in modern liners through finite element analysis all demonstrate peak stresses at the notches along the rim of the liners (Furmanski et al. 2009; Pruitt et al. 2013; Promsang 2013; Lam et al. 2013). Lam et al. (2013) found notch stresses of the Zimmer Longevity liner peaked under extreme abduction and anteversion, especially in the superior rim of the component, where most reported fractures occur (Ast et al. 2014; Tower et al. 2007; Halley et al. 2004). Furmanski et al. (2009) demonstrated that such malpositioning could result in impingement loading at the rim (**Figure 2.17**), which generated peak stresses close to or above the yield strength in one or more notches (**Figure 2.18**). A similar analysis by Pruitt et al. (2014) revealed these stresses could approach the ultimate tensile strength of crosslinked UHMWPE, especially in the event of liner dissociation. However, even implants that are within the recommend “safe zone” for alignment exhibit wear along the rim indicative of impingement. Such impingement may be the result of extreme loading as occurs during squatting or sitting cross-legged, which can results in notch stresses as high as 103 MPa, as shown by Promsang et al. (2013).

Even though investigations have been limited in scope, the aforementioned studies have provided evidence that notches included in acetabular liner designs can lead to elevated stresses near or above the yield, strength of UHMWPE which can contribute to fracture due to overloads – as seen with the deformed hip liner discussed in the above case study – or even the initiation and propagation of small cracks under cyclic loading. **Figure 2.14** demonstrates the wide variety of mechanisms that have been designed to improve rotational fixation for the liner, incorporating a variety of notch geometries despite very limited knowledge on their impact on crack growth. Considering the evidence for flaws, even in very young explants (Furmanski, Kraay, et al. 2011), further investigation of notch effects on crack behavior is warranted in both conventional and XLPE to fully comprehend failure mechanisms and potentially enhance device lifetimes.

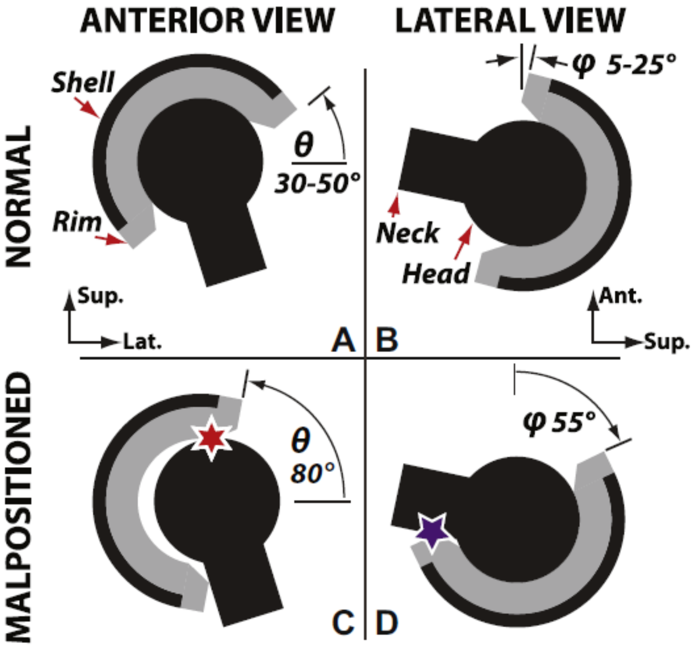

**Figure 2.17 |** Schematic illustrating how positioning can lead to impingement of the UHMWPE acetabular rim between the femoral head and acetabular shell. The “safe zone” for proper alignment is shown for (**A**) abduction and (**B**) anteversion. Malpositioning in the case of (**C**) excessive abduction leads to rim loading in the superior quadrant of the implant, resulting in elevated stresses or even dislocation. (**D**) Excessive anteversion can lead to posterior rim loading. (Furmanski et al. 2009)

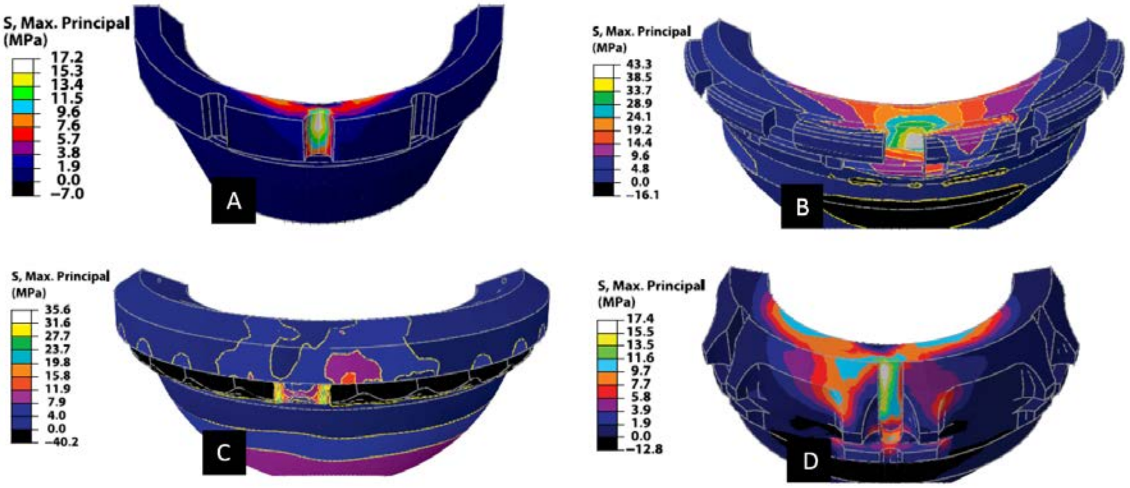

**Figure 2.18 |** Stress distribution in four different modern acetabular liners, as modeled using finite element analysis, including: (**A**) Zimmer Trilogy-Longevity®, (**B**) Sulzer/Zimmer Galante II/Converuse-Durasul®, (**C**) Smith and Nephew Reflection-XLPE$^{TM}$, and (**D**) Depuy S-Rom M®-Marathon$^{TM}$ liners. All four liner designs were loaded with a static 500 N over approximately 15-20 mm$^2$ to simulate impingement loading that may occur *in vivo*. Peak stresses were found in the notches of each device’s liner locking mechanism, and were near or above the yield stress of UHMWPE. (Furmanski et al. 2009)

## 2.4 Shoulder Replacements: Conformity and Thickness

Shoulder arthroplasty is the fastest growing orthopedic procedure in the market today, with just over 50,000 devices implanted each year (AAOS, 2010; Day et al., 2010). These include TSRs, in which the original anatomy of the joint is replicated as closely as possible; reverse shoulder replacements that reverses the ball-and-socket configuration to improve stability; and hemiarthroplasties, which only replace the humeral bearing surface. This section primarily focuses on the glenoid components used in TSRs.

While often treated as the "younger sibling" of the orthopedic world, TSRs have had a long history. Dr. Charles Neer II's first-implanted hemiarthroplasty dates back to 1953, but this design/method still remains in service today (Kurtz 2009). UHMWPE made its shoulder debut in the early 1970s, when the first polyethylene glenoid component was introduced in combination with Neer's humeral head (Kurtz 2009; Armstrong & Lewis 2013). Even with identical material composition to the hip and knee, the complexity of shoulder kinematics and limited joint space have significantly reduced TSR lifetime to as low as 5 years (Raiss et al. 2014; Deshmukh et al. 2005; Fox et al. 2009; Norris & Lachiewicz 1996).

The majority of TSR failures are associated with the glenoid component (K. I. Bohsali et al. 2006), which experiences contact stresses as high as those observed in tibial inserts (Terrier et al. 2009; Swieszkowski et al. 2003; Bartel et al. 1986). Glenoid design has evolved significantly over the past 30 years to accommodate these high stresses as well as a greater degree of joint motion seen at the shoulder. For example, increased radial mismatch between the glenoid and humeral head can increase patients' range of translation and rotational motion, but also increases contact surface stresses and instability (**Figure 2.19 A**) (Swieszkowski et al. 2003; Oosterom et al. 2003). Conforming glenoids reduce local contact stresses, but can lead to complex eccentric loading dubbed "rocking horse" motion (**Figure 2.19 B**) (Anglin et al. 2000; Gregory et al. 2009; Strauss et al. 2009; Armstrong & Lewis 2013; Karduna et al. 1998). With limited available bone stock in the shoulder joint, fixation of the glenoid under such edge loading can be compromised (Armstrong & Lewis 2013; Bicknell et al. 2007). Different fixation mechanisms for this UHMWPE component have been developed to address this issue, including multiple pegs, a single keel, or in some cases a keeled titanium base plate ("metal-backed") (**Figure 2.20**). Only a limited number of recent studies have explored the interplay of fixation mechanism and conformity on glenoid stability (Anglin et al. 2000; Oosterom et al. 2003; Karduna et al. 1998; Terrier et al. 2006; Severt et al. 1993).

The evolution of material composition has mimicked that seen in hip and knee arthroplasty. Changes in UHMWPE processing (e.g. the introduction and dismissal of Hylamer, the switch from gamma-in-air to gamma-inert sterilization, and the introduction of crosslinking) have all been incorporated into glenoid components. This "hand-me-down" nature of UHMWPE modifications not only brings the benefit of improved wear resistance, but also the tradeoffs exhibited with reduced resistance to crack propagation and oxidation. The manifestation of these compromises in shoulders has led to severe clinical consequences, including wear damage morphologies that span that of both hip and knee retrievals (Gunther et al. 2002; Farzana Ansari et al. 2014).

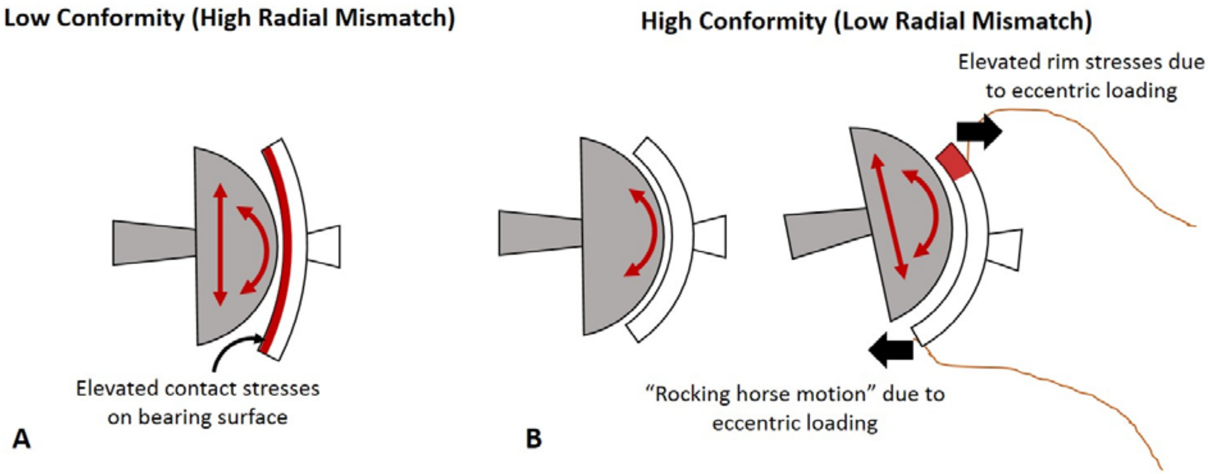

**Figure 2.19** | Illustration of radial mismatch and rocking horse motion of the glenoid component. Since shoulders simulate a partial ball-and-socket joint that enables translation and rotation, a radial mismatch between the humeral head and glenoid may be introduced into the design, leading to tradeoffs in range of motion, contact stress and stability in the glenoid component. . The image on the left shows a radial mismatch that enables translational motion, but also leads to greater bearing contact stress, increasing the propensity for subsurface cracking and delamination wear. The central illustration shows a conforming bearing that minimizes joint translation, but also reduces contact stresses and wear at the bearing surface. The far right illustrates eccentric loading that can occur due to a "rocking horse" phenomenon during translation for a more conforming glenoid-humeral head coupling.

**Figure 2.20** | Fixation mechanisms used on the backside of glenoids, including (A) pegs, (B) a keel and (C) a metal-backed keel.

The following case study examines several retrieved glenoids that experienced severe gross fracture *in vivo*. The explant cohort includes a range of material compositions and conformities, once again highlighting the importance of material-design interplay for UHMWPE TJR components.

### 2.4.1 Case Report: Analysis of Severely Fracture Glenoid Components

Sixteen explanted glenoid components with catastrophic fractures were identified from a larger collection of 68 retrievals (**Figure 2.21**). "Catastrophic" fracture was characterized by: (1) cracks traversing more than half the bearing surface (**Fig. 2.21 A**, **E**); (2) disintegration of the glenoid into multiple smaller fragments (**Fig. 2.21 G**, **H**, **J**, **M**, **N**); (3) fracture associated with severe wear-through (**Fig. 2.21 A**, **D**, **L**, **O**); (4) obvious loss of original glenoid geometry (**Fig. 2.21 B**, **C**, **I**, **J**, **P**); or breakage across the inner bearing surface (**Fig. 2.21 F**, **K**).

Explant information is presented in **Table 2.1**. Explant A was the only metal-backed component; the rest were all unsupported UHMWPE. All explants were cemented. The minimum thickness of each glenoid bearing surface was measured using a digital caliper.

**Table 2.1 |** Summary of patient and device information for 16 glenoids evaluated in this study. Letters in the first column correspond to images seen in **Figure 2.21**.

| Model | Age | Sex | Time *In Vivo* [years] | Sterilization | UHMWPE Formula | Fixation | Radial Mismatch [mm] | Minimum Thickness [mm] |
|---|---|---|---|---|---|---|---|---|
| **A** Zimmer Fenlin | 65 | M | 16 | Gamma Air | Conventional | Metal-backed Keel | 0 | 0.26 |
| **B** Tornier Aequalis | 62 | M | 4.9 | Gamma Air | Conventional | Keel | 7.5 | 2.20 |
| **C** Tornier Aequalis | 60 | M | 7 | Gamma Air | Conventional | Keel | 5.5 | 3.12 |
| **D** Depuy Global | 38 | M | 10.7 | Gamma Air | Hylamer™ | Pegs | 3 | 0.37 |
| **E** Depuy Global | 65 | F | 2.6 | Gas Plasma | Crosslinked (50 kGy), Remelted | Pegs | 5 | 3.06 |
| **F** Depuy Global | 75 | M | 2 | Gamma Air | Hylamer™ | Pegs | 3 | 1.76 |
| **G** Depuy Global | 61 | F | 7.7 | Gamma Air | Hylamer™ | Pegs | 3 | 1.34 |
| **H** Depuy Global | 69 | M | 9.5 | Gamma Air | Hylamer™ | Pegs | 3 | 1.44 |
| **I** Depuy Global | 41 | M | 19.6 | Gamma Air | Hylamer™ | Pegs | 3 | 2.52 |
| **J** Depuy Global | 44 | F | 22.3 | Gamma Air | Hylamer™ | Pegs | 3 | 2.92 |
| **K** Tornier Aequalis | 58 | M | 11.5 | Gamma Air | Conventional | Pegs | 4.5 | 1.98 |
| **L** Tornier Aequalis | 69 | M | 8.9 | Gamma Air | Conventional | Pegs | 4.5 | 1.77 |
| **M** Depuy Global | 58 | M | 17.2 | Gamma Air | Hylamer™ | Pegs | 3 | 1.35 |
| **N** Depuy Global | 47 | M | 17.5 | Gamma Air | Hylamer™ | Pegs | 3 | 2.03 |
| **O** Tornier Aequalis | 58 | F | 8.6 | Gamma Air | Conventional | Pegs | 10 | 1.33 |
| **P** Depuy Global | 51 | M | 16.2 | Gamma Air | Hylamer™ | Pegs | 3 | 0.72 |

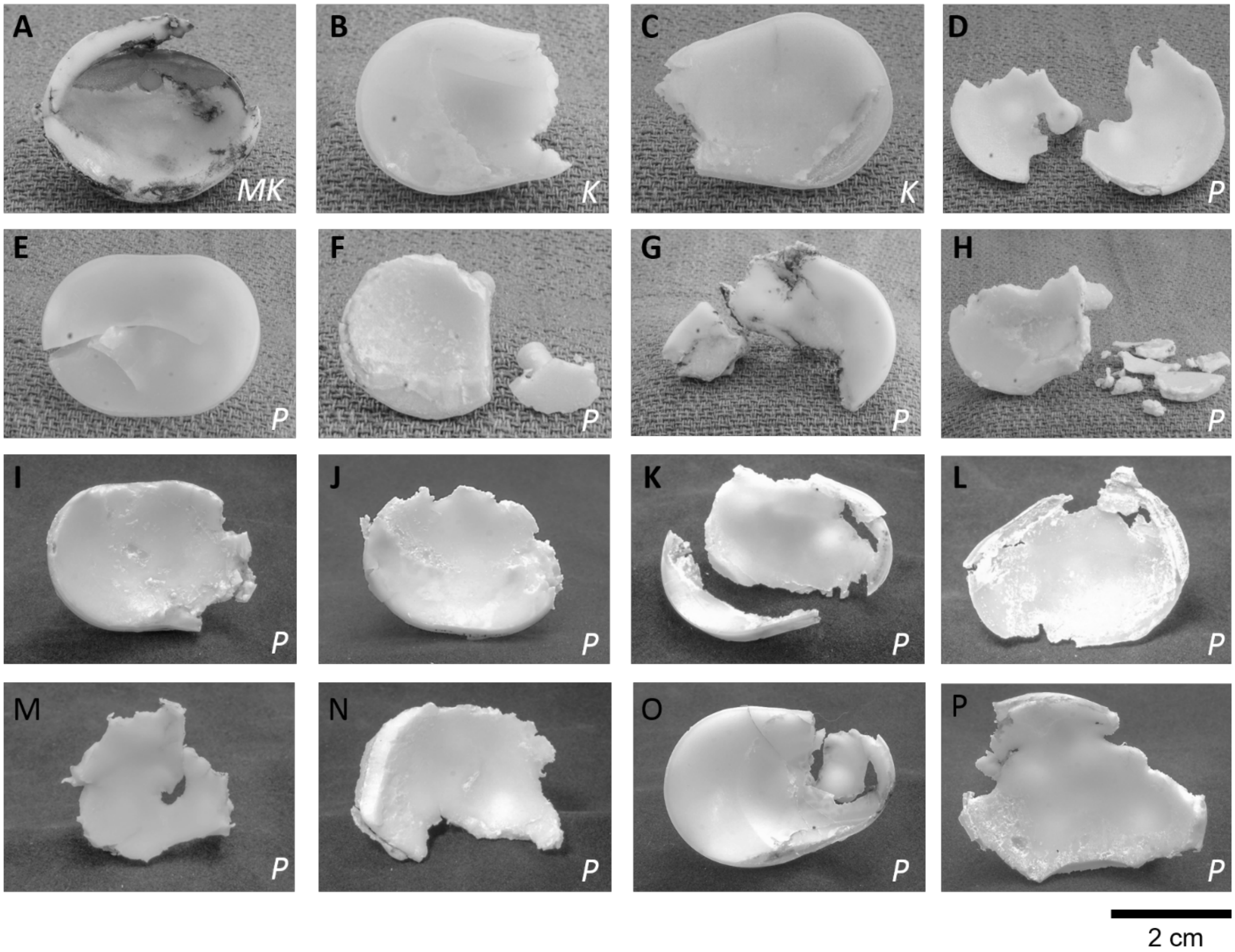

**Figure 2.21 |** The sixteen glenoids with severe fracture evaluated in this study. (**MK** = Metal-backed, Keeled; **P** = Pegged**;** **K** = Keeled).

### 2.4.2 Methods

*Fracture Mapping*

Gross fracture relative to original implant dimensions was recorded for each explanted glenoid. Original dimensions were estimated from manufacturer information, non-implanted devices, and other explants with minimal to no damage. Dimensions were entered into Solidworks (Dassault Systems, Waltham, Massachusetts) and 2D top-view drawings with a 1:1 size ratio were created for each glenoid. Fixation pegs and keels were used to align each fractured retrieval with a printout of its respective 2D outline. Digital images of the retrieval were then captured (Sony NEX-C3, Tokyo, Japan) and thresholded to highlight missing material using ImageJ (National Institutes of Health, Bethesda, Maryland). Images were then oriented, overlapped and scaled to a single reference glenoid size using Adobe Photoshop (San Jose, California) to map prevalent fracture locations for each brand.

*Fractography*

Fracture surfaces on three representative explants from each material cohort (XLPE, Hylamer™, conventional UHMWPE) were observed using optical microscopy (Infinivar CFM-2/S, Boulder, Colorado) and SEM (Hitachi TM-1000, Tokyo, Japan). Surfaces were sputter coated with gold-vanadium before SEM analysis.

*Oxidative Analysis*

Oxidation of three representative explants from each material cohort (XLPE, Hylamer™, conventional UHMWPE) were assessed using a FTIR spectrometer/microscope (Thermo-Scientific, Madison, WI, Nicolet iN10). Measurements were made versus depth through the thickness of the glenoid at the center of articulation and along the anatomical superior or posterior edge. Measurement parameters were 32 scans per 100-micron depth interval, using a wave number interval of 2 $cm^{-1}$ and an aperture of 100 square microns (Currier et al. 2013).

### 2.4.2 Results

*Retrieval Damage Analysis*

Gross observations of each glenoid revealed distinct bearing surface damage morphologies. Ten of the 16 explants (*Explants B-D*, *F-J*, *L*, and *N*), exhibited delamination, pitting and subsurface cracking, all damage consistent with fatigue wear. Such damage was extended across the entire bearing surface of these implants, and often prevalent along the rim or near fracture sites. *Explants A*, *K*, *M*, *O,* and *P* had little to no pitting damage, but did demonstrate significant wear-through and device thinning. *Explant E* was the only implant with no obvious delamination, pitting or wear-through.

Fractures were primarily located along the exterior rim of the 16 glenoids (**Figure 2.21, 2.22**). As seen in **Figure 2.22**, higher fracture frequency existed at the superior quadrant for Tornier Aequalis explants. Depuy Global implants saw a higher propensity for fracture along the entire exterior, with greatest levels in superior-posterior and superior-anterior regions. The metal-backed Zimmer Fenlin retrieval (**Figure 2.21 A**) revealed a fracture extending from the superior to inferior ends along the posterior side.

SEM analysis of *Explants E, J,* and *K* revealed distinctions between the three material cohorts represented in this study. *Explant J* (Hylamer™, gamma sterilized in air) displayed highly tortuous areas, significant cavitation, microcracking, and flat brittle regions (**Figure 2.23**). Cavitation and distortion were also seen on *Explant K* (conventional UHMWPE, gamma sterilized in air), in addition to striated tears in multiple regions across the surface (**Figure 2.24**). Fatigue striations were found across the entire fracture surface of *Explant E* (XLPE, remelted, gas plasma sterilization) (**Figure 2.25**). Differences in size and direction of the striated features are indicative of multiple crack fronts on the fractured surface. Two internal flaws were found on the fracture surface, including one at the superior edge of the implant.

*Oxidation Levels*

Oxidation profiles for *Explants E*, *J* and *K* are shown in **Figure 2.26**. Both the Hylamer™ (*Explant J*) and conventional (gamma sterilized) UHMWPE (*Explant K*) had elevated oxidation levels near the articulating surface at both the center and edge of the glenoid. Oxidation index values for these two implants exceeded 1.25, a threshold indicative of susceptibility to fracture due to oxidative embrittlement.(Currier et al. 2007) *Explant E* (XLPE, remelted, gas plasma sterilization) had a maximum oxidation index of 0.5 at the center of the articulating surface, well below this threshold.

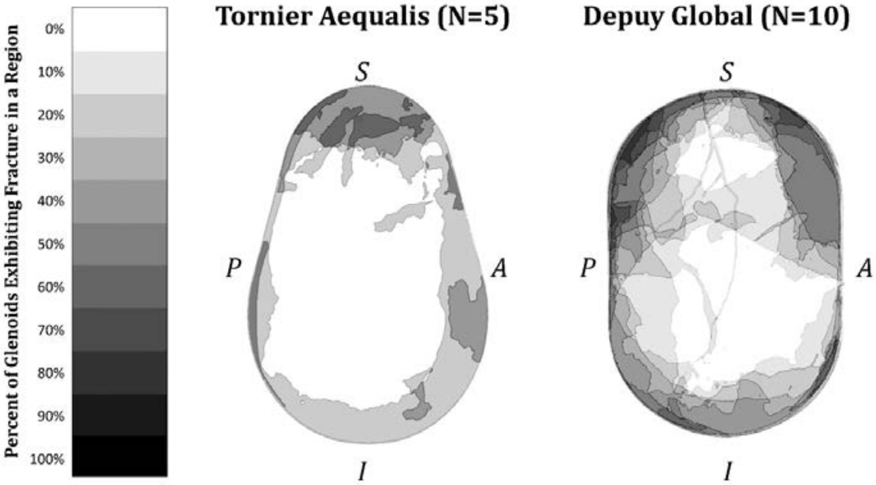

**Figure 2.22 |** Fracture maps for the 15 all-polyethyelene glenoids, grouped by device manufacturer. Each fracture map consists of overlapping images of individual glenoids scaled to a reference size and filtered to highlight fractured regions (shaded areas). Darker areas indicate a greater percentage of glenoids with fracture in that region. The maximum number of overlapping fractured regions was 3 out of 5 (60%) for the Tornier Aequalis and 8 out of 10 (80%) for the Depuy Global. The metal-backed Zimmer Fenlin explant evaluated in this study Is not shown due to a limited sample size (N=1). (S = Superior, P = Posterior, A = Anterior, I = Inferior)

### 2.4.3 Discussion

*Case Study Analysis*

This work illustrates the unique fracture mode that glenoid components can suffer *in vivo*. Such catastrophic damage ranges from through-thickness cracking to complete disintegration over an implantation time from 2 to 23 years, underscoring the unpredictability of this particular glenoid failure mode. Fractures occurred most often along the outer rim of the glenoid component in both Tornier and Depuy designs, and the most frequent site was the superior rim (**Figure 2.22**). This is consistent with radiographic evidence for dominant superior-posterior contact for a range of shoulder positions (Massimini et al. 2010). Fracture co-location in these areas confirms the likelihood of repetitive eccentric edge loading in glenoid components, which is uncommon in hip and knee devices.

Rim fracture was apparent in all glenoids, regardless of the degree of radial mismatch, which ranged from 0 (high conformity) to 10 mm (low conformity) (**Table 2.1**). Furthermore, the minimum thickness measured on each glenoid ranged from 0.3 mm to 3 mm, demonstrating some degree of wear-through due to elevated contact stresses. Both radial mismatch and reduced thickness are thought to contribute to increased contact stresses, as discussed later.

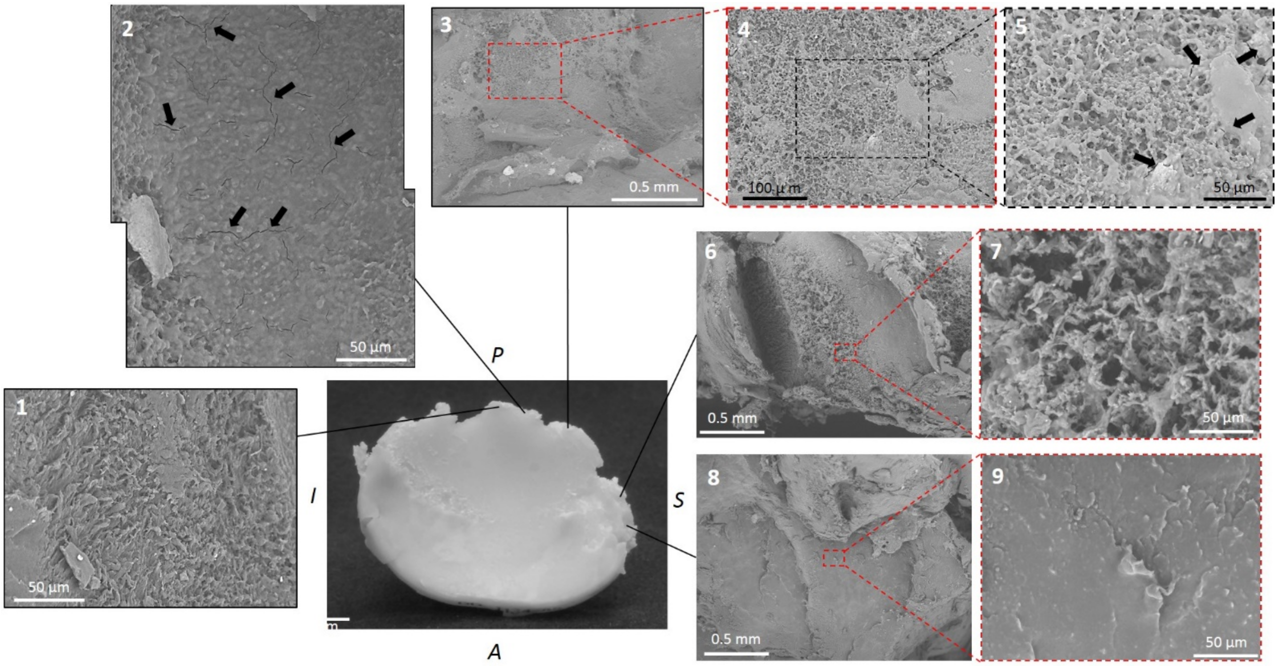

**Figure 2.23 |** Fractography analysis of a Hylamer$^{TM}$ glenoid gamma sterilized in air (*Explant J*). Regions 2 and 5 show microcracking on the fracture surface, highlighted by black arrows. SEM images in Region 1 shows some fibrillation and cavitation on the posterior side; cavitation and tortuosity are prevalent in Regions 3-7, most likely the result of oxidative degradation of the polymer. Regions 8 and 9 show relatively brittle flat surfaces. (*S = Superior, I = Inferior, A = Anterior, P = Posterior*)

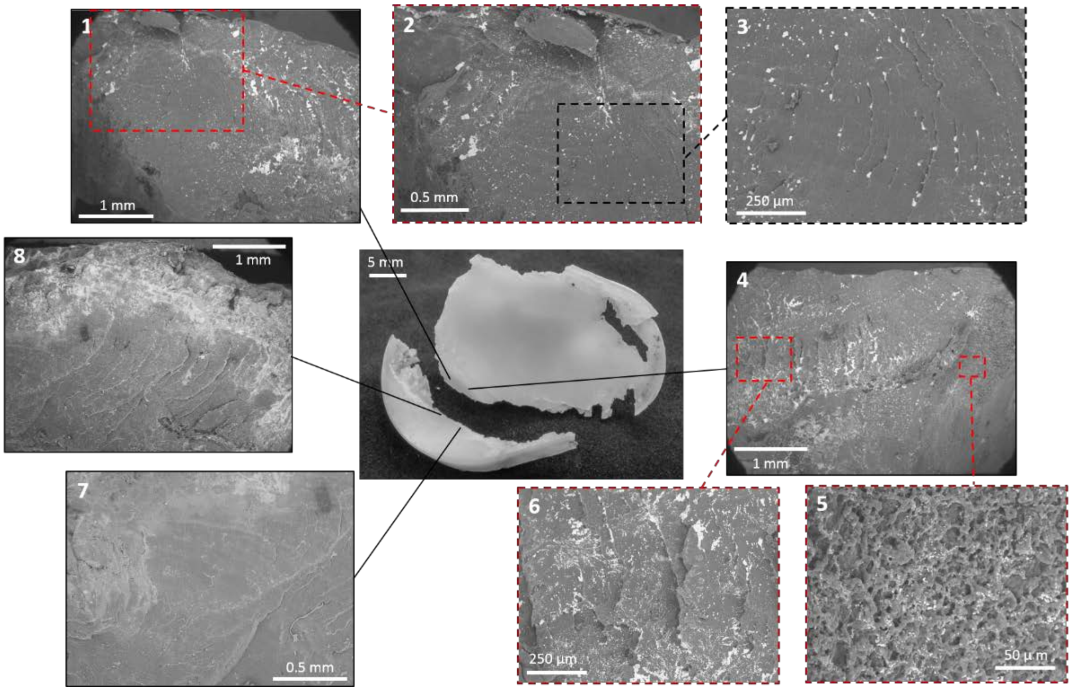

**Figure 2.24 |** SEM micrographs of *Explant K*, a conventional UHMWPE component that was gamma-sterilized in air. Striations are seen in almost all regions with varying degrees of tearing, highlighted by dashed lines and black arrows in Regions 3, 7 and 8. Cavitation in Region 5 is similar to that seen in **Figure 3**. (*S = Superior, I = Inferior, A = Anterior, P = Posterior*)

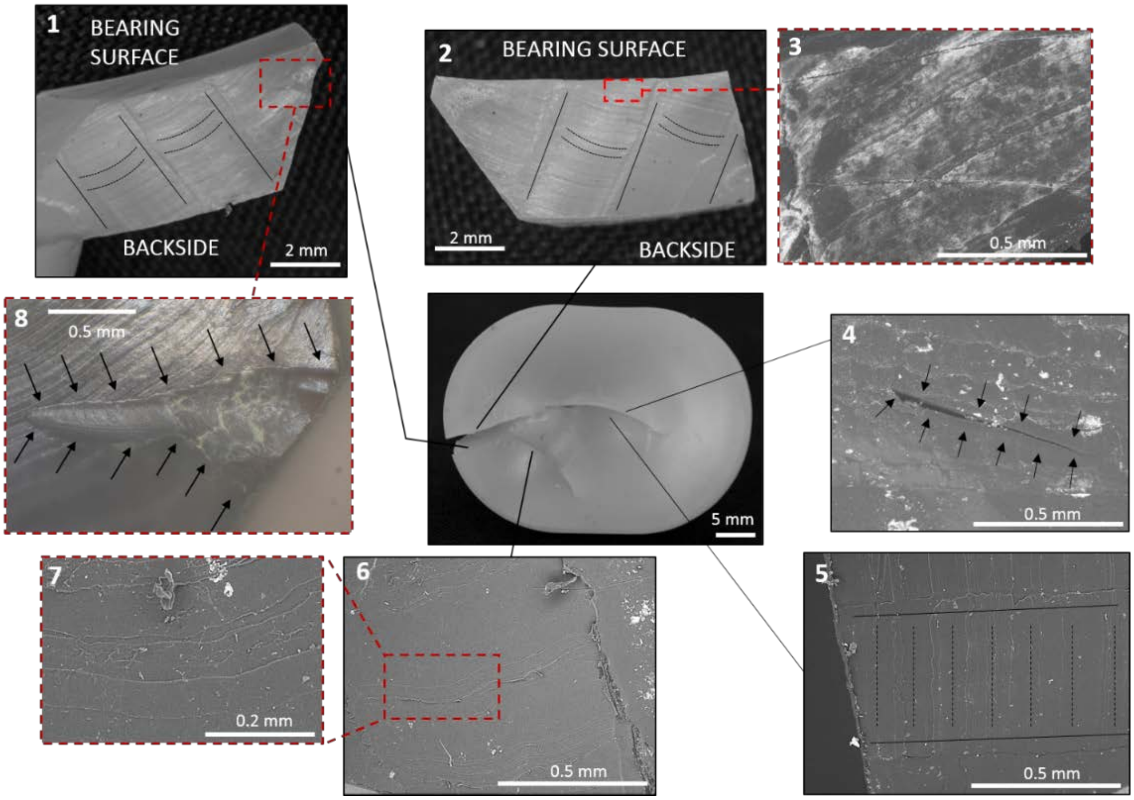

**Figure 2.25 |** Sample E from this cohort was composed of XLPE. Optical images in Regions 1 and 2 show the mated fracture surfaces of the crack at the superior edge of the component. Both surfaces exhibit perpendicular fatigue striations (highlighted with dashed lines and black arrows) propagating from the bearing surface to the backside of the implant as well as from the exterior to the interior of the devices. These striations are also seen under SEM in Regions 3, 5, 6 and 7, representative of crack growth under cyclic loading (fatigue). Regions 4 and 8 show internal flaws (outlined by red arrows) on the order of 1-2 mm in length which may have served as crack initiation sites. (*S = Superior, I = Inferior, A = Anterior, P = Posterior*)

All glenoids evaluated in this study were exposed to some degree of irradiation to promote sterilization and/or crosslinking. The majority of the fractured glenoids in this study were either conventional UHMWPE or Hylamer$^{TM}$, both subjected to gamma irradiation (25-40 kGy). Fractographic analysis of representative gamma-air sterilized implants in **Figures 2.23** and **2.24** show cavitation, material distortion and embrittlement consistent with bench testing evaluation of fatigue crack growth in sterilized and aged materials (Baker et al. 2003). FTIR analysis (**Figure 2.26**) confirms elevated oxidation levels near the bearing surface, concomitant with exposure to oxygen during sterilization and subsequent shelf aging. It should be noted that oxidation index values from FTIR analysis may be skewed due to post-explantation shelf aging in the laboratory. Nine of the glenoids were composed of Hylamer$^{TM}$, which has been shown to exhibit accelerated oxidation after gamma irradiation compared to conventional UHMWPE (Rockwood & Wirth 2002). Hylamer$^{TM}$ explants shown in **Figure 2.21** (*Explants D, F-J, M, N* and *P*) are the most severe cases of fracture in this cohort, including instances of severe wear-through (*Explant D*), disintegration (*Explant H*), and complete rim loss (*Explant M*).

The presence of a severely fractured remelted XLPE glenoid component (*Explant C*) in this study highlights the continued concern over clinical performance of glenoids that make use of crosslinked formulations of UHMWPE (XLPE).. The recent introduction of XLPE to TSR derives from its significant success in hip replacements in reducing wear and thus preventing the onset of osteolysis (Muratoglu et al. 1999; Muratoglu et al. 2001; McKellop, Shen, Lu, et al. 1999; Kurtz et al. 2011). To combat the tradeoff in oxidative resistance that accompanies higher doses of irradiation, XLPE implants can be annealed above the melt temperature ("remelted") to annihilate free radicals. Even with oxidative stability through remelting, XLPE exhibits a significant reduction in fatigue crack propagation resistance (Atwood et al. 2011; Baker et al. 2003). *Explant C* records the first such failure for an XLPE glenoid component.

*Explant C* failed in less than 3 years, one of the shortest durations of the glenoids evaluated from our retrieval collection. **Figure 2.24** reveals a microscopic flaw at the superior end of the device where fracture most likely initiated. Fractography shows distinct features indicative of stable crack growth under cyclic loading, with striations reflective of multiple crack fronts along the fractured surface. The same features have been documented on fracture surfaces for XLPE hip and knee components, as seen in the literature and in the two cases above (Furmanski et al. 2009; Ansari, Chang, et al. 2013; Pruitt et al. 2013). FTIR analysis in **Figure 2.26** reveals that oxidation levels are well below levels indicative of oxidative embrittlement, consistent with post-irradiation remelting processing to annihilate free radicals. *In vivo* oxidation processes would most likely be negligible for the XLPE explant since FTIR assessment of the retrieval occurred more than six months post-explanation; instead, post-explantation shelf oxidation of absorbed lipids is most likely to blame (Oral et al. 2012; Currier et al. 2010). Finally, the minimum thickness of *Explant C* shown in **Table 2.1** is comparable to the non-damaged areas of the glenoid, and little *in vivo* wear is seen on the bearing surface, consistent with a higher crosslinking density. However, this translates to a manufactured thickness of roughly 3 mm for this glenoid design, which combined with a moderate radial mismatch of 5 mm, is expected to experience contact stresses well above the yield strength of UHMWPE (Swieszkowski et al. 2003; Bartel et al. 1986). Thus, the catastrophic failure of *Explant C* can be attributed to several factors: elevated contact stresses, the presence of an internal flaw, and a reduced resistance to fatigue crack propagation due to crosslinking.

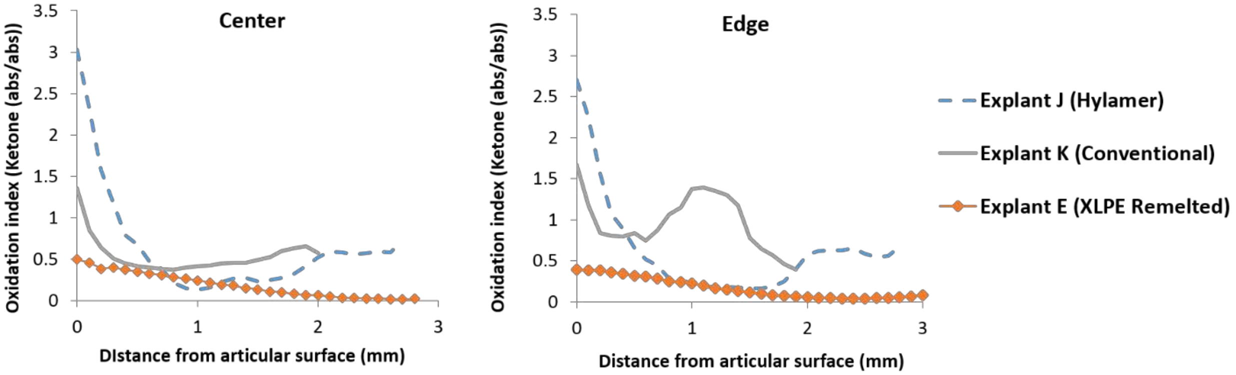

**Figure 2.26 |** Oxidation profiles for three representative glenoids from each material cohort (*Explant J*: Hyalmer$^{\text{TM}}$ gamma sterilized; *Explant K*: conventional gamma sterilized UHMWPE; and *Explant E*: remelted, gas plasma sterilized XLPE). Both gamma sterilized implants (*Explant J* and *Explant K*) exhibit elevated oxidation levels indicative of mechanical embrittlement.

*Glenoid Fracture: Reported Cases*

Provided TSR's more recent entry into the orthopedic market, analyses of explants are fairly limited in scope. A majority of studies dedicated to glenoid components, in particular, have assessed bearing surface damage using established methodologies for hips and knees, such as the Hood et al. (1986) method. Such protocols established primary damage morphologies including burnishing, scratching, pitting, delamination, abrasion, embedded bone cement debris, and surface deformation (Hood et al. 1983; McKellop 2007). The handful of studies evaluating glenoid retrievals similarly identified these damage modes, with a higher prevalence of pitting and delamination. Moreover, they also introduced unique morphologies including rim erosion (Scarlat & Matsen 2001), wear-through (Gunther et al. 2002; Nho et al. 2009), and fracture (Gunther et al. 2002; Nho et al. 2009).

Severe fracture, in particular, has been documented in other studies, as seen in **Figure 2.27**. Scarlat et al. (2001) reported 13 "severe" fractures in a cohort of 37 glenoids, all with similar damage morphologies to the retrievals above. Gunther et al. (2002) investigated 10 glenoids, of which 4 fractured; the authors noted that fracture occurred in all areas of the glenoid, but with preference for the posterior and superior quadrants. Four of 7 glenoids examined by Hertel et al. (2003) also exhibited fracture across the anterior-posterior (**Fig. 2.27 A**) and superior-inferior axes, as well as a 3-part fracture (**Fig. 2.27 B**). Finally, Nho et al. (2008) found 7 of 78 glenoids with severe fracture (**Fig. 2.27 C**), including 3 that were composed of Hylamer.

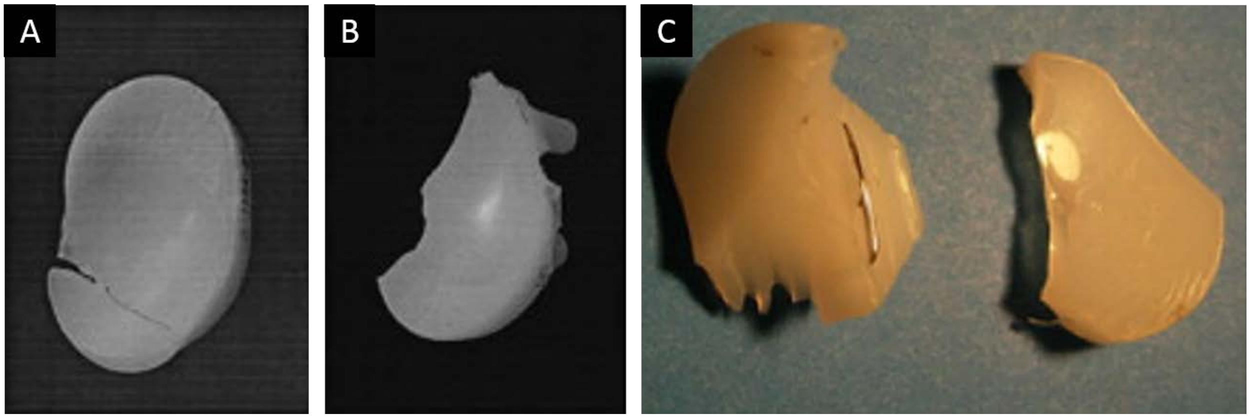

**Figure 2.27** | Examples of fractured glenoids. (A) and (B) are both Hylamer Depuy Global components with a radial mismatch of 4 mm (Hertel & Ballmer 2003). Material composition of (C) is unknown (Nho et al. 2009).

While the catastrophic fractures shown in **Figures 2.21** and **2.27** are recurring incidences, it is difficult to extrapolate the exact design-material issues at play that resulted in these failures due to inconsistent records of composition or manufacturing information. The fracture maps in **Figure 2.22** reflect predominance of rim fracture but general unpredictability as to exact initiation sites; Gunther et al. (2002) also confirmed that fracture was present in all quadrants (inferior, superior, anterior, posterior). Correlation of all damage modes with alignment does suggest a relationship between prevalence of wear patterns and device alignment, including retroversion or inferior placement of the glenoid and superior placement of the humeral head (Nho et al. 2009; Nho et al. 2008). Provided the variability of fracture locations in these studies and the 16 glenoids discussed above, it is difficult to establish similar comparisons between location and surgical placement. However, as seen in **Table 2.1**, the presence of a radial mismatch, or nonconforming bearing coupling, does appear to have a significant impact on fracture potential, as discussed in the following section.

### *Conformity, Thickness and Loading of Glenoid Components*

Optimal glenoid geometry remains an ongoing debate among manufacturers today (Iannotti et al. 1992; Karduna et al. 1997; Terrier et al. 2009; Anglin et al. 2000; Oosterom et al. 2003; Friedman 1992; Walch et al. 2002). Glenoid-humeral head conformity, in particular, sees significant variability across manufacturers, as seen in **Table 2.1**. Furthermore, the incidence of fracture seen in the above 16 glenoids occurred across the entire range of conformity values, corroborating findings from Nho et al. (2008). The disconnect between conformity and fracture propensity may in fact be due to trade-offs presented by both low and high radial mismatch (**Figure 2.19**). Low conformity (high radial mismatch) can elevate contact stresses by minimizing the distribution of loads at the bearing surface, resulting in sub-surface crack generation that can propagate under cyclic loading, as seen with delamination and pitting in knees (Bartel et al. 1986; Swieszkowski et al. 2003; Williams et al. 1998; Bartel et al. 1995). High conformity (low to or no radial mismatch) can decrease surface contact stresses (similar to hips). However, shoulder translation across the highly conforming glenoid can result in edge loading, increased rocking horse motion, and higher bending stresses at the exterior rim (Anglin et al. 2000; Oosterom et al. 2003).

The majority of the glenoid explants exhibited some degree of radial mismatch, suggesting a propensity toward fatigue wear damage as seen in TKR components. Delamination and pitting have been noted on retrieved gamma sterilized UHMWPE tibial components, primarily in the central regions of the tibial plateaus (Hood et al. 1983; Wright & Bartel 1986; Williams et al. 1998). Similar damage morphologies were noted on more than half of the explants in this study. However, unlike knees, this fatigue wear extended across the *entire* surface of what remained of each glenoid, consistent with significant translational motion in the joint. Furthermore, all explants (regardless of the presence of delamination and/or pitting) fractured along the external rim, indicating that edge loading in the shoulder may lead to implant failure more than any effects from elevated contact stresses.

Increased stresses due to decreasing conformity can be exacerbated by the limited thickness of glenoids. Implant thickness has long been a critical design factor for joint replacements. Reduced thickness, especially when coupled with a metallic backing, can drive up component stresses, leading to greater bearing surface wear or fracture. Glenoids are typically manufactured with an initial thickness of 3 to 6 mm, which is much lower than acetabular (4 to 8 mm) and tibial liners (6 to 10 mm) (Bartel et al. 1986). Computational analysis has demonstrated that contact stresses in UHMWPE for knee components below 8 mm exceed its yield strength, resulting in wear damage modes that span those seen in both hip and knee components (Bartel et al. 1986; Collier et al. 1991). A similar analysis by Swieszkowski et al. (2003) for TSRs found contact stresses to approach the yield strength of UHMWPE (20 MPa) for 4 mm thick glenoids with a 2 to 4 mm radial mismatch. Metal-backed implants achieved comparably higher stresses for the same thickness, accounting for *Explant A* (above) having the greatest degree of wear-through despite a fully conforming design (Swieszkowski et al. 2003). Such above-yield contact stresses has also been shown by Terrier et al. for a variety of glenoid conformities, thicknesses and loading scenarios (**Figure 2.28**), highlighting the enhanced propensity for crack initiation and fatigue crack propagation in shoulder replacements (Terrier et al. 2006). These reported stresses are complemented by retrieval studies that demonstrate incidences of delamination, subsurface cracking, pitting and fracture – even in modern devices that claim to minimize wear through crosslinking.

In conclusion, TSR components present a complex stress environment that is highly dependent on device design. Shoulders have historically borrowed UHMWPE compositional changes from those clinical formulations used in hip and knee arthroplasty. However, the severe fractures presented in this case study reflect distinctions between TSRs and predicate devices that must be considered in material selection. In particular, while similar in their lack of conformity, TKR and TSR components exhibit distinct failure modalities, with the latter primarily succumbing to significant edge loading that is unique to the shoulder. Provided this eccentric loading and the additional thickness and conformity constraints for glenoid designs, the use of XLPE in the shoulder may not be ideal for TSRs.

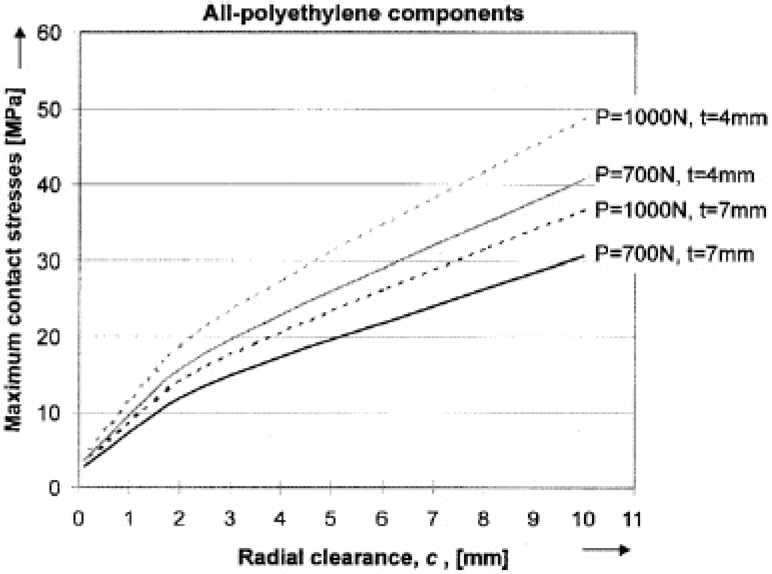

**Figure 2.28** | Contact stress as a function of conformity (radial clearance) and thickness). Terrier et al. (2006) demonstrate that contact stresses can exceed yield for thickness of 4 mm for radial mismatches of 3 to 5 mm.

## 2.5 Conclusions

The case studies presented above illustrate the severe consequences of *in vivo* fracture of UHMWPE in TJR. In particular, many of these designs succumbed to the pitfalls of crosslinking, whether that be through reduced resistance to fatigue crack propagation or oxidation by way of free radical reaction. Recent polymeric formulations have been developed to address oxidation, such as heat treatments above and below the melt temperature of UHMWPE or the addition of antioxidants such as Vitamin E. However, there is no experimental evidence that such solutions will resolve the diminished mechanical properties associated with crosslinking.

It is important to recognize the significant clinical benefits of crosslinking: wear-induced osteolysis has seen a significant reduction since the introduction of crosslinked UHMWPE, resulting in extended implant lifetimes. However, as shown by these case studies, the transition to using crosslinked UHMWPE in existing designs neglected to consider the interplay between design and reduced fatigue or fracture resistance. For shoulders, this has manifested through reduced thickness and varying conformity, geometrical variables that have been investigated by several authors (Bartel et al. 1986; Swieszkowski et al. 2003; Terrier et al. 2006). For hips and knees, notches that have been introduced to improve kinematic stability or fixation also serve as sites for crack initiation and subsequent fracture. Despite this clinical finding, little evidence exists regarding the influence a notch may have on crack growth under cyclic loading in UHMWPE.

The following two chapters outline existing knowledge regarding mechanisms of crack growth in UHMWPE, in the context of fracture mechanics theory. **Chapter 3** focuses on sharp crack growth under cyclic loading, with a brief overview of existing literature on fatigue of UHMWPE. **Chapter 4** describes theories regarding notch fatigue, and how fracture mechanics can used to predict fatigue crack initiation and propagation in the presence of a stress concentration. Both of these chapters lay the foundation for experimental fatigue work described in **Chapter 5** to elucidate how clinically-relevant notches seen in hip and knee replacements influence crack propagation.

# Chapter 3 – Fracture and Fatigue in UHMWPE: Theory and Practice

## 3.1 Theory: Fracture and Fatigue

Material fracture and fatigue accounts for over $119 billion annually in the United States (US Department of Commerce 1983) and has been the cause of hundreds of deaths throughout history (Campbell 2012). Since the early 1900s, significant effort has been dedicated to improving knowledge (and prevention) of fracture mechanisms to improve product lifetimes in structural, transportation, nuclear industries. Only recently has fracture and fatigue studies gained credibility in the medical device industry, prompted primarily by catastrophic device failures in both orthopedic and cardiovascular arenas (F Ansari et al. 2014; Grivas et al. 2007; S. A. Atwood et al. 2010; Ellman & Levine 2013; Yates et al. 2008; Arenas et al. 1999; Burstein 1986). As a result, numerous studies have since elucidated crack behavior in biomaterials, including: superelastic shape-memory Nitinol alloys to address fatigue fracture of vascular devices, particularly stents (McKelvey & Ritchie 1999; Pelton et al. 2008; Pelton 2011); transformation-toughened zirconia ceramics to understand the catastrophic rupture of hip femoral heads (Chevalier 2006; De Aza et al. 2002); pyrolytic carbon to assess the role of small crack growth and stress-corrosion cracking in heart valves (Ritchie 1996; Ritchie et al. 1990; Dauskardt et al. 1994); and UHMWPE to understand the role of sterilization, irradiation crosslinking and heat treatments on crack initiation and propagation (**Section 3.2**).

Inherently, fracture depends on the probability of flaw existence or formation within a material. Most preliminary material assessments evaluate the initiation of such a flaw under monotonic tensile or compression loading, producing a typical stress-strain material curve. However, such testing is generally limited to pristine, defect-free specimens in the laboratory, and such methodology rarely captures component behavior in the field. Microscopic cracks can be generated under cyclic loading well within the elastic (recoverable) regime of the material (fatigue), or can appear during manufacturing or installation. Thus, understanding material failure in the presence of a flaw becomes crucial to predicting its durability in an end application. Fracture mechanics enables a mechanistic knowledge of how materials break down in the presences of a flaw under static or cyclic loading. This approach can be broken into linear elastic (LEFM) or elastic plastic (EPFM) approaches, depending on the degree of plasticity ahead of a given crack. The following section outlines central parameters for both LEFM and EPFM that serve as predictors for crack growth and failure under static loading. Methodologies for assessing fatigue fracture will subsequently be discussed, with a particular focus on LEFM approaches.

### 3.1.1 Fracture Mechanics

#### *Energy Release Rate*

Griffith (1921) used an energy balance approach to provide one of the first quantifications of crack growth as a function of global stresses in a linear elastic solid (glass). He assumed that a crack would grow only if the net energy of the system is lowered. Considering a crack of length ***2a*** in an infinitely wide plate (**Figure 3.1**), an energy balance can be written as:

$$\in = \in_o + \Pi + W_s \qquad \textbf{eq. 3.1},$$

where $\in$ represents the energy of the system , $\in_o$ is the initial energy of the system, $\Pi$ is the strain energy stored by the system and $W_s$ is the work required to create new surfaces. Taking the derivative of this equation with respect to ***dA***, the change in crack area (related to the change in its length, ***da***, and sample thickness, ***B***):

$$\frac{d\in}{dA} = \frac{d\Pi}{dA} + \frac{dW_s}{dA} = 0 \qquad \textbf{eq. 3.2}$$

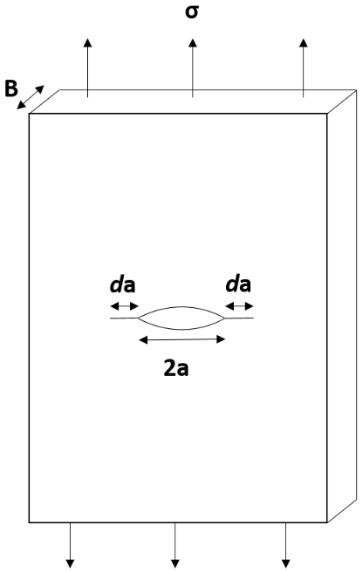

**Figure 3.1** | Infinitely wide plate of unit thickness composed of a linear elastic material containing an initial crack of length *2a*.

Here, the transition from increasing strain energy to a net decrease in energy can be found through the balance between potential energy and surface energy terms. Stress analyses by Inglis (1913) provided an estimate for changing strain energy:

$$\frac{d\Pi}{dA} = -\frac{\pi {\sigma_\infty}^2 a}{E} \qquad \textbf{eq. 3.3},$$

where ***E*** is the Young's modulus of the material. The work to create two new surfaces of length ***2a*** can be written in terms of the material's surface energy (assuming unit thickness),

$$W_s = 4a\gamma_s \qquad \textbf{eq. 3.4}$$

And deriving **eq. 3.4** with respect to area of the cracked surface:

$$\frac{dW_s}{dA} = 2\,\gamma_s \qquad \textbf{eq. 3.5}$$

Grouping terms and simplifying, the Griffith balance provides an energy approximation for fracture:

$$\frac{{\sigma_\infty}^2 \pi a}{E} = 2\gamma_s \qquad \textbf{eq. 3.6}$$

The left term was later classified by Irwin (1957) as the energy release rate (***G***) and the right side characterized as the materials resistance, ***R***.

### *Stress Intensity Factor*

The energy release rate quantifies the global change in energy as a result of crack growth, but does not described the local stress field that exists ahead of the crack tip. Irwin (1957) and Williams (1957) first described the near crack-tip stresses in a linear elastic body undergoing tensile loading as a *singularity* with respect to *r*, the radial distance ahead of the crack tip:

$$\begin{Bmatrix} \sigma_{xx} \\ \sigma_{yy} \\ \sigma_{xy} \end{Bmatrix} = \frac{K_I}{\sqrt{2\pi r}} cos\left(\frac{\theta}{2}\right) \begin{Bmatrix} 1\text{-}\sin\frac{\theta}{2}\sin\frac{3\theta}{2} \\ 1+\sin\frac{\theta}{2}\sin\frac{3\theta}{2} \\ \sin\frac{\theta}{2}\cos\frac{3\theta}{2} \end{Bmatrix} \qquad \textbf{eq. 3.7,}$$

where $\sigma_{xx}$, $\sigma_{yy}$, and $\sigma_{xy}$ represent the normal and shear stresses and ***r*** and ***Θ*** describe the polar coordinates ahead of the crack tip, as seen in **Figure 3.2**. Here, the stress intensity factor (***K***) is also introduced, a parameter that has become central to linear elastic fracture mechanics (LEFM). This factor represents the *driving force* behind crack growth. Stress intensity is specific to the type of external loading, and can be characterized as tensile opening (Mode I), in-plane shear (Mode II) or out-of-plane torsion (Mode III). Similar equations to those listed in **eq. 3.7** have been developed for Mode II and Mode III stress fields using $K_{II}$ and $K_{III}$, respectively. Since Mode I often generates most severe conditions for crack growth (Suresh 1998), it will remain the focus of this work.

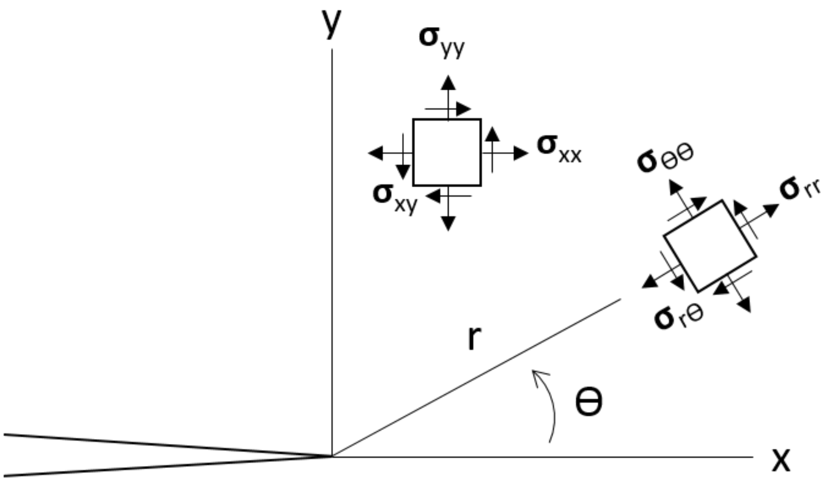

**Figure 3.2** | Coordinate systems defined ahead of the crack tip (Adapted from Suresh, 1998).

Stress intensity captures not only the local stress field ahead of the crack tip but also the displacement field. Furthermore, it can be written as a function of global stresses and crack geometry:

$$K_I = F\sigma_\infty\sqrt{\pi a} \qquad \textbf{eq. 3.8,}$$

where $\boldsymbol{\sigma_\infty}$ represents the far-field stress applied to the specimen, $\boldsymbol{a}$ characterizes the crack length, and $\boldsymbol{F}$ represents a geometric factor that accounts for specimen geometry. Stress intensity factors for a variety of specimen geometries and loading scenarios have been characterized by Tada, Paris and Irwin (1985). Note that the stress intensity factor for a crack of length $\boldsymbol{2a}$ has a geometric factor ($\boldsymbol{F}$) of 1 (Tada et al. 1985), and can be directly related to Griffith's energy release rate in linear elastic materials:

$$\frac{{K_I}^2}{E} = G \qquad \textbf{eq. 3.9}$$

The stress intensity at which a material can no longer resist fast fracture under the presence of a flaw is known as its fracture toughness ($\boldsymbol{K_c}$). Fracture toughness can be defined for each mode of loading ($\boldsymbol{K_{Ic}}$, $\boldsymbol{K_{IIc}}$, $\boldsymbol{K_{IIIc}}$), and is highly dependent on environmental conditions as well as specimen geometry. The latter requirement derives from the need to satisfy small-scale yielding conditions. The linear elastic solutions displayed above were developed in the case of infinitely sharp cracks growing in a fully elastic medium; however, LEFM can still be used with a small degree of inelastic deformation ahead of the crack tip. Such inelasticity occurs due to elevated stresses at the crack tip (i.e. as $r \rightarrow 0$), causing local yielding in a region known as the plastic zone. If the plastic zone remains small compared to the dimensions of both the specimen and the crack itself, LEFM can be used to accurately predict crack growth behavior under both cyclic and monotonic loading (**Figure 3.3**).

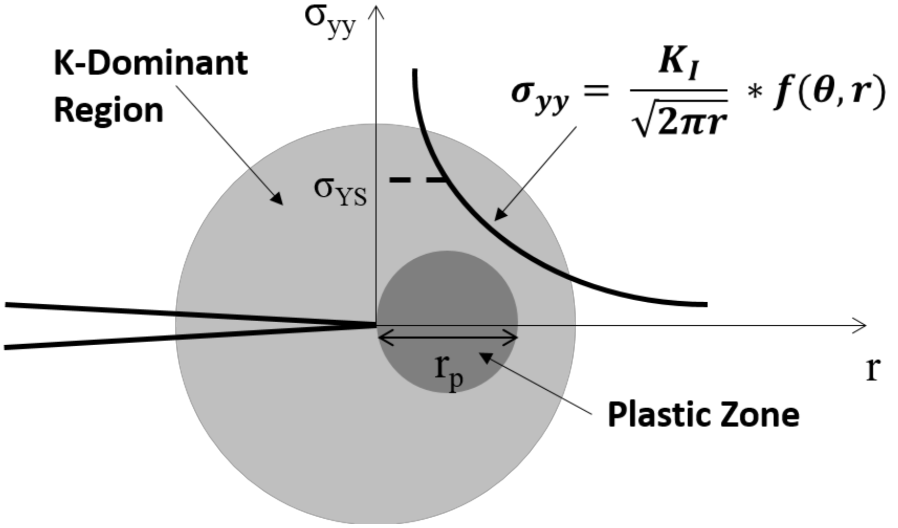

**Figure 3.3** | Region of K-dominance ahead of a sharp crack in a linear elastic material. For Mode I loading, local stresses in the tensile direction ($\sigma_{yy}$) approach and exceed the yield strength ($\sigma_{YS}$) as r approaches 0. This causes local plasticity at the notch tip and redistribution of load and material in a plastic zone ($r_p$). Small scale yielding conditions are satisfied when this plastic zone remains small relative to the K-dominant (linear elastic) region (Anderson 2005).

Conditions for small-scale yielding are outlined by several standards established by the American Society for Testing and Materials (ASTM). Many of these equation derive from Irwin's (1960) solution for the plastic zone size ($r_p$) under the conditions of plane stress and plane strain:

$$r_p = \frac{1}{3\pi}\left(\frac{K_I}{\sigma_y}\right)^2 \text{, plane strain} \quad \textbf{eq. 3.10}$$

$$r_p = \frac{1}{\pi}\left(\frac{K_I}{\sigma_y}\right)^2 \text{, plane stress} \quad \textbf{eq. 3.11}$$

Here, the plastic zone size is a function of not only the Mode I stress intensity, but also the yield stress of the material. As seen in **eq. 3.10** and **eq. 3.11**, the plastic zone size varies under conditions of plane strain (triaxial stress state) or plane stress (biaxial stress state). Stress triaxiality – predominantly in the center of thick specimens – can inhibit plastic zone growth, resulting in faster crack propagation rates than plane stress fields that typically exist at the free surfaces of a specimen (**Figure 3.4**). Specimen thickness can thus play a significant role in determining critical stress intensity values; for all material specimens, a minimum thickness is needed to ensure a large region of plane strain and thus measure the fastest crack growth regardless of geometry. Dimensions outlined by a number of ASTM standards (ASTM International 2013a; ASTM International 2012a; ASTM International 2013b) ensure LEFM validity and are often proportional to $\left(\frac{K_I}{\sigma_y}\right)^2$, where $K_I$ can represent the critical stress intensity or the maximum $K$ value achieved under cyclic loading.

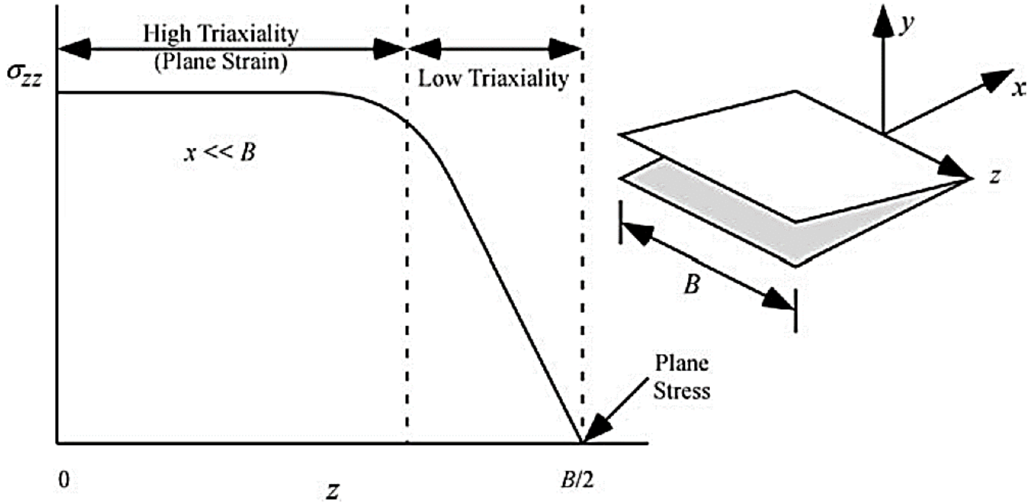

**Figure 3.4** | Out-of-plane stresses ahead of a sharp crack as a function of thickness. Total crack thickness is ***B***. Triaxial stresses are maintained near the center of the sample (***z*** < ***B/2***), impeding plastic zone growth and allowing for faster crack propagation. Near the edges, plane stress conditions are reached due to a decreasing $\sigma_{zz}$, resulting in a greater degree of plasticity near the edge of the sample (Anderson 2005).

## *J-Integral*

When the conditions of small-scale yielding, as described above, are not met, elastic-plastic fracture mechanics provides an alternative method for characterization of nonlinear crack growth. Rice (1968) established the theoretical foundation for a nonlinear fracture parameter, the ***J***-integral. This path-independent line integral encircles the crack tip to evaluate any tractions acting on the cracked body within that region:

$$J = \int \omega dy - \overline{\boldsymbol{T}} \cdot \frac{\partial \overline{\boldsymbol{u}}}{\partial s} ds \qquad \textbf{eq. 3.12,}$$

where $\boldsymbol{\omega}$ is the material's strain energy density, ***y*** is the distance normal to the crack plane, $\overline{\boldsymbol{T}}$ is the traction vector, $\overline{\boldsymbol{u}}$ is the displacement vector, and ***s*** is the contour length. This ***J*** -integral can be simplified to the rate of change of potential energy with respect to nonlinear crack advance, and for elastic crack growth, has been shown to be equal to ***G*** (Rice 1968).

Like ***K***, the ***J*** -integral fully defines the local stresses and strains ahead of a crack tip and can be related to global deformation of a cracked body. Hutchinson (1968) and Rice & Rosengren (1968) established the local stress fields – known as the "HRR fields" – as a function of ***J***:

$$\sigma_{ij} = \left(\frac{J}{\alpha \sigma_y \varepsilon_y I_n r}\right)^{\frac{1}{n+1}} \tilde{\sigma}_{ij}(\theta, n) \qquad \textbf{eq. 3.13},$$

where $\boldsymbol{\alpha}$ is a material constant, $\boldsymbol{I_n}$ is a function of the strain hardening component, ***n***, and $\tilde{\boldsymbol{\sigma}}_{\mathbf{ij}}$ is a dimensionless function that depends on not only the polar angle and strain hardening component, but also whether the specimen is plane stress or plane strain. Here, ***J*** exhibits a $\boldsymbol{r}^{-\frac{1}{n+1}}$ singularity, as compared to ***K***'s $\frac{\mathbf{1}}{\sqrt{\boldsymbol{r}}}$ singularity.

In the laboratory, ***J*** can be calculated from the change in absorbed strain energy, ***U***, of a specimen of thickness **B**, as obtained from load-displacement curves:

$$J = -\frac{1}{B}\left(\frac{\partial U}{\partial a}\right)_{\Delta} \qquad \textbf{eq. 3.14},$$

Critical nonlinear crack growth occurs when ***J*** exceeds a critical value for a material, $\boldsymbol{J_{IC}}$. While the ***J*** -integral accounts for nonlinear growth, specific geometry specimen requirements are needed to avoid excessive plastic behavior (blunting) at the crack tip. Sample specifications that meet the conditions for ***J*** -dominance are outlined by ASTM (ASTM International 2013a).

### 3.1.2 Fatigue

Component fracture is not necessarily isolated to single overloads that surpass the elastic limits or fracture toughness of a material. Cyclic loading well below yield can still generate and multiply microscopic damage, causing failure after tens to millions of cycles of use. In general, the fatigue lifetime of a material can be broken into several stages:

- nucleation of damage in a material at the nano- or microscale;
- coalescence of damage into visible dominant cracks;
- propagation of one or more of these cracks under a stable growth rate; and
- accelerated crack growth to failure known as fast fracture.

Assessing fatigue behavior of a material can be broken into two schools of thought: the total life approach or defect tolerant approach. The total life approach evaluates all of the above listed stages of material lifetime. In general, such approaches predict longer overall lifetimes for components or materials, since most specimens are manufactured to ensure that microscopic defects are eliminated. Under these starting conditions, roughly 80% of the fatigue life of most materials is devoted to the initiation of cracks. Furthermore, the total life approach allows for testing of final *component* design, which can involve multiple materials and variable loading conditions, to simulate real-world use as closely as possible.

The defect tolerant approach provides a more conservative approach to fatigue, and has its roots in the fracture mechanics and the aviation industry. In the 1950s, catastrophic and deadly failures of the Comet aircraft line highlighted the impact of stress concentrations and geometric features on fatigue crack initiation and propagation (Campbell 2012). Similar incidences in the aerospace industry – including catastrophic failures of the F-111 aircraft in 1969, and commercial Boeing 737 (Aloha Airlines Flight 243) and McDonnell Douglas DC-10 (United Airlines Flight 232) disasters in the late 1980s – convinced engineers of the realities of unavoidable material flaws, and efforts to incorporate fracture mechanics into cyclic loading took center stage. Defect-tolerant approaches have gained ground in fatigue-critical applications in aerospace, nuclear and medical device industries, where failure can lead to loss of human life.

The following sections outline the fundamentals behind both total life and defect tolerant approaches, pulling from the discussion on fracture mechanics in the previous section. Both methodologies have been utilized in UHMWPE assessment (discussed below), though defect tolerant approaches have been particularly useful in highlighting crack growth mechanisms, as will be addressed in **Section 3.2**.

### *Total-Life Approach*

The total life approach, also known as the "stress-life" or *S-N* approach, considers the crack initiation *and* propagation phases of fatigue. Methodologies can include both stress- and strain-based experiments that induce low or high cycle fatigue for various materials.

Wohler (1980) first provided an empirical characterization of fatigue using a stress-based total life approach. As seen in **Figure 3.5**, Wohler plotted a fully-reversible ($R = -1$) stress amplitude ($\sigma_a$ or $S$) as a function of the number of cycles to failure ($N_f$ or $N$). A semi-log *S-N* plot reveals a linear region, later described by Basquin (1910) as:

$$\sigma_a = A\left(N_f\right)^b \qquad \textbf{eq. 3.15}$$

where $A$ is the fatigue strength coefficient and $b$ is the fatigue strength exponent (-0.05 to -0.12 in more metals). For some materials, this linear region plateaus around $10^6$–$10^7$ cycles at a stress amplitude known as "endurance limit" ($\sigma_e$). The endurance limit has since evolved as a characterizing parameter for the total life approach, demarcating the stress amplitude below which the material has "infinite" (~10 billion cycles) life.

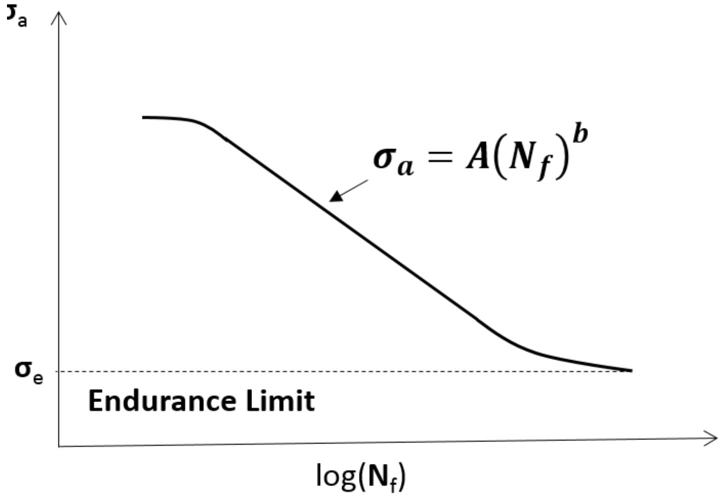

**Figure 3.5** | A typical Wohler (S-N) curve. The linear region can be described using the Basquin equation, an empirical relationship dependent on material constants *A* and *b*. The endurance limit is typically taken at $10^6$-$10^7$ cycles and represents a stress amplitude below which "infinite" life can be achieved.

Stress-based fatigue methods are well suited for high cycle fatigue lives, in which cyclic loading is below the plastic limit of the material, resulting in little to no permanent deformation at the macroscale. For loading at or near the yield strength of a material, strain-based approaches are often more appropriate. Such low-cycle fatigue situations are typical for lifetimes of hundreds to thousands of cycles, where appreciable plastic deformation of a material can incur significant damage. Strain-based approaches are also appropriate in situations in which structural constraint may determine cyclic deformation or where displacement-controlled deformation dictates actual use.

One such strain-life approach to fatigue was developed by Coffin (1954) and Manson (1954) using the cyclic strain amplitude:

$$\frac{\Delta\varepsilon}{2} = \varepsilon_a = \frac{\sigma_f'}{E}\left(2N_f\right)^b + \varepsilon_f'\left(2N_f\right)^c \qquad \textbf{eq. 3.16}$$

Here, $\boldsymbol{\varepsilon_f'}$ is the fatigue ductility coefficient, which for metals can be approximately equal to the true fracture ductility under monotonic loading; $\boldsymbol{c}$ is the fatigue ductility exponent (-0.5 to -0.7 for most metals); $\boldsymbol{\sigma_f'}$ is the fatigue strength coefficient (approximated by the true fracture strength under monotonic tension); $\boldsymbol{b}$ is the fatigue strength exponent as seen in **eq. 3.15**. **Figure 3.6** demonstrates how this Coffin-Manson relationship accounts for both plastic strains that may accumulate under cyclic deformation, as well as elastic strains that tend to fall under high cycle regime fatigue.

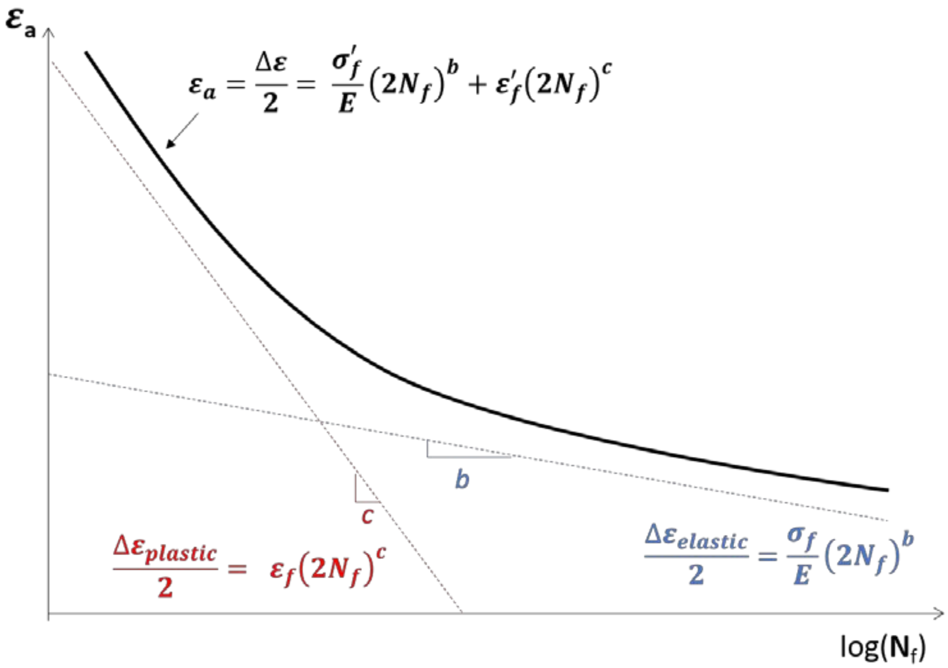

**Figure 3.6** | A strain-based approach to fatigue, as developed by Coffin (1954) and Manson (1954). The red and blue curves demonstrate how this approach accounts for both low cycle plastic strain accumulation and high cycle elastic strain deformation.

Such experimental methodologies have been adopted for polymeric materials due to their viscoelastic nature (Hertzberg & Manson 1980). A discussion of stress- and strain-controlled total life assessments for UHMWPE will be addressed in **Section 3.2**.

### *Defect Tolerant Approach*

An alternative – and more conservative – assessment of material fatigue is the defect-tolerant philosophy. This approach assumes that all components are inherently flawed, and thus focuses on the *propagation* stage of fatigue in which flaws grow until the component fails (conditions for fast fracture of an embedded crack are met). Defect-tolerant approaches rely on empirical laws and fracture mechanics theory, as reviewed in **Section 3.1.1**.

The size of an initial flaw varies depending on the material composition, the component design, and even the method of detection. Often, an initial flaw size will assume the limit of resolution for a detection technique, even if no cracks are detectable at this magnification. Such methods of crack detection include visual magnification, X-ray or ultraviolent imagining, dye-penetrant, and ultrasonic, magnetic or acoustic emission (Suresh 1998).

Linear elastic crack growth is characterized by observing crack velocity as a function of changing applied global (and by extension, local) stresses. Crack speed is typically expressed in terms of the change in crack length per cycle, or ***da/dN***. These values are plotted as a function of cyclic stress intensity (***ΔK***), where:

$$\Delta K = K_{max} - K_{min} \qquad \textbf{eq. 3.17}$$

$$K_{max} = F\sigma_{max}\sqrt{\pi a} \qquad \textbf{eq. 3.18}$$

$$K_{min} = F\sigma_{min}\sqrt{\pi a} \qquad \textbf{eq. 3.19}$$

A typically fatigue crack propagation (FCP) curve is shown as seen in **Figure 3.7**. The sinusoidal shape can be divided into three regions. Region A is typically categorized as the threshold region, in which crack growth remains stagnant or is undetectable. Region B contains stable growth and is characterized by a power law relationship developed by Paris, Gomez & Anderson (1961):

$$\frac{da}{dN} = C\,(\Delta K)^m \qquad \textbf{eq. 3.20}$$

This region is also known as the “Paris regime” with Paris constants ***C*** and ***m***. In Region C, $K_{max}$ values approach $K_c$, and crack growth rates increase rapidly as the sample approaches fast fracture.

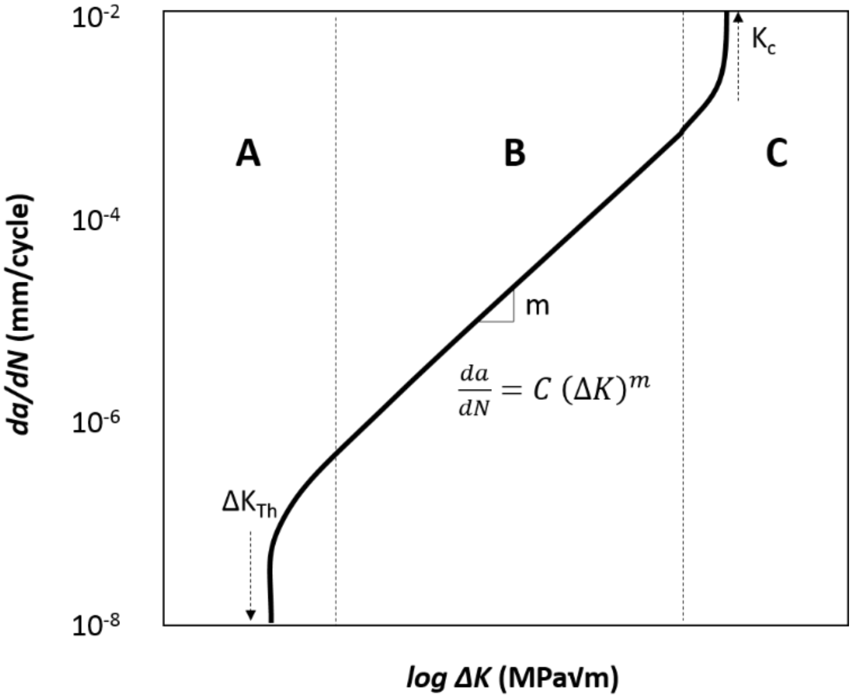

**Figure 3.7** | A typical fatigue crack propagation curve. The tree regions of crack growth are defined as (A) threshold behavior, (B) Paris regime and (C) fast fracture (Adapted from Suresh, 1998).

The FCP curve provides several empirical constants used to define material resistance to crack growth. Paris constants $C$ and $m$ have been characterized for several materials. Metals typically exhibit $m$ values between roughly 2 to 4, while ceramics demonstrate exceptional growth rates with $m$ ranging from 15 to 100. Polymers can similarly cover a large range of Paris slope constants that is highly dependent on frequency, environment, load history, $R$ ratio, and mean stress (Hertzberg & Manson 1980).

Region A of **Figure 3.7** provides an additional characterizing parameter for crack growth initiation known as the fatigue crack growth threshold ($\Delta K_{th}$). Ultimately, this region exhibits a substantial decrease in crack speed relative to decreasing $\Delta K$; this results in a drop-off at levels at or below $10^{-6}$ mm/cycle. Components in which the conditions for crack growth ($\Delta K$) do not meet $\Delta K_{th}$ are considered “safe” against crack inception and fatigue fracture. Due to the combination of a small crack size and low cyclic stress amplitude, this region is often dominated by non-continuum effects dictated by material microstructure. Threshold values are also highly sensitive to experimental methods; $\Delta K_{th}$ is heavily influenced by load ratio and local plasticity that results from load-shedding techniques (Suresh 1998; Ritchie 1977). Nonetheless, many studies agree that threshold values for metals can be determined at $10^{-8}$ mm/cycle, or less than 0.1 mm every $10^7$ cycles. Fatigue crack propagation data for many polymers do not typically extend below $10^{-6}$ mm/cycle (Hertzberg & Manson 1980). Instead, crack extension measured at this speed is considered the “inception” of stable crack growth ($\Delta K_{incep}$), and is often used as a substitute for $\Delta K_{th}$ (Baker et al. 2000).

### *A Brief Commentary on Elastic-Plastic Fatigue*

The use of LEFM to assess fatigue has limitations in materials where significant plastic deformation takes place ahead of the crack tip, as can occur in viscoelastic materials at high temperatures or in front of stress concentrations where high stresses are achieved. The natural inclination would be to adapt elastic-plastic fracture mechanics theory to cyclic loading cases. This has been performed by Dowling & Begley (1976) under the presumption of stable hysteresis of a given material during cyclic loading. However, even with such adjustments, elastic-plastic approaches to cyclic loading can easily violate two fundamental assumptions of the $J$-integral: proportional loading and elastic unloading. Both foundations are inherent to the constitutive plastic flow theory from which $J$ has been derived. A complete understanding of the constitutive behavior of a material under cyclic loading for different crack sizes would be necessary before employing cyclic $J$.

### 3.1.3 Mechanistic Aspects of Fatigue & Fracture

The quantitative approaches to characterizing fatigue and fracture alone are often not enough to fully diagnose the influence of microstructure, environment or loading on crack initiation and propagation. A mechanistic explanation of how cracks advance – or resist advance – can greatly enhance understanding both how fracture occurs as well as how to prevent against it.

Ritchie and coworkers (1988; 1999) presented the characterization of crack growth as a mutual competition *intrinsic* damage mechanisms that result in crack advance and *extrinsic* crack shielding that slow down crack growth. Intrinsic mechanisms can be generally described as those acting ahead of the crack. In ductile metals, plastic damage that accumulates at the highly-stressed crack tip leads to dislocation slip or debonding at interfaces that can result in void and microcrack nucleation that can eventually propagate to cleavage fracture (**Figure 3.8A**). Under cyclic loading, such ductile materials undergo intrinsic crack tip blunting and resharpening, resulting in characteristic striations often seen on fatigued fracture surfaces (Ritchie 1999; Laird & Smith 1962).

Resistance to crack growth often occurs behind the crack tip through extrinsic crack shielding events. These mechanisms serve to *shield* the crack tip from loading, often by way of inducing crack closure effects (i.e. reducing the applied $\Delta K$ to a smaller local $\Delta K_{eff}$), through zone shielding or contact shielding. Zone shielding occurs in the crack wake, compressing the crack tip and reducing the opening displacement during loading. In metals, this extrinsic mechanism can be manifested as plasticity-induced closure, in which constraint from bulk elastic material surrounding residually localized plasticized material closes the crack (Wolf 1970). In brittle ceramics, zone shielding can occur by way of microcracking or transformation toughening, resulting in local dilation that is similarly constrained by elastic material (Ritchie 1999; Ritchie 1988). Contact shielding retards crack growth by bridging the crack surfaces by fibers or grains, as seen in laminated composites or granular structures in ceramics (**Figure 3.8A**). Metal toughening by way of contact shielding may be imposed by way of increasing crack surface traction through roughening or minimizing the degree of unloading through wedging corrosive or environmental debris between crack surfaces to prevent cracks from closing completely. Finally, extrinsically slowing down crack growth can include crack deflection or meandering, in which embedded particles or microstructural features serve to impede crack advance and force a tortuous (and often slower) forward path (Ritchie 1999; Ritchie 1988).

The same intrinsic and extrinsic damage mechanisms are also present in polymers, and are highly sensitive to microstructure, environment/temperature, and loading (Hertzberg & Manson 1980; Pruitt & Chakravartula 2011). Two additional forms of extrinsic crack shielding are often seen in polymers: shear banding and crazing. Shear banding (**Figure 3.8B**) involves the localization of high strain along planes of maximum shear stress, often due to compressive loading, resulting in crack closure along the crack wake, as often seen in metals. Crazing (**Figure 3.8B**), or void formation between polymer fibrils, is common in amorphous polymer and results from tensile stress states. Such crazes bridge crack surfaces, and may even form between particle phases in a polymer to promote energy dissipation and slow down crack growth. The influence of crazing can be seen with cyclic loading, in which compressive forces imparted during unloading of a crack can result in craze breakdown and subsequent crack extension (Furmanski & Pruitt 2007a; Pruitt & Chakravartula 2011).

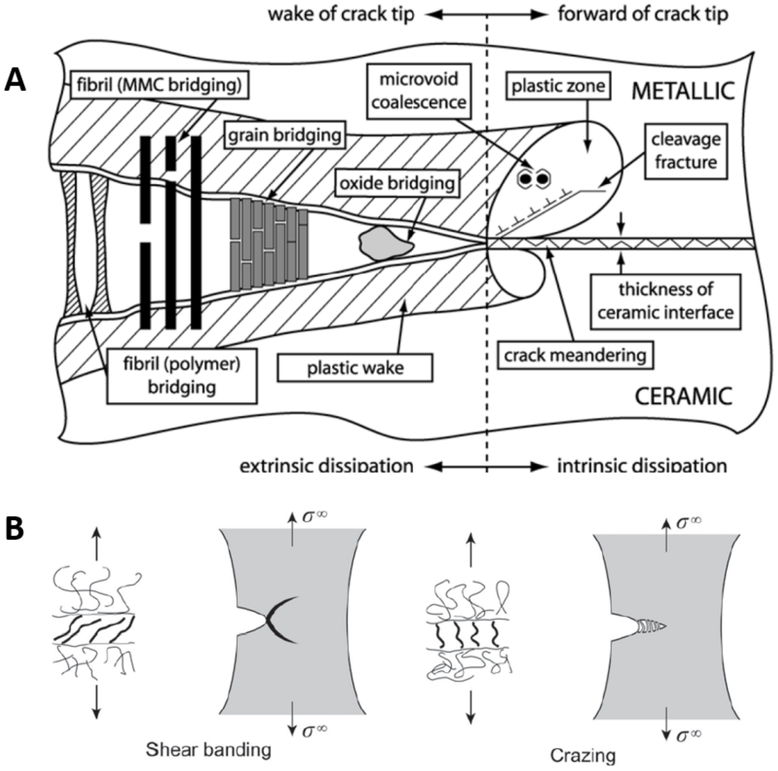

**Figure 3.8 |** (**A**) Illustrative description of intrinsic and extrinsic mechanisms seen in metals and ceramics (L. A. Pruitt & Chakravartula, 2011; adapted from R.O. Ritchie, 1999). (**B**) Extrinsic crack shielding mechanisms often seen in polymers (Pruitt & Chakravartula 2011).

## 3.2 Practice: Fracture and Fatigue in UHMWPE

Studies evaluating fracture and fatigue of UHMWPE date back to the early 1980s, with the first FCP assessment using linear elastic methods (Connelly et al. 1984). Before then, the study of UHMWPE was primarily driven by its performance in total joint replacements (TJRs), with a particular focus on the challenge of surface wear. As a result, little was known regarding the effects of crosslinking, sterilization, or processing conditions on crack growth. The past 30 years have seen not only the acceptance but even the expectation of fracture mechanics approaches to assessing fracture resistance of polymers used in orthopedic devices.

When considering the application of fracture mechanics theory in polymer failure, several additional considerations are required due to the viscoelastic nature of these materials. Fracture and fatigue are highly dependent on temperature, provided the dramatic transition in modulus and microstructure that can occur near $T_g$ or $T_{melt}$. Frequency and loading waveform can influence FCP curves significantly, highlighting the influence of creep effects on crack growth. Microstructural changes imparted through chemical backbone structure or the addition of crosslinking or changing molecular weight also effects crack growth and initiation in many polymers. Studies of UHMWPE fatigue and fracture provide a snapshot of these effects through an investigation of temperature, loading and microstructural effects, all of which are specific to *in vivo* conditions that this material typically operates under. (Hertzberg & Manson 1980)

### 3.2.1 UHMWPE Fracture Toughness

#### *Linear Elastic Fracture Toughness*

Values for the critical plane strain stress intensity ($K_{IC}$) for UHMWPE has remained elusive for researchers due to difficulties with experimental analysis and its high ductility (Kurtz et al., 1998; Pruitt, 2005). However, estimates of fracture toughness ($K_c$) have been derived from both monotonic tensile tests and FCP evaluations for various UHMWPE formulations. Cylindrical bars fractured under uniaxial tension have been used to estimate a critical flaw size for untreated and irradiated UHMWPE specimens (Gencur et al. 2003; Steven M. Kurtz et al. 1998). **Figure 3.9** shows typical embedded circular cracks and surface thumbnail cracks that can appear on the fractured surface. $K_c$ values can be estimated from these flaws using:

$$K_c = 1.13\sigma_{UTS}\sqrt{a}$$ , embedded circular crack **eq. 3.21**

$$K_c = 1.27\sigma_{UTS}\sqrt{a}$$ , surface thumbnail crack **eq. 3.22**

where $\sigma_{UTS}$ is the true ultimate tensile strength and $a$ is the radius of the internal flaw, as derived from the stress intensity equations for an elliptical crack (Tada et al. 1985; Steven M. Kurtz et al. 1998). **Table 3.1** lists fracture toughness values for UHMWPE materials obtained using this method.

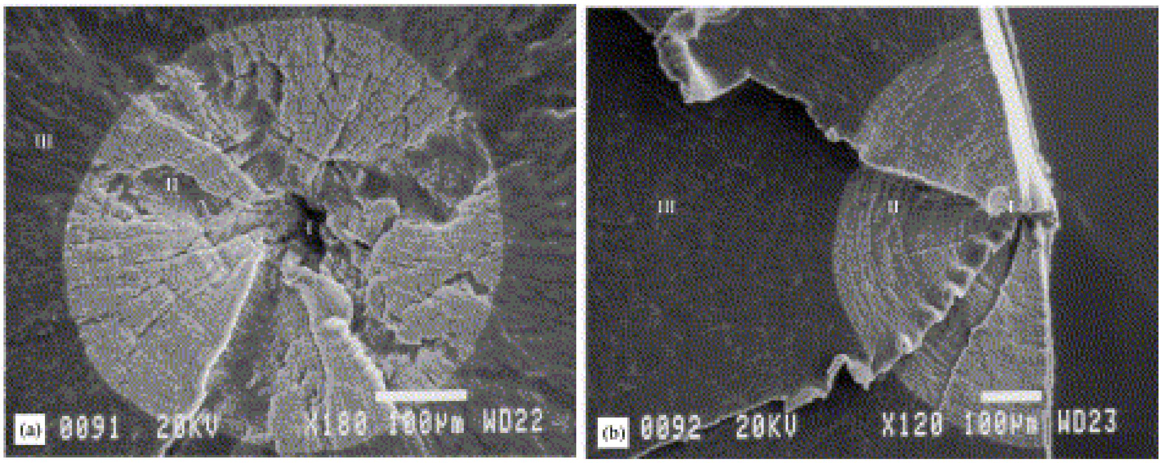

**Figure 3.9 |** SEM micrographs showing embedded and surface circular flaws on fractured cylindrical tensile samples of UHMWPE. The radius of these circular cracks serves as the critical flaw size for fracture toughness calculations (Gencur et al. 2003).

**Table 3.1 |** Fracture toughness values obtained from monotonic tensile tests on cylindrical specimens.

| **Formulation** | **Fracture Toughness** | **Reference** |
|---|---|---|
| Untreated UHWMPE (GUR 4150 HP) | 3.6 ± 0.4 MPa√m | (Steven M. Kurtz et al. 1998) |
| Untreated UHMWPE (GUR 1120) | 5.9 ± 0.9 MPa√m | |
| Untreated UHMWPE (GUR 1050) | 4.0 ± 0.5 MPa√m | (Gencur et al. 2003) |
| Low to Moderately Crosslinked UHMWPE (30 kGy) | 4.5 ± 0.02 MPa√m | |
| Highly Crosslinked and Submelt Annealed UHMWPE (100 kGy) | 2.8 ± 0.4 MPa√m | |
| Highly Crosslinked and Remelted UHMWPE (100 kGy) | 3.0 ± 0.6 MPa√m | |

Gencur et al. (2003) found that higher degrees of crosslinking, paired with a post-irradiation heat treatment, led to a substantial loss in fracture toughness, as seen in **Table 3.1**. As **eq. 3.21** and **eq. 3.22** indicate, fracture toughness correlates with true ultimate strength, which decreases with increasing radiation dosage and the addition of heat treatment above and below melt (**Table 1.2**). The estimates obtained for untreated UHMWPE are also close to those derived from the fast fracture regime of FCP data, where a $K_{max}$ value of 3 to 3.5 MPa√m has been obtained just before failure (Pruitt & Bailey 1998a; Furmanski & Pruitt 2007a). $K_{IC}$ values have also been estimated from plane strain elastic-plastic parameters ($J_{IC}$) using the relation:

$$J_{IC} = {K_{IC}}^2(1-\nu^2)/E \quad \textbf{eq. 3.23}$$

This has provided fracture toughness values on the order of 9–10.5 MPa√m. However, variations in testing methodologies and samples sizes has provided a wide range of $J_{IC}$ values (as discussed in the next section). Furthermore, excessive crack-tip blunting may overestimate toughness using elastic-plastic experimental methods (Pruitt 2005). As a result, a stronger reliance has been placed on FCP data due to the applicability of linear elastic methods for crack growth as well as extrapolation to cyclic-loading stress states that exist for TJRs *in vivo*.

#### *Elastic Plastic Fracture Toughness (J-Integral)*

The thickness constraints for implant geometries imposes limitations on the fracture toughness values gained by linear elastic methods, and has motivated an understanding of toughness from an elastic-plastic foundation. $J$-Integral methods have primarily been used to model toughness, and exhibited more refined discrepancies between microstructural changes than Izod impact tests and tensile tests (Medel et al. 2007). Untreated UHMWPE has demonstrated $J_{IC}$ values between 67 and 99 kJ/m$^2$, values fairly consistent with other semicrystalline and tough plastics (Medel et al. 2007; Rimnac et al. 1988; Steven M. Kurtz et al. 1998). Low to moderate crosslinking doses below 50 kGy exhibited an increase in crack initiation toughness; however, higher irradiation resulted in lower $J_{IC}$ values (A. Gomoll et al. 2002; Medel et al. 2007). Heat treatments similarly decreased toughness, both for above and submelt annealing processes (Medel et al. 2007; Cole et al. 2002). Gomoll et al. (2002) not only investigated initiation toughness, but characterized the steady state J-integral, $J_{ss}$, which reflects the resistance to crack propagation under stable crack growth. An overall decrease in $J_{ss}$ as a function of increasing irradiation parallels the decrease in FCP resistance found in these formulations, as discussed in the next section.

### 3.2.2 UHMWPE Fatigue Crack Propagation Studies (Defect Tolerant Approach)

Studies of crack propagation in UHMWPE have revealed a significant dependence on microstructure, manufacturing method, test temperature, frequency and waveform. Primary mechanisms by which UHMWPE can resist crack growth include its intrinsic plasticity, owing to its high molecular weight, and crystalline lamellae, which can deflect and slow down an advancing crack. Such toughening mechanisms have often been compromised due to changes in UHWMPE microstructure that accompany sterilization and irradiation protocols, heat treatments, and resin processing methods throughout the polymer's 60 year history in TJR design.

The effects of gamma or electron beam irradiation to sterilize and crosslink UHMWPE has been the focus of many FCP investigations of UHMWPE. **Figure 3.10** shows that with increasing crosslinking dosage, resistance to FCP decreases (Baker et al. 2003). Comparable slopes in the Paris regime for each FCP curve suggest similar mechanisms driving crack advance in both non-irradiated and irradiated material once a flaw has initiated. Such findings have been reproduced by numerous studies (Pruitt & Ranganathan 1995; Baker et al. 2003; Bradford et al. 2004; Baker et al. 1999b; Pruitt & Bailey 1998b; Cole et al. 2002; Oral, Godleski Beckos, et al. 2008; Atwood et al. 2011; Medel et al. 2007), and remain the focus of the debate on using highly crosslinked

UHMWPE in areas of high contact stress or near notches (Ries & Pruitt 2005; Furmanski et al. 2009; Pruitt et al. 2013).

SEM images of fractured surfaces for non-irradiated and irradiated specimens are shown in **Figure 3.11**. Non-irradiated UHMWPE displays distinct ductile tearing and surface buckling at roughly 45° angles. These "criss-cross" patterns are associated with blunting of the crack tip in the amorphous phases of the polymer and high localized strains just before material failure and subsequent crack extension (Bradford et al. 2004; Baker et al. 2003; Ries & Pruitt 2005). In irradiated UHMWPE, crosslinks are formed primarily in these amorphous regions, creating a networked polymer structure (Kurtz 2009; Ries & Pruitt 2005). This contributes to the shrinking and disappearance of ductile features with increasing crosslinking dosage as seen in **Figure 3.11B** and **C**, revealing a more flat, brittle fracture surface. Tensile properties of UHMWPE (see **Table 1.2** in Chapter 1) reveal a loss of true fracture strength and failure strain with increasing crosslinking, reflecting on the inability for crosslinked UHMWPE to accommodate plastic deformation at the crack tip (Baker et al. 2003).

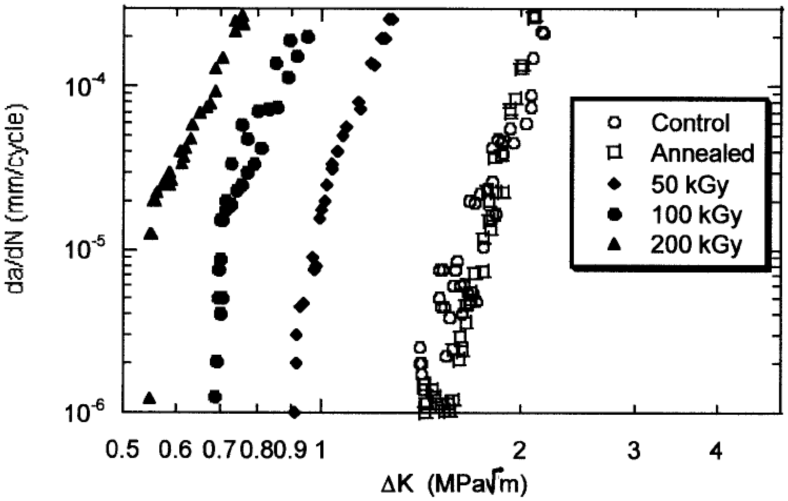

**Figure 3.10 |** FCP data for GUR 1050 UHMWPE with varying crosslinking dosages in comparison with untreated ("Control") and above-melt heat treated ("Annealed") materials. Faster crack growth correlated with increasing crosslinking (Baker et al. 2003).

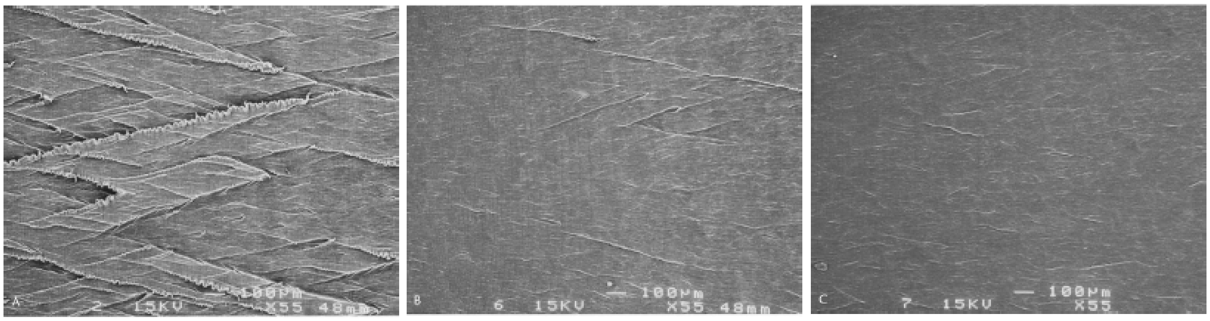

**Figure 3.11 |** SEM micrographs of fracture surface for GUR 1020 UHMWPE specimens with (A) no irradiation, (B) 50 kGy gamma irradiation and (C) 100 kGy gamma irradiation. Note the loss of ductile surface features ("criss-cross" markings) with increasing crosslinking dosage (Bradford et al. 2004).

The adverse effects of crosslinking on FCP resistance can also be associated with a reduction in crystalline quantity and quality. Increasing percent crystallinity can enhance UHMWPE's resistance to crack growth, as seen with fatigue evaluation of highly crystalline formulations. Highly pressurized UHMWPE, such as Hylamer, is known to increase UHMWPE crystallinity from 50% to as high as 70%. These high crystallinity polymers demonstrate a greater $\Delta K_{incep}$ than untreated UHMWPE (Baker et al. 2000; Pruitt, L, Simis, K, Bistolfi 2003), suggesting that the greater distribution of crystalline phases intercepts and deflects crack growth. Consequently, highly crystalline formulas are still being investigated, but have been limited in the past by oxidation related to irradiation crosslinking (**Section 1.3**).

The role of crystalline phases in deflecting crack growth was further supported by Atwood et al.'s (2010) evaluation of crystalline quantity and lamellae size in heat treated UHMWPE. The authors used a potassium permanganate etching procedure to remove the amorphous regions of both submelt and above-melt annealed crosslinked UHMWPE, which both promote better oxidative resistance. Under SEM imaging, the authors discerned a noticeable difference in lamellar size with heat treatments: annealing below the melt produced a greater number of thicker lamellae than untreated UHMWPE, while remelted UHMWPE had smaller lamellae and 5% reduction in crystallinity (Atwood et al. 2011). **Figure 3.12** shows that remelted crosslinked UHMWPE also had a reduced resistance to FCP compared to submelt annealed specimens. In separate studies, both Simis et al. (2006) and Medel et al. (2007) concluded that improvements in fatigue behavior of UHMWPE were more attributed to lamellae thickness changes than percent crystallinity. Nonetheless, it should be noted that the annealing processes are unable to redeem the reduction in FCP resistance that results from limited plasticity in crosslinked amorphous regions.

Pruitt et al. (1998) also demonstrated how manufacturing methods can introduce anisotropic behavior that influences FCP resistance. Consolidation and processing of UHMWPE generally takes one of two forms: a compression molded block or an extruded rod (Kurtz 2009). Extruded rods can cause chain alignment in the direction of extrusion, which can negatively impact crack growth depending on the orientation of the crack (**Figure 3.13**). For cracks growing parallel to aligned chains, the FCP behavior shifted toward faster growth (lower inception behavior) than cracks growing at a perpendicular orientation. Such orientation sensitivity was not apparent for compression molded samples.

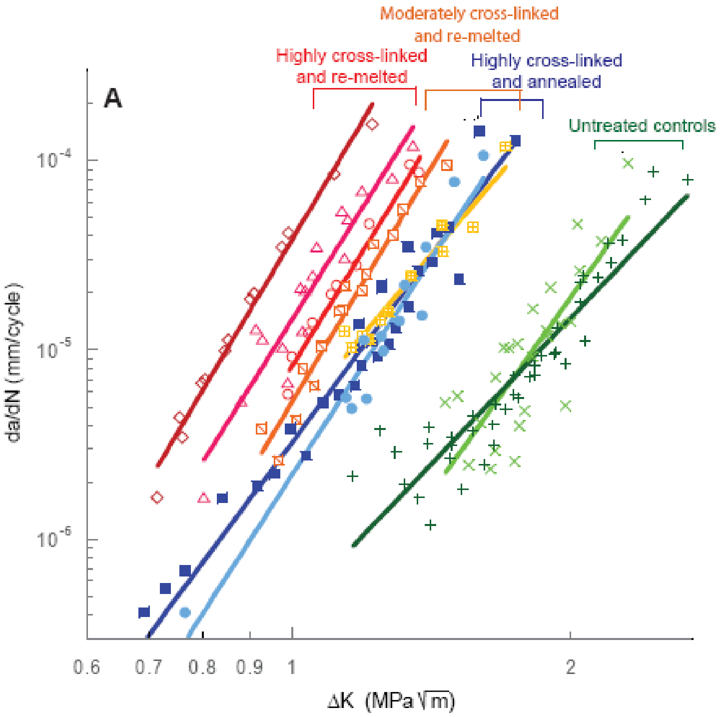

**Figure 3.12 |** FCP evaluation of untreated, highly crosslinked (90-100 kGy) and annealed (130°C), moderately crosslinked (50-75 kGy) and remelted (147°C), and highly crosslinked and remelted UHMWPE. Remelted specimens show a reduced resistance to FCP compared with annealed specimens, attributed to a reduction in lamellae size and quantity. All crosslinked specimens demonstrate faster crack growth than untreated UHMWPE (Atwood et al. 2011).

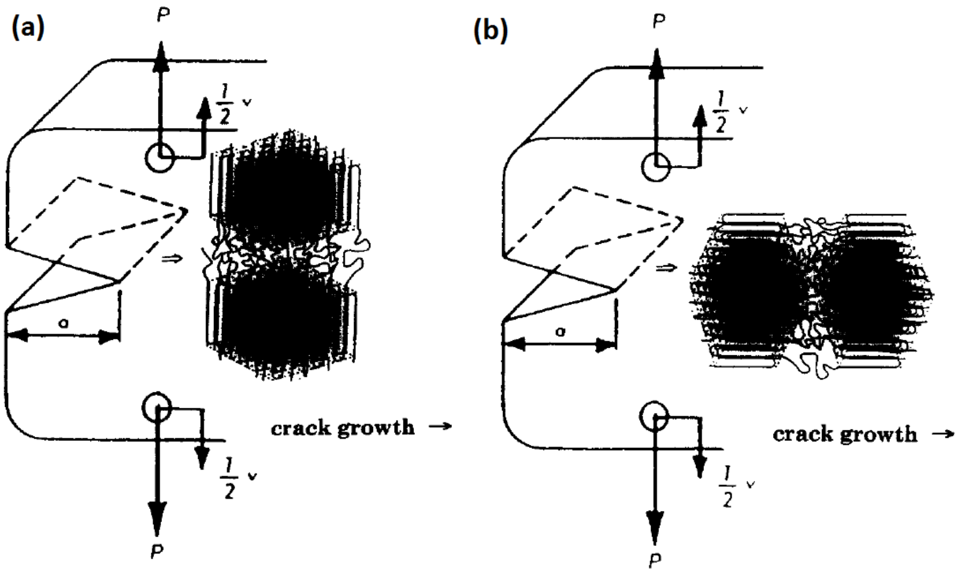

**Figure 3.13 |** Illustration of the chain orientation effects on crack growth, which can be induced by manufacturing effects. The drawing in (a) shows chain orientation perpendicular to crack growth, which can slow down crack propagation, while parallel chains in (b) can induce faster crack growth (Pruitt & Bailey 1998b).

With UHMWPE in TJR primarily operating at a temperature midway between its $T_g$ (–80°C) and melt (137°C), viscoelastic mechanisms can play a noticeable role in crack growth. Baker et al. (2000) evaluated FCP in UHMWPE at room temperature (21°C) and body temperature (37°C), finding the latter to be more conducive to faster FCP. Elevated temperatures were thought to increase viscous behavior at the crack tip and cause enhanced material breakdown via creep. Peak stresses have also been shown to dominate crack growth in UHMWPE through static (creeping) mode fatigue. Furmanski & Pruitt (2007) considered both cyclic and static modes of crack propagation for three loading scenarios: a constant $\boldsymbol{R}$ ratio of 0.1, a constant $\boldsymbol{R}$ ratio of 0.5, and a constant peak load with varying R ratios between 0.1 and 0.9. **Figure 3.14** shows how $\boldsymbol{R}$ ratio effects on FCP as a function of cyclic stress intensity ($\boldsymbol{\Delta K}$) effectively disappear when considering peak stress intensity ($\boldsymbol{K_{max}}$) instead.

Furmanki & Pruitt (2007a) provide evidence for UHMWPE as a creep-brittle material, or a viscoelastic material in which crack growth outpaces any creep-relaxation that would otherwise impede crack growth. Furthermore, UHMWPE does not exhibit the same extrinsic mechanisms that resist crack growth in many polymers. Such phenomena in polymers include crazing behind the crack tip or shear banding in the bulk, which can influence the driving force on the crack itself, as opposed to the material's intrinsic resistance to material failure. Crazes, in particular, often buckle and break down in compression resulting in crack advance, which is highly dependent on unloading and therefore cyclic stress intensity. UHMWPE does not exhibit crazing or shear-banding, and thus is primarily driven by an intrinsic phenomena that correlate with peak stresses ahead of the crack tip (Furmanski & Pruitt 2007a).

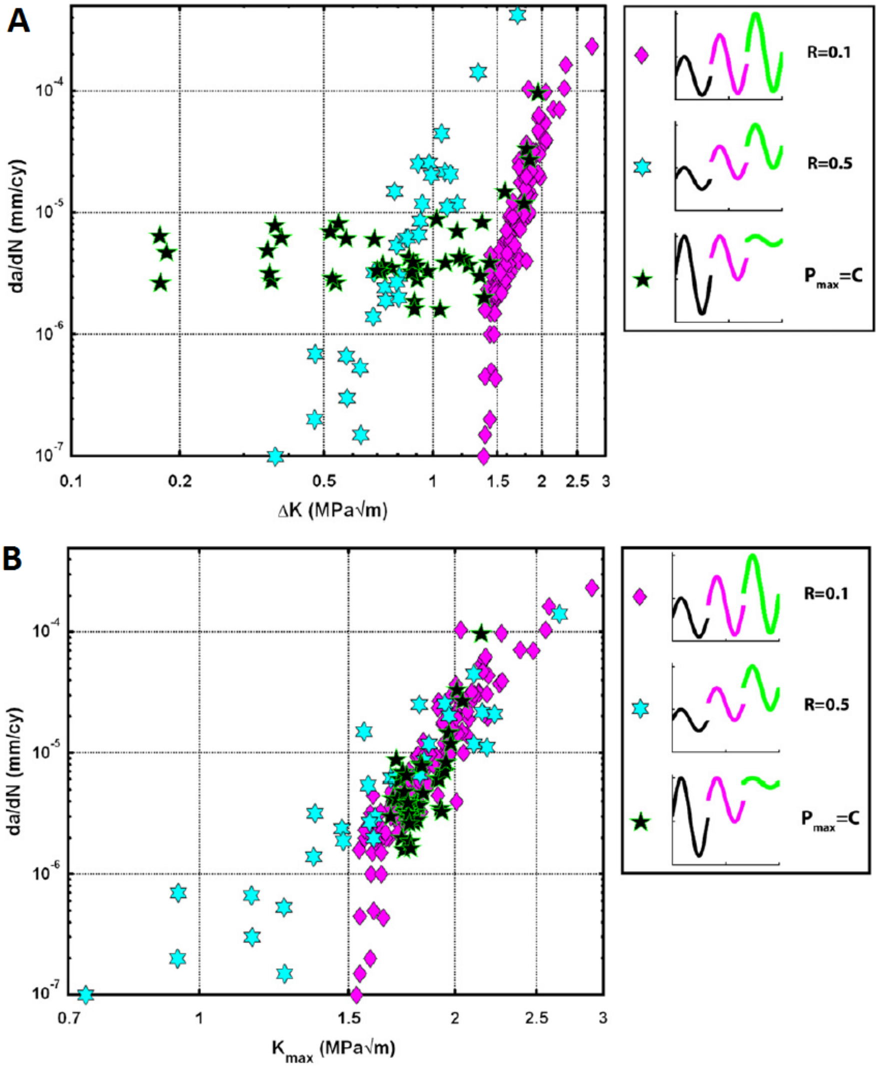

**Figure 3.14** | FCP of untreated UHMWPE for varying ***R*** ratios graphed against cyclic stress intensity (A) and peak stress intensity (B). The collapse of data in (B) demonstrates UHMWPE's tendency toward brittle crack behavior that is predominantly dictated by peak loads, as opposed to unloading effects that are reflected by cyclic stresses (Furmanski & Pruitt 2007b).

### 3.2.3 UHMWPE Fatigue Crack Initiation Studies (Total Life Approach)

The assessment of crack initiation has been well established for many metals and ceramics, but has proven more difficult for polymers. The generation of flaws in the latter can be a highly discontinuous process, initiated through internal cavitation, void growth, crazing, shear banding, or crystal deformation and plasticity (Lin & Argon 1994; Argon et al. 1997). Furthermore, experimental evaluation of crack initiation through a total life approach proves difficult with

UHMWPE: even substantial strains of 12-15% do not result in any visible rupture, provided the impressive failure strain that the polymer can achieve (Baker et al. 2003). Cyclic loading well above the yield strength of UHMWPE has exhibited rupture (Sobieraj et al. 2005a); however, such loading remains well above the elastic region of the material and can overestimate the true *in vivo* stress environment of TJR bearing surfaces.

Baker et al. (2003) performed a stress-life assessment of conventional and irradiated UHMWPE under fully tensile cyclic loading, using the onset of yield (12-15% strain) as a failure criteria. As seen in **Figure 3.15**, a low dosage of 50 kGy appeared to decrease the fatigue resistance. However, subsequent doses of irradiation substantially increased the number of cycles to yield able to be sustained at a particular load. Thus while crosslinking leads to faster crack propagation (**Figure 3.12**), it can reduce flaw initiation in the material, which can greatly increase the overall fatigue life.

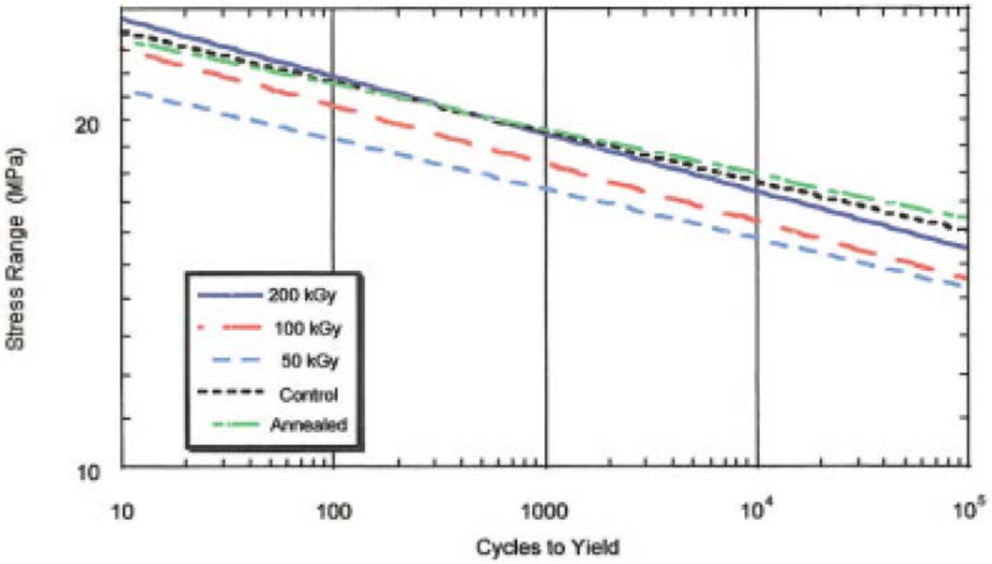

**Figure 3.15 |** Stress-life data for untreated (control), heat treated (annealed) and crosslinked UHMWPE. Life was defined as the number of cycles under gross specimen yield (Baker et al. 2003).

Medel et al. (2011) performed a similar assessment of fatigue crack initiation behavior of a wider range of UHMWPE formulations, including untreated, crosslinked, remelted crosslinked and submelt-annealed crosslinked. Like Baker et al., the authors found that increased crosslinking density increased the fatigue resistance through a stress-life assessment using a 12% specimen strain to demarcate failure. In contrast, coupling irradiation treatments with heat treatments above and below the melt temperature of UHMWPE to eradicate oxidation-prone free radicals dramatically decreased fatigue life. Such findings are primarily attributed to a reduced lamellae thickness due to similar findings with both annealed and remelted materials. Annealed materials tendency toward high percent crystallinity has a demonstrated effect in improving crack initiation and propagation resistance compared to remelted specimens, but overall lamellae slimming still limits its performance compared to untreated controls. Interestingly, similar findings were established through FCP analysis of highly crystalline polymers by Simis et al. (2006), in which enhanced lamellae thickness was associated with improved resistance to crack growth. Despite phenomenological differences in crack initiation and growth mechanisms, it appears that reduction of lamellae thickness through heating is quite detrimental to the entire fatigue life of the polymer. This has recently encouraged a rapid shift toward antioxidant infusion in newer material models in which lamellae quality is supposedly preserved; however, total-life assessments of the fatigue life of Vitamin E formulations has yet to performed.

### 3.2.4 UHMWPE Fracture & Fatigue Studies: Conclusions and Limitations

Investigations on the fatigue and fracture of UHMWPE demonstrate the importance of structure-property relationships in gross mechanical behavior of this polymer. Microstructural influences on crack initiation and growth have predominantly been revealed through retrospective evaluation of modified formulas that have been introduced to the TJR market over the years. As a result, many of the methods described above have become standard requirements before the introduction of novel materials into implants, not only in the orthopedic world but through the medical device market.

Over the three decades of fracture and fatigue characterization of UHMWPE, several authors have attempted to summarize how key influencers of crystallinity, crosslinking, lamellae size and percent crystallinity directly impact polymer performance through structure-property relationships (Baker et al., 1999;  Gomoll, Wanich, & Bellare, 2002; S.M Kurtz et al., 2002; Ries & Pruitt, 2005; Simis et al., 2006). Modulus has demonstrated a direct relationship with both crystalline quality and quantity: Gomoll et al. (2002) found a significant correlation between increasing modulus and lamellae thickness, while Simis et al. (2006) established that a larger percentage of crystalline phases also scales well with stiffness. Thus, the reduction in size and quality of crystalline lamellae in crosslinked UHMWPE materials decreases its modulus and thus is resistance to FCP (Ries & Pruitt 2005). In contrast, a lower stiffness reduces surface contact stresses and improves wear resistance, a hallmark of highly crosslinked UHMWPE in modern TJRs. Similarly, heat treatments directly play with crystalline quality and size. Annealing below the melt temperature of UHMWPE increases crystallinity, leading to a higher modulus and greater resistance to FCP, but increased contact stresses that can diminish wear resistance. The link between microstructure and these tradeoffs in fatigue and wear demonstrate significant limitations in UHMWPE as a bearing material in TJR, and have prompted continual reinvention of this material. **Table 3.2** summarizes these microstructural influences on fatigue and fracture in particular.

In addition, irradiation and post-irradiation annealing of UHMWPE both contribute to a reduction in ultimate properties of the material (Ries & Pruitt 2005). This promotes the likelihood of fracture under monotonic or cyclic loading at lower stresses and strains, despite differences in crystalline morphology. As discussed in **Chapter 1**, the impressive ductility of UHMWPE is achieved through chain disentanglement and stretching in the plastic region. Crosslinking in the amorphous region and changes the size and prevalence of crystalline regions puts limitations on the degree of unraveling. Furthermore, studies demonstrating the reduction in ultimate stress and strain properties have predominantly focused on smooth specimens under fully tensile monotonic or cyclic load. The addition of notches can interact with microstructures described above. Stress risers in UHMWPE TJR components from which cracks often initiate and propagate create a complex triaxial stress state near the notch tip. While uniaxial loading results in chain alignment, stretching and general anisotropic morphology, triaxiality can inhibit crystal rotation and chain mobility, altering gross mechanical properties including yield and ultimate stress/strain.  Such triaxiliaty is not well-represented in the uniaxial and smooth specimen testing methods discussed in this chapter. **Chapter 4** provides a summary of theoretical and practical approaches to notch fatigue.

**Table 3.2** | Summary of literature review findings on the influence of microstructure on UHMWPE fatigue and fracture.

| Microstructural Feature | Change in Microstructure Due to UHMWPE Processing | Impact on UHMWPE Fatigue Resistance | References |
|---|---|---|---|
| **Crosslinking** | ↑ **Irradiation** *(Gamma Sterilized or XLPE)*<br>↓ **Pre-irradiation Antioxidants** *(Blended Vitamin E)* | **↑ Crosslinking ↓ Resistance to Fatigue Crack Propagation**<br>**↑ Crosslinking ↑ Resistance to Fatigue Crack Initiation**<br>*Gamma irradiation results in crosslinking in the amorphous region of UHMWPE, reducing chain mobility. This reduces void nucleation and subsequent crack initiation, but significantly increases crack propagation due to reduced ductility.* | Atwood 2011; Baker 1999; Baker 2001; Bradford 2004; Cole 2002; Furmanski 2011; Gencur 2006; Goldman 1998; Medel 2007; Meyer 2001; Nusbaum 1979; Oral 2013; Oral 2006; Pascual 2012; Pruitt 1998b; Pruitt 1995; Puértolas 2006; Ries 1996; Simis 2006; Sobieraj 2013; Tanaka 2008; Urriés 2004 |
| **Percent Crystallinity** | ⇧ **Irradiation** *(Gamma Sterilized or XLPE)*<br>↑ **High Pressure Crystallization**<br>↑ **Irradiation + Annealing < Melt** *(Annealed XLPE)*<br>↓ **Irradiation + Annealing > Melt** *(Remelted XLPE)* | **↑ Percent Crystallinity ↑ Resistance to Fatigue Crack Propagation, Initiation**<br>*A higher crystalline quantity can inhibit crack initiation and slow down crack propagation by encouraging crack deflection around lamellae structures.* | Atwood 2011; Baker 2003; Bhateja 1979; Choudhury 1997; Gencur 2006; Medeln 2007; Niinomi 2001; Oral 2009; Oral 2006; Pascual 2012; Puértolas 2006; Simis 2006; Tanaka 2008 |
| **Lamellae Thickness** | ⇧ **Irradiation** *(Gamma Sterilized or XLPE)*<br>↑ **High Pressure Crystallization**<br>⇩ **Irradiation + Annealing < Melt** *(Annealed XLPE)*<br>↓ **Irradiation + Annealing > Melt** *(Remelted XLPE)* | **↑ Lamellae Thickness ↑ Resistance to Fatigue Crack Propagation**<br>*Thicker lamellae can inhibit crack propagation by encouraging greater crack deflection.* | Baker 2003; Bhateja 1979; Medel 2007; Simis 2006 |
| **Oxidation**<br>↓ Molecular Weight<br>↑ Density | ↑ **Irradiation*** *(Gamma Sterilized or XLPE)*<br>⇧ **Irradiation + Annealing < Melt*** *(Annealed XLPE)*<br>X **Irradiation + Annealing > Melt*** *(Remelted XLPE)*<br>X **Irradiation + Antioxidant*** *(Blended Vitamin E)* | **↑ Oxidation ↓ Resistance to Fatigue Crack Propagation**<br>**↑ Oxidation ↓ Resistance to Sliding Fatigue (Delamination Wear)**<br>*Free radicals released during irradiation can oxidize in the presence of oxygen, causing chain scission, the reduction in molecular weight and the creation of bulky oxidative byproducts that interfere with chain mobility. Subsequent reduction in resistance to fatigue crack initiation and propagation encourages subsurface crack formation, resulting in delamination and pitting wear or gross component fracture.* | Atwood 2011; Baker 2000; Choudhury 1997; Ge 2011; Goldman 1998; Huot 2010; Micheli 2012; Oral 2006; Oral 2008; Oral 2004; Reeves 2000; Ries1996; Villarraga 2004; Wang 2006; Young 2000 |
| **Fusion Defects** | ↑ **Irradiation*** *(Gamma Sterilized or XLPE)*<br>↓ **Irradiation + Antioxidant*** *(Blended Vitamin E)* | **↑ Fusion Defects ↓ Resistance to Sliding Fatigue (Delamination Wear)**<br>*Grain boundaries between UHMWPE particles can experience elevated oxidation levels due to free radical release during irradiation and subsequent exposure to oxygen. Chain scission between particles can coalesce into microscopic cracks that then propagate under cyclic contact stresses during sliding.* | (Cornwall 1997; Gul 2003; Shibata 2003; Shibata 2005; Tomita 1999) |

**KEY**: ↑↓ Significant Increase/Decrease ⇧⇩ Minor Increase/Decrease X No Change/Prevention *Microstructural change only occurs with exposure to oxygen on the shelf or *in vivo*.

# Chapter 4 – Notch Fracture & Fatigue in UHMWPE: Theory and Practice

## 4.1 Theory: Notch Effects on Crack Initiation and Propagation

Engineering components – including total joint replacements – often rely on intricate features such as fillets, shoulders, grooves or holes to enable fixation between modular structures or to serve as mechanical leverage between moving parts. These geometric discontinuities can significantly alter the local stresses and strains within a material, resulting in material deformation that deviates from that predicted for the global system.

Several mathematical approaches to quantify notch effects on fatigue and fracture have been developed, predominantly using metallic materials. The following sections discuss a handful of these approaches that are commonly used in predictive failure analysis, and some that have been recently developed to provide a more sophisticated description of crack initiation and growth near a notch. First, approximations of the local notch stress and strain field ahead of a notch under monotonic loading will be presented, laying a foundation for more complex notch fatigue theory addressed in later sections.

### 4.1.1 Characterizing the Local Notch Stress-Strain Field

*Elastic Stress Concentration Factor*

Perhaps the simplest – and most ubiquitous – characterization of notch effects on the local stress-strain environment is the theoretical elastic stress concentration factor, $\boldsymbol{k_t}$:

$$k_t = \frac{\sigma_{local}}{\sigma_{nominal}} \qquad \textbf{eq. 4.1}$$

The stress concentration factor relates the peak local stress to the average far-field (nominal) stresses, and is a scalar function of the geometry of the stress riser and the type of loading that is applied. One such relationship was developed by Inglis (1913) for an elliptical feature in a flat plate pulled in tension (**Figure 4.1**):

$$\sigma_y = \sigma_\infty \left(1 + 2\frac{c}{d}\right) = \sigma_\infty \left(1 + 2\sqrt{\frac{c}{\rho}}\right) \qquad \textbf{eq. 4.2}$$

Here, the vertical local stress, $\boldsymbol{\sigma_y}$**,** is a function of the ellipse proportions (long axis $\boldsymbol{c}$, short axis $\boldsymbol{d}$, and radius of curvature $\boldsymbol{\rho}$) and the far-field stress, $\boldsymbol{\sigma_\infty}$**.** Note that this relationship suggests that an infinitely sharp crack (i.e. $\boldsymbol{\rho} \rightarrow 0$) will lead to infinite stresses at the crack tip, which no material is capable of resisting. This complexity motivated Griffith's energy approach to develop the concept of fracture toughness (see **Chapter 3**) (Griffith 1921).

Values for $\boldsymbol{k_t}$ for many additional geometries can be found in stress analysis handbooks such as that by Peterson (Peterson 1959).

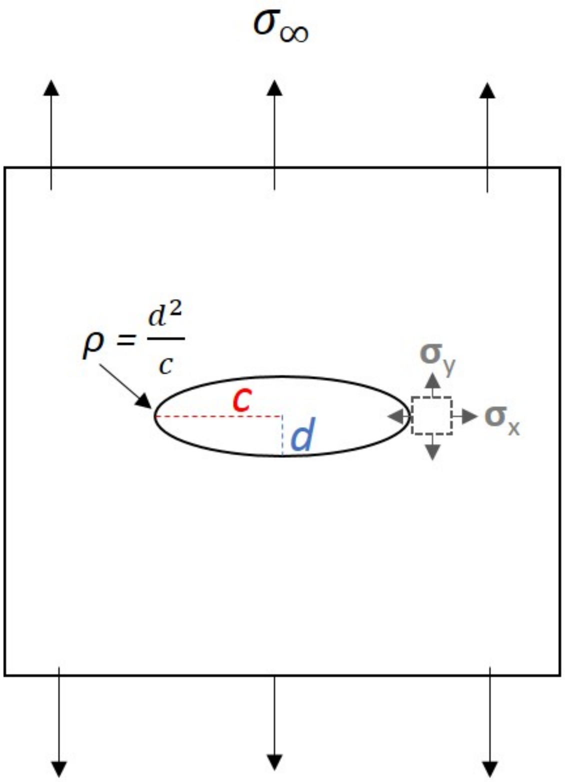

**Figure 4.1** | Elliptical hole in a flat plate pulled in tension.

*Neuber's Rule*

Local elevated stress can cause some degree of yielding at the notch tip. In these cases, typical elastic approaches to estimating local stresses become inaccurate. Under elastic considerations, the elastic stress concentration factor and elastic strain concentration factor are equal, as stress and strain are linearly related by Hooke's law under these conditions. However, notch plasticity results in a deviation from this linear relationship, and $k_t$ under predicts local strains (**Figure 4.2**).

Neuber's rule presents a rough approximation of local plastic stresses and strains by recognizing that the stress ($k_\sigma$) and strain concentration factors ($k_\varepsilon$) are distinct entities and can be related to the elastic stress/strain concentration factor by their geometric mean:

$$k_\sigma = \frac{\sigma}{S} \qquad \textbf{eq. 4.3a}$$

$$k_\varepsilon = \frac{\varepsilon}{e} \qquad \textbf{eq. 4.3b}$$

$$k_t = \sqrt{k_\sigma k_\varepsilon} \qquad \textbf{eq. 4.3}$$

Here, $S$ and $e$ are the global stress and strain, respectively, and $\sigma$ and $\varepsilon$ are the local equivalents.

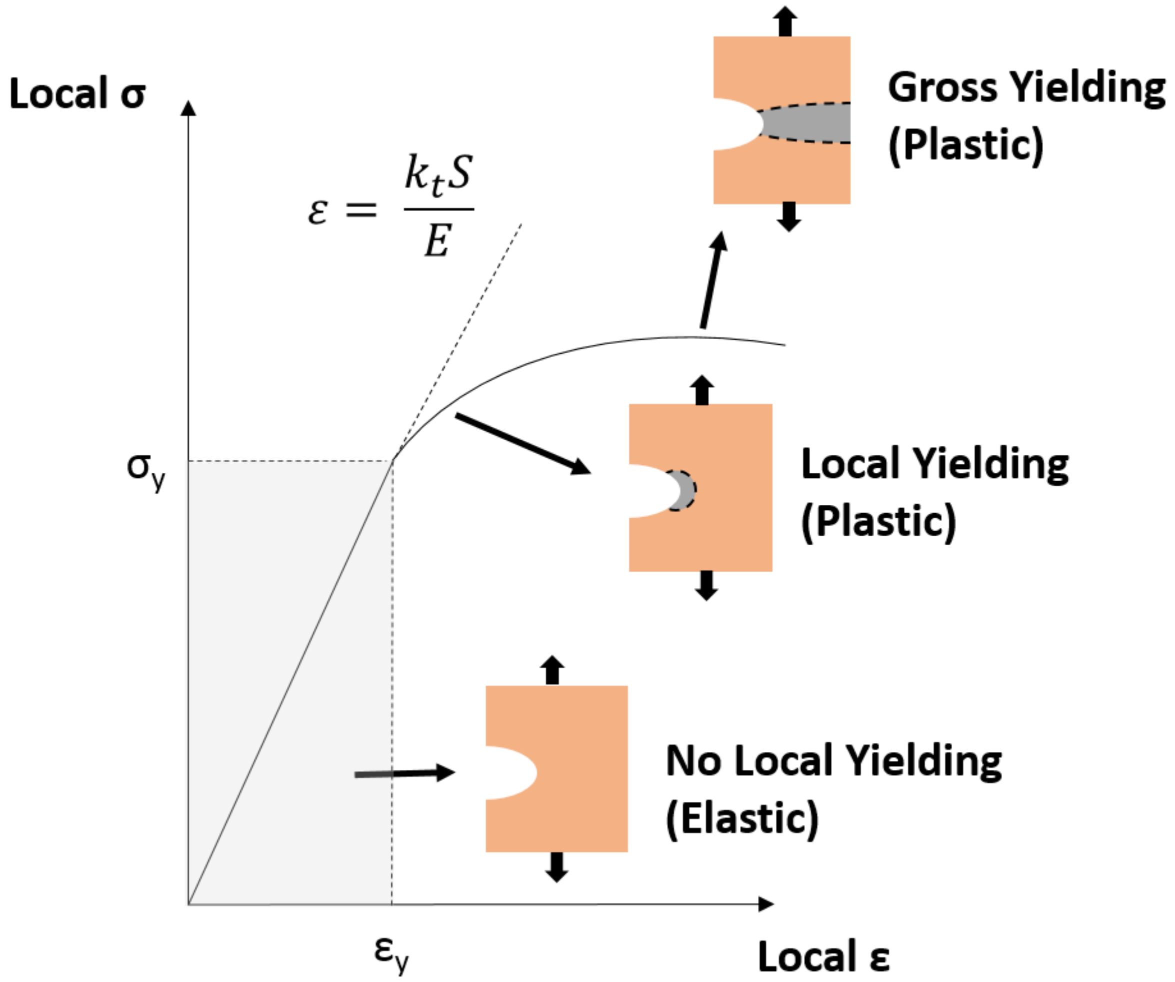

**Figure 4.2 |** Illustration depicting the true local stress/strain ahead of a notch in comparison with the predicted stress/strain using the elastic stress concentration factor ($k_t$). Once plasticity occurs, $k_t$ underestimates the local strains significantly. Such deviations are exacerbated as local plasticity extends throughout the bulk (gross plasticity).

The relationship between the elastic and plastic concentration factors is shown in **Figure 4.3**. As can be seen, after yielding, Neuber's rule accounts for higher changes in strain relative to stress with an increase in $\boldsymbol{k_\varepsilon}$ and a decrease in $\boldsymbol{k_\sigma}$.

Local notch plasticity can have pronounced effects on both crack initiation and growth. Neuber's rule accounts for these local changes in stress and strain, and serves as a basis for some notch fatigue approaches that integrate both plastic and elastic cyclic stress-strain behavior ahead of notches, as discussed later in this chapter.

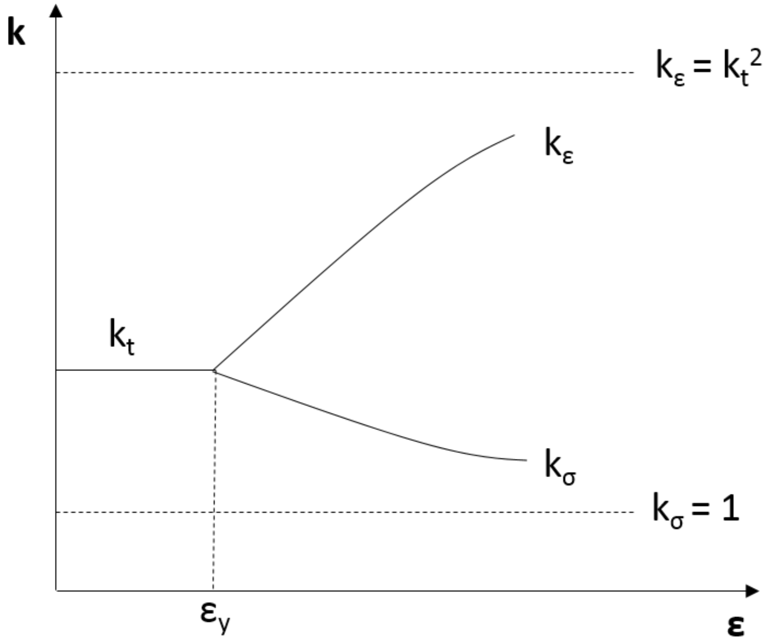

**Figure 4.3 |** Illustration of the relationship between the elastic stress concentration factor (***$k_t$***) and the strain and stress concentration factors (***$k_\sigma$***, ***$k_\varepsilon$***). While ***$k_\sigma$*** and ***$k_\varepsilon$*** are equivalent to each other and to ***$k_t$*** under elastic loading, they deviate sharply in the plastic region, where strain increases are much larger relative to that of stress increases ahead of a notch. Each factor approaches a limiting case in which gross yielding occurs and local notch effects diminish (i.e. ***$S$*** = ***$\sigma$***).

*Blunt Crack Elastic Fields*

The stress concentration factor provides an estimate of the peak elastic stress at or near the notch tip. A more robust model of the entire elastic stress field ahead of a notch can be modeled using linear elastic fracture mechanics (LEFM). Creager & Paris (1967) provided a characterization of the stress field ahead of a blunt crack (**Figure 4.4**) using the stress intensity factor for an equivalent sharp crack:

$$\begin{Bmatrix} \sigma_{xx} \\ \sigma_{yy} \\ \sigma_{xy} \end{Bmatrix} = \frac{K_I}{\sqrt{2\pi r}} cos\left(\frac{\theta}{2}\right) \begin{Bmatrix} 1\text{-}\sin\frac{\theta}{2}\sin\frac{3\theta}{2} \\ 1+\sin\frac{\theta}{2}\sin\frac{3\theta}{2} \\ \sin\frac{\theta}{2}\cos\frac{\theta}{2}\cos\frac{3\theta}{2} \end{Bmatrix} - \frac{K_I}{\sqrt{2\pi r}}\frac{\rho}{2r} \begin{Bmatrix} \cos\frac{3\theta}{2} \\ -\cos\frac{3\theta}{2} \\ \sin\frac{3\theta}{2} \end{Bmatrix} \quad \textbf{eq. 4.4}$$

Here, ***$K_I$*** is the tensile opening mode (Mode I) stress intensity for an equivalent sharp crack, ***$r$*** is the distance from the origin, and ***$\rho$*** is the radius of curvature of the blunt crack tip. Note that the origin in this case is at a distance ***$\rho/2$*** behind the notch tip, as shown in **Figure 4.4**. At this distance (***$r$*** = ***$\rho/2$***), the maximum notch tip tensile stress is equivalent to:

$$\sigma_{yy,\,\max} = \frac{2K_I}{\sqrt{2\pi r}} \qquad \textbf{eq. 4.5}$$

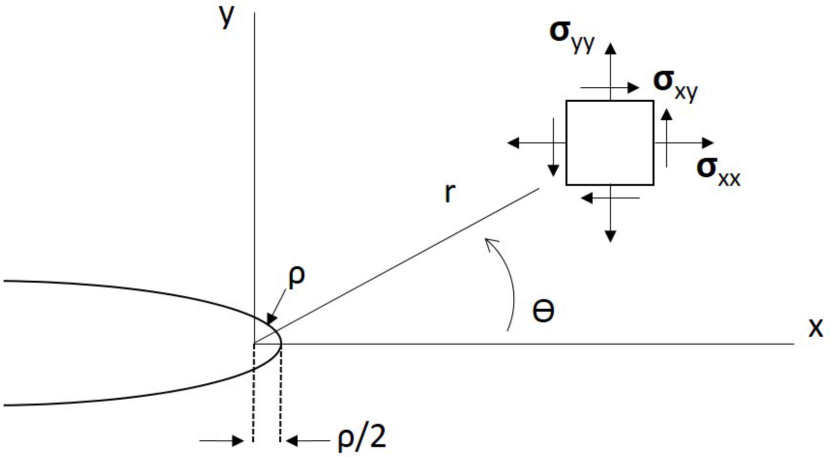

**Figure 4.4 |** Coordinate system for blunt crack elastic stress fields (adapted from Creager & Paris, 1967).

While this approximation only provides an estimation for elastic stress fields for blunt cracks (i.e. sharp crack-like notches), the Creager & Paris equations (above) have served as the foundation for LEFM approaches toward fatigue crack propagation, as seen in **Section 4.1.2.2**.

### 4.1.2 Notch Fatigue

The introduction of a geometric discontinuity (such as a notch) can result in the local concentration of any far-field stress to values near or above the yield strength of the material. Under cyclic loading, the repetitive elevation of local stresses can result in the accumulation of nano- or microscale plastic deformation over time, eventually coalescing into a propagating crack. Total life and defect tolerant approaches to fatigue discussed in **Chapter 3** can be utilized to evaluate both fatigue crack initiation and propagation ahead of notches using the approach illustrate in **Figure 4.5**. Here, a strain-life methodology evaluates flaw initiation, through cyclic loading of a specimen under a global strain that is equivalent to the local strains seen near a notch (i.e. $\Delta e = k_t \Delta \varepsilon$). Crack propagation studies then utilize fracture mechanics theory, limited to cracks that have escaped any notch influence.

While founded upon previously established theory, the methodologies represented in **Figure 4.5** are often too simplistic for the accurate description of crack inception and growth near a notch. In particular, the transition from initiation to propagation behavior is ill-defined; cracks that initiate near a notch may in fact grow under the notch influence, altering its driving force and resulting crack velocity. Adjustment are thus needed to provide a more thorough understanding of fatigue mechanisms near a notch. Several authors have attempted to remedy this problem by providing adjustments to the above approach or suggesting a single universal characterizing parameter to predict notch crack initiation and growth for any notch geometry (Taylor & Wang 2000; Taylor 1999; Taylor & O'Donnell 1994; Pluvinage 2003; Pluvinage 2001; Dowling 1979b; Lukáš 1987; Haddad & Dowling 1980; Smith & Miller 1978; Lukáš & Klesnil 1978; Schijve 1982; Kujawski 1991). The following sections outline several of those approaches, starting with stress-life ("total life") evaluations to highlight size effects in notch fatigue that distinguish it from monotonic rupture. Efforts to remedy the discrepancy in monotonic versus cyclic models are then discussed using total life and fracture mechanics theories, sometimes in combination. Finally, considerations of local notch plasticity are discussed, and proposed modifications to LEFM parameters and elastic-plastic analyses are introduced.

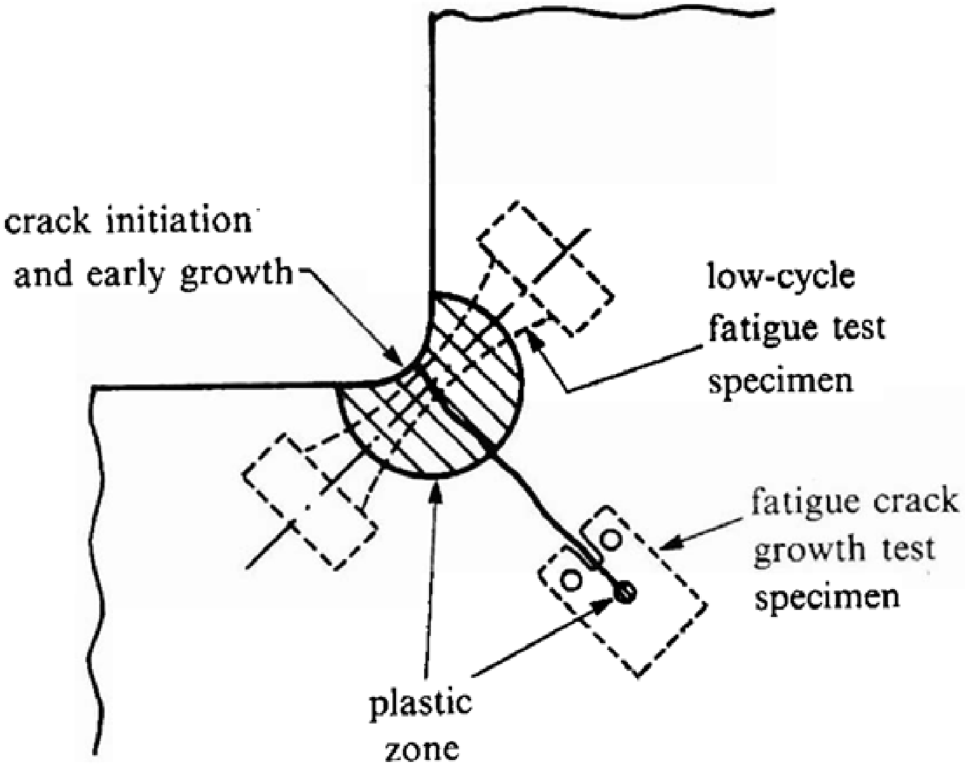

**Figure 4.5 |** Typical experimental approaches to evaluating crack initiation (strain-controlled total life approach) versus crack propagation (fracture mechanics approach) (Suresh 1998).

### 4.1.2.1 Total Life Approach: Notch Sensitivity

Similar to the elastic stress concentration factor, the fatigue notch factor, $k_f$, relates the fatigue life in notched members to that of smooth members at $10^6$ or $10^7$ cycles to failure ($N_f$):

$$k_f = \frac{\Delta\sigma_e}{\Delta\sigma_{e,notch}} \quad \textbf{eq. 4.6}$$

Here, the nominal stress amplitude achieved at a given $N_f$ for a smooth member ($\Delta\sigma_e$) is compared to the reduced nominal stress amplitude as the same $N_f$ for a notched component ($\Delta\sigma_{e,notch}$) to capture the reduction in fatigue strength. First estimations of $k_f$ can be made using $k_t$; in other words, the fatigue lifetime of a notched component with a stress concentration factor of $k_t$ that is subjected to a nominal cyclic stress of $\Delta S$ can be predicted by the equivalent lifetime of a smooth component subjected to a nominal stress of $k_t\Delta S$. This approach, also known as the "hot spot stress approach", considers the maximum local stress at the root of the notch ($\Delta\sigma_{max}$) to be of the primary predictor of failure (Taylor 1999; Pluvinage 2001; Pluvinage 1998). However, empirical studies show that notched components sometimes perform better than as predicted by $k_t$, and generally $k_f < k_t$ for small notch radius values (Dowling 1993; Suresh 1998). The distinction between the fatigue behavior of small and large notch radii is referred to as the "size effect" seen in notch fatigue (Taylor 1999; Kujawski 1991; Dowling 1993).

To deal with this discrepancy, the notch sensitivity factor has been introduced, $q$:

$$q = \frac{k_f - 1}{k_t - 1} \qquad \textbf{eq. 4.7}$$

The value of $q$ varies from 0 (no notch effect on fatigue strength) to 1 (maximum effect, $k_f = k_t$). In general, ductile materials display a greater notch sensitivity, with a more pronounced deviation between $k_f$ and $k_t$ than brittle materials.

Several authors have proposed empirical relationships between $k_f$ and $k_t$. For example, Neuber proposed the following relationship, where $\rho'$ is a material constant with distance units (Neuber 1958):

$$k_f = 1 + \frac{k_t - 1}{1 + \frac{\rho'}{\rho}} \qquad \textbf{eq. 4.8}$$

Several additional estimations for $k_f$ have been proposed (Neuber 1958; Klesnil & Lukáš 1992; Taylor & O'Donnell 1994; Peterson & Sines 1959; Mitchell 1979), all of which rely on a material constant that is derived from experimental analysis.

### *Causes of Notch Sensitivity*

The apparent increase in fatigue strength for smaller radii has been explained using the "critical volume approach" (Taylor 1999; Pluvinage 2001; Pluvinage 1998): for failure to occur, the average local cyclic stress ($\Delta\sigma_{notch}$) must exceed the endurance limit of the material ($\Delta\sigma_e$) over some critical volume ahead of the notch. This critical volume has been simplified into a singular critical point (Peterson 1959), critical distance (Neuber 1946; Siebel & Stieler 1955; Taylor 1999), and critical area (Dowling 1993). The last characterization provides the most intuitive understanding of this volumetric approach, with the critical area characterized as a two-dimensional stress gradient ($d\sigma/dx$) that exists ahead of a stress riser (**Figure 4.6**). A notch creates the highest stresses at the notch tip, as estimated by $k_tS$. That stress drops off rapidly with increasing distance from the notch tip, creating a stress gradient that is dependent on the radius of the notch tip. Blunter notches (larger notch radius) have a greater stress gradient than sharper notches (smaller notch radius), and thus *sustain elevated stresses for a greater distance* ahead of the notch tip, despite have a lower $k_t$. This becomes particularly important in the case of high cycle fatigue, in which failure is predicated upon statistical probability of flaw formation and coalescence before stable crack processes can occur. A larger stress gradient creates a larger process zone and thus a higher statistical probability for crack initiation. Sharper notches have a smaller process zone due to a smaller notch, which can enhance resistance to crack initiation and thus contribute to a reduced notch sensitivity (i.e. $k_f < k_t$) compared to blunter notches.

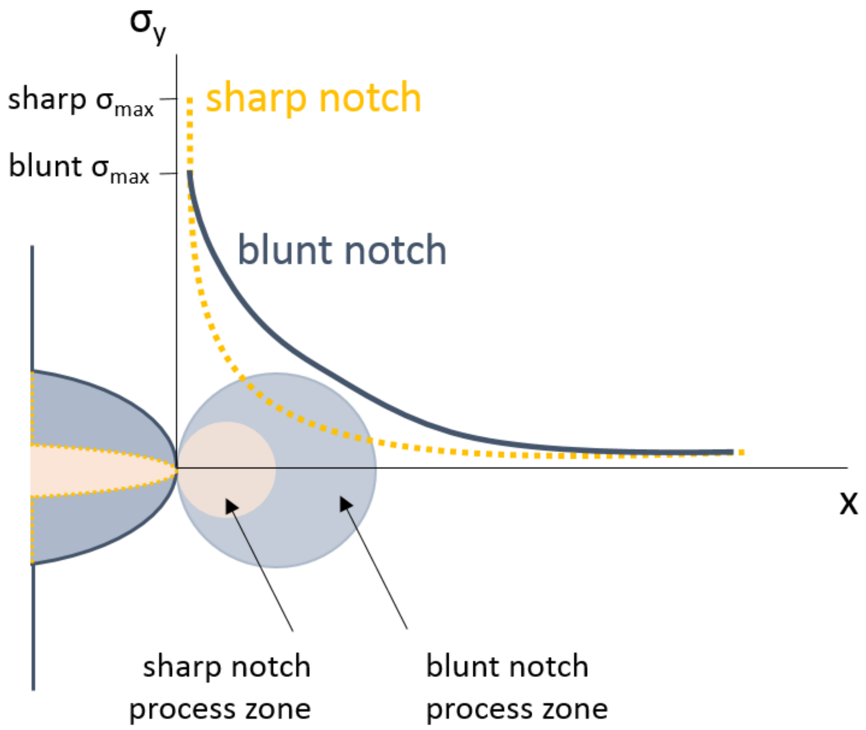

**Figure 4.6 |** Illustration comparing the process zone of a sharp and blunt notch. Sharp notches produce a higher peak stress near the notch tip, resulting in a higher $k_t$ than blunt notches. However, the drop-off in stress from that peak stress (i.e. the stress gradient) is steeper for sharp notches compared to blunt notches. This results in a smaller area of material ahead of the notch tip that is subjected to elevated stresses. In other words, the notch process zone of a sharp notch is smaller than that of a blunt notch, potentially resulting in a lower statistical probability of flaw initiation and a reduced notch sensitivity.

Another argument for the volumetric approach considers material microstructure. The comparative size of process zones and microstructures (such as grain sizes) has suggested that the latter features may play a role in flaw initiation. For example, small grains that are similar in size to notch process zones may effectively distribute stresses evenly across a small dimension, thereby decreasing peak stresses (Dowling 1993). On the other hand, grains that are larger than the process zone may not experience elevated notch stresses at all, diminishing any probability of flaw formation. Even this "weakest link" argument favors improved fatigue life for sharper notches, since peak stresses that may drive up grain boundary tension, dislocation slip and crack formation are limited to a finite volume smaller than the grain itself (Dowling 1993; Pluvinage 1998; Pluvinage 2001).

Notch sensitivity may also occur due to the extent of yielding ahead of the notch. For example, at high stress amplitude values (low cyclic fatigue lives), full yielding can extend beyond the vicinity of the notch itself, causing gross specimen yielding and mitigating any effect of the notch on fatigue behavior ($k_f = 1$) (**Figure 4.2**). Lowering the cyclic stress can scale back the plasticity to a localized notch yield zone, potentially improving fatigue life by dissipating local elastic energy. While this plasticity effect may influence notch sensitivity, the observation of the $k_f < k_t$ effect even for full elastic cyclic loading indicates that plasticity alone cannot account for changing crack behavior in the vicinity of a notch, supporting the existence of a stress gradient or a weakest link effect as discussed above.

*The Local Strain Approach*

The notch sensitivity parameter (***q***) provides a quick predictor for fatigue behavior of a notched component, but relies upon tabulated values for a given material. Determining this parameter for novel materials requires both notched and smooth component fatigue data, which can be both time consuming and costly. Another approach allows for notch fatigue predictions using only smooth specimen data called the local strain approach. This methodology is restricted to loading scenarios in which yielding only occurs locally, if at all (**Figure 4.2**). Under this assumption, Neuber's rule (**eq. 4.3**) can be simplified by assuming that global stresses remain elastic and are thus related linearly by Hooke's law ($S = Ee$); **eq. 4.3** can then be simplified to:

$$\sigma\varepsilon = \frac{(k_t S)^2}{E} \qquad \textbf{eq. 4.9}$$

**Figure 4.7** shows how this equation, a hyperbola, can be coupled with the stress-strain curve for a material that relates $\sigma$ and $\varepsilon$ to solve for the local stress-strain notch environment. The resulting local stresses and strains can then be compared to stress-life data for smooth specimens to estimate the component lifetime.

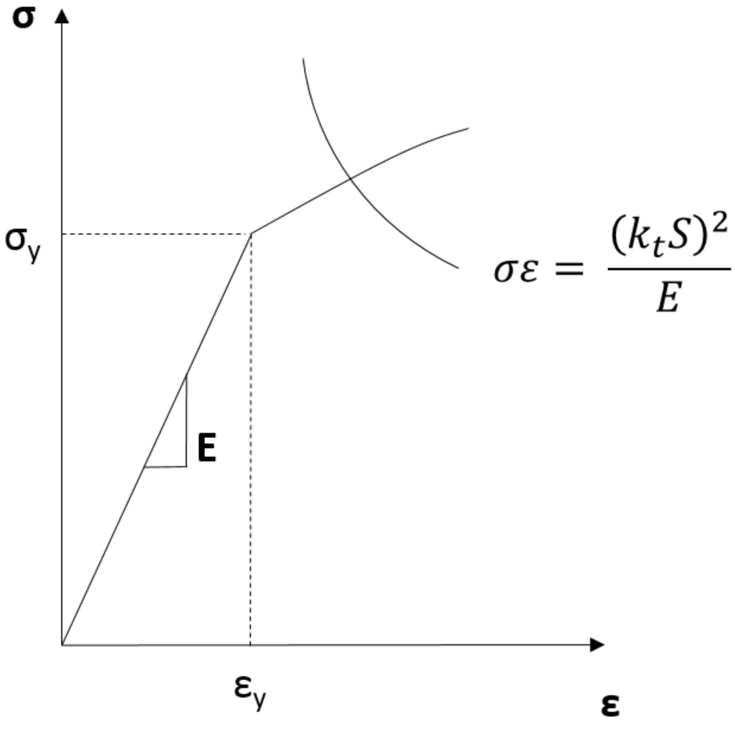

**Figure 4.7 |** Under conditions of local yielding, Neuber's rule can be used in conjunction with a material's stress-strain curve to solve for the local maximum stress and strain ahead of a notch. Images adapted from Dowling (1993).

*Limitations of the Total Life Approach*

The notch fatigue factor presents several limitations in translatability to commercial parts. First, reliance on tabulated sensitivity data to derive fatigue factors demonstrates the need for a robust empirical dataset for a given material, which can cost both time and money to obtain. Secondly, notch fatigue factors can under-predict the fatigue life of component as much as 45% (Taylor & Wang 2000), leaving the need for more reliable predictors. Finally, as with all total life approaches to fatigue, the mechanisms behind crack initiation and propagation are not readily attained from $\boldsymbol{k_f}$. Due to the influence that notches can have on the local stress environment, as seen with Neuber's Rule or the stress concentration factor, one can assume that local changes also influence the driving force behind a crack, warranting the need for crack propagation studies. Furthermore, as will be shown in the following section, failure of a notched component may not necessarily be dominated by crack initiation processes; flaws that accrue near a notch face a complex stress-strain state that can slow down or even stop crack growth, known as crack saturation (Frost & Dugdale 1957; Suresh 1998). Thus, knowing the conditions under which cracks propagate ahead of notches become paramount to predicting fatigue lifetimes. Fracture mechanics approaches developed to address not only crack growth but also crack initiation are discussed in the following section.

### 4.1.2.2 Fracture Mechanics Approaches to Notch Fatigue

*LEFM Approaches to Crack Propagation near Notches*

Stress intensity factors for sharp cracks growing from an edge or in the center of a plate are typically found in tabulated form, as seen in Tada, Paris, & Irwin (1985). Similar tabulated equations for stress intensity factors are available for cracks emanating from notches (Nisitani 1978; Newman 1971), but limited to only a handful of notch geometries found in engineering components.

Several authors have attempted to remedy this through numerical solutions and analytical expressions that account for changing geometry of the notch, such as its depth ($\boldsymbol{D}$), length ($\boldsymbol{c}$), tip radius of curvature ($\boldsymbol{\rho}$) or stress concentration factor ($\boldsymbol{k_t}$) (Smith & Miller 1978; Lukáš 1987; Lukáš & Klesnil 1978; Smith & Miller 1977; Rooke 1980; Kujawski 1991; Dowling 1979a; Dowling 1979b; Schijve 1982; El Haddad et al. 1979). In general, these authors follow the same general approach, which includes a slight deviation of the LEFM assumption of similitude. As discussed in **Chapter 3**, LEFM principles assume that for a given material under a specific loading environment, the near-tip stresses for a sharp crack will be the same regardless of crack size or specimen dimensions, as long as the stress intensity, $\boldsymbol{K}$, is the same (the concept known as "similitude"). The introduction of a notch, however, results in a differentiation between local notch-tip and far-field bulk specimen stress fields that can act upon a growing crack. As a result, the influence of a notch is not only dependent on its geometry and the host material's properties, but also on the *crack length*.

To compensate for this deviation from similitude, stress intensity solutions for cracks growing ahead of notches can be divided into short and long crack approximations. Dowling (1979) presents the most generalized version of this approach, outlined below. Short cracks emanating from notches grow within a notch-affected zone, and are subject to the local notch stress field. Dowling modeled this short crack as an edge crack (***l***) growing from a free surface under the influence of the maximum peak stress (**$k_tS$**) at the notch in the absence of a crack (**Figure 4.8A**):

$$K_s = 1.12k_tS\sqrt{\pi l} \qquad \textbf{eq. 4.10}$$

The factor of 1.12 is a free surface correction factor (Tada et al. 1985; Dowling 1979b). Cracks eventually grow long enough such that the notch depth, ***c***, comes into consideration, and nominal stress intensity solution for sharp cracks can be used:

$$K_l = FS\sqrt{\pi a} = FS\sqrt{\pi(c+l)} \qquad \textbf{eq. 4.11}$$

Here, ***F*** is a geometrical correction factor that accounts for specimen geometry, and can be found in tabulated form (Tada et al. 1985). The transition between these two solutions, seen in **Figure 4.8B**, occurs at a specific transition length, ***l****. This crack length marks the transition from a notch-affected zone to bulk specimen stresses; in other words, ***l**** is the size of the local notch stress field. The transition length can be calculation by setting **$K_s$** and **$K_l$** equal to one another:

$$l^* = \frac{c}{\left(\frac{1.12k_t}{F}\right)^2 \mp 1} \qquad \textbf{eq. 4.12}$$

Here, a negative sign is used in the denominator for circular notches, while a positive sign is reserved for deep or edge notches. The value of ***l**** typically falls within a range of 1/20 to 1/4 the size of the notch radius, ***ρ***, with sharp notches approaching a limit at $\rho/5$ (Dowling 1979a).

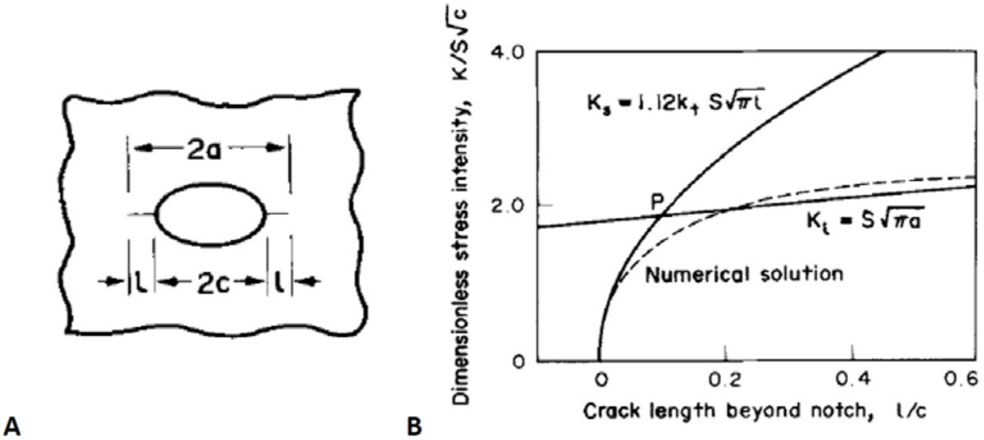

**Figure 4.8 |** Dowling (1979a) presents an approach for characterizing the driving force behind crack growth in the vicinity of a notch. Here, crack growth emanating from an elliptical hole of longitudinal length ***2c*** (**A**) is modeled using a numerical solution (**B**, dashed line) and compared to limiting stress intensity solutions for short (**$K_s$**) and long cracks (**$K_l$**). Point ***P*** corresponds to a transition length (***l****) that demarcates the boundary of the local notch stress field (Dowling 1979b).

Around the same time Dowling published these limiting cases for notch crack stress intensities, several authors adopted similar descriptions distinguishing between "short" and "long" crack growth. Distinctions between these descriptions primarily exist for short crack stress intensities (**Table 4.1**); long crack approximations generally follow **eq. 4.11 (**above). Each equation derives from the similar idea that the local notch stresses play a direct role on small crack growth. Unlike Dowling's approximation, where the local stresses are represented only by the elastic peak stress ($k_tS$), Schijve (1982), Kujawski (1991), and Lukas (1978, 1987) use more complex local notch stress expressions to derive their small crack stress intensities. Smith & Miller (1977, 1978) derived their short crack approximation by comparing the crack length in unnotched and notched specimens at equivalent crack growth speeds for simple notch geometries. El Haddad's method for small crack growth primarily derives from empirical data, with the inclusion of a new material constant ($l_o$ or $a_o$) (El Haddad et al. 1979). This material constant as served as the foundation for several "critical distance" methods, as discussed in the previous section (Pluvinage 1998; Pluvinage 2001; Pluvinage 2003; Tanaka 1983; Taylor 2008). However, deriving this constant is dependent on availability of fatigue data from unnotched specimens.

**Table 4.1 |** Summary of expressions for stress intensity (K for all crack lengths OR $K_S$ / $K_L$ for short or long cracks, respectively) developed to describe crack growth emanating from a notch.

| **Reference** | **Stress Intensity Factor ($K_s$)** |
|---|---|
| Dowling (1979a) | $K_s = \sigma_{local}\sqrt{\pi l} = 1.12 k_t S\sqrt{\pi l}$ **for $l \leq l^*$**<br>$K_L = FS\sqrt{\pi a} = FS\sqrt{\pi(c_o + l)}$ **for $l > l^*$**<br>$K_s(l^*) = K_L(l^*)$ ***OR*** $l^* = \dfrac{c_o}{\left(\frac{1.12k_t}{F}\right)^2 - 1}$ |
| Schijve (1982) | $K_s = \sigma_{local}\sqrt{\pi l} = Ck_t S\sqrt{\pi l}$ **for $l \leq l^*$**<br>$^{\pm}K_L = FS\sqrt{\pi a} = FS\sqrt{\pi(c_o + l)}$ **for $l > l^*$**<br>$K_s(l^*) = K_L(l^*)$ ***OR*** $l^* = \dfrac{c_o}{\left(\frac{Ck_t}{F}\right)^2 - 1}$<br>$C = 1.1215 - 3.21\left(\frac{l}{\rho}\right) + 5.16\left(\frac{l}{\rho}\right)^{1.5} - 3.73\left(\frac{l}{\rho}\right)^2 + 1.14\left(\frac{l}{\rho}\right)^{2.5}$ |
| Smith & Miller (1977, 1978) | $K_s = \left[1 + 7.69\sqrt{c_o/\rho}\,\right]^{1/2} S\sqrt{\pi l}$ **for $l < 0.13\sqrt{c_o \rho}$**<br>$^{\pm}K_L = S\sqrt{\pi a} = S\sqrt{\pi(c_o + l)}$ **for $l \geq 0.13\sqrt{c_o \rho}$** |
| Kujawski (1991) | $K = \sigma_{local}\sqrt{\pi l} = Qf\,\frac{k_t S}{2}\left[\left(1 + 2\frac{l}{\rho}\right)^{-\frac{1}{2}} + \left(1 + 2\frac{l}{\rho}\right)^{-3/2}\right]\sqrt{\pi l}$<br>$f = 1$ **for $x/\rho < 0.2$**<br>$f = 1 + \frac{\tan(\pi/2k_t)}{2.8}\left(\frac{x}{\rho} - 0.2\right)$ **for $x/\rho \geq 0.2$**<br>$Q = 1.22$ for a through-thickness crack |
| Lukas & Klesnil (1978); Lukas (1987) | $K = \sigma_{local}\sqrt{\pi l} = \dfrac{Fk_t}{\sqrt{1 + 4.5(l/\rho)}} S\sqrt{\pi l}$ |
| El Haddad (1979) | $K = \sigma\sqrt{\pi(l + l_0)},\ l_0 = \frac{1}{\pi}(\Delta K_{Th}/\Delta\sigma_e)^2$ |

$\rho$ = notch root radius
$S$ = farfield stress
$k_t$ = stress concentration factor
$l$ = crack length emanating from notch

$c_o$ = notch depth
**F** = specimen geometry factor (Tada et al. 1985)
$\Delta K_{Th}$ = sharp crack threshold cyclic stress intensity
$\Delta\sigma_e$ = smooth specimen endurance limit

$l^*$ = transition length between long crack ($K_L$) and short crack ($K_s$) approximations
$Q$ = shape factor, as found in (Creager & Paris 1967)

Short and long crack approximations for the stress intensity factor can be utilized for predictive modeling of a given flaw in conjunction with the Paris law for linear crack growth, where $\boldsymbol{C}$ and $\boldsymbol{m}$ are material constants:

$$\frac{dl}{dN} = C\Delta K^{m} \qquad \textbf{eq. 4.13}$$

Considering an initial flaw of $\boldsymbol{l}$ that is shorter than $\boldsymbol{l^*}$, the number of cycles to grow the crack to a final length ($\boldsymbol{l_f}$) can be determined through integration of **eq. 4.13** from $\boldsymbol{l}$ to $\boldsymbol{l^*}$ using $\boldsymbol{K_s}$ (below, using Dowling's approximation in **eq. 4.10**) and from $\boldsymbol{l^*}$ to $\boldsymbol{l_f}$ using $\boldsymbol{K_l}$ (**eq 4.11**):

$$N_f = \frac{l^{*(1-\frac{m}{2})} - l_f^{(1-\frac{m}{2})}}{C(1-\frac{m}{2})(1.12k_t\Delta S\sqrt{\pi})^m} + \frac{(c+l_f)^{(1-\frac{m}{2})} - (c+l^*)^{(1-\frac{m}{2})}}{C(1-\frac{m}{2})(\Delta S\sqrt{\pi})^m} \quad \textbf{eq. 4.14}$$

The above breakdown of crack initiation and propagation ahead of a notch allows for the extraction of notch geometry effects through the consideration of both $\boldsymbol{k_t}$ and $\boldsymbol{l^*}$.

The behavior of short cracks in the vicinity of a notch using the stress intensities mapped in **Table 4.1** has been documented for some metals. For example, Saxena and colleagues (1985) evaluated crack growth in blunt notch CT specimens ($\boldsymbol{\rho} = 6.35$ mm, $\boldsymbol{k_t} = 2.24$) of austenitic steel in a wet hydrogen environment. The authors used the Dowling approximation to model short crack stress intensity and found that these cracks grew almost twice as fast as long cracks at a given $\boldsymbol{\Delta K}$, but with a strong dependence on loading frequency. The authors suggest that lower test frequencies allow enough time for corrosive interactions to take place near the crack tip, which tend to have a greater influence on small cracks (whether or not in the vicinity of a notch) compared to long cracks.

Similar studies of notch-emanating cracks were performed by Shin & Smith (1988) using double and singled edge notched specimens ($\boldsymbol{\rho} = 0.4$ to 1.4 mm, , $\boldsymbol{k_t} = 12.4$ to 29) of stainless steel and aluminum, and by Tanaka & Nakai (1983) in center-notched specimens ($\boldsymbol{\rho} = 0.16$ mm, $\boldsymbol{k_t} = 8.48$) of low carbon steel. The two studies also found elevated short crack growth relative to long cracks at a given $\boldsymbol{\Delta K}$, which they associated with a diminishing crack closure effect due to a shorter wake on these small cracks (**Figure 4.9A**). Both studies demonstrated that short and long crack behavior overlap when mapped with $\boldsymbol{\Delta K_{eff}}$ values as opposed to $\boldsymbol{\Delta K}$, which considers the $\boldsymbol{K_{cl}}$ value that can be measured experimentally (**Figure 4.9B**). Further support for the crack closure argument derives from the primary location of deviations between short and long crack growth at low $\boldsymbol{\Delta K}$ values, a region where crack closures tends to have a greater influence on long crack growth (Suresh & Ritchie 1984).

Crack closure also explains the phenomenon of decelerating short crack growth with increasing $\boldsymbol{\Delta K}$ into a nonpropagating crack, also seen in **Figure 4.9A**. As crack elongate, their wakes also grow, increasing the propensity for plasticity-induced closure, especially in an area of notch plasticity. The phenomenon of nonpropagating cracks has also been seen using the stress-life approach: Frost and colleagues found that a given $k_t$, a lower stress amplitude is needed to generate a nonpropagating flaw than to grow that flaw until final failure (**Figure 4.10**) (Frost et al. 1999; Frost 1960). Other similarly reported data (Frost & Dugdale 1957; Dowling 1979b) suggests that the fatigue life for some materials may instead be dominated by crack propagation and not initiation events, as is traditionally seen in total life assessments of fatigue. This may also be the reason why the $k_f < k_t$ effect is seen for high cycle fatigue tests in which little plasticity may exist at the notch tip.

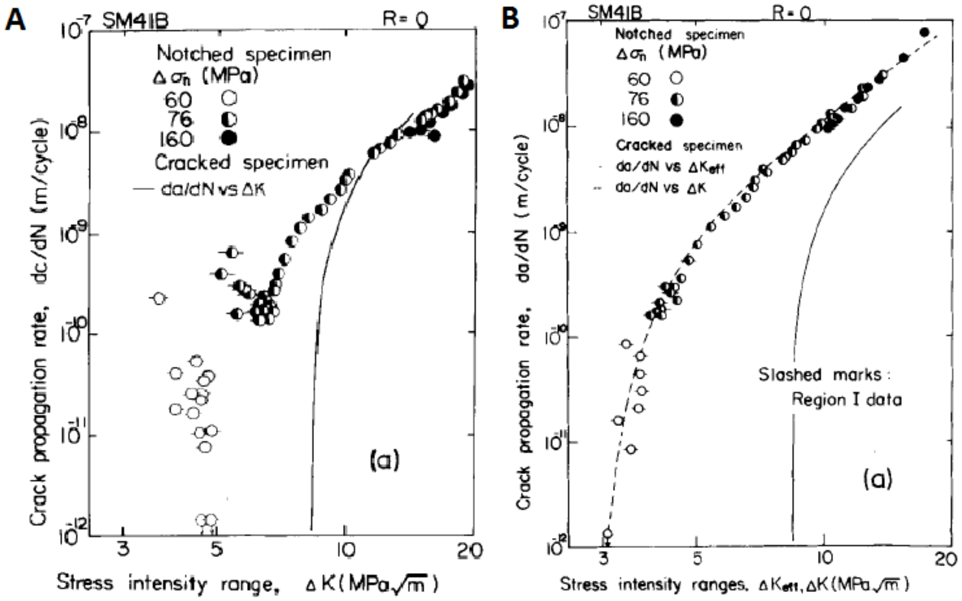

**Figure 4.9 |** FCP data obtained for short cracks growing from a crack-like notch in low carbon steel (JS SM41B) with a root radius of 0.16 mm. (**A**) Short crack data ahead of notches is shown to grow at an elevated speed compared to long crack data at the same $\Delta K$, or even exhibit crack speed below $\Delta K_{th}$. Data obtained for mean stress $\Delta\sigma_n$ = 60 MPa demonstrate decreasing crack speed until a nonpropagating crack phenomenon occurs. (**B**) Mapping long and short crack data against $\Delta K_{eff}$ to account for crack closure effects negates any short crack growth effects or mean stress effects in this case (Tanaka & Nakai 1983).

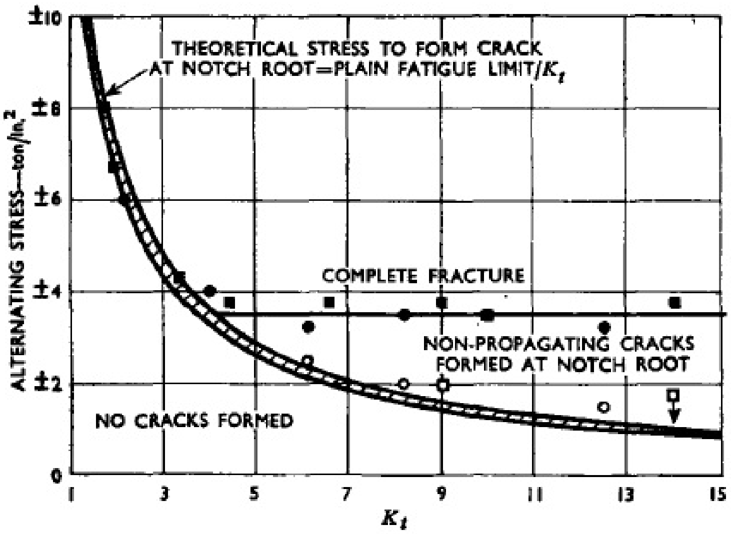

**Figure 4.10 |** High cycle fatigue data for specimens of mild steel machined with various notch geometries comparing the alternating stress needed to initiate a crack at the notch root (open symbols) versus the stress need to cause fracture (filled symbols). Crack initiation is defined here as the initiation of a flaw and subsequent saturation of its growth, which is shown to occur at lower alternating stresses than final fracture events (Frost et al. 1999).

*LEFM Approaches to Crack Initiation at Notches*

As discussed above, the local notch stress field dictates the driving force behind crack propagation. When assessing a notch's contribution to crack initiation, however, local strain is often considered instead. In **Section 4.1.2.1**, the local strain approach was used in conjunction with Neuber's rule to identify the local strains at the notch tip and determined the fatigue life using smooth specimen strain-life data. However, such approaches are often tedious and reliant upon existing fatigue datasets.

Fracture mechanics enables the isolation of initiation and propagation phases through a combination of total life and fracture mechanics philosophies. To bridge the local stress and strain characterizations of near-notch tip fields, Wilson (1974) demonstrated that estimates of the local notch stress field such as $k_t$ or Neuber's rule (**eq. 4.3**) provided reasonable correlations with a unique value of the true local notch strain, even if yielding occurs. In other words, a value $k_tS$ would account for any notch geometry that can be described by $k_t$, but only correlate with one local notch strain value at the applied *S*. As a result, mapping crack initiation lifetimes as a function of $k_tS$ would be equivalent to mapping lifetimes against the local strain environment.

Dowling extended this idea to a fracture mechanics regime by arguing that the local strain near a sharp, crack-like notch can be defined in terms of an equivalent stress intensity factor. Using the Creager & Paris (1967) estimation in **eq. 4.4**, the peak stress at the notch tip can be written as:

$$\sigma = \frac{2K}{\sqrt{\pi\rho}} \qquad \textbf{eq. 4.15}$$

where $\rho$ is the notch radius of curvature and $\sigma$ is the peak notch-tip stress, which is equivalent to $k_tS$. Thus, we can rewrite **eq. 4.15** as:

$$k_tS = \frac{2K}{\sqrt{\pi\rho}} \qquad \textbf{eq. 4.16}$$

Or in the case of cyclic loading:

$$k_t\Delta S = \frac{2\Delta K}{\sqrt{\pi\rho}} \qquad \textbf{eq. 4.17}$$

Thus instead of plotting crack initiation lifetimes as a function of $k_t\Delta S$, the fracture mechanics term $\Delta K/\sqrt{\rho}$ can be used, as shown by Barsom & McNicol (1974). This succinctly accounts for both local strains through equivalence with $k_t\Delta S$ and notch geometry through the radius $\rho$ (see example in **Figure 4.11**). Crack initiation can be defined as the time it takes for the crack to escape the local notch stress field. This occurs when the crack length reaches the "transition length" ($l^*$), or the length where short and long crack approximations for crack growth are equivalent (e.g. **eq. 4.12**).

Similar to a stress-life plot, an LEFM-based endurance limit can be extrapolated from **Figure 4.11**, producing a threshold stress intensity, $(\Delta K/\sqrt{\rho})_{th}$, below which cracks will not grow. Kim et al. (1979a) demonstrate that this limit can be related to the plastic behavior of a material through its yield strength ($\sigma_y$) and work hardening coefficient ($n$):

$$\left(\frac{\Delta K}{\sqrt{\rho}}\right)_{th} = \sigma_y\sqrt{\frac{n+1}{2}} \qquad \textbf{eq. 4.18}$$

In other words, the crack initiation endurance limit will increase with higher strength (greater yield) and a steeper work hardening behavior. This is primarily related to the reduction in notch plastic zone size for materials with a greater yield and work hardening coefficient, reducing the critical volume in which flaws can develop (Kim et al. 1979).

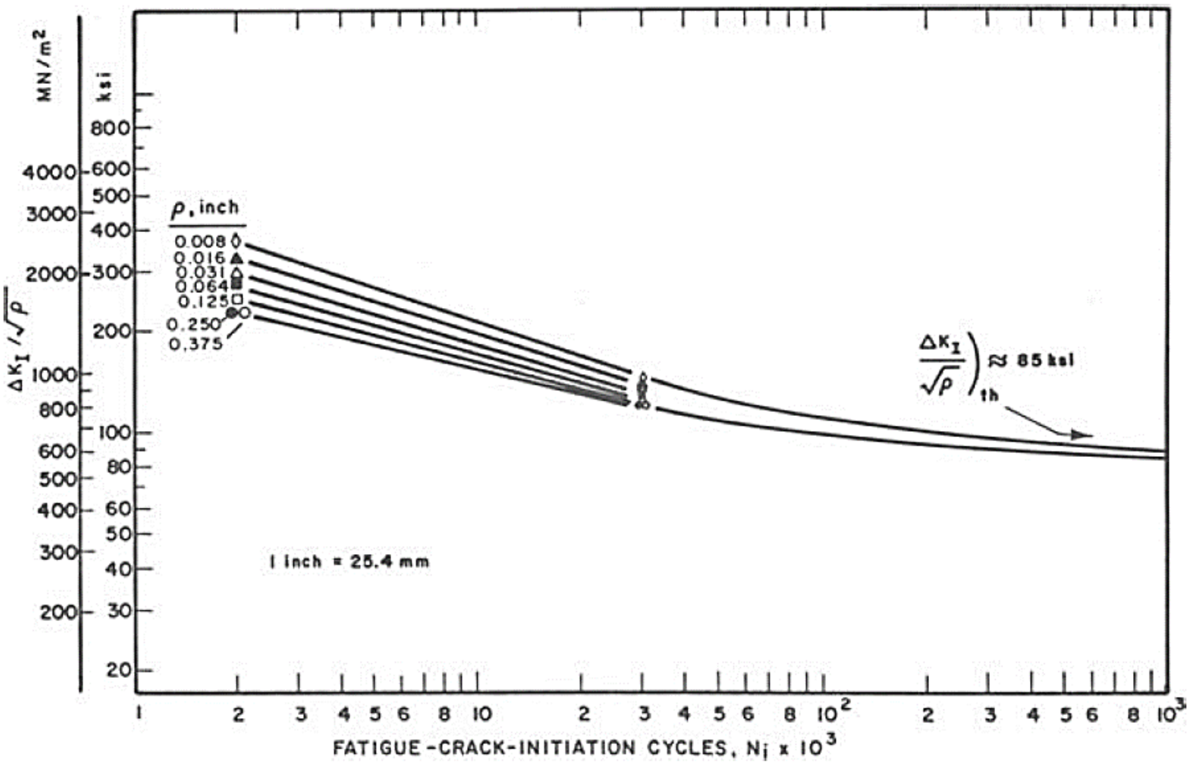

**Figure 4.11 |** Fatigue crack initiation mapped as a function of the cyclic stress intensity for HY-130 steel. Note that the data approaches an endurance limit of $(\Delta K/\sqrt{\rho})_{th}$ (Barsom & McNicol 1974).

### *Notch Plasticity and Limitations in using LEFM*

As with all LEFM approaches, the above discussion of short and long crack stress intensity factors is contingent on small scale yielding (SSY) relative to the crack size. This becomes problematic for many sharp notches in ductile materials, in which the transition length approaches $\boldsymbol{\rho}/5$. For $\boldsymbol{\rho}$ less than 1 mm, the transition length approaches sub-millimeter values, which can be readily consumed by a notch plastic zone during loading before stable crack growth can be achieved (**Figure 4.12**). SSY can thus be violated, considering the notch plastic zone ($\boldsymbol{r_p}$) to be significantly larger than any crack length emanating from a notch ($\boldsymbol{l}$). Once the crack escapes the local notch field, the notch depth ($\boldsymbol{c}$) is then taken into consideration for the crack length ($\boldsymbol{c} + \boldsymbol{l}$), which can restore applicability of LEFM for predicting crack growth as long as the crack tip plastic zone remains within SSY requirements (Dowling 1979a).

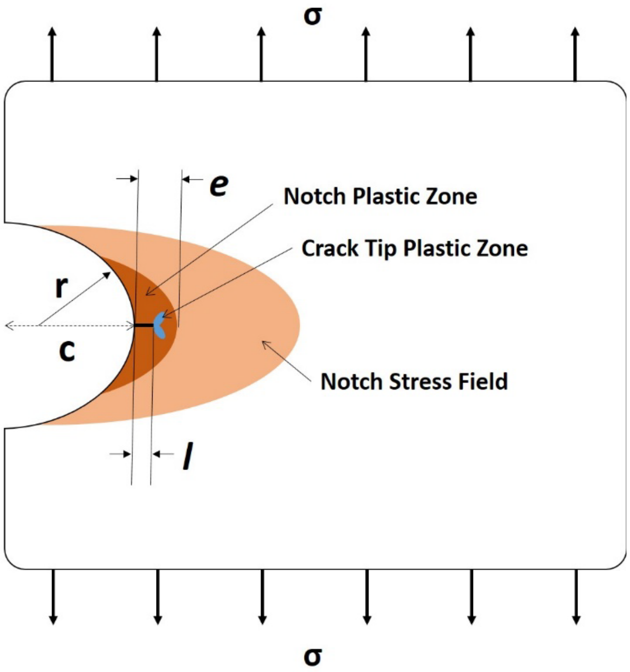

**Figure 4.12 |** Since the notch creates a local region of elevated stresses relative to the bulk, local yielding can occur near the notch tip that can engulf any cracks emanating from the tip. This can violate SSY requirements for LEFM approximations, especially when the crack is still within the notch stress field, as shown above.

Using the Creager & Paris model for the elastic stress field near a crack tip (**eq. 4.4**), Dowling derived an estimate for the notch plastic zone ($r_p$), where $\rho$ is the notch radius, $k_t$ is the stress concentration factor, $S$ is the far-field stress and $\sigma_y$ is the yield stress (**Figure 4.13**):

$$r_p = \rho\left[\left(\frac{k_t S}{\sigma_y}\right)^{\frac{2}{3}} - 1\right] \qquad \textbf{eq. 4.19}$$

Dowling shows reasonable agreement between this equation and the notch plastic zones predicted from plane stress finite element analysis of steel by Hammouda and Miller (1979). For cracks smaller than the transition length, **eq. 4.19** predicts that local notch stresses barely above yield ($k_t S/\sigma_y$ = 1.1 to 1.3) can result in engulfing of the crack by the plastic zone, especially for sharp notches in which the transition length (~ $\rho$/5) is small. This limits the short crack stress intensity predictions for crack driving force since SSY requirements are called into question at crack lengths less than the transition length. Proposals for elastic-plastic approaches to cracks in this regime are discussed below. For $l > l^*$, LEFM stress intensity values are not thought to differ significantly from plasticity modified values, assuming SSY at the crack tip is still preserved.

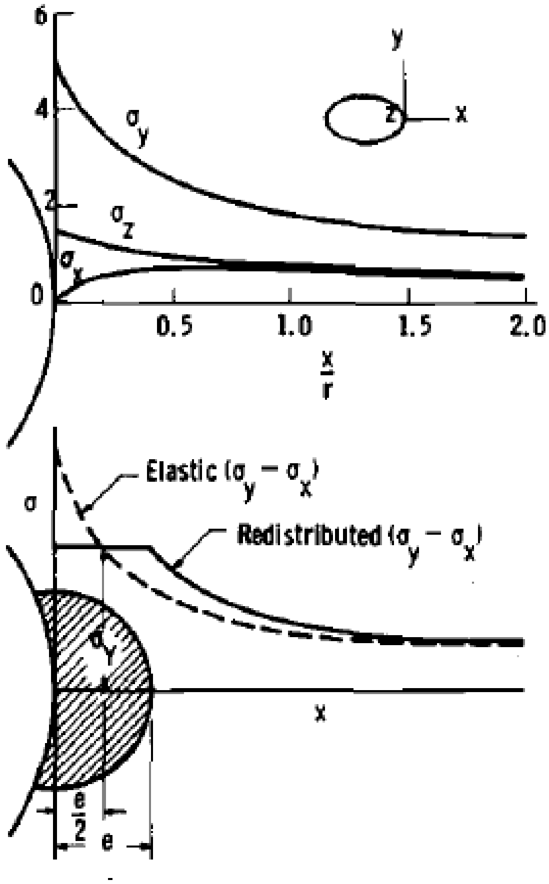

**Figure 4.13 |** Estimation of plastic zone size (here labeled ***e***) using elastic crack analysis by Creager & Paris (Creager & Paris 1967; Dowling 1979a).

LEFM approaches to crack initiation can avoid the challenges associated with local plasticity in some limited cases. As discussed above, the $\Delta K/\sqrt{\rho}$ term can be directly related to $k_tS$, which directly correlates to a unique value of local strain for any notch geometry (Wilson 1974). However, the equivalence between $k_tS$ and $K$ is predicated upon the assumption of a *crack-like* notch, with a small radius of curvature. For these geometries, the prediction of $k_t$ using $K$ and **eq. 4.16** are within 10% of finite element calculations of $k_t$, but deviate as much as 33% for blunt notch geometries, such as a circular hole in an infinite plate (Dowling 1979a). As a result, deviations in $\Delta K/\sqrt{\rho}$ curves may exist between two notch geometries with the same $k_t$, such as a deep, elliptical notch versus as a circular hole.

To avoid this complication, Dowling (1979a) suggests that the $\Delta K/\sqrt{\rho}$ should be dropped and replaced by $k_t\Delta S$, using finite element methods to calculate $k_t$. Even this solution, however, has certain limitations. The uniqueness of local strain for a given $k_tS$ can be at elevated stresses above the yield stress, as demonstrated by Wilson in **Figure 4.14**. Furthermore, conditions of plane strain and plane stress can influence local notch strains such that geometric equivalence does not always hold true.

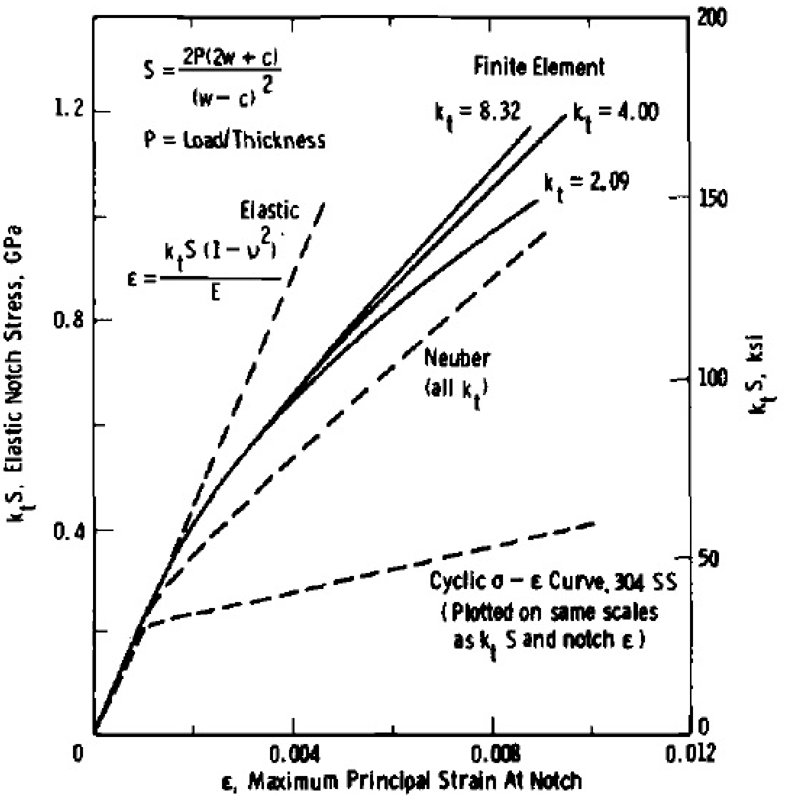

**Figure 4.14 |** Solutions for local notch stress using elastic stress concentration factors, Neuber's solution and finite element models. Deviations between three different notch geometries, represented by three stress concentration factors, occur just at roughly two times the yield strength. While the elastic and Neuber solutions present unique local strain values for a given $k_tS$, large loads approaching the gross specimen plasticity may result in significant notch size dependency for fatigue crack initiation studies. (Wilson 1974)

Local notch plasticity thus presents significant challenges for quantitatively predicting the fatigue lives of notched components. However, it is worth noting the tradeoffs of notch plasticity on crack initiation and growth from a qualitative perspective. In a flawless system, the presence of plastic strains ahead of a notch can be regarded as the onset of non-recoverable deformation. Such permanent damage can accumulate under cyclic loading at the nano- or micro-scale to result in crack nucleation. For example, in crystalline materials that rely on ductile mechanisms of dislocation motion during yielding, dislocation pile-up at grain boundaries or other inclusions can result in elevated local stresses that can generate microcracking (Callister 2003). These flaws can coalesce into a macroscale crack, increasing the driving force behind crack growth, and promoting its escape from any notch plasticity that would otherwise inhibit its growth.

On the other hand, once a flaw is formed, the presence of notch plasticity can counteract brittle crack growth. Notch plasticity enables local ductility and energy dissipation near a crack tip, reducing the driving force under a given far-field load. Such permanent deformation is akin to crack tip plastic zones in ductile materials, which serves as an intrinsic resistance to crack growth in many metals and polymers (Ritchie 1999). Under constant cyclic displacement, notch plastic zones can cause crack saturation, disabling crack growth (Frost & Dugdale 1957; Dowling

1979a). Overload events that drive up the notch plastic zone size, eventually overtaking the crack and impeding its growth even at longer lengths. However, once cracks escape the transition length, linear elastic driving forces can regain ground. Thus, in the case of crack propagation, the larger notch plastic zone can decrease the probability of cracks escaping into linear elastic regimes, increasing this intrinsic resistance to fatigue-driven failure.

*Elastic-Plastic Fracture Mechanics Approaches to Notch Crack Growth*

Provided the likelihood of small cracks growing into larger notch plastic zones for sharp stress concentrations, several authors have presented elastic-plastic fracture mechanics approaches to more accurately predict growth under yielding (Hammouda & Miller 1979; Dowling & Begley 1976; Haddad & Dowling 1980; Haddad et al. 1978). However, such methods have been applied for a only a few materials due to limitations associated with elastic-plastic driving force derivations under cyclic loading, as discussed in **Section 3.1**. Furthermore, several of these methods have only been evaluated on specific specimen geometries. No record of application of these methods for viscoelastic materials that display significant hysteretic stress-strain cyclic loading exists.

## 4.2 Practice: Notch Effects on UHMWPE Deformation and Fatigue

Recent reports of fractured UHMWPE components from total joint replacements reveal the dangers of stress concentrations in modern designs. As discussed above, there are several theoretical approaches to study the influence of a notch on fatigue crack initiation and propagation, primarily in linear elastic materials. Today, few of these approaches have been adopted in evaluating notch effects on UHMWPE, both under monotonic or cyclic loading. Instead, studies that do examine notch effects in this polymer have been limited to monotonic rupture and stress-life characterizations, neither of which capture crack initiation versus propagation behaviors. Nonetheless, such research does provide some insight into the local notch stress-strain environment for UHMWPE under tensile and compressive loading, as discussed below.

### 4.2.1 Monotonic and Low Cycle Fatigue Behavior of Notched UHMWPE

*Uniaxial Deformation of Notched UHMWPE*

The most robust evaluation of notch behavior in UHMWPE to date has been performed by Sobeiraj and colleagues (Sobieraj et al. 2008a; Sobieraj et al. 2005b; Sobieraj et al. 2013). This body of work presents the evaluation of failure mechanisms in clinically-relevant formulations of UHMWPE under both monotonic rupture and low-cycle stress-controlled loading. Cylindrical dogbone specimens of UHMWPE were evaluated under both loading conditions, and three general geometry conditions were considered: a smooth specimen, a moderate notch ($\boldsymbol{\rho}$ = 0.9

mm, $k_t = 2.1$) and a deep notch ($\rho = 0.45$ mm, $k_t = 2.7$). Material cohorts evaluated include virgin UHMWPE, conventional, gamma sterilized (30 kGy) UHMWPE, moderately crosslinked (65 kGy) annealed or remelted UHMPWE, and highly crosslinked (100 kGy) annealed, sequentially annealed or remelted UHMWPE.

Monotonic testing found that in general, notches increased the yield strength of the material (called “notch strengthening”) and decreased its ultimate tensile strength (called “notch hardening”) relative to smooth specimens (**Figure 4.15**). In addition, increasing the notch severity enhanced these trends. The authors suggest that higher yield strength most likely results from triaxiality of stresses that exist near the notch tip (Sobieraj et al. 2005b; Sobieraj et al. 2013). Such triaxiality limits uniaxial alignment of lamellae structures, delaying the onset of crystal slip and eventual plastic deformation that takes place in smooth specimens (**Chapter 1**, **Figure 1.5**). Heat treatments appeared to impact yield properties much more than irradiation, most likely due changes in crystalline size associated with annealing and remelting (**Figure 4.15A**). Such changes in crystal geometry directly impact lamellae slip during yield. As expected, annealed materials generated a greater increase in yield strength in comparison to remelted materials, provided their larger lamellae size and increased resistance to alignment under deformation.

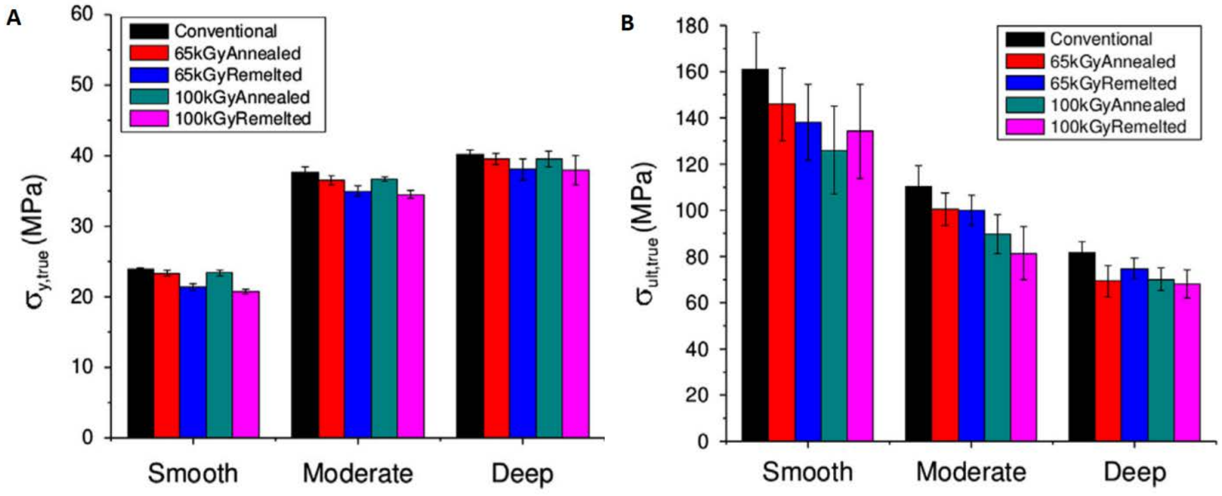

**Figure 4.15 |** Summary of (**A**) yield and (**B**) ultimate strength data for notched cylindrical specimens of five UHMWPE formulations. Notching results in an increases in yield strength, but a decrease in ultimate tensile strength (Sobieraj et al. 2013).

All formulations of UHMWPE saw a reduction in ultimate properties with notching (**Figure 4.15B**). Both virgin and conventional UHMWPE displayed the most ductility compared to crosslinked and heat treated materials for notched configurations (Sobieraj et al. 2005b; Sobieraj et al. 2013). Sobeiraj et al. argued that increased crosslinking in the amorphous regions limited stretching and disentanglement within the polymer’s plastic regime, and contributed to lower ultimate properties as compared to non-crosslinked formulations.

Fouad (2010) presented a similar experimental analysis of the uniaxial tensile behavior of notched UHMWPE (untreated GUR 1020), this time exploring four notch geometries (radii = 1, 2, 4 and 8 mm) in comparison with smooth specimens. Results demonstrated similar trends to that seen by Sobeiraj et al., with increasing notch severity leading to an increase in true yield strength, and a decrease in true ultimate strength and strain (**Figure 4.16**). Like Sobeiraj, Fouad attributes this notch strengthening and decreased ultimate properties with local triaxial stresses ahead of the notch that inhibit lamellar rotation. Fouad noted that true ultimate stress for notches with a radius of 4 mm or less were nearly the same, demonstrating a 60% drop compared to smooth specimens. As seen in **Figure 4.16A**, smooth specimens achieve higher ultimate properties due to a final strain hardening behavior that results from chain alignment and stretching; the more severe notch geometries truncate this unraveling, reaching a critical stress that the tangled chains can no longer sustain. This effect is most dramatic when observing the fracture strain as a function of notch radius (**Figure 4.16B**).

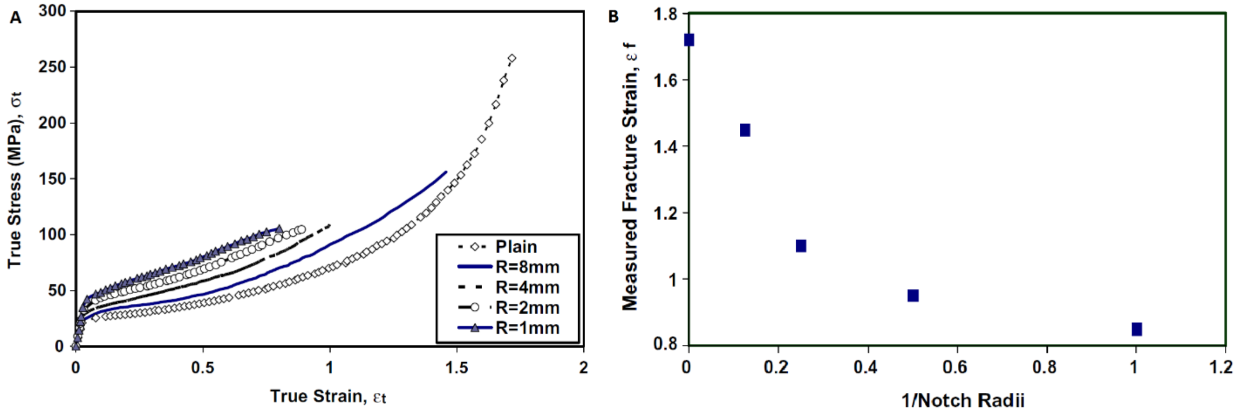

**Figure 4.16** | (**A)** True stress strain data for untreated UHMWPE (GUR 1020), exhibiting the influence that notches (R = radius) can have on yield and ultimate properties. (**B**) The fracture strain as a function of notch radii. (Fouad 2010a)

The lack of chain alignment in notched specimens was also supported by Fouad's observations of specimens near fracture: smooth specimens whitened and then became translucent near fracture, while notched specimens only demonstrated whitening near the gauge length. Furthermore, Fouad utilized differential scanning calorimetry (DSC) to measure crystallinity in deformed and undeformed specimens of both smooth and notched cohorts. Crystallinity was found to decrease upon deformation for smooth specimens by 6%, attributed to chain slip, lamellae break down and disentanglement that occurs during tensile deformation. Notched specimens saw a 9% increase in local crystallinity, however; Fouad attributes this to the inhibition of the aforementioned tensile deformation mechanisms.

Fractography of monotonic specimens by Sobeiraj et al. (2005, 2008) revealed distinctions between crack initiation sites of smooth versus notched specimens. Smooth specimens consistently demonstrated flaw initiation near a microvoid, followed by a region of slow crack growth and eventual fast fracture (**Figure 4.17A**). On the other hand, crack initiation in notched specimens tended to occur at a random internal site or near the notch tip, followed immediately by fast fracture (**Figure 4.17 B,C**). Fouad recorded fracture initiation at the specimen edge for both unnotched and notched geometries. However, like Sobieraj et al., he does note a shift from "semi-ductile" to "semi-brittle" fracture mechanisms, with notched samples demonstrating less fibrillation and a more smooth surface (Fouad 2010a).

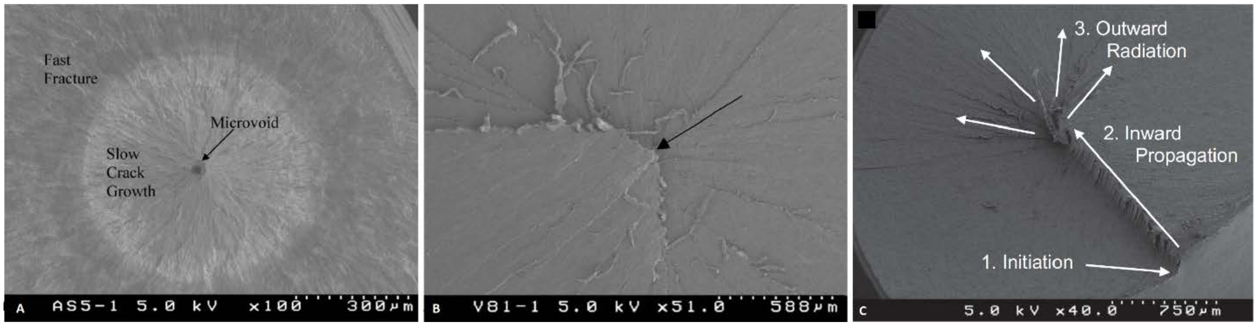

**Figure 4.17 |** SEM images of fracture surfaces for tensile-tested cylindrical dogbones including: (**A**) a smooth specimen (highly crosslinked and remelted) exhibiting a two-stage fracture pattern initiating from a microvoid; (**B**) a moderately notched specimen (formulation not specified) exhibiting fast fracture from a random internal site; and (**C**) a moderately notched specimen (highly crosslinked and sequentially annealed) demonstrating initiation near the exterior notch tip, following by internal propagation and outward fast fracture. (Sobieraj et al. 2005a; Sobieraj et al. 2008a)

*Notch Fatigue of UHMWPE*

In conjunction with their monotonic tensile specimen work, Sobeiraj and colleagues also present the only known notch fatigue evaluation of clinically-relevant formulations of UHMWPE (Sobieraj et al. 2013). Using the moderate and deep notch geometries described above, the authors performed a low cycle fatigue evaluation stress-life evaluation of cylindrical dogbones specimens in a 37° PBS bath. All specimens were cycled under tension-tension loading at a stress ratio of R = 0.04-0.05. Testing was stopped either when the specimen fractured or when it reached run-out (>250,000 cycles). Fatigue data was mapped by the Basquin relationship (**eq. 3.15**), and results are shown in **Table 4.2**.

**Table 4.2 |** Summary of SN fatigue data obtained for various UHMWPE formulations. Values listed for **A** and **b** refer to Basquin equation fitting constants (Sobieraj et al. 2013). *(XL = crosslinked)*

| **Material** | **Geometry** | **# Samples** | **Runout Samples** | **Stress Levels** | **$R^2$** | **A [MPa]** | **b** |
|---|---|---|---|---|---|---|---|
| Conventional (30 kGy) | Moderate | 29 | 0 | 6 | 0.863 | 16.17 | -0.038 |
| | Deep | 27 | 1 | 6 | 0.804 | 16.31 | -0.037 |
| Moderately XL (65 kGy) Annealed | Moderate | 32 | 2 | 5 | 0.432 | 14.19 | -0.021 |
| | Deep | 31 | 2 | 5 | 0.536 | 13.84 | -0.020 |
| Moderately XL (65 kGy) Remelted | Moderate | 45 | 10 | 10 | 0.387 | 13.69 | -0.017 |
| | Deep | 36 | 4 | 7 | 0.445 | 13.79 | -0.023 |
| Highly XL (100 kGy) Annealed | Moderate | 44 | 10 | 9 | 0.543 | 14.38 | -0.019 |
| | Deep | 38 | 3 | 7 | 0.588 | 15.38 | -0.029 |
| Highly XL (100 kGy) Remelted | Moderate | 48 | 6 | 9 | 0.280 | 14.19 | -0.022 |
| | Deep | 35 | 2 | 9 | 0.579 | 13.47 | -0.019 |

As seen in the above table, the study included an impressive cohort of 365 samples spread across the material cohorts of conventional, moderately crosslinked annealed, moderately crosslinked remelted, highly crosslinked annealed or highly crosslinked remelted UHMWPE. Even with this large body of data, statistical trends were incredibly difficult to obtain; $R^2$ correlation values ranged from as low as 0.280 to 0.863, and were highest for conventional materials (**Figure 4.18**). As a result, few significant statistical differences were found between datasets. Sobeiraj and colleagues do note that conventional UHMWPE had higher *A* intercept and *b* slope values than all other materials, consistent with previous smooth specimen fatigue studies which show crosslinking dosage to positively correlate with increased resistance to crack initiation (Medel et al. 2007; Baker et al. 2003).

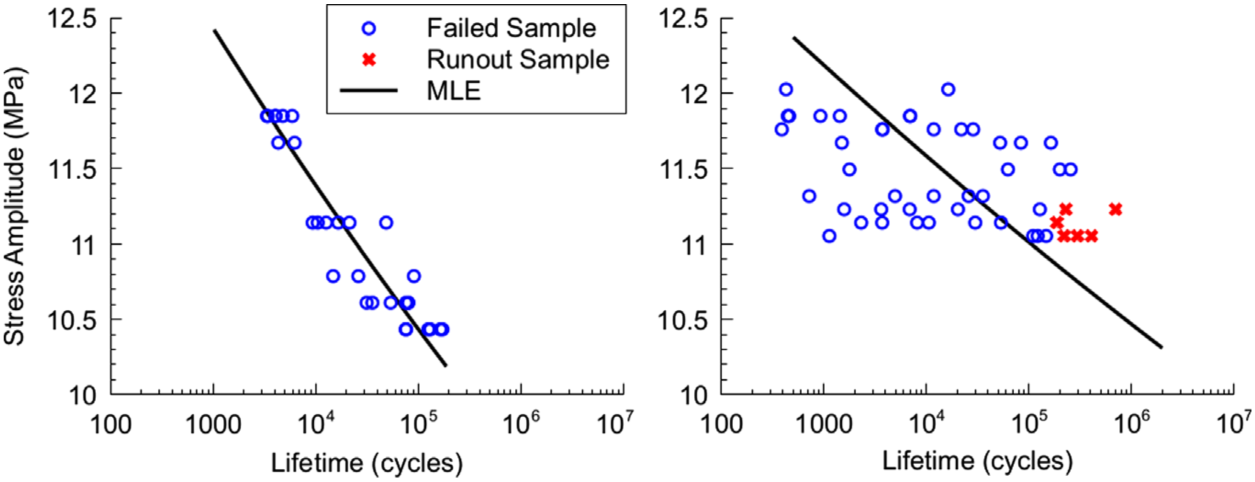

**Figure 4.18 |** Representative stress-life plots for moderately notched samples of conventional UHMWPE ($R^2$ = 0.86) (LEFT) and highly crosslinked (100kGy) remelted UHMWPE ($R^2$ = 0.28) (RIGHT).

The high degree of scatter does highlight the limitations of stress-life analysis in comparing notch fatigue behavior in different formulations of UHMWPE. Sobeiraj and colleagues suggest that such scatter in the crosslinked samples is due to this polymer's higher sensitivity to machining flaws used in the notching procedure. This argument is consistent with fatigue crack propagation studies for smooth specimens, which do predict faster fatigue crack growth for crosslinked samples compared to virgin materials (Atwood et al. 2011; Baker et al. 1999b). Even with such low scatter, the authors used maximum likelihood estimation (MLE) to find a significant difference between moderate and deep notch geometries in all material cohorts except the moderately crosslinked and remelted material. As seen with the data in **Table 2.2**, differences in notch severity do not appear consistent across material types, which may also be due to the relatively close values of $k_t$ used in this assessment. Furthermore, the analytical and statistical assessment of fatigue data used in this study has been called into question (Pascual et al. 2012).

### 4.2.2 Cyclic Compression, Compression-Tension & Crack Initiation

*In vivo* loading of joint replacements can encompass multiaxial cyclic stresses leading to both compressive and tensile stresses near a stress concentration (**Chapter 2**). Many fatigue evaluations of UHMWPE primarily focus on tensile loading, as Mode I crack loading is often presumed to be the greatest driver of crack growth. When evaluating crack initiation and growth ahead of notches, compressive cyclic loading should also be considered due to the generation of residual tensile stresses away from the crack tip (Pruitt & Suresh 1993; Suresh 1998). The role of such residual tensile stress on the initiation of propagation Mode I cracks has been demonstrated for several polymers (Pruitt & Suresh 1993; Pruitt et al. 1992; Pruitt & Suresh 1994), including UHMWPE.

Pruitt and colleagues (1995) performed fully compression and compression-tension cyclic loading on GUR 415 UHMWPE with a notch root radius of 0.144 mm. The authors demonstrated that both loading conditions resulted in crack initiation, though cracks saturated after roughly 200,000 cycles to lengths of 0.06 to 0.21 mm. Under compressive loading, the final crack saturation length demonstrated a linear correlation with increasing load ratio for $R \geq 25$. Compression-tension loading also resulted in crack saturation lengths of 0.09 to 0.12 mm. Similar work by Baker et al. (Baker 2000) for GUR 4150HP UHMWPE specimens that were untreated, sterilized and/or aged under various conditions demonstrated similar saturation crack lengths under a compressive load ratio of $\boldsymbol{R} = 30$. The authors also found that final saturation lengths were longer when testing took place in 37°C compared to room temperature. All specimens in this study contained a notch root radius of 0.127 mm.

The above studies demonstrate that compression and compression-tension loading in UHMWPE can lead to the generation of flaw sizes that have been documented on retrieved implants (Furmanski, Kraay, et al. 2011). The saturation of these cracks in the laboratory is most likely associated with crack closure effects that accumulate as cracks lengthen and exhaustion of the residual tensile field. Thus, tensile loading is also needed to propagate flaws *in vivo*. While the above studies are limited to very small notch sizes (<0.15 mm), they demonstrate that both compressive and tensile stresses near notches may be detrimental to UHMWPE fatigue strength.

### 4.2.3 Static Loading & Crack Initiation: A Viscoelastic Approach

UHWMPE crack initiation under static and fatigue loading have been evaluated using both elastic plastic fracture mechanics (EPFM) and LEFM, respectively (Baker et al. 2003; Medel et al. 2007; A. Gomoll et al. 2002; Rimnac et al. 1988; Steven M. Kurtz et al. 1998). However, these studies have been limited to crack initiation from a sharp (<0.15 mm) notch, and moreover, have not taken the viscoelastic properties of UHMWPE into account. Sirimamilla and colleagues (2013) considered such time-dependent behavior using a viscoelastic fracture theory developed by Williams (1977). This theory utilizes the elastic-plastic $\boldsymbol{J}$ parameter to describe crack initiation time ($\boldsymbol{t_i}$) and crack propagation velocity ($\boldsymbol{da/dt}$):

$$t_i = A\left(\frac{J_o}{J_c}\right)^{-m} \qquad \textbf{eq. 4.20}$$

$$\frac{da}{dt} = Q\left(\frac{J_o}{J_c}\right)^{m+1} \qquad \textbf{eq. 4.21}$$

Here, $m$ is a time-dependent exponent (lower $m$ implies greater time dependence), $A$ and $Q$ are material constants, $J_o$ is the energy release rate for a blunt notch immediately after application of a load, and $J_c$ is the critical energy release rate for crack initiation.

Using the above theory, the authors investigated crack initiation in blunt round CT specimens for a single radius of 0.25 mm in two highly crosslinked (65 kGy or 100 kGy) and remelted UHMWPE formulations. $J_o$ was determined using a 2D plane strain finite element model with a Three Network Model (TNM) that was calibrated using both creep and monotonic strain-to-failure tests (Sirimamilla et al. 2013; Furmanski, Sirimamilla, et al. 2011). Time to crack initiation as well as mechanisms of crack initiation (multi-layered or single-layered) were recorded by video camera (**Figure 4.19**). If multi-layered, the distance between initiation points was recorded as $\delta$.

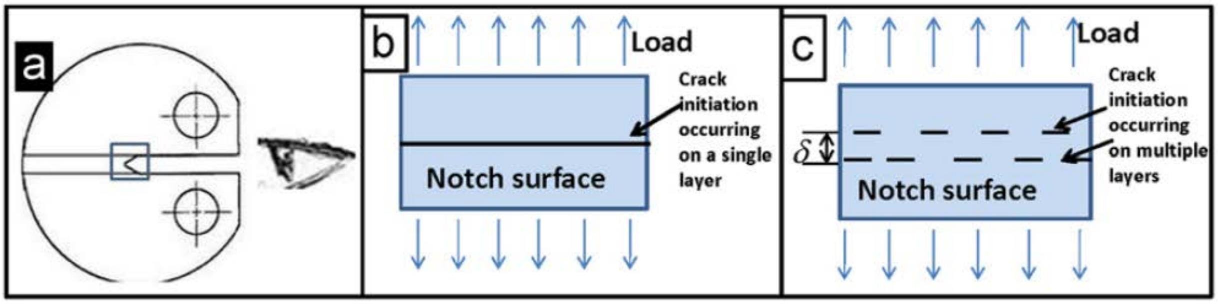

**Figure 4.19 |** Schematic illustrating how crack initiation was recorded using a camera viewing crack formation from the front to determine if it initiated on a single layer (b) or multiple layers at a distance $\delta$ (c). (Sirimamilla et al. 2013)

The authors found that multi-layered crack initiation tended to dominate the initiation mechanism for all samples. Furthermore, a greater $\delta$ resulted in a longer $t_i$ (**Figure 4.20A**). Specimens irradiated with 100 kGy were harder to initiate than those with 65 kGy, having both a larger initiation time as well as a higher ratio of initiation time to time-to-failure. Crack growth velocity after initiation, however, was faster for 100 kGy specimens (**Figure 4.20B**).

Findings from this study demonstrated consistency with previous analysis of both fatigue crack initiation (Baker et al. 2003; Medel et al. 2007) and fatigue crack propagation (Atwood et al. 2011; Baker et al. 1999b): In general crosslinking appear to improve resistance to crack initiation under static loading, while it diminishes resistance to crack propagation. The occurrence of multilayered initiation demonstrates that notches may distribute stresses evenly near the notch tip, resulting in an increased likelihood of crack inception, but also an increased time to initiation if occurring at multiple locations. Sirimamilla and colleagues did note that instances of single-layered initiation primarily occurred near the side-grooves machined on the samples to encourage an even crack front. This highlights the sensitivity of crack initiation to high stress concentrations, as might be present due to manufacturing defects or tool damage incurred during implantation.

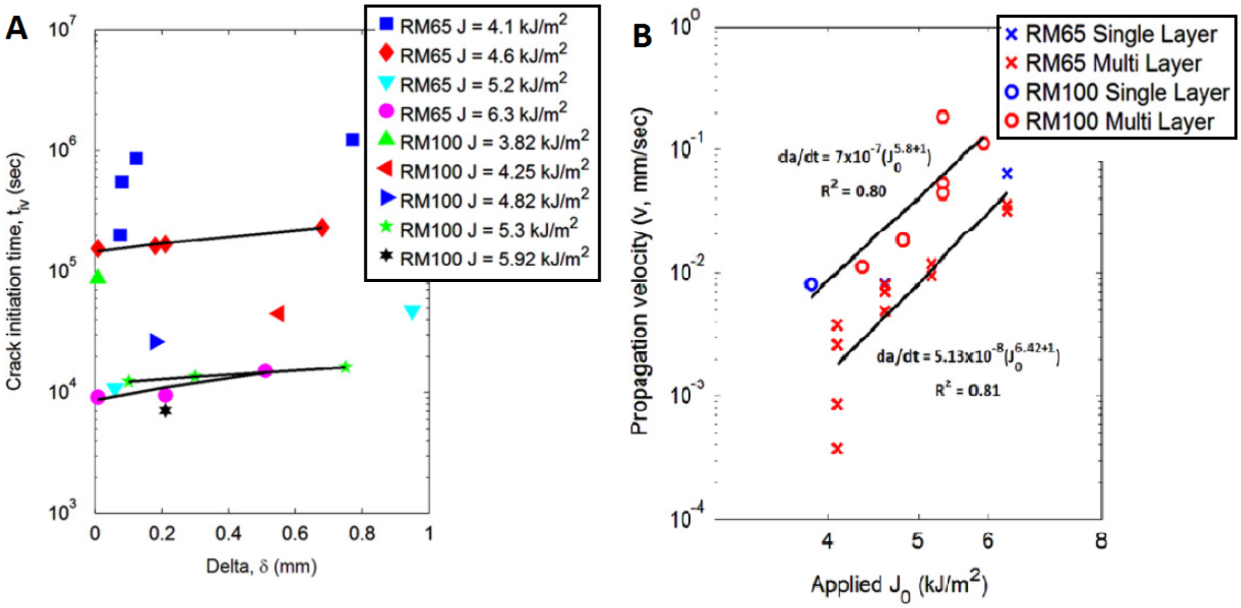

**Figure 4.20 |** Summary of crack initiation (**A**) and propagation (**B**) behavior for crack initiation studies. The time for crack initiation to occur increases as the spacing between multiple initiation points (*δ*) increased. Crack speed was faster in 100 kGy materials compared to 65 kGy materials. *RM = Remelted* (Sirimamilla et al. 2013)

While only a limited number of single-layered specimens were noted, crack velocity in these specimens were noted to be greater than multi-layered specimens tested at the same $J_o$. Video analysis of crack initiation in these specimens revealed a tortuous crack front as a result of crack "jumping" between each crack initiation site. This leads to local mode III tearing, which the authors associated with the diamond pattern seen on fracture surfaces for both monotonic and fatigue specimens (Sirimamilla et al. 2013).

To date, Sirimamilla and colleagues present the only analysis of blunt notch specimens using a viscoelastic approach. The importance of viscoelasticity in UHMWPE crack growth has been established in previous fatigue studies (Furmanski & Pruitt 2007b; Furmanski & Rimnac 2011). Sirimamilla et al. demonstrate that when considering creep mechanisms, trends in crack initiation and propagation for crosslinked samples are consistent with previous studies (Atwood et al. 2011; Baker et al. 1999b). The propensity toward multi-layered crack initiation presents a novel crack initiation resistance mechanism for UHMWPE not previously detected for specimens under cyclic loading. However, more studies are needed to understand whether this multi-layered initiation is present for all formulations of UHMWPE, including non-crosslinked specimens or those that have not undergone post-irradiation heat treatment. Furthermore, the authors only evaluated a single notch geometry (radius of 0.25 mm) under tensile loading in this study. Provided the wide variation in both notch shapes and loading conditions hip and knee components, continued assessment of notch effects under both monotonic and cyclic loading for several geometries is needed.

### 4.2.4 The Case for Continued Notch Fatigue Evaluation of UHMWPE

While studies of notch influence on material fatigue have traversed several decades, evaluation of notch effects on UHMWPE behavior are fairly limited in scope. With the advent of novel UHMWPE formulations, many of which exhibit a certain degree of irradiation crosslinking, a more standardized approach to assessing the notch influence on crack initiation and growth is needed to prevent catastrophic failures that have recently appeared in the literature.

In choosing an appropriate method for this continued study, both previous literature on UHMWPE and theoretical notch theories must be taken into account. Total life approaches to notch fatigue have historically provided a succinct methodology for tabulating notch sensitivity data for various engineering components. However, such data does not exist for UHMWPE, nor is its discovery a trivial task. Smooth specimen stress-life evaluations of UHMWPE have been limited to low cycle fatigue evaluations (Sobieraj et al. 2013) or studies that document life in terms of cycles to yield, as opposed to failure (Medel et al. 2007; Baker et al. 2003). This is primarily due to UHMWPE's impressive versatility when flawless – joint replacement components can and often do survive past $10^9$ cycles of use (Kurtz 2009). Considering that fatigue evaluations are limited in frequency due to hysteretic heating of the polymer, obtaining high cycle fatigue data for smooth and notched specimens presents a costly procedure. Furthermore, as seen with low cycle fatigue stress-life data by Sobeiraj and colleagues (2013), such data presents significant scatter for clinically-relevantformulations of UHMWPE, and thus may not be appropriate for elucidating predictive tools for fatigue.

Instead, fracture mechanics presents a more practical methodology for assessing UHMWPE notch fatigue. Several studies over the past three decades have demonstrated the applicability of LEFM for assessing UHMWPE growth (Connelly et al. 1984; Baker et al. 2000; Bradford et al. 2004; Baker et al. 2003; Atwood et al. 2011; Medel et al. 2007; Ebru Oral, Christensen, et al. 2006; Oral, Malhi, et al. 2008; Pruitt & Bailey 1998a). Moreover, this robust foundation of LEFM work has led to the general acceptance of the stress intensity factor ($K$) a characterizing parameter within the orthopedic field. Efforts to adapt this parameter to fit the challenge of assessing notch fatigue in UHMWPE can facilitate the eventual standardization of future testing used for preclinical evaluation.

For this reason, the following chapter outlines an LEFM-based approach to assess fatigue crack propagation (FCP) in clinically-relevant formulations of UHMWPE. The Dowling (1979a) estimation of short and long crack limiting cases of stress intensity is used, not only due to its simplicity compared to other sources, but also its direct application to square compact tension specimens that have frequently been used for UHMWPE FCP testing (Saxena et al. 1985; Dowling & Wilson 1984). This allows for direct comparison with readily available sharp crack growth data. Furthermore, this method has not been used on any polymeric materials to date, allowing this study to broadly examine its applicability to more ductile materials.

The primary focus on FCP is also based on observations of retrieved components. As documented in studies by Furmanski (2011) and Patterson (2012), cracks can be seen in retrieved devices in as little as 1 month after implantation. These cracks range in size from 0.1 to 0.3 mm, well outside the transition length for a notch radius of 1. As will been seen in the next chapter, UHMWPE components used in joint replacements contain grooves, ledges, fillets, and other design features that range from 0.25 mm to 3 mm in size. Thus, retrieved devices reveal that cracks that coalesce *in vivo* are growing within and beyond a notch-affected zone, and understanding such propagation mechanisms in this region is warranted.

# Chapter 5 – Notch Effects on Crack Propagation in UHMWPE

## 5.1 Introduction

The recent evolution in UHMWPE processing has introduced several microstructural changes that primarily focus on improving the wear and oxidative resistance of this polymer to improve TJR durability. Today, several iterations of UHMWPE exist, led by a new cohort of "gold standards" that are moderately to highly crosslinked (50-100 kGy). These crosslinked formulas are often coupled with a heat treatment above ("remelted") or below ("annealed") the melt temperature, or the blended with an antioxidant (e.g. Vitamin E) to eliminate free radicals and prevent against oxidation. Due to their longer history, many laboratory and clinical studies have concentrated on crosslinked and remelted/annealed formulations, with highly crosslinked and remelted UHMWPE having demonstrated the greatest wear and oxidative resistance (Atwood et al. 2011). However, this material comes with tradeoffs in ultimate tensile strength, ductility, fatigue crack propagation and initiation resistance and toughness (Baker et al. 2003; Baker et al. 2000; Atwood et al. 2011; Pruitt 2005; Kurtz et al. 2002; Sobieraj & Rimnac 2009a; Ries & Pruitt 2005; Urriés et al. 2004; Puértolas et al. 2006). Few recent studies have evaluated crosslinked Vitamin E blended UHMWPE, and found similar trends between reduced FCP and increased irradiation dosage (Oral, Godleski Beckos, et al. 2008; Ebru Oral, Christensen, et al. 2006). The clinical consequences of these reduced mechanical properties has manifested in two ways *in vivo*: fatigue wear (delamination and pitting) seen on many non-conforming bearings (knees, shoulders) and catastrophic fracture emanating from stress concentrations seen in hip and knee UHMWPE components.

This latter mechanism of failure by way of fracture initiating at a stress concentration has been well-documented clinically (see **Chapter 2**); however, most studies investigating fracture have primarily focused on crack behavior without consideration of notch stress fields seen in many components. **Chapter 3** provided an overview of these investigations, demonstrating the usefulness of linear elastic fracture mechanics (LEFM) in assessing relative resistance to fatigue crack propagation (FCP) for various formulations of UHMWPE. In **Chapter 4**, several theoretical approaches to notch fatigue developed for crystalline materials (metals) were presented, many of which use LEFM principles modified to consider local notch stress fields. The following work describes efforts to utilize the theory presented in **Chapter 4** to develop a robust LEFM-based assessment of FCP in clinically-relevant formulations of UHMWPE.

The aim for this chapter is to present computational and experimental work to evaluate notch crack growth under cyclic loading for three relevant materials: virgin UHMWPE (UHMWPE), highly crosslinked and remelted UHMWPE (RXLPE), and highly crosslinked and Vitamin E blended UHMWPE (VXLPE). The latter two materials represent modern-day materials that possess greater resistance to both wear and oxidation. Notched specimens were designed to mimic commercial UHMWPE components used in TJR today. FCP of cracks growing ahead of several notch geometries is presented for all three material groups, using theory examined in **Chapter 4** to appropriately calculate the driving forces behind crack growth. Computational work has been performed to provide insight into the applicability of such theory for UHMWPE, and lay the foundation for any notch fatigue work that may be performed for future iterations of this polymer.

## 5.2 Materials

For both computational and experimental work, three clinically relevant formulations of UHMWPE were chosen to evaluate notch effects on crack growth: virgin UHMWPE (**UHMWPE**), highly crosslinked (75 kGy) and remelted UHMWPE (**RXLPE**), and highly crosslinked (75 kGy) and Vitamin E blended (0.1 wt%) UHMWPE (**VXLPE**). Raw materials were supplied by Orthoplastics (United Kingdom) and were consolidated via compression molding of a GUR 1020 resin.

Material properties for each formulation was obtained from tensile true stress-strain data performed by Cambridge Polymer Group, Inc. (Boston, Massachusetts). Dogbone specimens for each material were machined on a CNC mill as specified in ISO 527-2 (2012). Testing was performed at 30 mm/min and 150 mm/min for N=5 samples of each material. Raw data was processed according to ISO 527-1 (2012) and ASTM D638 (2014) in a custom Matlab code (R2012a, Nattick, Massachusetts) that extracted material properties listed in **Table 5.1**. Representative true stress-strain curves for UHMWPE, RXLPE, and VXLPE are shown in **Figure 5.1**.

**Table 5.1** | Tensile true stress-strain properties for three formulations of UHMWPE (N = 5). Values reported as means and standard deviations, with ranges denoted in parentheses. Statistical significance is noted as numerical superscripts.

| Material Property | Displacement Rate [mm/min] | Virgin UHMWPE **(UHMWPE)** | Crosslinked (75 kGy) & Remelted UHMWPE **(RXLPE)** | Vitamin E (0.1 wt%) Blended & Crosslinked (75 kGy) UHMWPE **(VXLPE)** |
|---|---|---|---|---|
| Modulus [MPa] | 30 | **378 ± 18** $^{2,3}$<br>*(346 - 389)* | **334 ± 8** $^{1,3}$<br>*(325 - 345)* | **460 ± 21** $^{1,2,3}$<br>*(431 - 487)* |
| | 150 | **388 ± 24** $^{3}$<br>*(365 - 424)* | **365 ± 8** $^{3}$<br>*(361 - 378)* | **457 ± 17** $^{1,2,3}$<br>*(431 - 476)* |
| True Yield Strength [MPa] | 30 | **17.8 ± 2.1** $^{2,3}$<br>*(14.5 - 19.6)* | **15.3 ± 1.0** $^{1,3}$<br>*(14.5 - 16.8)* | **20.6 ± 0.7** $^{1,2,3}$<br>*(19.9 - 21.5)* |
| | 150 | **19.5 ± 1.3** $^{3}$<br>*(18.1 - 20.9)* | **17.1 ± 1.9** $^{3}$<br>*(14.8 - 19.6)* | **22.5 ± 0.9** $^{1,2}$<br>*(20.9 - 23.1)* |
| True Yield Strain | 30 | **0.046 ± 0.003**<br>*(0.041 - 0.049)* | **0.045 ± 0.004**<br>*(0.042 - 0.051)* | **0.044 ± 0.002**<br>*(0.04 - 0.046)* |
| | 150 | **0.051 ± 0.004**<br>*(0.044 - 0.055)* | **0.049 ± 0.010**<br>*(0.038 - 0.064)* | **0.049 ± 0.003**<br>*(0.043 - 0.052)* |
| True Ultimate Strength [MPa] | 30 | **183 ± 20** $^{2}$<br>*(156 - 203)* | **130 ± 37** $^{1,3}$<br>*(83 - 172)* | **150 ± 32**<br>*(105 - 191)* |
| | 150 | **187 ± 26** $^{2,3}$<br>*(161 - 226)* | **127 ± 31** $^{1,3}$<br>*(91 - 170)* | **146 ± 19** $^{1,3}$<br>*(118 - 168)* |
| True Ultimate Strain | 30 | **4.0 ± 0.3** $^{2,3}$<br>*(3.5 - 4.3)* | **3.0 ± 0.4** $^{1,3}$<br>*(2.5 - 3.4)* | **3.0 ± 0.3** $^{1,3}$<br>*(2.7 - 3.4)* |
| | 150 | **4.1 ± 0.2** $^{2,3}$<br>*(3.8 - 4.4)* | **2.9 ± 0.3** $^{1,3}$<br>*(2.6 - 3.4)* | **3.0 ± 0.2** $^{1,3}$<br>*(2.7 - 3.3)* |

$^{1}p<0.05$ *vs. UHMWPE;* $^{2}p<0.05$ *vs. RXLPE;* $^{3}p<0.05$ *vs. VXLPE*

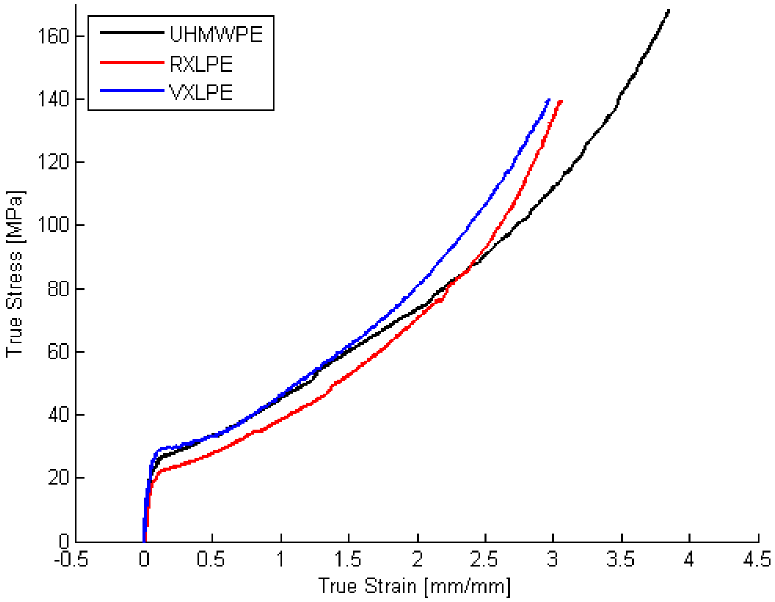

**Figure 5.1 |** True stress-strain data for three UHMWPE formulations, all obtained at 150 mm/min strain rate and in ambient conditions. Crosslinked formulations show greater strain hardening and less ductility (strain at failure) than non-irradiated samples. RXLPE exhibited the lowest yield strength, while VXLPE demonstrated the highest.

Fatigue testing was performed on notched compact tension (CT) specimens shown in **Figure 5.2**. The following dimensions were consistent for all specimens: width, $W$ = 25.4 mm; length, $L$ = 31.75 mm; notch width, $t$ = 3.12 mm; pin-hole diameter, $d$ = 5.334 mm; thickness, $B$ = 8.13 mm. Initial notch lengths were kept consistent at $c_o$ = 8.89 mm, though notch geometries were varied to achieve the following five notch-tip radii ($\rho$): 0.13 mm ("sharp" specimen), 0.75 mm, 1 mm, 2 mm, and 3 mm. The latter four radii were determined from measurements of notch-like features seen on hip acetabular liners and knee tibial inserts from a variety of manufacturers.

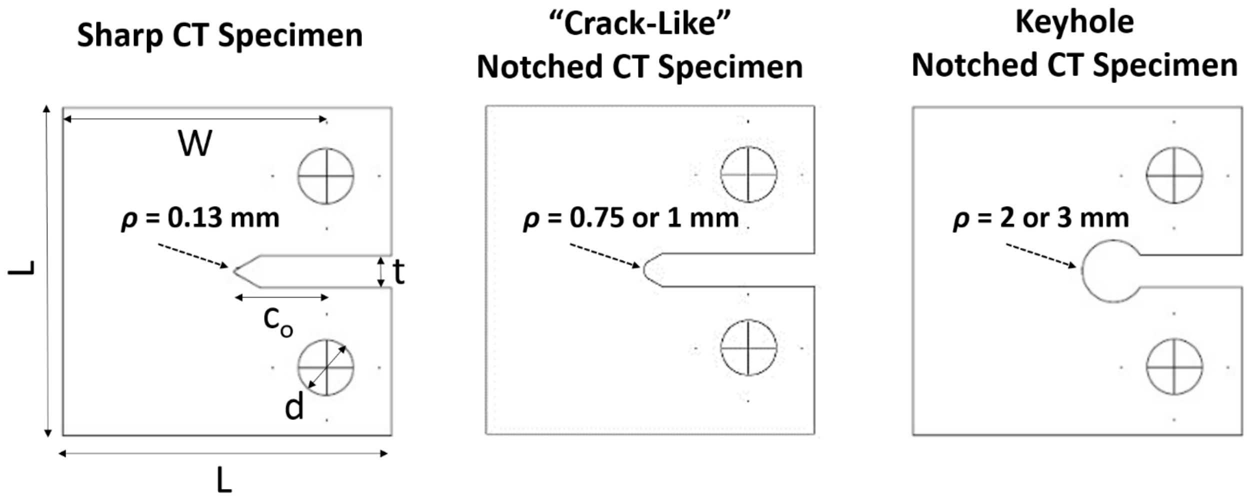

**Figure 5.2 |** CT specimen dimensions used in fatigue analysis, including sharp and notched geometries. Notched specimens included crack-like blunt notch geometries (0.75 mm or 1 mm notch-root radius) and blunt keyhole notch geometries (2 or 3 mm notch-root radius). All other dimensions of the CT specimens were kept consistent, including the length of the notch ($c_o$).

## 5.3 Computational Analysis

### 5.3.1 Methods

Finite element analysis (FEA) was performed on all four notched CT specimens (**Figure 5.2**) using ABAQUS (version 6.12) to calculate three values for each notch geometry: the stress concentration factor ($k_t$), the stress intensity for various crack lengths ($K$), and the notch plastic zone at various loads ($r_p$). True stress-strain data obtained from tensile testing were used to model constitutive behavior for each material (UHMWPE, RXLPE and VXLPE).

Stress concentration factors and stress intensity factors were determined using 2D plain strain models. Each CT specimen was modeled as a half-plane, invoking symmetry conditions (**Figure 5.3A**). Linear elastic material deformation was assumed, and models for the four notched specimens contained 1300 to 4300 8-node quadratic elements, with a biased mesh near the crack tip. To calculate $k_t$, an arbitrary vertical load was applied as a distributed pressure along the top-half of the loading pin-hole and the corresponding peak notch tip stress in the vertical (S22) direction was noted. The global stress was calculated by modeling the top-half of the specimen as a prismatic beam of thickness $B$ and width $W$ undergoing combined tension and bending due to the application of force $P$ at the pin-hole (Dowling & Wilson 1984; Wilson 1974):

$$S = \frac{2P(2W+c)}{B(w-c)^2} \qquad \textbf{eq. 5.1}$$

The same 2D half-plane models were used to determine stress intensity factors for varying crack lengths (**Figure 5.3A, Inset**). Cracks of lengths 0.1 to 6 mm were inserted into each model by relaxing boundary conditions on near-notch tip nodes to allow for 2D movement of the crack face. Corresponding $K$ values were extracted for a constant load at each crack length. Element failure was not modeled; rather, the stress intensity prior to crack advance was recorded.

Notch plastic zones were determined using 3D CT specimen models exhibiting elastic and plastic behavior (uniaxial true stress/strain data) (**Figure 5.3B**). Models of the four notches contained 14000 to 30000 20-node quadratic elements on average, with a biased mesh near the crack tip. A load in the vertical direction was applied, and the Von Mises stresses were compared to the yield strength of each material (**Table 5.1**). Loads varied from 200 to 500 N, reflecting the maximum loads used during experimental evaluation (farfield stress, $S$ = 11 to 27 MPa). The notch plastic zone size was recorded as the distance ahead of the notch root where the Von Mises stresses first exceeds the yield strength. Stress intensity calculations from 2D models were also verified by adding cracks to 3D models and obtaining an average stress intensity value at the near-tip nodes.

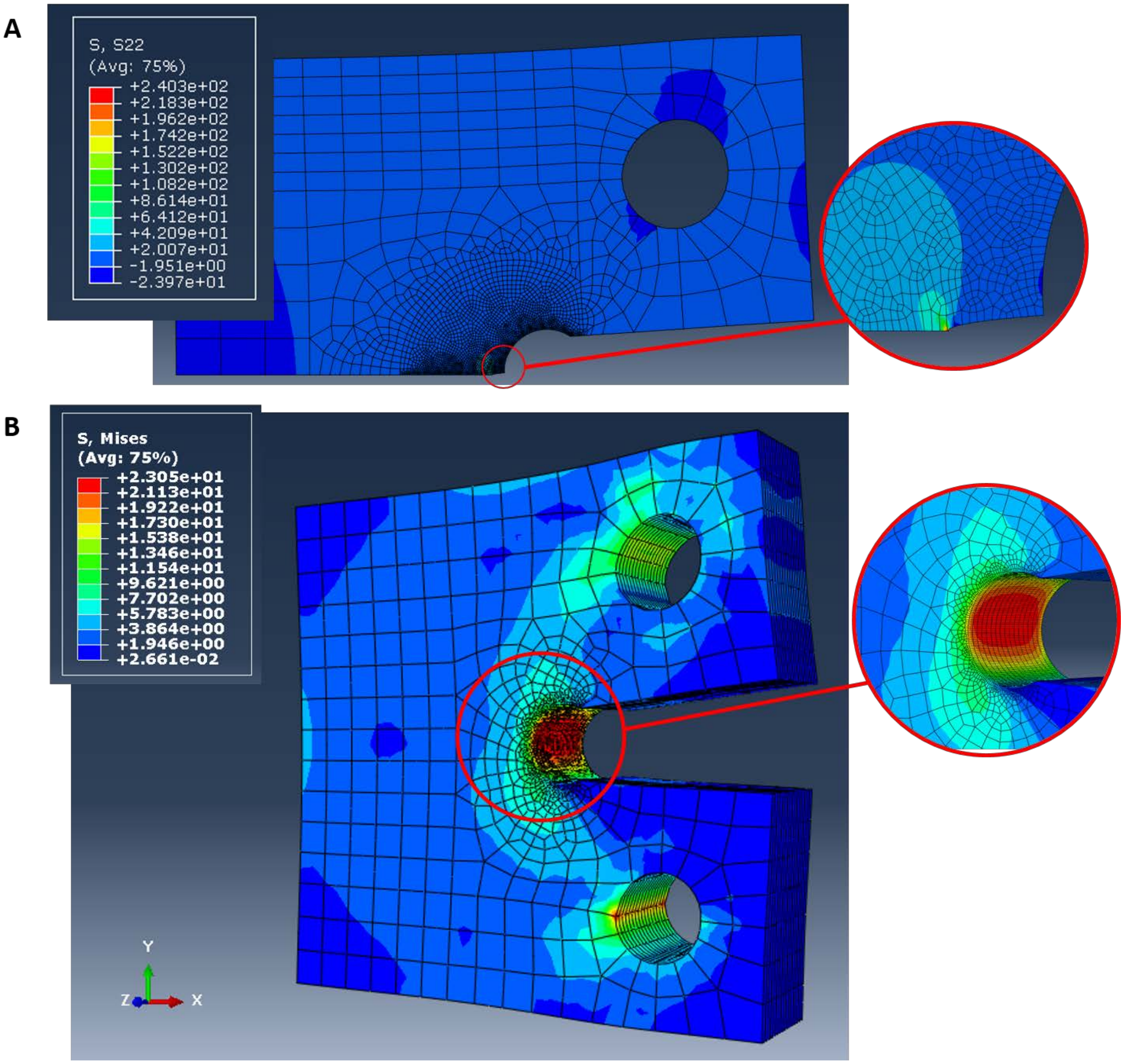

**Figure 5.3** | (A) Plane strain 2D model of half-plane CT specimen with a 2 mm notch root radius and 1 mm crack for the calculation of stress intensity. S22 stresses are perpendicular to the crack plane. (B) Deformed 3D model of full CT specimen with a 2 mm notch root radius. Insert shows notch root Von Mises stresses, which were used to determine the extent of plasticity (notch plastic zone size) in the X direction (along direction of crack growth). All stresses are shown in MPa.

FEA results were compared to analytical approximations for both the stress intensity factor and notch plastic zone for each of the four notch geometries. Expressions for the stress intensity factor of cracks emanating from notches were discussed in **Chapter 4** and reproduced on the next page in **Table 5.2**.

Analytical expressions for estimating the notch plastic zone size at an applied load are shown in **Table 5.3**. This table includes formulas developed to describe the linear elastic stress distribution ahead of notches, as developed by Kujawski (1991), Glinka & Newport (1987), Timoshenko & Goodier (2014), Bhattacharya & Kumar (1995) and Chen & Pan (1978). Stresses were calculated ahead of each notch geometry using these expressions; the distance ahead of the notch at which the stress exceeds the yield strength for each material cohort was recorded as the notch plastic zone size. Note that Dowling's expression for the notch plastic zone size described in **Chapter 4** (**equation 4.19**, **Figure 4.13**) was also included in the comparison, which is originally derived from the Creager & Paris blunt crack elastic stress fields (Dowling 1979a; Creager & Paris 1967).

To contrast the linear elastic stress distributions discussed above and listed in **Table 5.3**, Neuber's Rule (**eq. 4.3**) (Neuber 1946) was also used to estimate the notch plastic zone size while considering the plastic stress/strain response that occurs after yield. Neuber's rule was used in combination with true stress/strain data obtained for each material to extrapolate an adjusted peak stress that considers post-yield deformation. This peak local stress was then inserted into Dowling's notch plastic zone size expression (replacing $k_tS$).

**Table 5.2 |** Summary of expressions for stress intensity (K for all crack lengths OR $K_S$ / $K_L$ for short or long cracks, respectively) developed to describe crack growth emanating from a notch.

| **Reference** | **Stress Intensity Factor ($K_s$)** |
|---|---|
| Dowling (1979a) | $K_s = \sigma_{local}\sqrt{\pi l} = 1.12k_t S\sqrt{\pi l}$ **for $l \leq l^*$**<br>$^{\pm}K_L = FS\sqrt{\pi a} = FS\sqrt{\pi(c_o + l)}$ **for $l > l^*$**<br>$K_s(l^*) = K_L(l^*)$ ***OR*** $l^* = \dfrac{c_o}{\left(\frac{1.12k_t}{F}\right)^2 - 1}$ |
| Schijve (1982) | $K_s = \sigma_{local}\sqrt{\pi l} = Ck_t S\sqrt{\pi l}$ **for $l \leq l^*$**<br>$^{\pm}K_L = FS\sqrt{\pi a} = FS\sqrt{\pi(c_o + l)}$ **for $l > l^*$**<br>$K_s(l^*) = K_L(l^*)$ ***OR*** $l^* = \dfrac{c_o}{\left(\frac{Ck_t}{F}\right)^2 - 1}$<br>$C = 1.1215 - 3.21\left(\frac{l}{\rho}\right) + 5.16\left(\frac{l}{\rho}\right)^{1.5} - 3.73\left(\frac{l}{\rho}\right)^2 + 1.14\left(\frac{l}{\rho}\right)^{2.5}$ |
| Smith & Miller (1977, 1978) | $K_s = \left[1 + 7.69\sqrt{c_o/\rho}\,\right]^{1/2} S\sqrt{\pi l}$ **for $l < 0.13\sqrt{c_o\rho}$**<br>$^{\pm}K_L = S\sqrt{\pi a} = S\sqrt{\pi(c_o + l)}$ **for $l \geq 0.13\sqrt{c_o\rho}$** |
| Kujawski (1991) | $K = \sigma_{local}\sqrt{\pi l} = Qf\,\frac{k_t S}{2}\left[\left(1 + 2\frac{l}{\rho}\right)^{-\frac{1}{2}} + \left(1 + 2\frac{l}{\rho}\right)^{-3/2}\right]\sqrt{\pi l}$<br>$f = 1$ **for $x/\rho < 0.2$**<br>$f = 1 + \frac{\tan(\pi/2k_t)}{2.8}\left(\frac{x}{\rho} - 0.2\right)$ **for $x/\rho \geq 0.2$**<br>$Q$ = 1.22 for a through-thickness crack |
| Lukas & Klesnil (1978); Lukas (1987) | $K = \sigma_{local}\sqrt{\pi l} = \dfrac{Fk_t}{\sqrt{1 + 4.5(l/\rho)}} S\sqrt{\pi l}$ |
| El Haddad (1979) | $K = \sigma\sqrt{\pi(l + l_0)},\ l_0 = \frac{1}{\pi}(\Delta K_{Th}/\Delta\sigma_e)^2$ |

$^{\pm}K_L$ formula for compact tension specimen geometry shown in **eq. 5.9** (Tada et al. 1985).

$\boldsymbol{\rho}$ = notch root radius
$\boldsymbol{S}$ = farfield stress
$\boldsymbol{k_t}$ = stress concentration factor
$\boldsymbol{l}$ = crack length emanating from notch
$\boldsymbol{c_o}$ = notch depth
**F** = specimen geometry factor (Tada et al. 1985)
$\boldsymbol{\Delta K_{Th}}$ = sharp crack threshold cyclic stress intensity
$\boldsymbol{\Delta\sigma_e}$ = smooth specimen endurance limit

$\boldsymbol{l^*}$ = transition length between long crack ($\boldsymbol{K_L}$) and short crack ($\boldsymbol{K_s}$) approximations
$\boldsymbol{Q}$ = shape factor, as found in (Creager & Paris 1967)

**Table 5.3 |** Summary of expressions for the notch plastic zone size ($r_p$). Note that this includes expressions for stress distributions, which are then compared to the yield strength, as well as analytical expression derived from blunt crack stress intensity approximations (Dowling, 1979a).

| **Reference** | **Notch Plastic Zone Size ($r_p$)** |
|---|---|
| Kujawski (1991) | $\sigma_{yy} = f\frac{k_t S}{2}\left[\left(1+2\frac{l}{\rho}\right)^{-\frac{1}{2}} + \left(1+2\frac{l}{\rho}\right)^{-3/2}\right]$<br>$f = 1$ **for $x/\rho$ < 0.2**<br>$f = 1 + \frac{\tan(\pi/2k_t)}{2.8}\left(\frac{x}{\rho} - 0.2\right)$ **for $x/\rho \geq 0.2$**<br>$r_p = x(\sigma_{yy} \cong \sigma_{yield})$ |
| Glinka & Newport (1987) | $\sigma_{yy} = k_t S\left[\left(1 - 0.235\left(\frac{x}{\rho}\right)^{\frac{1}{2}}\right) - 1.22\left(\frac{x}{\rho}\right) + 1.28\left(\frac{x}{\rho}\right)^{\frac{3}{2}} - 0.337\left(\frac{x}{\rho}\right)^{2}\right]$<br>$r_p = x(\sigma_{yy} \cong \sigma_{yield})$ |
| Usami (1985) | $\sigma_{yy} = \frac{k_t S}{3}\left[1 + \frac{1}{2}\left(1+\frac{x}{\rho}\right)^{-2} + \frac{3}{2}\left(1+\frac{x}{\rho}\right)^{-4}\right]$<br>$r_p = x(\sigma_{yy} \cong \sigma_{yield})$ |
| Timoshenko & Goodier (1951) | $\sigma_{yy} = S\left[1 + \frac{1}{2}\left(1+\frac{x}{2}\right)^{-2} + \frac{3}{2}\left(1+\frac{x}{2}\right)^{-4}\right]$<br>$r_p = x(\sigma_{yy} \cong \sigma_{yield})$ |
| Chen & Pan (1978) | $\sigma_{yy} = k_t S\sqrt{\frac{\rho}{\rho+8x}}$<br>$r_p = x(\sigma_{yy} \cong \sigma_{yield})$ |
| Bhattacharya & Kumar (1995) | $\sigma_{yy} = k_t S\sqrt{\frac{\rho}{\rho+4x}}$ and $0 \leq x \leq \frac{\rho}{4}({k_t}^2 - 1)$<br>$r_p = x(\sigma_{yy} \cong \sigma_{yield})$ |
| Dowling (1979a) | $r_p = \rho\left(\left(\frac{k_t S}{\sigma_{yield}}\right)^{2/3} - 1\right)$ |
| Neuber (1946) | $r_p = \rho\left(\left(\frac{k_t^* S}{\sigma_{yield}}\right)^{2/3} - 1\right)$<br>$k_t^* = \sqrt{k_\sigma k_\varepsilon} = \frac{\sqrt{\sigma\varepsilon E}}{S}$ (see **Chapter 4**, **eqs. 4.3, 4.10**) |
| $\boldsymbol{\rho}$ = notch root radius<br>$\boldsymbol{S}$ = farfield stress<br>$\boldsymbol{k_t}$ = stress concentration factor<br>$\boldsymbol{k_t^*}$ = Neuber's stress concentration factor<br>$\boldsymbol{x}$ = distance ahead of notch tip | $\boldsymbol{\sigma_{yield}}$ = yield strength<br>$\boldsymbol{E}$ = Young's modulus<br>$\boldsymbol{\sigma}$ = true stress<br>$\boldsymbol{\varepsilon}$ = true strain |

### 5.3.2 Results

*Stress Concentration Factor*

Stress concentration factors for each notched CT specimen are listed in **Table 5.4**. Values were consistent with those calculated using stress intensity estimations (Dowling & Wilson 1984).

**Table 5.4 |** Linear elastic stress concentration factors ($k_t$) as determined through FEA.

| **Notch Root Radius** | 0.75 mm | 1 mm | 2 mm | 3 mm |
|---|---|---|---|---|
| **Stress Concentration Factor ($k_t$)** | 3.80 | 3.32 | 2.40 | 2.01 |

*Stress Intensity Factor*

**Figure 5.4** shows stress intensity factor plots as a function of crack length for all four notched CT specimens. Analytical solutions presented in **Table 5.2** are compared with this FEA results. The solutions can be divided into two categories: (1) those that combine "short" and "long" crack limiting cases to approximation the true solution and (2) those that capture the changing stress intensity in a single expression. Note that the approach developed by El Haddad (1979) was not included in this comparison since it requires a material-specific characterizing length parameter ($l_o$) that has not yet been obtained for UHMWPE.

For all five expressions and the FEA solution, it is clear that the stress intensity transitions from a fast-rising exponential curve near the notch tip to a more stable relationship with the crack length as the crack extends away from the notch tip. The transition length ($l^*$) where the near-notch $K$ value plateaus to "long crack" behavior is highlighted for each approximation in the curves in **Figure 5.4** and **Table 5.5**. These values were calculated for expressions developed by Dowling (1979a), Schijve (1980), and Smith & Miller (1977, 1978) by the following condition:

$$K_S(l^*) = K_L(l^*) \qquad \textbf{eq. 5.2}$$

The transition lengths for equations presented by Kujawski (1991) and Lukas & Klesnil (1978) were determined where the slope of each stress intensity curve approached zero, such that

$$\frac{dK(l)}{dl} < 0.25 \qquad \textbf{eq. 5.3,}$$

and where the change in slope dropped below a threshold of 2%:

$$\frac{\frac{dK(l+1)}{dl} - \frac{dK(l)}{dl}}{\frac{dK(l)}{dl}} < 0.02 \quad \textbf{eq. 5.4}$$

The transition length can be interpreted as the size of the "notch-affected zone" (Dowling 1979a), or the volume ahead of the notch in which cracks are directly influenced by the local notch stress field (as opposed to bulk specimen stresses, as exists outside the zone). Since each stress intensity expression is a function of $k_t$ or $\rho$, the size of this notch-affected zone depends on the notch geometry. As seen in **Table 5.5**, the values of the notch-affected zone increased with increasing notch root radius. The Dowling approximation consistently predicted the smallest notch-affected zone, while the Schijve approximation predicted the largest.

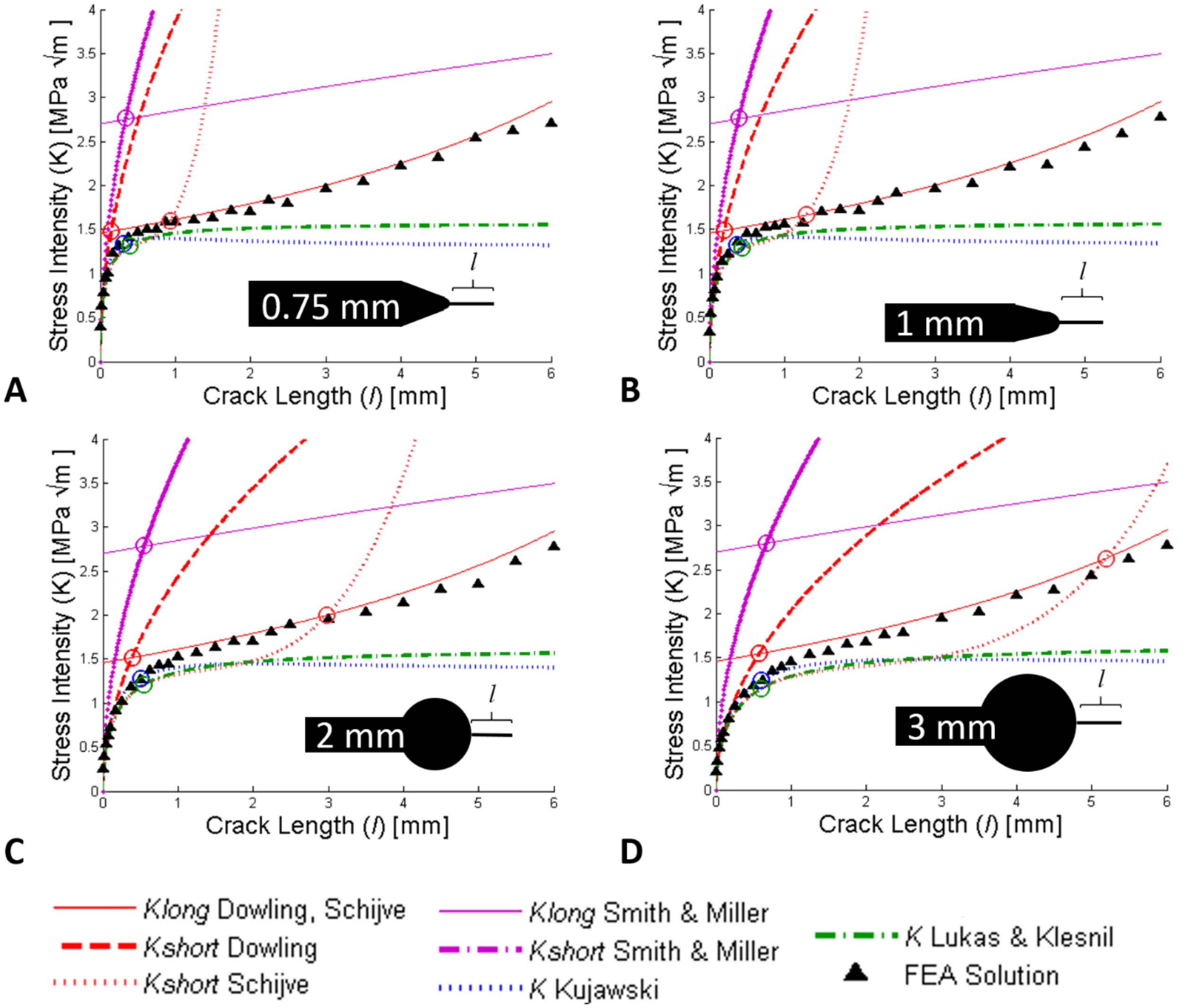

**Figure 5.4 |** Comparison of analytical expressions with FEA solutions for stress intensity of cracks emanating from the four notch-root radii (for CT specimen dimensions shown in **Figure 5.2**). Expressions presented by Smith & Miller (1977, 1978), Dowling (1979a) and Schijve (1980) present unique estimations for short crack stress intensity approximations (dashed red, purple lines), which all transition to long crack limiting cases (solid red, purple lines) as seen in **Table 5.2**. Kujawski (1991) and Lukas & Klesnil (1978) capture this transition in single expression (blue and green dashed lines, respectively). The transition from "short" to "long" crack behavior (i.e. the size of the notch-affected zone, as delineated by the abscissa) are noted by the circular symbols. Crack-like notches are shown in (**A**) and (**B**), while blunt notches are shown in (**C**) and (**D**).

**Table 5.5 |** Size of the notch-affected zone (i.e. "transition lengths") as determined by each stress intensity approximation shown in **Figure 5.4**. All values are listed in millimeters.

| **Notch Root Radius** | **0.75** | **1** | **2** | **3** |
|---|---|---|---|---|
| Dowling (1979a) | 0.15 | 0.20 | 0.39 | 0.59 |
| Schijve (1982) | 0.93 | 1.29 | 2.98 | 5.19 |
| Smith & Miller (1977) | 0.34 | 0.39 | 0.55 | 0.67 |
| Kujawski (1991) | 0.31 | 0.36 | 0.51 | 0.60 |
| Lukas & Klesnil (1978) | 0.39 | 0.44 | 0.54 | 0.60 |

### *Notch Plastic Zone*

**Figure 5.5** shows the notch plastic zone geometry for each notch-root radii for UHMWPE, RXLPE and VXLPE. Each 2D slice was taken along a central XY plane (mid-thickness for each specimen) to view the notch plastic zone under the conditions of plane strain. Images demonstrate general uniformity of the plastic zone for each notch root radius.

**Figure 5.6** compares the notch plastic zone size (measured along the direction of crack extension) for UHMWPE at various maximum loads with previously published analytical solutions for all four notch root radii. (**Appendix A** shows results for all notch geometries and materials, including RXLPE and VXLPE.) Linear elastic analytical solutions were consistently higher than that obtained using FEA, most likely due to overestimation of local stresses that accompanies the use of linear elastic factors, such as $k_t$, when plasticity occurs (**Chapter 4**, **Figure 4.2**). Substituting the $k_tS$ term with peak stresses calculated using Neuber's rule attempts to account for this overestimation, leading to lower predictions of notch plastic zone size; however, as seen in **Figure 5.6**, these grossly underpredict the local plastic zone size.

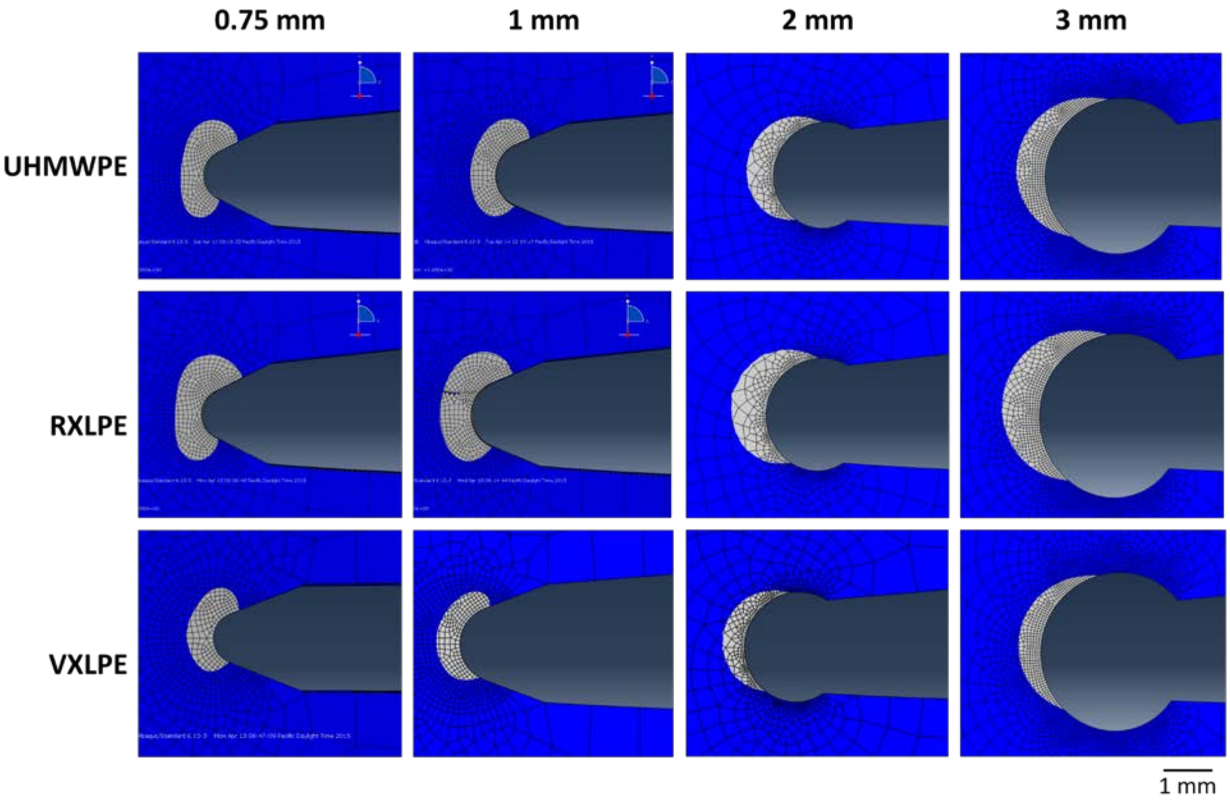

**Figure 5.5 |** Notch plastic zones obtained at a load of 400 N as determined by FEA for UHMWPE, RXLPE and VXLPE. Material elements with a Von Mises stress above the yield strength for each material (**Table 5.1**, 500 mm/min rate) are shown in white, while any elements below yield are shown in blue.

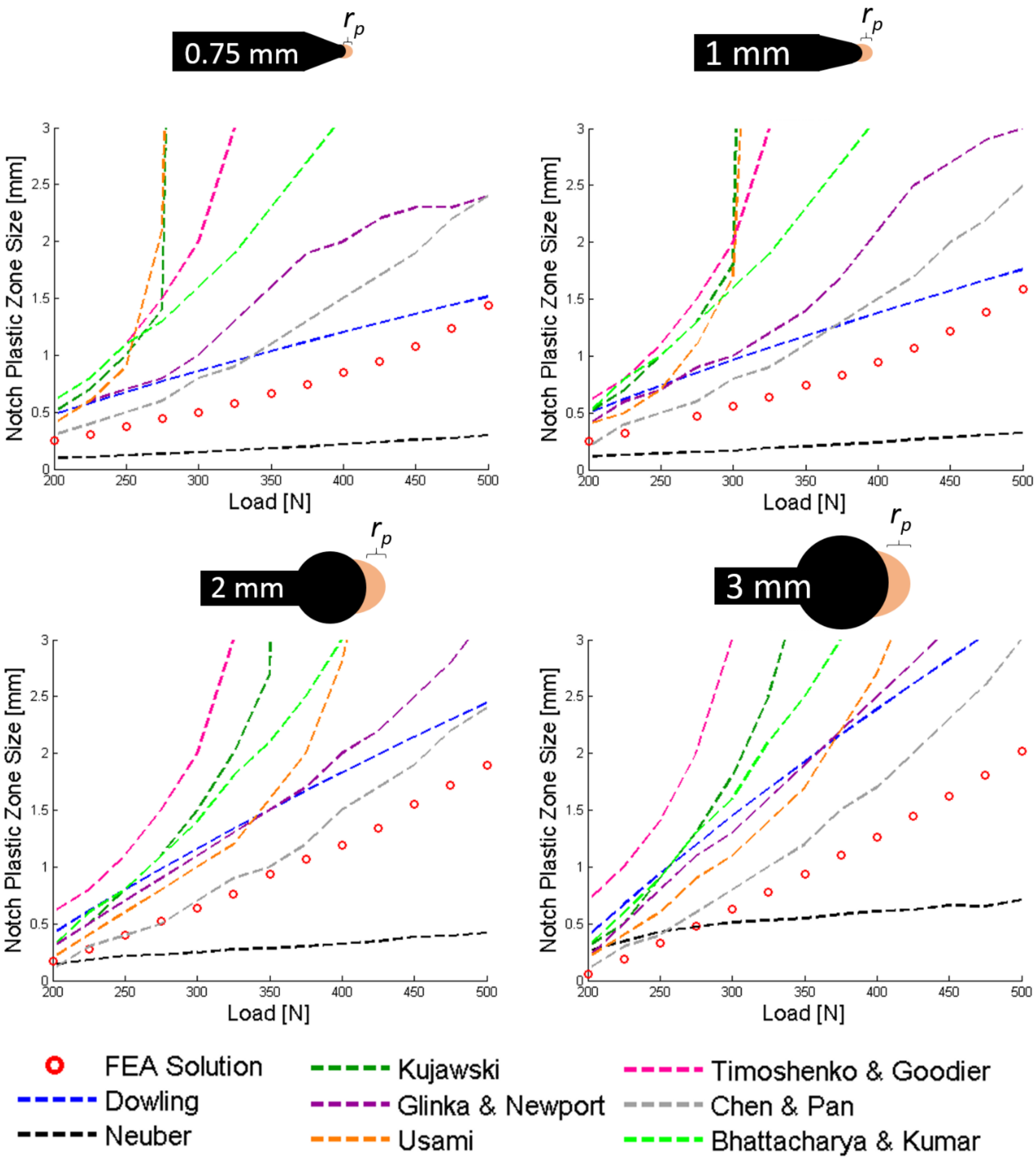

**Figure 5.6 |** Comparison of analytical solutions with FEA results for the notch plastic zone ($r_p$) in UHMWPE as a function of maximum applied load for crack-like notches (0.75 mm and 1 mm, TOP) and keyhole type notches (2 mm and 3 mm, BOTTOM). Most of the analytical expressions overestimate the notch plastic zone, most likely due to the use of linear elastic estimates of stress near the notch tip. Neuber's Rule (1946) was used in combination with Dowling's approximation for the notch plastic zone to account for large strains (and reduced stresses) that accompany plastic deformation in ductile materials, but grossly underestimated the plastic zone size for both notch shapes. These trends also occurred for VXLPE and RXLPE (**Appendix A**).

The FEA solutions presented in **Figure 5.6** and **Appendix A** demonstrated a continuous relationship between the notch plastic zone size ($r_p$) and applied load (and by extension, the farfield stress), allowing for an accurate curve fit using Microsoft Excel. The following second-order polynomial form was used to fit all 12 notch plastic zone curves (4 notch root radii x 3 materials):

$$r_p = ax^2 + bx + c \qquad \textbf{eq. 5.5}$$

Here, $\boldsymbol{x}$ is either the applied tensile load, $\boldsymbol{P}$, or the farfield stress, $\boldsymbol{S}$. **Tables 5.6** and **5.7** displays the values for constants $\boldsymbol{a}$, $\boldsymbol{b}$, and $\boldsymbol{c}$ for each material-notch combination as a function of both $\boldsymbol{P}$ and $\boldsymbol{S}$. An $R^2$ value of 0.99 was achieved for all 24 sets of curve-fitting constants.

**Table 5.6 |** Summary of second-order polynomial constants used to model the notch plastic zone size as a function of applied tensile load (***P***) for the CT specimens shown in **Figure 5.2**. ($R^2 = 0.99$)

| **Material** | **Notch Root Radius, *ρ*** [mm] | **Fitting constants for:** $\boldsymbol{r_p} = a\boldsymbol{P}^2 + b\boldsymbol{P} + c$ | | |
|---|---|---|---|---|
| | | *a* | *b* | *c* |
| **UHMWPE** | 0.75 | 8.0E-06 | -1.5E-03 | 0.24 |
| | 1 | 8.0E-06 | -1.9E-03 | 0.33 |
| | 2 | 6.0E-06 | 1.9E-03 | -0.42 |
| | 3 | 4.0E-06 | 3.4E-03 | -0.79 |
| **RXPLE** | 0.75 | 2.0E-05 | -6.9E-03 | 1.05 |
| | 1 | 2.0E-05 | -7.2E-03 | 1.05 |
| | 2 | 1.0E-05 | 2.0E-04 | -0.21 |
| | 3 | 7.0E-06 | 3.3E-03 | -0.84 |
| **VXPLE** | 0.75 | 5.0E-06 | 2.0E-04 | -0.02 |
| | 1 | 3.0E-06 | 9.0E-04 | -0.14 |
| | 2 | 3.0E-06 | 2.4E-03 | -0.55 |
| | 3 | 5.0E-06 | 2.1E-03 | -0.65 |

**Table 5.7 |** Summary of second-order polynomial constants used to model the notch plastic zone size as a function of applied farfield stress (***S***) for the CT specimens shown in **Figure 5.2**. ($R^2 = 0.99$)

| **Material** | **Notch Root Radius, *ρ*** [mm] | **Fitting constants for:** $\boldsymbol{r_p} = i\boldsymbol{S}^2 + j\boldsymbol{S} + kC$ | | |
|---|---|---|---|---|
| | | *i* | *j* | *k* |
| **UHMWPE** | 0.75 | 2.8 E-03 | -3.6 E-02 | 0.33 |
| | 1 | 2.8 E-03 | -2.7 E-02 | 0.24 |
| | 2 | 1.9 E-03 | 3.5 E-02 | -0.42 |
| | 3 | 1.5 E-03 | 6.3 E-02 | -0.79 |
| **RXPLE** | 0.75 | 6.0 E-03 | -1.3 E-01 | 1.05 |
| | 1 | 7.0 E-03 | -1.3 E-01 | 1.05 |
| | 2 | 4.0 E-03 | 3.6 E-03 | -0.21 |
| | 3 | 2.4 E-03 | 6.1 E-02 | -0.84 |
| **VXPLE** | 0.75 | 1.6 E-03 | 3.3 E-03 | -0.02 |
| | 1 | 1.2 E-03 | 1.6 E-02 | -0.14 |
| | 2 | 1.1 E-03 | 4.5 E-02 | -0.55 |
| | 3 | 1.6 E-03 | 3.9 E-02 | -0.65 |

### 5.3.3 Discussion

*Stress Intensity Factor for Cracks Emanating from Notches*

No single analytical solution provided a completely accurate prediction of stress intensity for all cracks lengths ahead of each of the four blunt-notched CT specimens evaluated. The primary deviation for all expressions occurred near the transition of cracks from near-notch to bulk conditions. Most analyses tended to provide a strong correlation for very short cracks (under 0.5 mm for crack-like notches; under 1 mm for blunt notches), with expressions by Kujawski (1991), Lukas & Klesnil (1978, 1987) and Schijve (1980) presenting the best predictions of the FEA solution of $K$ in this region. Only Dowling (1979a) proposed a solution that reasonably predicts *both* short and long crack stress intensities, but with large deviations near the transition length.

The accuracy of expressions by Schijve, Lukas & Klesnil and Kujawski likely derives from their similar approaches to deriving the stress intensity equation. Both Schijve and Lukas & Klesnil used an analysis by Newman (1971; 1976) in which numerical methods (boundary collocation) are used to assess cracks emanating from an elliptical hole in an infinite sheet under tensile load (Schijve 1982). Schijve uses this analysis in combination with his previous notch stress gradient analysis (Schijve 1980), in which the stress distribution ahead of a notch is shown to be a function of only the peak stress ($k_t S$) and the notch root radius ($\rho$). This latter dependency is taken into account through the geometric factor $C$ (**Table 5.3**). Lukas & Klesnil (1978, 1987) use Newman's data to develop a generalized curve-fit for small cracks emanating from notch, explaining why this expression also presents a close fit to the FEA solution for short crack data. Deviations for this proposed solution tend to occur once the crack escapes the notch-affected zone (i.e. crack lengths longer than the transition length). This is explained by Lukas (1987), who recognized that the range of validity for their expression is limited to small ratios of $l/\rho$ due to the fitting constants used by the authors for Newman's solution. Lukas predicts that for a 2 mm notch shown in **Figure 5.4C** with a $k_t$ of 2.40, the expression for stress intensity would be valid for cracks up to than 1.5 to 2 mm, which is only slightly larger than the transition length.

Kujawski's stress intensity equation demonstrates similar form to that of Lukas & Klesnil, including slightly undershooting the FEA solution for stress intensity. As seen in **Table 5.3**, Kujawski uses a modified local stress expression derived from the elastic stress fields for a blunt crack presented by Creager & Paris (1967). Kujawski compared the results of his stress intensity expression for Newman's solution for cracks emanating from an ellipse (Newman 1976) as well as Nisitani's solution for cracks growing from an edge notch (Nisitani 1978), and similarly found his expression to slightly underpredict numerical solutions for $K$ for long cracks.

Smith & Miller offered a more empirical approach, comparing crack growth in unnotched and notched specimens. They define the "notch effect" as the difference in crack lengths between notched and unnotched specimens for the same instantaneous crack velocity. Looking at variety of notch shapes, the authors derive a single expression for several notch geometries to characterize the notch-affected region as $0.13\sqrt{D\rho}$. This approximation, while effective for the handful of notch geometries evaluated by Smith & Miller, grossly ***K*** for the CT specimens evaluated in this study, as seen in **Figure 5.4**.

Dowling's short and long crack approach provided a good estimate for ***K*** for very short and very long cracks, but deviations of 17-40% from FEA stress intensity solutions occurred near the transition length for the four blunt notch root radii evaluated. Dowling argues that within the notch-affected zone, "short" cracks behave similarly to long cracks emanating from a free surface, driven by a global stress that is equivalent to the peak local stress ($k_tS$) with a free surface correction factor of 1.12 (**Figure 5.7A**). However, as Schijve (1980) notes, two limitations are presented by this interpretation: first, the edge is not in fact a straight line as assumed by Dowling and second, the stress distribution ahead of the notch is not a linearly decreasing function (**Figure 5.7B**). On the other hand, the expression by Schijve appears to overcompensate for this issue for blunt notches, only transitioning to the more accurate long crack approximation at very large transition lengths compared to not only the Dowling approach, but also expressions presented by Kujawski, Smith & Miller, and Lukas & Klesnil (**Figure 5.4**).

Despite deviations seen at the transition length, Dowling's approach presents the only known methodology that has been utilized for LEFM fatigue evaluation of notch crack growth in CT specimens. Saxena and Wilson (1985) utilized this approach to map crack growth in 18Mn-5Cr austenitic steel demonstrating elevated short crack velocities relative to long crack growth at a given $\Delta K$, a phenomenon that has been noted in other materials even when no notch is present (Suresh & Ritchie 1984). The authors confirm that specimen dimensions and crack lengths did not violate LEFM validity, thus eliminating notch plasticity as cause for elevated short crack growth. Saxena and Wilson's work demonstrated the applicability of Dowling's approach in obtaining FCP data for CT specimens in particular. This, combined with the reasonable accuracy of Dowling's equations for both short and long cracks, motivated the use of Dowling's approach for experimental work on UHMWPE, addressed in **Section 5.3**.

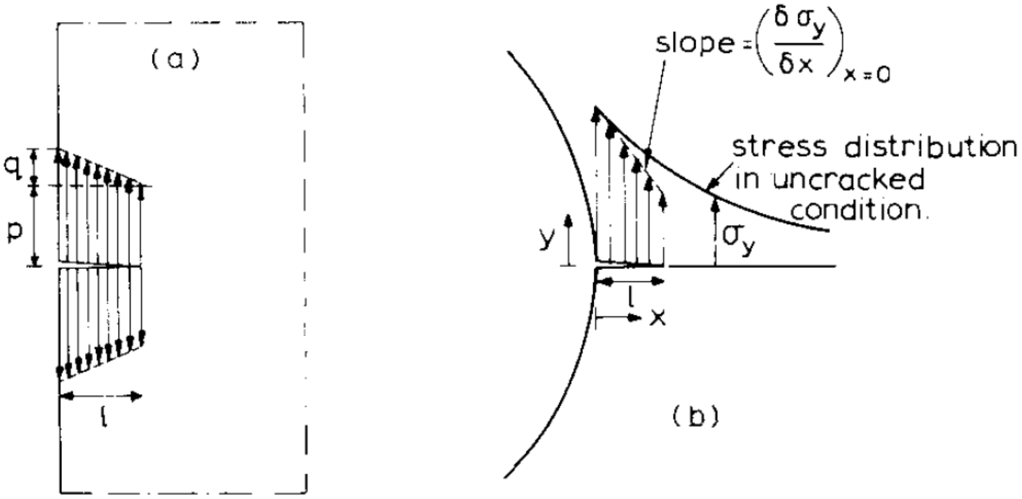

**Figure 5.7 |** Illustration presented by Schivje (1982), demonstrating the limitations in characterizing crack growth from a notch only using a free surface correction factor (A) versus a more detailed notch stress gradient (B).

*Notch Plastic Zone*

For all three materials, none of the analytical expressions evaluated provided an accurate picture of the notch plastic zone, as determined using FEA (**Figure 5.6**). Equations by Dowling (1979a), Kujawski (1991), Usami (1985), Chen & Pan (1978), Timoshenko & Goodier (1951), Bhattachary & Kumar (1995), and Glinka & Newport (1987) primarily use geometric descriptors of the notch to extrapolate a local stress field, and then compare this stress field to a single parameter (yield strength, $\sigma_y$). All seven stress expressions led to an overestimation of the plastic zone size for one or more of the notch geometries evaluated. This is most likely due to the use of linear elastic stress field predictors to estimate local plasticity effects, which can grossly overestimate post-yield stresses (**Figure 4.2, Chapter 4**). For example, Dowling's equation overpredicted the plastic zone size by anywhere from 8% to 500%, with higher deviations existing at lower loads. While the actual plastic zone sizes are small – Dowling predicts a 0.3 mm plastic zone for a 2 mm notch loaded at 200 N, which FEA shows has a 0.1 mm plastic zone – the deviations are significant with respect to short cracks that may initiate at these stress risers. Chen & Pan provided a closer approximation, especially for notch plasticity ahead of 2 mm and 3 mm geometries in VXLPE (**Appendix A**), but again with deviations upward of 50% for sharper, crack-like notch geometries.

Neuber's rule attempted to avoid these deviations by accounting for large increases in strain relative to stress that are characteristic of post-yield material behavior. Using a modified stress concentration factor and directly sampling the true stress-strain curve of the material, a revised local peak stress for each notch geometry at each load was obtained, which was then directly inserted into Dowling's equation for the notch plastic zone size. However, as seen in **Figure 5.6**, this grossly underestimates the plastic zone size for each notch geometry, deviating as much as Dowling's plastic zone prediction. As a result, this attempt at a nonlinear stress/strain estimation of notch plasticity was not deemed appropriate. A more robust characterization of notch plasticity is clearly needed, which better integrates post-yield material properties of UHMWPE. Some approaches for estimating the local notch stress using plasticity parameters such as the Ramberg-Osgood constants do exist (Glinka 1985b; Glinka 1985a), but such constants have not been established for UHMWPE.

Since none of the notch stress field approximations provided a reasonable fit for *all* FEA solutions, a second-order polynomial was fit to the data to ensure the notch plastic zone size was not over- or underestimated for later experimental evaluation. **Tables 5.6** and **5.7** provides a summary of polynomial constants obtained for each material-notch combination as a function of load $\boldsymbol{P}$ or farfield stress $\boldsymbol{S}$, respectively. It should be noted that these constants are specific to the geometry used in this study, as well as the material properties embedded in each FEA model. Furthermore, limitations exist with the FEA solutions in comparison to experimental conditions, with particular regard to loading. Models were loaded with a single tensile load to simulate local stresses and calculate the plasticity ahead of the notch. However, cyclic loading would introduce unloading that would cause local constraint of stretched material near the notch by bulk elastic material in the rest of the specimen. Residual tensile stresses imparted by compression could potentially creater a smaller cyclic notch plastic zone than predicted by the model (Suresh 1998).

However, it is thought that such deviations are minimal compared to the discrepancies between the linear elastic expression listed in **Table 5.3** and the FEA solution, and thus the custom fit data would still provide a better approximation of notch plasticity.

### *Conclusions from Computational Analysis*

The above computational analysis demonstrates that notch geometry (namely, the notch-root radius influences the near-notch tip stress field through both the elastic stress intensity values driving crack growth and the plastic zone generated at a notch. This has direct implications for design of components, especially those with notch radii seen the above work. These radii can directly influence the notch-affected zone, in which cracks are driven by a lower – yet exponentially increasing – stress intensity that directly relates to the peak stresses at the notch ($\boldsymbol{k_t S}$) and the notch root radius ($\boldsymbol{\rho}$). The larger the root radius, the larger this zone, and the higher potential for a reduced crack growth rates due to a lower overall $\Delta \boldsymbol{K}$.

Notch plastic zones that engulf an existing crack can have the opposite effect: plasticity can serve to decrease crack-tip stresses, resulting in a lower driving force than that predicted by LEFM stress intensity factors. The notch plastic zone potentially provides a material with additional intrinsic resistance to crack growth, enhancing the role of a crack-tip plastic zone in increasing energy dissipation and blunting a crack tip (Hammouda & Miller 1979; Ritchie 1999). Under constant cyclic displacement, this can diminish the growth rate and even lead to non-propagating cracks (“crack saturation”), as shown by Hammouda & Miller (1979) and Frost (1960). It is important to note that for short cracks (crack lengths within the notch-affected zone), LEFM validity is called into question when such flaws can be overtaken in size by a notch plastic zone. However, once a crack grows beyond the length of a given notch plastic zone or escapes the notch-affected zone and transitions into a long crack, linear elastic driving forces regain legitimacy and any increased intrinsic resistance to crack propagation created by a notch plastic zone is diminished.

The FEA solution for the notch plastic zone size reveals that an increasing notch-root radius leads to a faster rate of increase of the notch plastic zone size, as seen in **Figure 5.8** below. While sharp, crack-like notches can produce a notch plastic zone at a lower far-field stress due to higher local peak stresses, notch plastic zones ahead of blunt notches rapidly catch up and surpass those for sharper notches at a given load. Such plastic zones have contradictory effects on crack initiation versus crack growth: In the absence of a crack, a larger plastic zone – associated with a larger stressed volume ahead of a blunt notch root (Schijve 1980) – increases the statistical probability of flaw formation through void nucleation, dislocation pile-up, grain boundary dissociation or other typical nano- or micro-scale damage accumulation mechanisms (Ritchie 1999; Kim et al. 1979; Suresh 1998; Callister 2003). Thus, resistance to crack initiation, especially at high cycle fatigue, may be reduced ahead of blunt notches in comparison to sharper geometries, a phenomenon referred to as the “size effect” or “notch sensitivity” (see **Chapter 4**) (Taylor 1999; Schijve 1980). Such reduced resistance to crack nucleation can occur even in the absence of above-yield stresses.

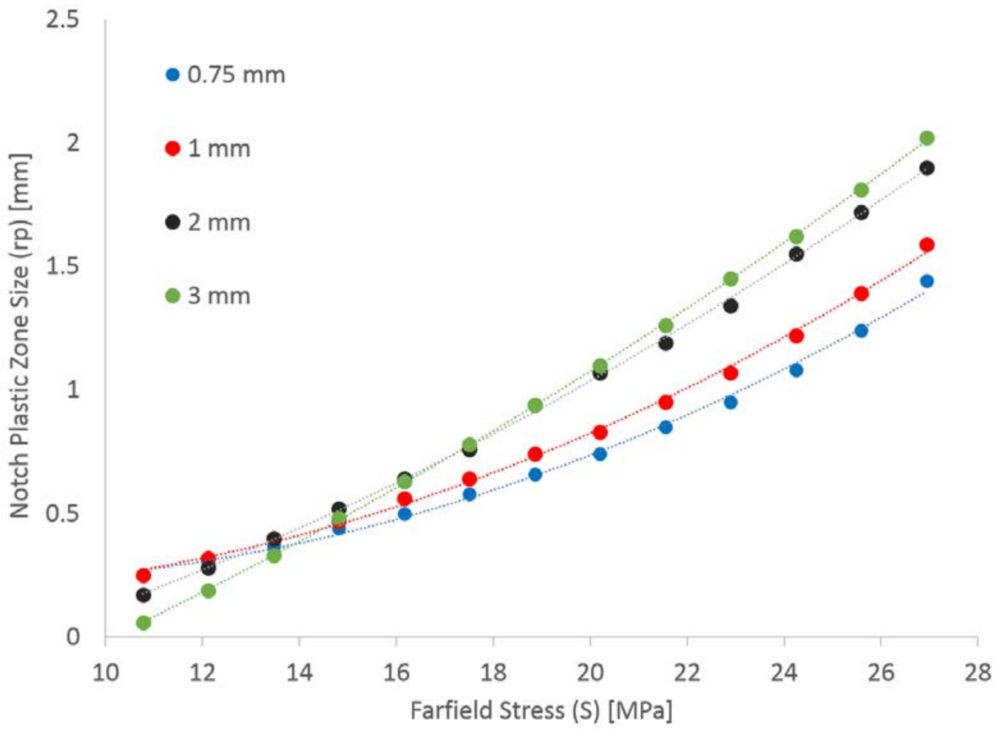

**Figure 5.8 |** The notch plastic zone for the blunt notched CT specimens used in this study as a function of peak applied load for four notch root radii for UHMWPE. Plastic zone sizes were determined using finite element analysis, and show second-order polynomials fit to each data. While plastic zones are generated for sharper crack-like notches at a lower load, blunt notch plastic zones quickly overtake their size at stresses of 15 MPa and above (or a tensile load of 275 N and above), despite having a lower stress concentration factor and peak stress.

Tradeoffs in the effects of notch plasticity on crack behavior are important to consider when evaluating not only component design, but also experimental evaluation of notch effects that solely explore crack initiation or propagation. The following section outlines experimental evaluation of fatigue crack growth in notched specimens of UHMWPE, taking both the elastic and plastic notch stress fields into consideration. Using the analytical approach for both stress intensity presented by Dowling (1979a), fatigue data was collected for short and long cracks in UHMWPE formulations, both within and ahead of a notch plastic zone as predicted using expressions by Chen & Pan (1978).

## 5.4 Fatigue Testing

### 5.4.1 Methods

*Specimen Preparation*

Sharp and notched CT specimens shown in **Figure 5.2** were machined from raw material using a CNC milling machine. Sharp, 0.75 mm and 1 mm notches were machined using a slitting saw in which blade teeth were ground to the specified radius of curvature. The 2 and 3 mm radii were incorporated into the overall CT specimen geometry through a keyhole design. A sharp slitting saw was used to first insert a notch into the specimen, and then a standard drill bit expanded the notch tip to the appropriate radius of 2 or 3 mm, keeping the overall notch length (***$c_o$***) consistent at 8.89 mm.

Before testing, each specimen was hand polished on a flat surface to improve crack visualization using increasing grades of sand paper (600, 800, 1200 and 2400 grit). Datum dots were placed on one side of the specimen for later image analysis. A precrack was inserted at the notch tip using a sharp razor blade under an Olympus SZ40-STB1 stereoscope. Precrack lengths were between 0.1 mm and 1 mm, depending on the transition length for the specimen's notch radius (**Table 5.5**). Precrack lengths on both sides of each CT specified were verified to be within ±10% using an Olympus BH-2 microscope at 10X magnification.

A total of 15 material-notch combinations (3 materials *x* 5 notch radii) were evaluated. At least N=5 samples were tested for each material-notch combination.

*Fatigue Testing Methodology*

To assess crack growth near a notch, the Dowling (1979a) stress intensity approximations were based on previously discussed computational work (**Section 5.2**), and reproduced below for convenience:

$$K_s = 1.12 k_t S \sqrt{\pi l} \qquad \textbf{eq. 5.6}$$

$$K_L = \frac{P}{B\sqrt{W}} f\left(\frac{a}{w}\right)$$

$$where \qquad a = c_O + l$$

$$and \quad f\left(\frac{a}{w}\right) = \frac{(2+\propto)}{(1-\propto)^{1.5}}\left(0.886 - 4.64 \propto - 13.32 \propto^2 - 14.72 \propto^3 - 5.6 \propto^4\right) \qquad \textbf{eq. 5.7}$$

The long crack stress intensity above is found in tabulated form for CT specimens in Tada (1965). Stress concentration factors used in the short crack approximation were obtained from each FEA model, as listed in **Table 5.4**.

The transition length at which the crack driving force transitions from short crack to long crack behavior provides an estimate of the notch elastic stress field, also known as the notch-affected zone. Transition lengths between short and long crack approximations for each notch root radius were determined using Matlab (Nattick, Massachusetts). The value of ***$K_s$*** and ***$K_l$*** at fictitious crack lengths between 0.01 and 2 mm were plotted to find the transition lengths reproduced below in **Table 5.8**.

**Table 5.8 |** Size of the notch-affected zone ("transition length") as a function of notch-root radii, as determined using Dowling (1979a).

| **Notch Root Radius [mm]** | 0.75 | 1 | 2 | 3 |
|---|---|---|---|---|
| **Transition Length [mm]** | 0.15 | 0.20 | 0.39 | 0.59 |

In addition, the size of the notch plastic zone obtained at each maximum load (***$P_{max}$***) was determined using the second-order polynomial fits obtained for each set of FEA data, shown by

**eq. 5.8** and **Table 5.6**, as discussed in **Section 5.2**. If crack lengths were longer than this value at a given load, their growth was assumed to be subject to small scale yielding conditions and were categorized as “elastic”. Crack lengths smaller than the plastic zone at a given load were assumed to be engulfed by the notch plastic zone and their growth was deemed “plastic”. **Figure 5.9** summarizes the categorization of crack growth based on the degree of notch influence.

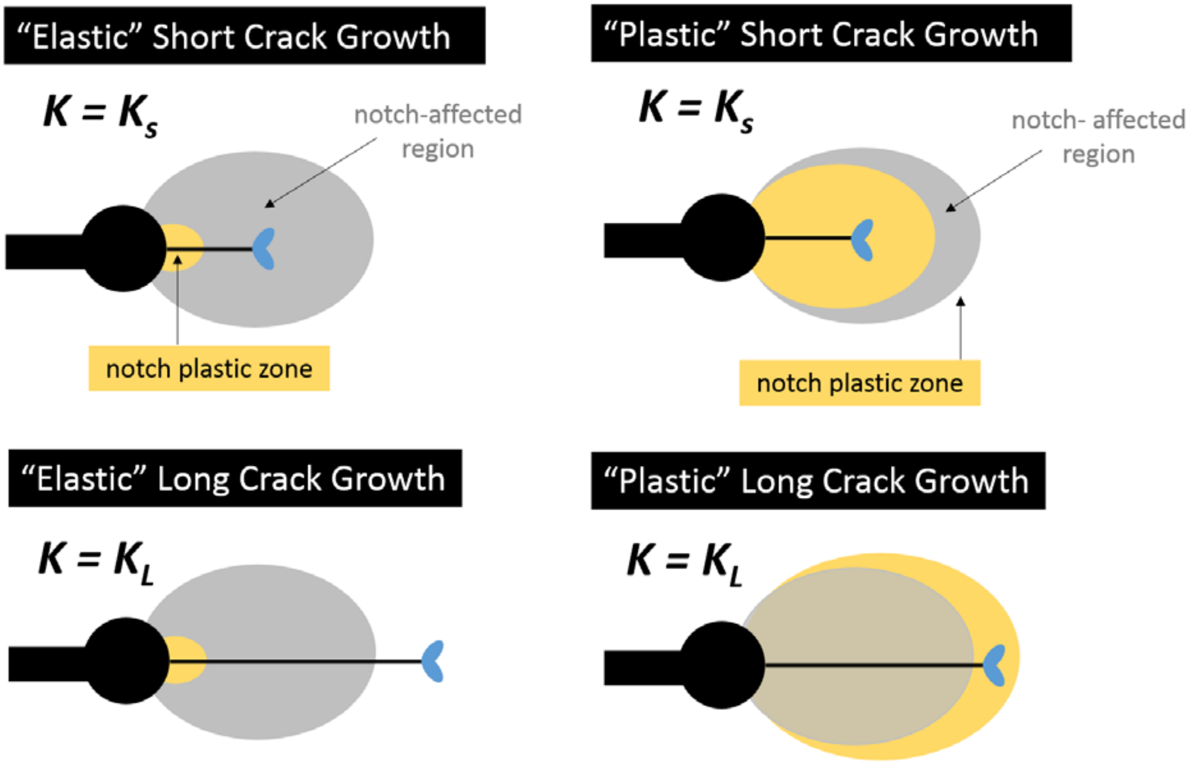

**Figure 5.9 |** Illustration of four categories of crack growth, as would vary with the notch root-radius, the material yield strength, the crack length and applied load. The crack-tip plastic zone is denoted in blue.

To determine the FCP resistance curve for each material, the crack speed was plotted as a function of cyclic stress intensity using the Paris equation (Paris et al. 1961):

$$\frac{da}{dN} = C\Delta K^m \qquad \textbf{eq. 5.8}$$

Note that the cyclic stress intensity (***ΔK***) can either be determined through short or long crack approximations, depending on the crack length relative to the transition length for each notch geometry.

Fatigue testing was performed on a servohydraulic Instron 8871 at room temperature using a sinusoidal wave function at a frequency of 5 Hz. An air gun was directed at the crack tip to minimize hysteretic heating effects (Baker et al. 2003; Baker et al. 2000; Atwood et al. 2011). Tensile-tensile loading was performed at a load ratio of ***R*** = 0.1, with increasing ***ΔP*** (and therefore increasing ***ΔK***). Crack growth was monitored using a Sony XCD-SX910 Camera (Tokyo, Japan) and Infinivar (CFM-2/S) microscope lens under lighting from an AmScope LED ring light. A LabView (version 7.1) program provided autonomous control of the camera to record the crack length at various intervals. Photos were taken at every 5,000, 10,000 or 20,000 cycles, depending on the crack velocity; a minimum change in crack length of 10 microns was needed to ensure detection of crack growth by the camera lens. For lower $\Delta K$ values, this enabled recording for a minimum crack speed of $10^{-6}$ mm/cycle, near previously reported $\Delta K_{incep}$ values for UHMWPE (Baker et al. 2003; Baker et al. 2000). Semi-automatic processing of the crack length images was achieved using ImageJ (v1.47) and Matlab (R2012a) to enable consistent identification for the crack tip using pixel analysis.

### *Fractrography*

Fracture surfaces of CT specimens from each a material cohort (UHMWPE, R-XLPE, V-XLPE) were examined using scanning electron microscopy (SEM) (Hitachi TM-1000, Tokyo, Japan). Each surface was sputter-coated with gold-vanadium to enhance visualization of the surface. Careful attention was paid to where images were taken relative to the start of crack growth to determine if crack was either shorter or longer than the notch plastic zone to delineate “plastic” versus “elastic” growth.

## 5.4.2 Results

### *Fatigue Testing*

**Figure 5.10** shows results from FCP testing of all three formulations for cracks lengths that were longer than the notch plastic zone (deemed “elastic” data, filled symbols) and thus only subject to small-scale yielding (crack-tip plasticity). Within each material cohort, the data from all four notch geometries clearly overlaps with the sharp control data (‘+’ symbols), supporting the notion that notches do not influence the cyclic crack growth once crack lengths exceed the transition length and are experiencing small-scale yielding conditions.

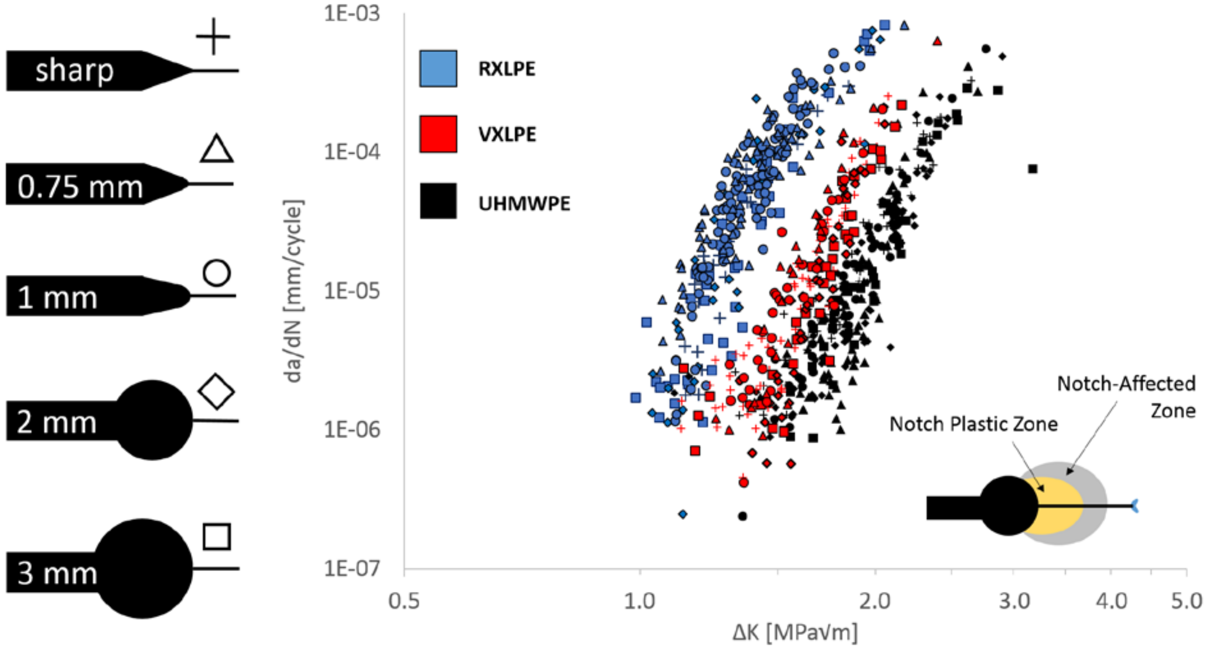

**Figure 5.10 |** FCP data obtained for cracks emanating from various notch geometries, for crack lengths longer than both the notch-affected zone and the notch plastic zone ("elastic" data). Symbol shapes correspond to different notch-root radii, as seen in the illustrative legend to the left of the graph. Colors correspond to each material cohort evaluated (UHMWPE, RXLPE and VXPLE). Notch data overlaps closely with sharp data ('+' symbols on the graph).

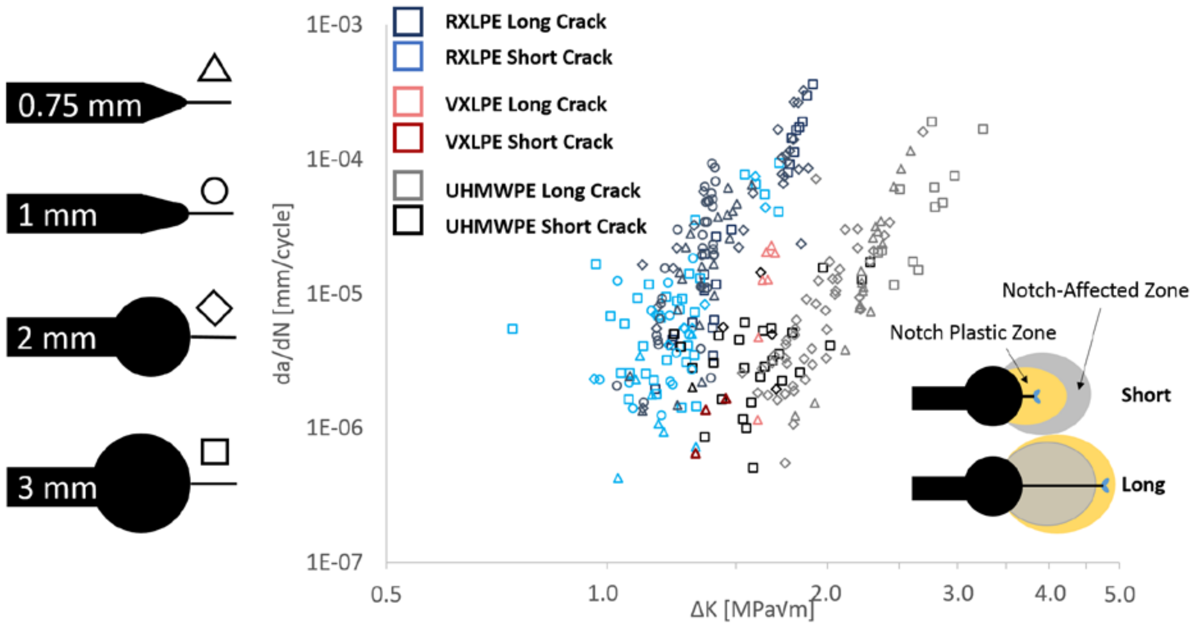

**Figure 5.11 |** FCP data obtained for cracks engulfed within the notch plastic zone, mapped using both short and long crack stress intensities ("plastic" data). Symbol shapes correspond to different notch-root radii, as seen in the illustrative legend to the left of the graph. Colors correspond to each material cohort evaluated (UHMWPE, RXLPE and VXPLE).

Dowling (1979a) suggests that the long "plastic" data shown in **Figure 5.11** should be characterized as "elastic" data, since the total crack length taken in account in **eq. 5.10** includes both the flaw length ($l$) as well as the notch length ($c_o$). **Figure 5.12** shows only long crack "elastic" and "plastic" for all material cohorts. For the RXPLE and UHMWPE datasets – for which more "plastic" data was collected – there appears to be some overlap between both "elastic" and "plastic" long crack data, but with additional scatter. UHMWPE crack growth appears to deviate more for the 3 mm notch-root radius in particular at higher $\Delta K$ values, leading to a slightly shallower Paris slope ($m$). On the other hand, RXLPE exhibits greater deviations for low $\Delta K$ values, shifting the apparent threshold behavior higher. Such discrepancies between "elastic" and "plastic" data call into question Dowling's assumption that notch plasticity effects disappear once cracks transition out of the local notch stress field. As a result, any long "plastic" data will remain characterized as "plastic" (open symbols) to facilitate later discussion.

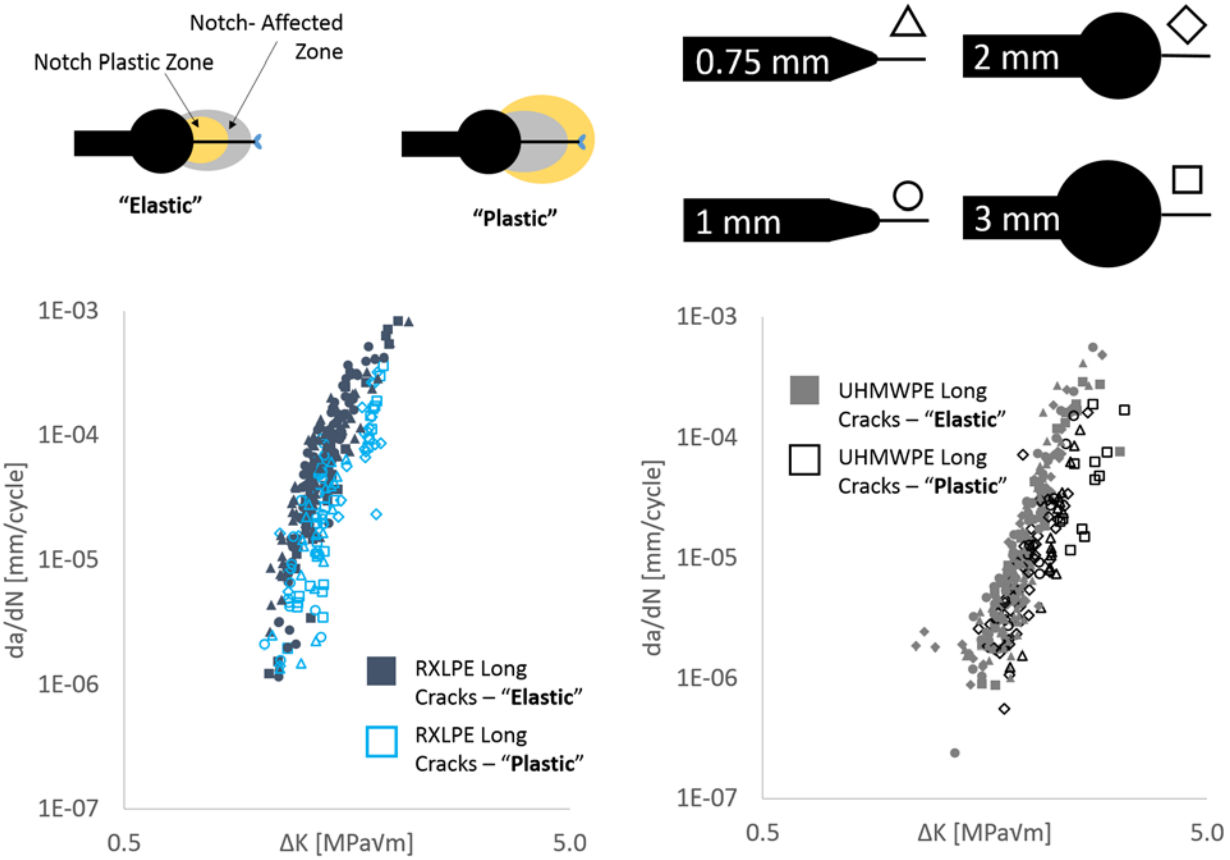

**Figure 5.12 |** FCP data obtained for long cracks, including data outside the notch plastic zone ("elastic", filled symbols) and engulfed in the notch plastic zone ("plastic", open symbols). Symbol shapes correspond to different notch-root radii, as seen in the illustrative legend in the top left.

**Figure 5.13** shows all data collected, overlapping the "elastic" data from **Figure 5.10** and "plastic" data from **Figure 5.11**. It is clear that these datasets reasonably overlap, revealing a trend in FCP performance regarding the three material types: virgin UHMWPE (black) demonstrates the most resistance to FCP, RXLPE (blue) has the least resistance to crack growth, and VXLPE (red) lands between these two formulations.

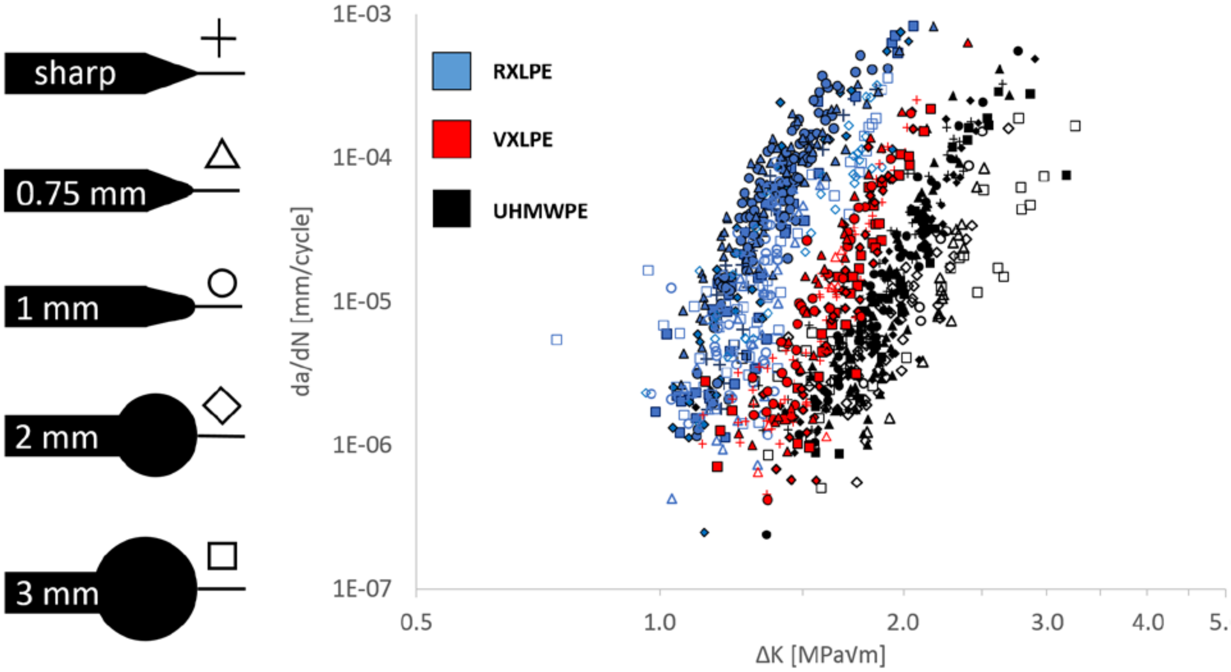

**Figure 5.13 |** All FCP data for cracks emanating from various notch geometries. Symbol shapes correspond to different notch-root radii, as seen in the illustrative legend to the left of the graph. Colors correspond to each material cohort evaluated (UHMWPE, RXLPE and VXPLE). Filled symbols indicated crack growth was measured for cracks growing ahead of any notch plasticity ("elastic" data); open symbols indicate cracks were growing within a notch plastic zone ("plastic" data).

The data in **Figure 5.13** can be broken down into short versus long crack growth for RXPLE and UHMWPE, as seen in **Figure 5.14**. As seen for RXPLE (**Figure 5.14A**), much of the plastic data corresponds to "short cracks" that are less than the transition length. Plastic data for UHMWPE (**Figure 5.14B**) similarly demonstrates preference for "short cracks" as well, and displays more scatter than RXPLE.

To better illustrate the implications of the above fatigue results with regard to cracks growing in RXPLE versus UHMWPE, crack lengths were measured at constant cyclic load for a subset of notch-root radii. **Figure 5.15** shows the results of this assessment for the 3 mm geometry, evaluated at a constant cyclic load of 38-380 N. Note that the starting crack length was below the transition length for a 3 mm notch-root radius, and thus within the notch-affected zone. Furthermore, a maximum load of 380 N generates a notch plastic zone that theoretically engulfs this initial crack length. Despite this, the crack in RXLPE grew faster at the same starting $\Delta K$ than that in UHMWPE, which in contrast demonstrates a steady-state crack length up to 60,000 cycles. Such trends were also seen for 1 mm and 2 mm notch geometries up to 60,000 cycles.

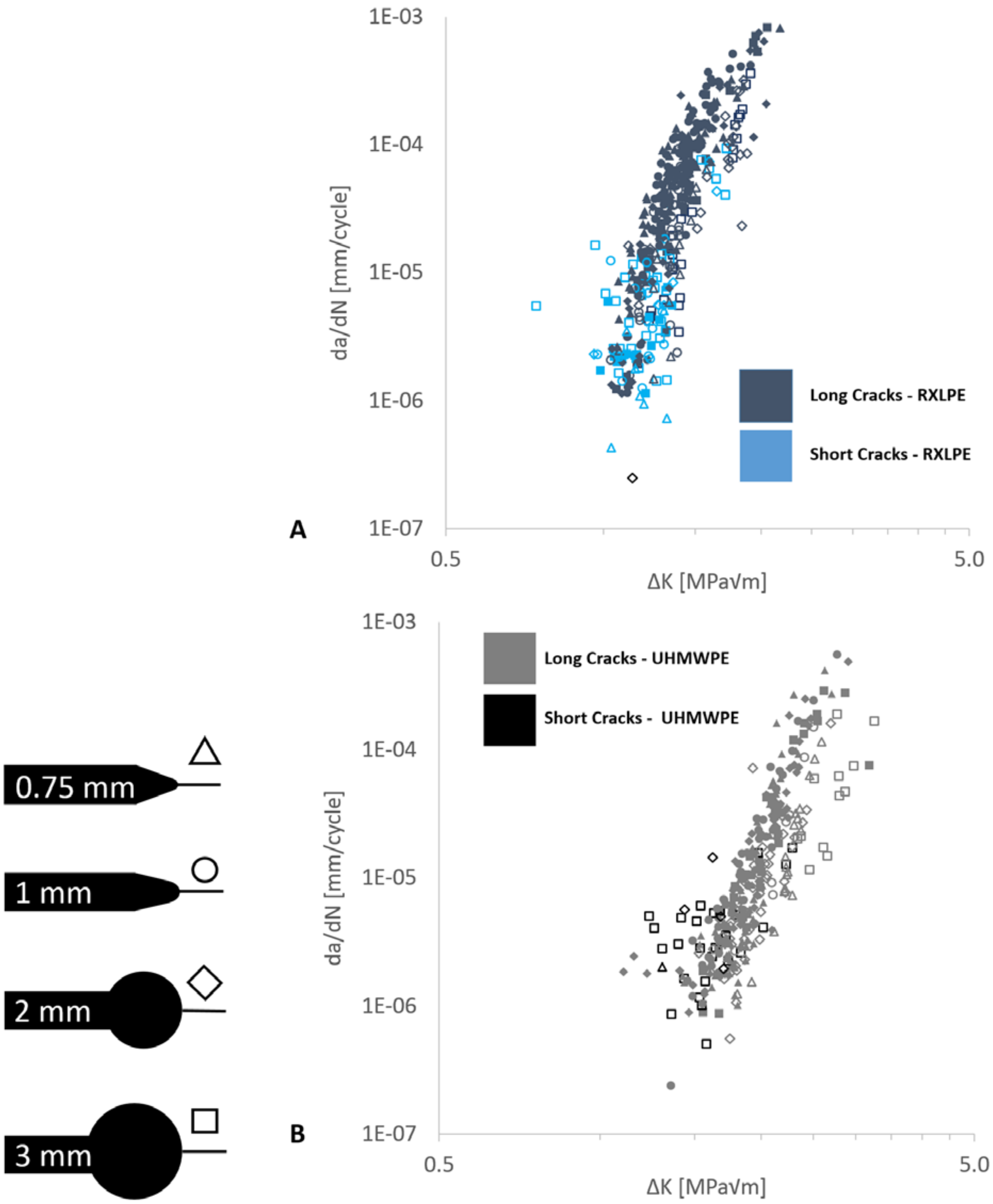

**Figure 5.14** | FCP data delineated by short and long crack growth, i.e. cracks growing within or outside the notch-affected zone, respectively. Data collected for VXLPE only contained long crack growth, and thus was not included. Symbol shapes correspond to different notch-root radii, as seen in the illustrative legend to the left of the graph.

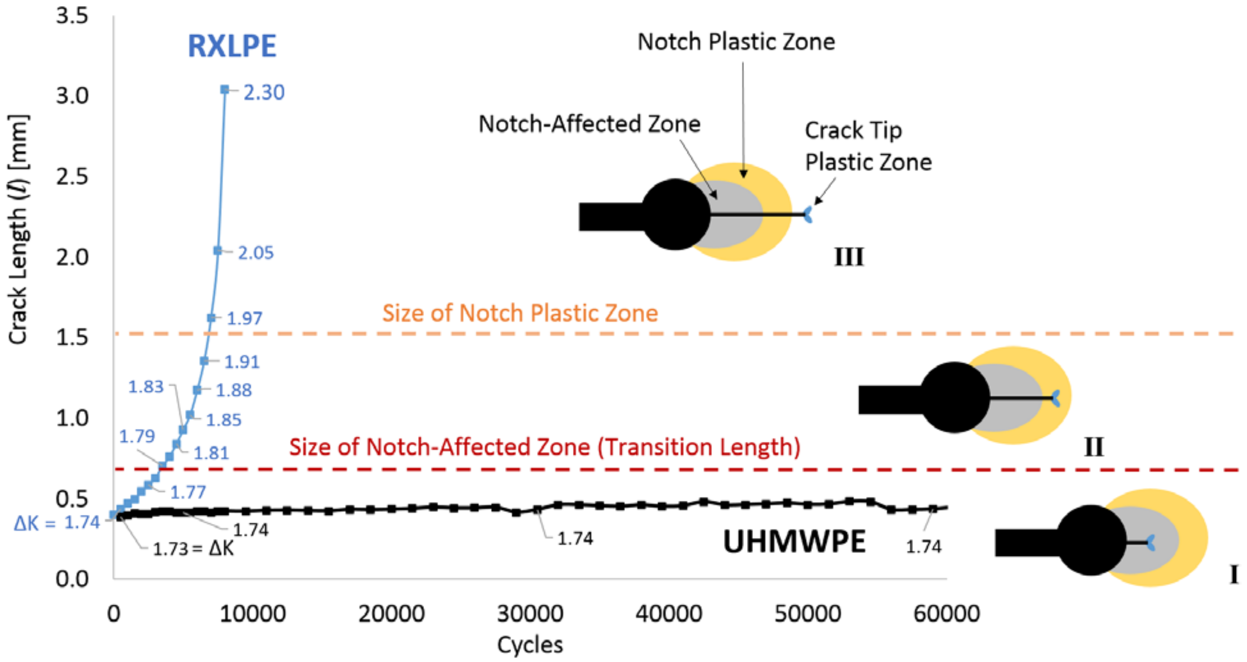

**Figure 5.15** | Crack length as a function of cycles passed, as recorded for a 3 mm notch-root radius at a constant cyclic load of 38 to 380 N. Cyclic stress intensity (***ΔK***) is noted along each material curve, increasing only as a function of crack length in this case. RXPLE demonstrates increased crack length at a smaller number of cycles, allowing the crack to grow from a region inside both the plastic and notch-affected zone (**I**) to a "long crack" within the notch plastic zone (**II**) and finally to a region without any notch influence (**III**).

### *Fractography*

SEM analysis of representative fracture surfaces from each specimen cohort (each notch-root radius and each material formulation) are shown in **Figures 5.16**. Fracture surfaces taken roughly 1 mm ahead of the crack growth starting point are shown, highlighting long crack behavior that grows ahead of the notch-affected zone ("elastic" growth). UHMWPE shows distinct features from both RXLPE and VXLPE, with criss-cross markings aligned at 45° angles and demonstrated rippling associated with large surface strains before rupture. Fractures surfaces for RXLPE and VXLPE show a marked reduction in these ductile features, with much smaller criss-cross patterns. VXLPE shows slightly more surface fibrillation than RXLPE. Striations are apparent in all images, with no differences in spacing between materials or notch geometry. **Figure 5.17** compares "elastic" long crack with "plastic" short crack fracture surfaces for RXPLE and UHMWPE. No differences across the four notch-root radii are apparent for all of the formulations of UHMWPE evaluated.

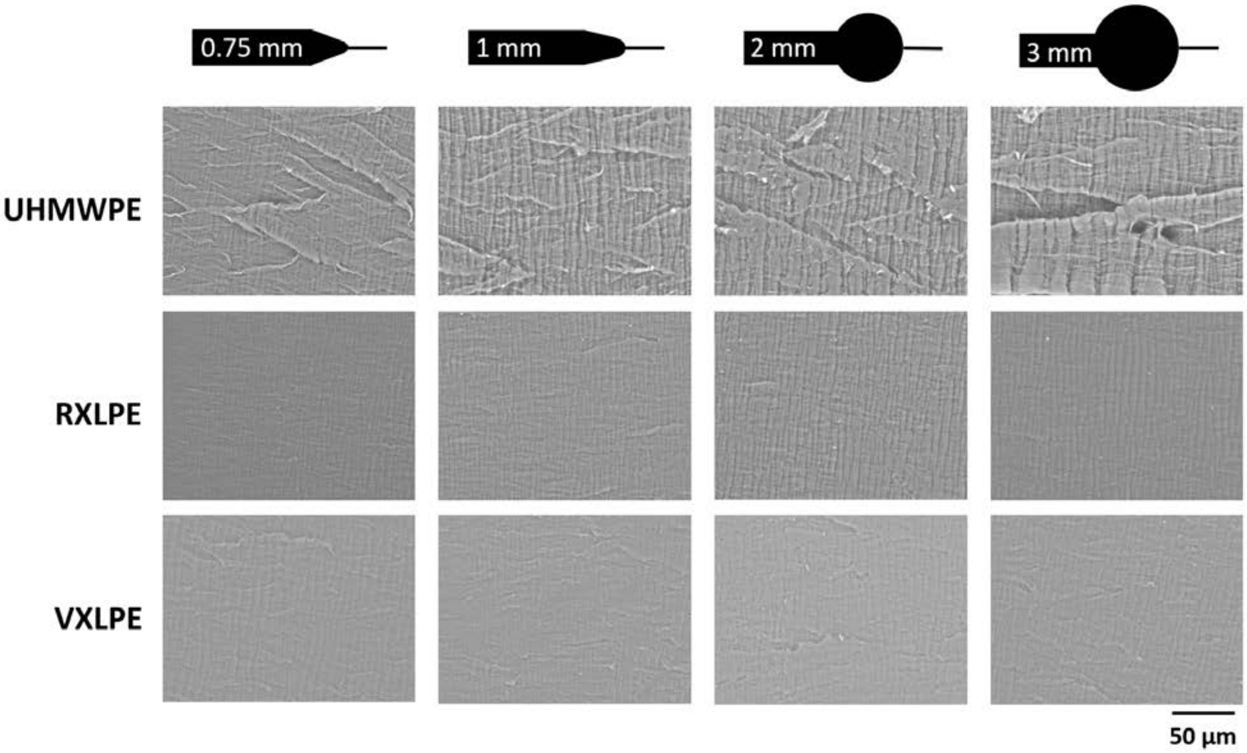

**Figure 5.16 |** SEM images of fractures surfaces taken roughly 1 mm from the start of the precrack. All images were taken where cracks fell into the category of a long crack growing under "elastic" conditions (i.e. ahead of the notch plastic zone). UHMWPE samples demonstrate greater ductile features (rippling, multi-layered criss-cross failure features) than both RXLPE and VXLPE.

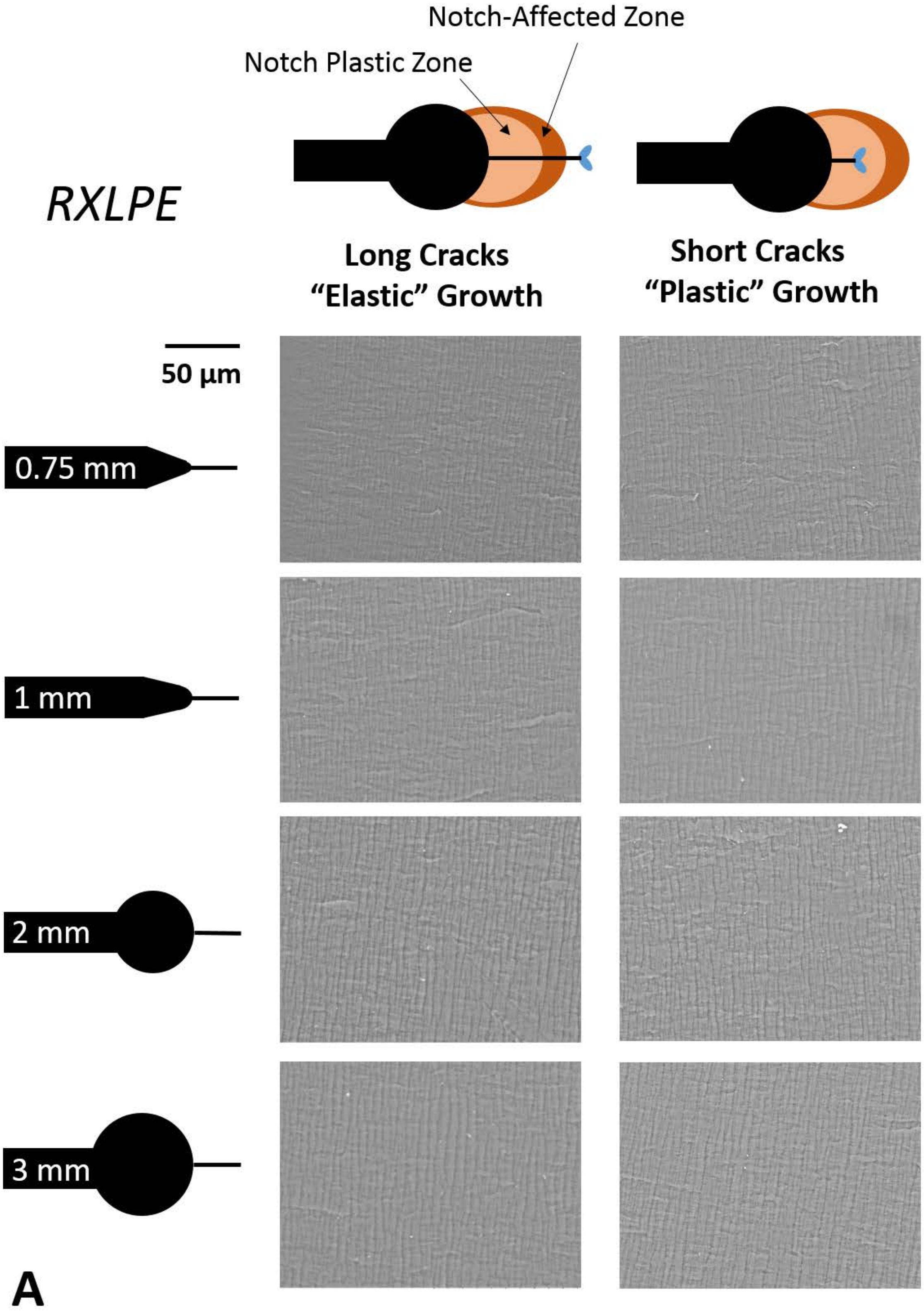

**Figure 5.17 |** SEM images of CT specimen fracture surfaces, taken in regions of long crack "elastic" growth (LEFT) and short crack growth engulfed in the plastic zone (RIGHT) for (**A**) RXLPE and (**B**) UHMWPE. Fracture surface morphologies are consistent across all notch geometries and plasticity conditions.

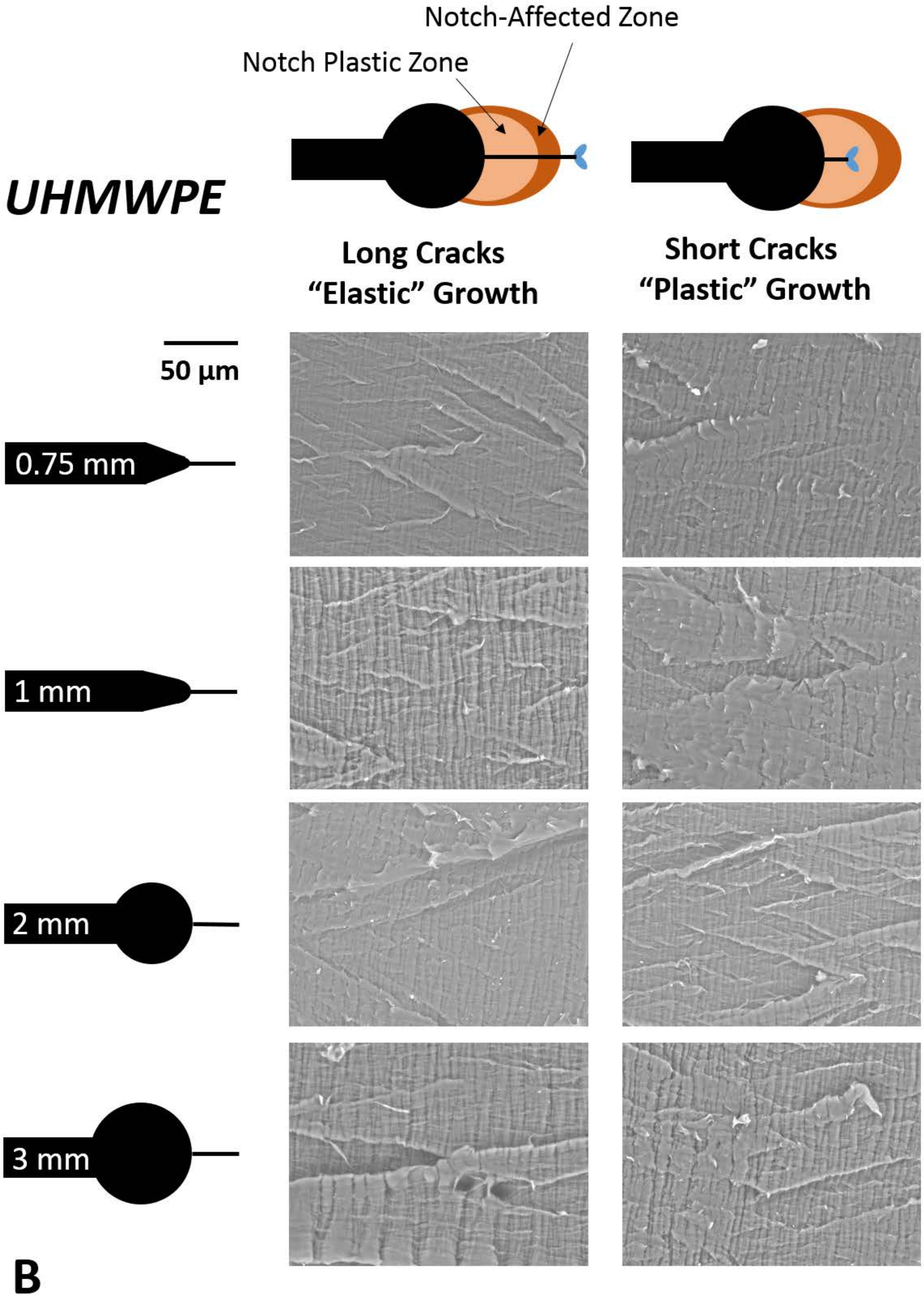
Notch-Affected Zone
Notch Plastic Zone
UHMWPE
Long Cracks
"Elastic" Growth
Short Cracks
"Plastic" Growth
50 µm
0.75 mm
1 mm
2 mm
3 mm
B

**Figure 5.17 (B)**

### 5.4.3 Discussion

The above work demonstrates the applicability of LEFM stress intensity approximation for measuring crack growth emanating from notches under cyclic loading of UHMWPE using the Dowling method. Fatigue crack growth data mapped using adjusted stress intensity expressions (**eqs. 5.6** and **5.7**) overlapped with sharp crack data (**Figure 5.13**), supporting the use of the Dowling approximation in providing a reasonable estimation for crack driving force ahead of sharp and blunt notch geometries. **Figure 5.10** in particular shows that fatigue crack growth beyond the notch-affected zone in which small scale yielding is preserved is fairly congruent with sharp cracks growing in the material bulk. For the geometries of 0.75, 1, 2 and 3 mm evaluated here, this implies that cracks as short as 0.15, 0.20, 0.39 and 0.50 mm, respectively, will be subject to sharp crack driving forces (i.e. will have no notch effect) when notch plasticity is limited (**Table 5.5**).

The results in **Figure 5.14** show that short cracks growing within the notch-affected zone are often engulfed by notch plasticity, and yet still exhibit reasonable overlap with sharp crack data when mapped with LEFM parameters. Note that short cracks did not exhibit higher crack velocities compared to long cracks at a given $\Delta K$, as has been documented in metals for short cracks growing ahead of notches (Saxena et al. 1985) or even for sharp small cracks within a material bulk (Suresh & Ritchie 1984). This implies that short cracks in UHMWPE *do* obey the similitude conditions imposed by LEFM, and thus are not subject to microstructural features or crack closure effects that have influenced short crack growth in other materials (Saxena et al. 1985; Suresh & Ritchie 1984; Tanaka & Nakai 1983; Shin & Smith 1988). This is consistent with the size discrepancy between short cracks tested here, which are from 0.1 to 2 mm in magnitude, and crystalline structures typically of interest for UHMWPE, which are typically tens of nanometers to micrometers in scale. Furthermore, preliminary studies on crack closure in UHMWPE have been unable to detect this phenomenon for long cracks (Varadarajan 2007).

The characterization of these short cracks as “plastic” does question the validity of the use of a $\Delta K$ parameter in describing their driving force. This may in fact be the reason for the scatter seen in **Figure 5.13** and **5.14** for UHMWPE compared with RXLPE and VXLPE, which sees increased plastic mechanisms of deformation near the crack tip due to a lack of crosslinking (Baker et al. 1999b; Baker et al. 2000; Atwood et al. 2011; Medel et al. 2007; Pruitt 2005; Furmanski & Pruitt 2007b). Short crack “elastic” data was difficult to obtain provided the specimen geometries used in this study. It is possible that elevated crack growth as seen by Saxena (1985) and others for short cracks may be achieved within a purely elastic local notch stress field. However, the above work demonstrates that the necessary force needed to generate a $\Delta K$ causing a short crack to grow at a rate of $10^{-6}$ mm/cycle was enough to create substantial notch plasticity the exceeded the flaw size. Future work utilizing alternative geometries would be needed to produce such “elastic” short crack growth. Alternatively, Dowling & Begley (1976) have demonstrated that the use of $\Delta J$ parameter can serve to minimize this scatter in fatigue data for metals; however, this parameter comes with its own caveats with regard to unproportional loading and inelastic unloading seen with viscoelastic materials (**see Chapter 3**).

The congruency of data within each material cohort suggests that crack growth ahead of notches in UHMWPE defers to microstructural influences (i.e. crosslinking, crystallinity, lamellae structure) rather than design factors. As a result, previous literature on sharp crack growth under cyclic loading for different formulations of UHMWPE can be leveraged to explain the distinctions between the three cohorts tested here. The sharp crack and notch-emanating crack growth results shown in **Figure 5.13** are consistent with previous FCP analysis of sharp crack growth in UHMWPE, comparing the introduction of crosslinking (Baker et al. 1999b; Baker et al. 2000; Atwood et al. 2011; Medel et al. 2007), post-irradiation heat treatment (Atwood et al. 2011; Medel et al. 2007; Puértolas et al. 2006; Bradford et al. 2004; Ebru Oral, Malhi, et al. 2006b) and the blending of Vitamin E (Ebru Oral, Christensen, et al. 2006; Oral et al. 2004). Crosslinking has been shown to reduce mechanical properties (such as strain-to-failure, seen in **Figure 5.1**) and resistance to crack growth by introducing covalent bonding between backbone structures in the amorphous regions of the polymer (Baker et al. 1999b; Baker et al. 2000; Atwood et al. 2011; Medel et al. 2007). This results in reduced intrinsic plasticity available to the material during any deformation, limiting strain-to-failure bulk properties that also manifest show up at the crack tip (Pruitt 2005; Kurtz et al. 2002). The impact of crosslinking can be seen in fractography images shown in **Figure 5.16**: both RXLPE and VXLPE fracture surfaces show smaller ductile features of criss-crossing, fibrillation and rippling compared to unirradiated UHMPWE. These features have consistently been attributed to large strains before material failure, leading to stretching and subsequent material recoil after rupture (Connelly et al. 1984; Rimnac et al. 1988; Baker et al. 2000; Bradford et al. 2004; Atwood et al. 2011; Medel et al. 2007). It should be noted that the striations apparent on all SEM images are not fatigue striations concomitant with cyclic crack advance, as they do not change with increasing $\boldsymbol{\Delta K}$ and they have been recorded for both cyclic (Connelly et al. 1984) and static (Rimnac et al. 1988) evaluations of crack extension in UHMWPE.

Both RXPLE and VXPLE were treated with the same crosslinking radiation dosage (75 kGy), thus accounting for their reduced resistance to FCP compared with UHMWPE. However, the distinctions between these two formulations in their behavior derives from the post- or pre-irradiation treatments performed to improve the oxidative resistance of this material. Within the past decade, post-irradiation heat treatments in which XLPE is heated above its melt temperature and then cooled have demonstrated success in eliminating free radicals within the polymer bulk, thereby diminishing the potential for oxidation when exposed to oxygen on the shelf or in the body (Atwood et al. 2011; Kurtz 1999). However, such treatments have demonstrated a reduction in crystalline quality and quantity: remelting UHMWPE and then cooling results in reduced percent crystallinity as well as smaller lamellae thickness (Atwood et al. 2011; Ries & Pruitt 2005; Medel et al. 2007; Puértolas et al. 2006; Ebru Oral, Malhi, et al. 2006b). Crystallinity has been shown to improve resistance to FCP attributed to increased crack deflection (Baker et al. 2000; Simis et al. 2006). Diminishing lamellae thickness and percent crystallinity through remelting has a significant impact on reducing its mechanical properties, including yield strength as seen in **Figure 5.1** and fatigue strength seen in **Figure 5.13** and other studies (Atwood et al. 2011; Medel et al. 2007; Ebru Oral, Malhi, et al. 2006b; Pruitt 2005).

VXPLE involves a pre-irradiation blending of the antioxidant Vitamin E into the UHMWPE resin before consolidation, which has demonstrated success in reduced oxidation under simulated aging (Oral et al. 2004; Ebru Oral, Christensen, et al. 2006; E Oral et al. 2006). However, blending the antioxidant into polymer before irradiation can inhibit crosslinking mechanisms in the amorphous region upon exposure to gamma or electron beam rays, leading to a reduced crosslinking density at a given dosage compared to non-antioxidant blended materials (Oral, Godleski Beckos, et al. 2008). In other words, the crosslinking density of VXLPE may be lower than RXLPE in this study, despite having the same crosslinking doses of 75 kGy. As a result, VXLPE demonstrates similar FCP resistance to sharp crack studies for UHMWPE that have received a lower crosslinking irradiation dosage of 50 kGy (Atwood et al. 2011; Baker et al. 1999b). Furthermore, studies of blended VXLPE demonstrate that the introduction of the antioxidant does not lead to any changes in crystallinity, thereby retaining the original microstructure exhibited by virgin UHMWPE that is lost with RXLPE (Ebru Oral, Christensen, et al. 2006).

## 5.5 Summary and Conclusions

Fatigue crack growth ahead of stress concentrations was evaluated head of four notch geometries for three material formulations of UHMWPE. The results demonstrated that cyclic crack growth can be successfully mapped using an approximation established by Dowling (1979a). Computational analysis demonstrates that such an approximation does have some limitations in predicting crack driving force, particularly around the region in which cracks escape the notch-affected zone. These limitations may additionally be the cause for scatter seen in the fatigue data in **Section 5.3**. However, issues with notch plasticity may overshadow these mathematical discrepancies with regard to increased scatter.

Ultimately, cyclic crack growth ahead of notches in UHMWPE appear to defer more to microstructural influences than geometry. Crack growth resistance was strongest for virgin UHMWPE formulations. Crosslinking diminished the resistance to FCP, and subsequent annealing of the polymer to improve oxidation resistance proved to be the most detrimental to its fatigue resistance. VXLPE was able to retain more resistance to FCP, but most likely due to a reduced crosslinking density. These results are consistent with previous studies of sharp crack data, again highlighting the minimal influence that geometry has on crack growth.

Notch plasticity was unavoidable in most testing of short cracks on the chosen notch-root radii in this study. As a result, the experimental dataset is limited in its use of linear elastic parameters to describe local driving forces. Nonetheless, “plastic” short crack data appears to closely overlap with both “elastic” long crack and sharp crack data, suggesting that $\Delta K$ may be used for relative comparisons of FCP between UHMWPE formulations. The “plastic” short crack data did not demonstrate typical small crack behavior (i.e. elevated velocities at a given $\Delta K$ compared with long cracks) seen in some metallic materials; however, such effects may be present under “elastic” growth conditions, and warrant future study.

# Chapter 6 – Conclusions

## 6.1 Study Significance

Today, joint replacement surgery is one of the most successful medical device stories, with roughly 1 million devices implanted each year in the US and a lifespan of 10-20 years *in vivo* (AAOS 2014; Pruitt & Chakravartula 2011). In the next 10-15 years, that number is expected to quadruple, with receiving patients trending to younger ages yet with higher expectations for TJR performance (Kurtz et al. 2005; Kurtz et al. 2009). This performance has been – and continues to be – concomitant with the durability of the engineered materials used in hip, knee and shoulder implants. With higher loading and longer lives expected for younger patients, the focus of this material burden has shifted to the UHMWPE polymer bearing. While the robust 50 year history of UHMWPE in TJR has fueled this device's success and popularity, in recent years it has frequently been cited as the Achilles' heel in pushing the boundaries of TJR *in vivo* performance. Wear of UHMWPE leads to debris formation that can initiate pathways to osteolysis and subsequent *in vivo* loosening (Harris 1995). Irradiation crosslinking to minimize wear can generate free radicals which may result in oxidization of the polymer on the shelf or in the body, leading to mechanical embrittlement (Currier et al. 2007). Heat treatments then used in combination with irradiation to prevent against oxidation can further compromise the resistance to fatigue crack propagation and lead to component fracture (Atwood et al. 2011; Urriés et al. 2004). Ultimately, UHMWPE exhibits clear tradeoffs in performance that still challenge orthopedic manufacturers today and fuel the ongoing efforts at optimizing microstructure of this polymer to enable long-term use of these devices.

While the majority of microstructural changes to UHMWPE have focused on treating issues of wear and oxidation, the study of the fracture resistance of UHMWPE has developed a strong following in the past 30 years. In particular, the application of linear elastic fracture mechanics (LEFM) has demonstrated how various processing treatments to improve wear and toughness – such as sterilization, manufacturing, irradiation crosslinking, high pressure/temperature consolidation, post-irradiation heat treatments and antioxidant infusion – can influence crack growth within UHMWPE. These studies have primarily evaluated fatigue crack propagation (FCP) for sharp cracks growing in the polymer bulk, exclusively focusing on structure-property relationships between microstructure (e.g. crosslinking density, molecular weight, percent crystallinity, lamellae size, and lamella orientation) and crack advance. This work has served to elucidate instances of clinical fracture *in vivo*, from surface cracking and fatigue wear to the catastrophic fractures that often emanate from stress concentrations. This latter consequence of reduced resistance to FCP for UHMWPE provides a basis for this work, which sought to integrate the exploration of materials microstructure with the influence of component design.

The results presented in **Chapter 5** present the first known effort at utilizing familiar LEFM principles in combination with clinically-relevant stress risers to evaluate notch fatigue in UHMPWE. In doing so, this work builds upon previously established knowledge and methods to deliver translatable information that can directly influence implant design today. This also serves to complement previous studies that evaluate notch fatigue using stress-life approaches, providing a balanced approach to crack initiation and propagation mechanisms in UHMWPE under local notch stresses (Sobieraj et al. 2013). With this new focus on material-design interplay in UHMWPE, new standards can be developed that better simulate the *in vivo* fracture behavior of this polymer.

Not only does this present the first LEFM-based evaluation of notch crack growth for UHMWPE, but it also presents on the only-known effort for applying such theory to a polymer. The majority of the theories discussed in **Chapter 4** and computational evaluated in **Chapter 5** derive from fully crystalline materials that do not exhibit the nonlinear deformation and viscoelastic behavior common with many polymer systems. This work demonstrates that such theory can translate to polymeric materials, though continued study in this area is warranted to fully elucidate the influence of frequency, temperature, load ratio/mode, and microstructure on short crack growth ahead of notches. With the general shift to biodegradable polymeric structures for medical applications to lighter and stronger polymer-based composites used in aerospace and automotive industries, there exists a need for simplified and uniform notch fatigue assessment. The data presented here on UHMWPE lays a foundation for future LEFM-based notch fatigue work that can be leveraged for future research.

## 6.2 Notch Fatigue in UHMWPE: Summary and Discussion

*Summary of Computational Work*

Finite element analysis (FEA) was utilized to assess both the LEFM stress intensity of cracks growing near and beyond a notch-tip, as well as to measure the notch plastic zone size t varying loads. This was directly compared to several analytical expressions for both stress intensity and the local notch stress distribution. No single expression for either parameter was found to accurately reflect the results from the FEA analysis. An expression develop by Dowling (1979a), which uses the elastic stress concentration factor to quantify local peak stresses, was deemed the best solution for predicting stress intensity for very short and very long cracks. However, deviations up to 40% were seen near the “transition” length, making the crack behavior upon exiting the notch-affected zone difficult to model.

The notch plastic zone size also proved challenging to predict. Several linear elastic expressions that have been developed for the local stress field were compared to FEA results, all of which overestimated the local notch plastic zone size. Furthermore, these deviations varied for each expression, making the choice of an appropriate approach difficult. In the end, the formula for local notch stress developed by Chen & Pan was deemed best for blunt notch geometries (2 and 3 mm; $\boldsymbol{k_t}$ = 2.40, 2.01) while Dowling’s equation was used for sharper dimensions (0.75 and 1 mm, $\boldsymbol{k_t}$ = 3.80, 3.32). Both these formulas overpredicted the plastic zone by as much as 100%, which can be double the size of a short crack. A more accurate notch plastic zone prediction which uses plasticity properties will be needed to more accurately predict the degree of plasticity relative to the crack size.

### *Summary of Experimental Work*

This study utilized an LEFM approach proposed by Dowling (1979a) to characterize the driving force of crack growth ahead of notches under cyclic loading. Short cracks growing within the vicinity of the notch and long cracks extending far head of the notch were shown to have congruent FCP data to sharp cracks growing in the material bulk. Based on Dowling's expression for short crack stress intensity, this implies that the driving force for cracks growing near a notch, in what is known as the notch-affected zone, is dependent on the notch geometry through the elastic stress concentration factor. However, these local changes in driving force do not change the inherent behavior of the crack under cyclic tensile loading, and similar FCP behavior can be obtained for UHMWPE.

Short cracks growing within all three UHMWPE formulations evaluated were often engulfed by notch plasticity during growth: for the CT specimen geometries evaluated, the necessary far-field stresses needed to produce an above-threshold $\Delta K$ for a short crack often exceeded yield near the notch. As a result, the majority of the short crack data grew within an elastic-plastic stress environment. When mapped with LEFM parameters against long and sharp crack data, short crack growth was consistent, but exhibited increased scatter. Such scatter may be due to the use of linear elastic parameters for predicting crack growth in which small scale yielding conditions may be violated. However, the agreement between all data sets still allowed for distinctions to be made between each material cohort, suggesting that even under elastic-plastic conditions, crack growth ahead of notches defers to microstructural influences rather than notch design.

Provided the alignment for notch-emanating and sharp crack data, similar trends in FCP resistance were obtained for the three UHMWPE formulations evaluated. RXLPE (remelted, highly crosslinked) presented the least resistance to FCP, consistent with microstructural changes during irradiation and post-irradiation heat treatment that lead to decreased local plasticity, lower percent crystallinity and smaller lamellae (Ries & Pruitt 2005; Steven M. Kurtz et al. 1998; Atwood et al. 2011). VXLPE demonstrated slightly improved resistance to fatigue, most likely due to a reduced crosslinking density compared to RXLPE and the avoidance of annealing procedures that compromise crystalline quality and quantity (Oral, Godleski Beckos, et al. 2008; Ebru Oral, Christensen, et al. 2006). Untreated UHMWPE demonstrated the best FCP resistance, consistent with previous studies (Baker et al. 1999a; Atwood et al. 2011; Medel et al. 2013).

### *Comparison with Literature on LEFM-Based Notch FCP Studies*

The majority of analytical and experimental studies attempting to measure short crack growth from notches using fracture mechanics has been performed for crystalline materials, especially metals. The predominant finding of this body of work has been the lack of similitude seen between short and long crack behavior, which has also been seen for "small" cracks that are growing in the bulk: small cracks driven by low $\Delta K$ values generally grow at a faster rate than equivalent long cracks. Suresh & Ritchie argue that small crack growth effects are due to one of four reasons: (1) invalidity of LEFM parameters within regions of large plasticity relative to crack size (such as near a notch); (2) diminishing crack closure effects for short cracks at low $\Delta K$ thresholds relative to long cracks; (3) microstructure influences; or (4) environmental influences. Several authors have studied the behavior of short cracks in front of notches and found one or more of these effects to occur. For example, Saxena et al. (1985) evaluated FCP in blunt notch CT specimens of austenitic steel, and found elevated short crack growth only for low frequency tests in a corrosive environment, while high frequency loading eliminated any corrosive interaction and related aberrations in short crack growth. Both Shin & Smith (1988) (double and singled edge notched specimens of steel and aluminum) and Tanaka & Nakai (1983) (center-notched specimens of low carbon steel) demonstrated how distinctions between short and long crack growth ahead of notches disappeared when mapped against $\Delta K_{eff}$ values as opposed to $\Delta K$, accounting for crack closure effects. Dowling & Belgey (1976) have also shown that elastic-plastic fracture mechanics can compensate for local plasticity effects that otherwise violate conditions for LEFM validity, showing congruency between short and long crack data when mapped against a $\Delta J$ parameter.

This work demonstrates that these small crack effects are less pronounced for UHMWPE. Short crack behavior appears to overlap reasonably well with long crack behavior, though with enhanced scatter. It is believed that such scatter is most likely associated with the use of $\Delta K$ for evaluating crack growth in a highly plastic region ahead of the notch. The use of a $\Delta J$ parameter as established by Dowling (1976) and Dowling & Begley (1976) may improve the correlation of short and long crack data. Crack closure effects in UHMWPE have not been documented thoroughly; however, preliminary evidence has shown that closure does not take place for sharp crack growth in crosslinked forms of the polymer (Varadarajan 2007). While corrosive interactions are not specifically an issue for UHMWPE, temperature has been shown to influence sharp crack FCP in UHMWPE (Baker et al. 2003; Baker et al. 2000). For notched specimens, higher temperatures would enhance the viscoelastic behavior of UHMWPE near the notch, potentially increasing notch plasticity and thereby leading to greater scatter.

This work presents the first known effort at applying LEFM-based notch fatigue theory to a polymer. While a discussion of previous work is warranted, distinctions between metal and polymer mechanical behavior (especially viscoelastic effects) should be considered. A handful of studies have investigated notch effects on polymer fracture and fatigue (Sobieraj et al. 2013; Sobieraj et al. 2010; Constable et al. 1970; Lu et al. n.d.), but none of them utilize the LEFM-based method presented in this work.

### *Comparison with Literature on UHMWPE Fracture and Fatigue*

Some recent studies have been performed to investigate the fracture and fatigue behavior of notched UHMWPE formulations. Sobieraj et al. presented a robust body of work (Sobieraj et al. 2008a; Sobieraj et al. 2008b; Sobieraj et al. 2013)for two notch severities with moderate ($k_t$ = 2.1) and deep ($k_t$ = 2.7) geometries for several formulations of UHMWPE with varying irradiation dosage and annealing treatments. Increasing notch severity demonstrated an increase in yield strength and a decrease in ultimate properties under monotonic loading, associated with a limitation in chain disentanglement and alignment near the notch. Such findings were replicated by Fouad (2010) for virgin UHMWPE, both through experimental and computational methods. The triaxial stress state near the notch is thought to limit chain motion, resulting in a higher threshold for chain slip (higher yield) and a greater potential for chain breakage at lower stresses (lower ultimate stress/strain) (Fouad 2010b).

Under cyclic loading, such changes in monotonic properties may manifest as distinctions between crack growth for different notch-too radii, since each geometry produces a distinct volume of triaxially stressed material. No differences were found in this work, which investigated four radii from 0.75 to 3 mm, which is much wider than that studied by Sobieraj et al. (2008a, 2008b, 2013) or Fouad (2010). Differences between notch geometries were primarily accounted for with the stress intensity approximation, which depended not only on the stress concentration factor, but also on the transition length of each blunt specimen. While specimens with a blunter notch produced a larger notch-affected zone, the short crack behavior that existed within this region did not display any distinctions from sharper crack growth at the same cyclic stress intensity.

Instead, the role of triaxial stress may appear through crack imitation events ahead of a notch, which was not evaluated in this study. Sobieraj et al. (2013) provided the only known evaluation of fatigue crack initiation using a stress-life approach, finding that notches appeared to have a statistically significant effect, but differed for each UHMWPE formulation evaluated. However, the authors evaluated only a small range of notch severity ($\boldsymbol{k_t}$ = 2.1 to 2.7) and did so at elevated cyclic loads often above yield, making interpretation of the data difficult. Nonetheless, Sobieraj and colleagues found virgin UHMWPE to be the least resistance to fatigue crack initiation, which may be related to the greater intrinsic plasticity of this unirradiated polymer.

Ultimately, the work presented here presents some insight into the mechanisms behind crack propagation in notched UHMWPE, complementing the work that has been performed using both LEFM and stress-life techniques. However, the study of notch fatigue in UHMWPE is limited; several proposals for future work is discussed in **Section 6.3**.

### *Clinical Implications*

As seen in **Chapter 2**, catastrophic fracture of UHMWPE components used in modern hip and knee replacements often originates at notch-like features in these devices. Reports on these types of failure have grown significantly in recent years, often associated with the advent of highly crosslinked formulations of UHMWPE that have shown reduced resistance to sharp crack FCP. This study demonstrates that the concern over the use of highly crosslinked formulations remains even when considering crack growth ahead of the notches in these devices. Remelted XLPE, in particular, demonstrates a reduction in resistance to FCP relative to virgin UHMWPE as well as Vitamin E infused XLPE for both short and long cracks growing within or beyond the notch-affected zone.

This does not imply, however, that notch geometry is irrelevant when it comes to notch fatigue. First, this study is limited to the study of the propagation of cracks that already exist in the material, but not the generation of those cracks. Studies of fatigue crack initiation at notches are necessary to determine the effect – if any – of notch radius on flaw formation under varying loads and how this may influence the overall fatigue life of TJR components. Furthermore, considering the overlapping behavior of short and long cracks in all three formulations of UHMPWE, it can be inferred that design changes that lower the $\Delta K$ of any cracks already present near a notch can reduce the speed of growth. The notch-affected zones derived from Dowling's expression are larger for blunt notch geometries, thus allowing for a larger volume of material in which cracks are driven by a lower – albeit fast-rising – $\Delta K$ value compared to cracks of the same size growing in the bulk.

Considering this last point, it is interesting to note that the available studies of retrieved UHMWPE components document cracks in acetabular cups on the order of 0.1 to 0.3 mm in length (Furmanski, Kraay, et al. 2011; Paterson et al. 2012). These lengths are on the order of the transition lengths reports for the four notch radii evaluated in this study (0.75, 1, 2 and 3 mm), which are all derived from features seen in hip and knee devices. In the cohort of devices evaluations, Furmanski et al. (2011) noted some that were explanted in less than one year of service – some even after only one month *in vivo* – suggesting that initial loading, implantation or even manufacturing may lead to the generation of small defects in these UHMWPE components. For smaller even smaller design features – such as the liner locking rim on an acetabular cup – these lengths exceed the transition length, acting as "sharp" cracks that are no longer influenced by the notch.

To optimize both material composition and design in future iterations of TJR components, continued study of UHMWPE fatigue crack propagation *and* initiation both in the bulk and ahead of notches is needed. At this time, no standards exist for assessing FCP in UHMWPE; previous work has primarily derived from ASTM standards primarily developed for metals. Not only is a standard method of evaluating FCP in UHMWPE needed, but the consideration of notch fatigue should be a necessary component of that standard. This work provides a solid foundation demonstrating the applicability of Dowling's approximation for stress intensity in evaluating notch FCP in UHMWPE. While the findings do imply that the notch influence does not significantly impact FCP in the three materials evaluated, future formulations of UHMWPE are already tailoring the polymer's microstructure in more intricate ways, which may interact with short cracks in a notch-affected zone differently than seen in RXLPE and VXLPE. Provided the vital role that notches play in the design of joint replacement components composed of UHMWPE, notch fatigue should remain a key preclinical evaluation of materials used in this application.

## 6.3 Strengths and Limitations of Study

### *Strengths of Study*

While fatigue has historically been a large part of materials testing for UHMWPE used in TJRs, the interplay of design with material performance has been limited. Only a handful of studies have recently investigated notch effects on UHMWPE mechanical behavior, and most of those have been limited to monotonic loading. This work provides an established framework (LEFM) to investigate an unanswered problem (notch fatigue) that has direct impact on product design and development today.

The experimental methodology used in this study was largely derived from previous work on FCP in UHMWPE for sharp cracks. As a result, the data obtained can be directly compared to historical trends and offer additional insight on conclusions from this work without concerns regarding material origins, specimen dimensions (especially thickness), specimen manufacturing, precrack formation, or crack measurement techniques. At this time, there is a lack of standard method for evaluating FCP using LEFM methods for even sharp crack growth, leading to a variety of specimen geometries and testing conditions that makes direct comparison limited. This work sought to avoid such issues through modification of preexisting specimen geometries and the most common testing conditions for UHMWPE. As a result, much of the methodology is easily translatable to labs that are equipped to perform fatigue testing using fracture mechanics, and can be readily applied to novel UHMWPE materials.

A second strength of this analysis was the computational analysis performed regarding stress intensity solutions. LEFM has gained significant ground in the medical device community as a useful means of predicting fatigue life and preventing against catastrophic failure. However, in the orthopedic community, adopters of LEFM in assessing FCP has not always been cognizant of the fundamentals of the theory, leading to specimen size alterations or under-reporting of relevant Paris fitting constants to provide a complete picture of crack behavior under cyclic loading in different formulations of UHMWPE. This work seeks to provide a robust assessment of all available LEFM approaches to crack growth and a full understanding of the limitations of parameters used in the experimental analysis.

Finally, this work evaluates notch fatigue in a robust cohort of materials, allowing for the elucidation of microstructural effects. The three materials provide for a comparison of crosslinking dosage, post-irradiation treatment, and antioxidant infusion. RXPLE and VXPLE also present to state-of-the-art materials that have been FDA approved and integrated into many current iterations of devices, thus allowing for this data to be translated to many components used to treat patients today.

### *Limitations of Study*

One of the primary limitations of this work is the use of LEFM parameters to characterize crack growth in regions of significant plasticity. For all notch geometries, the load needed to achieve a $\Delta K$ above the threshold for crack growth for a short crack was enough to generate a large region of notch plasticity which ultimately engulfed the crack. This likely violates small scale yielding conditions that are required for the use of $K$ to characterize the driving force. Under monotonic loading, this condition would necessitate the used of an elastic-plastic $J$ integral to account for nonlinear deformation that would occur near the crack tip. However, under cyclic loading, the use of $J$ introduces its own caveats: $J$ assumes nonlinear *elastic* recovery and proportional loading near the crack tip, both conditions that may be violated for materials that exhibit hysteresis, including viscoelastic polymers.

For this reason, ***K*** was primarily utilized in this study, but with questionable interpretation. As a result of this, the results presented in this study should be used as a relative comparison between material cohorts rather than a predictive tool for UHMWPE fatigue. The predictive power of this work is further inhibited by constraints in the testing methodology. All testing took place in ambient conditions (room temperature with air cooling) under tensile-tensile loading at a single frequency, disregarding any *in vivo* effects such as body temperature (37° C), variable loading, and lubrication. Temperature and frequency have been shown to have an influence on UHMWPE FCP (Baker et al. 2000), as well as polymer fatigue in general (Hertzberg & Manson 1980). In addition, optical measurements of crack growth have a proven track record for long (> 1 mm) crack growth in UHMWPE; however, for the particular assessment of small cracks, this technique may be severely limited in its accuracy and efficiency.

Despite these limitations, it should be noted that the experimental design of this work largely mimics that which exists for clinically-relevant UHMWPE in the orthopedic world. The results demonstrate that even ***ΔK*** can provide a reasonable assessment of the relative behavior between each material cohort evaluated. Since the introduction of LEFM to the study of UHMWPE fatigue in the 1980s, this theory has primarily been used as a comparative tool, with predictive behavior primarily determined through total life (stress-life) evaluations of components under simulated use. LEFM studies have since gained ground, reserved primarily for elucidating microstructural influences on crack growth under different testing conditions and specimen sizes. The methodology discussed in work, while limited in its tractability in fracture mechanics audiences, does provide a tangible approach for the orthopedics community today.

## 6.4 Future Work

### *Fatigue Crack Initiation*

Retrieval studies demonstrate that cracks can develop in UHMWPE TJR components in as little as one month after use (Furmanski, Kraay, et al. 2011; Paterson et al. 2012). The mechanism of crack initiation has yet to be determined, however. While implantation and manufacturing may create unseen defects, loading effects (both monotonic and cyclic) have yet to be ruled out in their role of creating flaws. Sobieraj et al. (2013) performed the only study to date evaluated notched UHMWPE components using a stress-life approach, finding the methodology to produced significant scatter and require detailed statistical analysis that has spurred debate (Pascual et al. 2012). Furthermore, to ensure a realistic experimental duration, Sobieraj et al. were limited to evaluating these specimens under high cyclic loads that were often above yield, leading to conditions of gross specimen plasticity that do not reflect *in vivo* use. Thus, the traditional means of studying fatigue crack initiation may not be appropriate for UHMWPE.

Instead, an LEFM based method may prove more effective. Barsom and McNicol (1974) proposed a notch-geometry dependent parameter, $\Delta K/\sqrt{\rho}$, which can be mapped against the number of cycles to crack initiation. Initiation lengths can be dependent on the application in question, or defined as the transition length when cracks begin to behave as they would if no notch were present. This term allows for the combination of both stress and design, ideally providing an exponential material curve that can be extrapolated to very low cyclic stresses or very blunt notches that are difficult to evaluate within days of constant testing. Furthermore, this alternative stress-life characterization may even provide with a given threshold, $(\Delta K/\sqrt{\rho})_{Th}$, providing not only a stress limit, but also an associated design optimization for preventing against fatigue crack initiation.

### *Elastic-Plastic Analysis*

The use of the $J$-integral for evaluating cyclic crack growth has remained controversial, provided the potential violations of nonlinear elastic theory from which the parameter was derived (Anderson 2005; Suresh & Ritchie 1984; Dowling & Begley 1976; Dowling 1976). Dowling (1976) and Dowling & Begley (1976) proposed a methodology for using a $\Delta J$ parameter to minimize these theoretical challenges and map crack growth in gross plasticity. The authors assumed that any cyclic plasticity that occurs manifests as stable hysteresis loops, allowing for mathematical manipulation of $J$-integral theory to satisfy proportional loading (Dowling & Begley 1976; Suresh & Ritchie 1984). This elastic-plastic cyclic fatigue work has since been extrapolated to characterizing short fatigue cracks near notches in combination with a material constant, $l_o$, introduced by El Haddad for use in LEFM assessments of notch fatigue (El Haddad et al. 1979; Haddad & Dowling 1980). While sufficient evidence for the use of $\Delta J$ to evaluate notch fatigue exists, the applicability of such theory and assumptions for use with UHMWPE or other viscoelastic polymeric materials will need to first be established analytically before such methods can be employed.

### *Loading Effects on Notch Crack Initiation & Propagation*

*In vivo* loading involves complex motions that result in cyclic stresses in TJR components that may be tensile or compressive in nature, and with different stress amplitudes throughout a single day of use. Future work should consider the influence of loading on crack growth ahead of notches. For example, computational stress analyses of tibial components in knees demonstrates that tibial posts on posterior-stabilized implants may experience both tensile and compressive cyclic loading under flexion-extension movements. Overload events, such as when a patient falls, should also be examined, as such low cycle, high loads can generate local plasticity that can either mitigate growth for an existing crack or create a region of damage that may formulate a flaw. Compressive loading on sharp notched specimens of UHMWPE has been shown to initiate cracks from 0.05 to 0.11 mm in length – on par with the transition lengths for each of the radii evaluated in this study, and at the lower spectrum for cracks seen in retrieved devices (Pruitt et al. 1995; Baker et al. 2000; Furmanski, Kraay, et al. 2011). Crack initiation and propagation for blunter notch geometries would provide valuable insight with regard to residual tensile or compressive stresses generated ahead of the notch tip. Finally, mixed-mode fatigue has had limited study for UHMWPE in general (Elbert et al. 1994), but would warrants further investigation near notches considering the shear and tensile/compressive axial forces seen at the tibial post for knees.

### *Alternative Materials & Microstructural Influence*

With the tradeoffs in wear, oxidation and fatigue that currently limit the lifetime of UHMWPE components, several efforts are underway to optimize its microstructure to improve durability. VXLPE represents the one of the more recent addition to the FDA-approved list of viable UHMWPE formulations for TJR. Many versions of this antioxidant-infused blend exist, with varying degrees of Vitamin E (0.1 wt% to 0.5 wt% being the most common) as well as irradiation dosage and concomitant crosslinking density. One concern regarding this particular formulation is the plasticizing effect that increased Vitamin E doses may have on polymer behavior (Wolf et al. 2006; Oral et al. 2004). Further mechanical study, especially in the area of notch plasticity and subsequent notch fatigue, is warranted to evaluate this plasticizing effect, if any.

Evidence of future formulations has also hinted at some key microstructural changes that may influence notch FCP in UHMWPE. High pressure temperature processing of highly crosslinked UHMWPE has demonstrated improvements in mechanical properties, including sharp crack FCP, due to the enhancement of crystalline quality and quantity (Simis et al. 2006). Considering evidence that triaxial stresses inhibit chain motion and alignment near a notch (Sobieraj et al. 2013; Fouad 2010b), the increase in the size of UHMWPE crystalline regions may further inhibit any plastic mechanisms that would otherwise slow down crack growth. Study of notch FCP in these highly crystalline formulations should be coupled with evaluation of lamellae orientation and percent crystallinity to see if fatigue loading may in fact result in some anisotropic behavior in unnotched versus notched specimens. Anistropic effects on notch FCP should also be investigated for mechanically deformed UHMWPE, such as Biomet's ArCom XL (Sobieraj & Rimnac 2009a), which may include residual stresses that would influence the notch-affected zone.

Finally, novel polymers have been flirting with the orthopedic market in recent years, including polycarbonate urethanes such as DSM Biomedical's Bionate® (Khan et al. 2005a; Khan et al. 2005b) and carbon-reinforced PEEK (Sonntag et al. 2012). Provided the tendency for existing TJR manufactures to pair old designs with novel polymer formulations, thorough evaluations of notch fatigue of these new polymers is needed and should become a standard component in the preclinical evaluation of these biomaterials.

# References

AAOS, 2010. Shoulder Joint Replacement. *American Association of Orthopaedic Surgeons (AAOS).*

AAOS, 2014. Total Joint Replacement. *American Association of Orthopaedic Surgeons (AAOS).*

Alberton, High & Morrey, 2002. Dislocation After Revision Total Hip Arthroplasty An Analysis of Risk Factors and Treatment Options. *The Journal of Bone & Joint Surgery*, 84(10), pp.1788–1792.

Anderson, 2005. *Fracture Mechanics: Fundamentals and Applications, Third Edition*, CRC Press.

Anglin, Wyss & Pichora, 2000. Mechanical testing of shoulder prostheses and recommendations for glenoid design. *Journal of shoulder and elbow surgery / American Shoulder and Elbow Surgeons ... [et al.]*, 9(4), pp.323–31.

Ansari, Farzana et al., 2014. Analysis of Surface Damage on Retrieved Total Shoulder Replacements: A Comparison to Hips and Knees. In *World Congress Biomechanics*. Boston, Massachusettes.

Ansari, Patten, et al., 2013. Designing for Crosslinked UHMWPE Implants: Clinical Consequences of Stress Concentrations. In *Volume 1B: Extremity; Fluid Mechanics; Gait; Growth, Remodeling, and Repair; Heart Valves; Injury Biomechanics; Mechanotransduction and Sub-Cellular Biophysics; MultiScale Biotransport; Muscle, Tendon and Ligament; Musculoskeletal Devices; Multiscale Mech*. ASME, p. V01BT38A002.

Ansari, Chang, et al., 2013. Fractography and oxidative analysis of gamma inert sterilized posterior-stabilized tibial insert post fractures: report of two cases. *The Knee*, 20(6), pp.609–13.

Ansari, F, Major & Norris, 2014. Unscrewing instability of modular reverse shoulder prosthesis increases propensity for in vivo fracture: a report of two cases. *Journal of shoulder* ….

Arenas et al., 1999. Ceramic femoral head fractures in total hip replacement. *International Orthopaedics*, 23(6), pp.351–352.

Argon et al., 1997. Novel mechanisms of toughening semi-crystalline polymers.

Armstrong & Lewis, 2013. Design Evolution of the Glenoid Component in Total Shoulder Arthroplasty. *JBJS Reviews*, 1(2), pp.e2–e2.

Ast et al., 2014. Fractures of a single design of highly cross-linked polyethylene acetabular liners: an analysis of voluntary reports to the United States Food and Drug Administration. *The Journal of arthroplasty*, 29(6), pp.1231–5.

ASTM International, 2014a. ASTM D638-14:Standard Test Method for Tensile Properties of Polymers.

ASTM International, 2013a. *ASTM E1820-13: Standard Test Method for Measurement of Fracture Toughness*,

ASTM International, 2012a. *ASTM E399-12e3: Standard Test Method for Linear-Elastic Plane-Strain Fracture Toughness KIc of Metallic Materials*,

ASTM International, 2013b. *ASTM E647-13a: Standard Test Method for Measurement of Fatigue Crack Growth Rates*,

ASTM International, 2013c. *ASTM F2580-13: Standard Practice for Evaluation of Modular Connection of Proximally Fixed Femoral Prosthesis*,

ASTM International, 2009a. *F1829-98: Standard Test Method for Static Evaluation of Glenoid Locking Mechanism*,

ASTM International, 2009b. *F1875-98: Standard Practice for Fretting Corrosion Testing of Modular Implant Interfaces: Hip Femoral Head-Bore and Cone Taper Interface*,

ASTM International, 2011. *F2009-00: Standard Test Method for Determining the Axial Disassembly Force of Taper Connections of Modular Prostheses*,

ASTM International, 2012b. *F2028-08: Standard Test Method for Dynamic Evaluation of Glenoid Loosening for Dissociation*,

ASTM International, 2014b. *F2028-14 Standard Test Methods for Dynamic Evaluation of Glenoid Loosening or Disassociation*,

ASTM International, 2010. *Standard Specific for Shoulder Prosthese*,

Atwood, Sara a et al., 2010. Corrosion-induced fracture of a double-modular hip prosthesis: a case report. *The Journal of bone and joint surgery. American volume*, 92(6), pp.1522–5.

Atwood, Sara A et al., 2010. Corrosion-induced fracture of a double-modular hip prosthesis: a case report. *The Journal of bone and joint surgery. American volume*, 92(6), pp.1522–5.

Atwood et al., 2011. Tradeoffs amongst fatigue, wear, and oxidation resistance of cross-linked ultra-high molecular weight polyethylene. *Journal of the Mechanical Behavior of Biomedical Materials*, 4, pp.1033–1045.

De Aza et al., 2002. Crack growth resistance of alumina, zirconia and zirconia toughened alumina ceramics for joint prostheses. *Biomaterials*, 23(3), pp.937–945.

Baker, Bellare & Pruitt, 2003. The effects of degree of crosslinking on the fatigue crack initiation and propagation resistance of orthopedic-grade polyethylene. *Journal of biomedical materials research. Part A*, 66(1), pp.146–54.

Baker, Hastings & Pruitt, 2000. Compression and tension fatigue resistance of medical grade ultra high molecular weight polyethylene: the effect of morphology, sterilization, aging and temperature. *Polymer*, 41(2), pp.795–808.

Baker, Hastings & Pruitt, 1999a. Study of fatigue resistance of chemical and radiation crosslinked medical grade ultrahigh molecular weight polyethylene. *Journal of biomedical materials research*, 46(4), pp.573–81.

Baker, Hastings & Pruitt, 1999b. Study of fatigue resistance of chemical and radiation crosslinked medical grade ultrahigh molecular weight polyethylene. *Journal of biomedical materials research*, 46(4), pp.573–81.

Baker, Pruitt & Bellare, 2001. Ultra-small angle X-ray scattering to detect fatigue damage in polymers. *Journal of materials science letters*, pp.1163–1164.

Bal et al., 2008. Tibial post failures in a condylar posterior cruciate substituting total knee arthroplasty. *The Journal of arthroplasty*, 23(5), pp.650–5.

Banks, Harman & Hodge, 2002. Mechanism of anterior impingement damage in total knee arthroplasty. *The Journal of bone and joint surgery. American volume*, 84-A Suppl, pp.37–42.

Barsom & McNicol, 1974. Effect of stress concentration on fatigue crack initiation in HY-130 steel. *ASTM STP*, 559, pp.183–204.

Bartel et al., 1995. Stresses in polyethylene components of contemporary total knee replacements. *Clinical orthopaedics and related research*, (317), pp.76–82.

Bartel, Bicknell & Wright, 1986. The effect of conformity, thickness, and material on stresses in ultra-high molecular weight components for total joint replacement. *The Journal of bone and joint surgery. American volume*, 68(7), pp.1041–51.

Bartel, Davy & Keaveny, 2006. *Orthopaedic biomechanics: mechanics and design in musculoskeletal systems*, Pearson/Prentice Hall.

Basquin, 1910. The exponential law of endurance tests. *Proceedings of the American Soceity for Testing and Materials*, 10, pp.625–30.

Bhateja, Rieke & Andrews, 1979. Impact fatigue response of ultra-high molecular weight linear polyethylene. *Journal of Materials Science*, 14(9), pp.2103–2109.

Bhattacharya & Kumar, 1995. Rotational factor using bending moment approach under elasto-plastic situation—I. Notch 3PB geometry. *Engineering fracture mechanics*.

Bicknell et al., 2007. Glenoid vault endosteal dimensions: an anthropometric study with special interest in implant design. *Journal of shoulder and elbow surgery / American Shoulder and Elbow Surgeons ... [et al.]*, 16(3 Suppl), pp.S96–101.

Biomet Inc, 1999a. *Bio-Modular Shoulder System Summary of Safety and Effectiveness (K992119),* Rockville, MD.

Biomet Inc, 1999b. *Bipolar Shoulder Prosthesis Summary of Safety and Effectiveness (K991585),* Rockville, MD.

Birman et al., 2005. Cracking and impingement in ultra-high-molecular-weight polyethylene acetabular liners. *The Journal of arthroplasty*, 20(7 Suppl 3), pp.87–92.

Blumenfeld et al., 2011. Fracture of a cross-linked polyethylene liner: a multifactorial issue. *The Journal of arthroplasty*, 26(4), pp.666.e5–8.

Bohl et al., 1999. The Coventry Award. The effects of shelf life on clinical outcome for gamma sterilized polyethylene tibial components. *Clinical orthopaedics and related research*, (367), pp.28–38.

Bohsali, KI, MA & Rockwood Jr, 2006. Complications of total shoulder arthroplasty. *J Bone Joint Surg [Am]*, 88(10), pp.2279–2292.

Bohsali, Kamal I, Wirth & Rockwood, 2006. Complications of total shoulder arthroplasty. *The Journal of bone and joint surgery. American volume*, 88(10), pp.2279–92.

Bozic et al., 2009. The epidemiology of revision total hip arthroplasty in the United States. *The Journal of bone and joint surgery. American volume*, 91(1), pp.128–33.

Bozic et al., 2010. The epidemiology of revision total knee arthroplasty in the United States. *Clinical orthopaedics and related research*, 468(1), pp.45–51.

Bradford et al., 2004. Fatigue Crack Propagation Resistance of Highly Crosslinked Polyethylene. *Clinical Orthopaedics and Related Research*, 429(429), pp.68–72.

Bragdon et al., 2004. Biologic fixation of total hip implants. Insights gained from a series of canine studies. *The Journal of bone and joint surgery. American volume*, 86-A Suppl, pp.105–17.

Brien et al., 1990. Dissociation of acetabular components after total hip arthroplasty. Report of four cases. *The Journal of bone and joint surgery. American volume*, 72(10), pp.1548–50.

Burger, de Vaal & Meyer, 2007. Failure analysis on retrieved ultra high molecular weight polyethylene (UHMWPE) acetabular cups. *Engineering Failure Analysis*, 14(7), pp.1329–1345.

Burstein, 1986. Failure analysis of a total hip femoral component: a fracture mechanics approach. *Case Histories Involving Fatigue and Fracture …*.

Callaghan et al., 2002. Tibial post impingement in posterior-stabilized total knee arthroplasty. *Clinical orthopaedics and related research*, (404), pp.83–8.

Callister, 2003. *Material Science and Engineering, an Introduction* 6th ed., John Wiley & Sons, Inc.

Campbell ed., 2012. Introduction to Fatigue and Fracture. In *Fatigue and Fracture - Understanding the Basics*. ASM International.

Chacon, Virani & Shannon, 2009. Revision arthroplasty with use of a reverse shoulder prosthesis-allograft composite. *The Journal of Bone & …*.

Charnley, 1961. Arthroplasty of the hip. A new operation. *Lancet*, 1(7187), pp.1129–32.

Charnley, 1963. Tissue Reactions to Polytetrafluorethylene. *The Lancet*, 282(7322), p.1379.

Chen, Pan & Chen, 1978. Collection of papers on fracture of metals. *Metallurgy Industry Press, Beejing*.

Chevalier, 2006. What future for zirconia as a biomaterial? *Biomaterials*, 27(4), pp.535–43.

Chiu et al., 2004. Fracture of the polyethylene tibial post in a NexGen posterior-stabilized knee prosthesis. *The Journal of Arthroplasty*, 19(8), pp.1045–1049.

Choudhury & Hutchings, 1997. The effects of irradiation and ageing on the abrasive wear resistance of ultra high molecular weight polyethylene. *Wear*, 203-204, pp.335–340.

Chuinard et al., 2006. Humeral problems in reverse total shoulder arthroplasty. *Reverse Shoulder Arthroplasty. …*.

Clarke, Math & Scuderi, 2004. Polyethylene post failure in posterior stabilized total knee arthroplasty. *The Journal of Arthroplasty*, 19(5), pp.652–657.

Coffin, 1954. A study of the effect of cyclic thermal stresses on a ductile metal. In *Transactions of the American Society of Mechanical Engineering*. pp. 931–950.

Cole, Lemons & Eberhardt, 2002. Gamma irradiation alters fatigue-crack behavior and fracture toughness in 1900H and GUR 1050 UHMWPE. *Journal of biomedical materials research*, 63(5), pp.559–66.

Collier et al., 1990. The biomechanical problems of polyethylene as a bearing surface. *Clinical orthopaedics and related research*, (261), pp.107–13.

Connelly et al., 1984. Fatigue crack propagation behavior of ultrahigh molecular weight polyethylene. *Journal of orthopaedic research : official publication of the Orthopaedic Research Society*, 2(2), pp.119–25.

Constable, Culver & Williams, 1970. Notch root radii effects in the fatigue of polymers. *International Journal of Fracture Mechanics*, 6(3).

Cornwall et al., 1997. Surface degradation features and microstructural properties of ultra-high molecular weight polyethylene (UHMWPe). *Journal of Materials Science: Materials in Medicine*, 8(5), pp.303–309.

Creager & Paris, 1967. Elastic field equations for blunt cracks with reference to stress corrosion cracking. *International Journal of Fracture Mechanics*.

Cuff et al., 2011. Torsional stability of modular and non-modular reverse shoulder humeral components in a proximal humeral bone loss model. *Journal of Shoulder and Elbow …*.

Currier et al., 2010. In vivo oxidation in remelted highly cross-linked retrievals. *The Journal of bone and joint surgery. American volume*, 92(14), pp.2409–18.

Currier et al., 2013. In vivo oxidation in retrieved highly crosslinked tibial inserts. *Journal of biomedical materials research. Part B, Applied biomaterials*, 101(3), pp.441–8.

Currier et al., 2007. In vivo oxidation of gamma-barrier-sterilized ultra-high-molecular-weight polyethylene bearings. *The Journal of arthroplasty*, 22(5), pp.721–31.

D'Angelo et al., 2010. Two stage fracture of a polyethylene post in a 9-year-old posterior-stabilized knee prosthesis: a case report. *Journal of medical case reports*, 4, p.65.

Dauskardt et al., 1994. Cyclic fatigue and fracture in pyrolytic carbon-coated graphite mechanical heart-valve prostheses: role of small cracks in life prediction. *Journal of biomedical materials research*, 28(7), pp.791–804.

Day et al., 2010. Prevalence and projections of total shoulder and elbow arthroplasty in the United States to 2015. *Journal of shoulder and elbow surgery / American Shoulder and Elbow Surgeons ... [et al.]*, 19(8), pp.1115–20.

Delaynay, 2014. The Charnley Total Hip Replacement: The Gold Standard of primary hip replacement, 36 years on. *Maitrise Orthopedique*.

Depuy, 2013. *PINNACLE® Hip Solutions: Polyethylene Surgical Technique (Catalog)*, DePuy Synthes Joint Reconstruction.

Depuy Inc, 2003. *510(k) Summary Delta Shoulder (K021478)*, Rockville, MD.

Depuy Inc, 1999. *Global Advantage Shoulder Summary of Safety and Effectiveness (K992065)*, Rockville, MD.

Deshmukh et al., 2005. Total shoulder arthroplasty: long-term survivorship, functional outcome, and quality of life. *Journal of shoulder and elbow surgery / American Shoulder and Elbow Surgeons ... [et al.]*, 14(5), pp.471–9.

Doorn et al., 1996. Tissue reaction to metal on metal total hip prostheses. *Clinical orthopaedics and related research*, (329 Suppl), pp.S187–205.

Dowling, 1979a. Fatigue at notches and the local strain and fracture mechanics approaches. *PRoceedings of the Eleventh National Symposium on Fracture Mechanics: Part I*, ASTM STP 6.

Dowling, 1976. Geometry effects and the J-integral approach to elastic-plastic fatigue crack growth. *ASTM special technical publication*.

Dowling, 1993. Mechanical behavior of materials : engineering methods for deformation, fracture, and fatigue.

Dowling, 1979b. Notched member fatigue life predictions combining crack initiation and propagation. *Fatigue & Fracture of Engineering Materials & Structures*, 2(2), pp.129–138.

Dowling & Begley, 1976. Fatigue crack growth during gross plasticity and the J-integral. *ASTM special technical publication*, (590), pp.82–103.

Dowling & Wilson, 1984. Results of elastic analysis of bluntly notched compact specimens. *Engineering Fracture Mechanics*, 20(3), pp.569–572.

Drake, O'Connor & Edwards, 2010. Indications for reverse total shoulder arthroplasty in rotator cuff disease. *Clinical Orthopaedics and Related …*.

Duffy et al., 2009. Fracture of a cross-linked polyethylene liner due to impingement. *The Journal of arthroplasty*, 24(1), pp.158.e15–9.

Dumbleton, 2002. A literature review of the association between wear rate and osteolysis in total hip arthroplasty. *The Journal of Arthroplasty*, 17(5), pp.649–661.

Dumbleton, 1981. *Tribology of Natural and Artificial Joints (Google eBook)*, Elsevier.

Dumbleton, Manley & Edidin, 2002. A literature review of the association between wear rate and osteolysis in total hip arthroplasty. *The Journal of Arthroplasty*, 17(5), pp.649–661.

Edidin et al., 1999. Plasticity-induced damage layer is a precursor to wear in radiation-cross-linked UHMWPE acetabular components for total hip replacement. *The Journal of Arthroplasty*, 14(5), pp.616–627.

Elbert et al., 1994. Fatigue crack propagation behavior of ultra high molecular weight polyethylene under mixed mode conditions. *Journal of biomedical materials research*, 28(2), pp.181–7.

Ellman & Levine, 2013. Fracture of the modular femoral neck component in total hip arthroplasty. *The Journal of arthroplasty*, 28(1), pp.196.e1–5.

Espehaug et al., 2009. 18 years of results with cemented primary hip prostheses in the Norwegian Arthroplasty Register: concerns about some newer implants. *Acta orthopaedica*, 80(4), pp.402–12.

Ewald, 1975. Metal to plastic total knee replacement. *The Orthopedic clinics of North America*, 6(3), pp.811–21.

Eyerer et al., 1987. Characterization of UHMWPE hip cups run on joint simulators. *Journal of biomedical materials research*, 21(3), pp.275–91.

Favard, Levigne & Nerot, 2011. Reverse prostheses in arthropathies with cuff tear: are survivorship and function maintained over time? *… and Related Research®*.

Fehring et al., 1999. Motion at the modular acetabular shell and liner interface. A comparative study. *Clinical orthopaedics and related research*, (367), pp.306–14.

Fisher et al., 1994. The effect of sliding velocity on the friction and wear of UHMWPE for use in total artificial joints. *Small*, 175, pp.219–225.

Fouad, 2010a. Experimental and numerical studies of the notch strengthening behaviour of semi-crystalline ultra-high molecular weight polyethylene. *Materials & Design*, 31(3), pp.1117–1129.

Fouad, 2010b. Experimental and numerical studies of the notch strengthening behaviour of semi-crystalline ultra-high molecular weight polyethylene. *Materials & Design*, 31(3), pp.1117–1129.

Fox et al., 2009. Survival of the glenoid component in shoulder arthroplasty. *Journal of shoulder and elbow surgery / American Shoulder and Elbow Surgeons ... [et al.]*, 18(6), pp.859–63.

Frost, 1960. Notch effects and the critical alternating stress required to propagate a crack in an aluminium alloy subject to fatigue loading. *Journal of Mechanical Engineering Science*.

Frost & Dugdale, 1957. Fatigue tests on notched mild steel plates with measurements of fatigue cracks. *Journal of the Mechanics and Physics of Solids*, 5(3), pp.182–192.

Frost, Marsh & Pook, 1999. *Metal fatigue*, Mineola, New York: Dover Publications, Inc.

Furman et al., 2008. Tibial post wear in posterior-stabilized knee replacements is design-dependent. *Clinical orthopaedics and related research*, 466(11), pp.2650–5.

Furmanski et al., 2009. Clinical fracture of cross-linked UHMWPE acetabular liners. *Biomaterials*, 30(29), pp.5572–82.

Furmanski, Kraay & Rimnac, 2011. Crack initiation in retrieved cross-linked highly cross-linked ultrahigh-molecular-weight polyethylene acetabular liners: an investigation of 9 cases. *The Journal of arthroplasty*, 26(5), pp.796–801.

Furmanski & Pruitt, 2007a. Peak stress intensity dictates fatigue crack propagation in UHMWPE. *Polymer*, 48(12), pp.3512–3519.

Furmanski & Pruitt, 2007b. Peak stress intensity dictates fatigue crack propagation in UHMWPE. *Polymer*, 48(12), pp.3512–3519.

Furmanski & Rimnac, 2011. Crack propagation resistance is similar under static and cyclic loading in crosslinked UHMWPE: a pilot study. *Clinical orthopaedics and related research*, 469(8), pp.2302–7.

Furmanski, Sirimamilla & Rimnac, 2011. Mechanics of Time-Dependent Materials and Processes in Conventional and Multifunctional Materials, Volume 3 T. Proulx, ed. , 3, pp.295–301.

Ge, Kang & Zhao, 2011. One-year biodegradation study of UHMWPE as artificial joint materials: Variation of chemical structure and effect on friction and wear behavior. *Wear*, 271(9-10), pp.2354–2363.

Gencur, Rimnac & Kurtz, 2003. Failure micromechanisms during uniaxial tensile fracture of conventional and highly crosslinked ultra-high molecular weight polyethylenes used in total joint replacements. *Biomaterials*, 24(22), pp.3947–3954.

Gencur, Rimnac & Kurtz, 2006. Fatigue crack propagation resistance of virgin and highly crosslinked, thermally treated ultra-high molecular weight polyethylene. *Biomaterials*, 27(8), pp.1550–7.

Gerrits & Tervoort, 1992. Deformation mechanisms during uniaxial drawing of melt-crystallized ultra-high molecular weight polyethylene. *Journal of Materials Science*, 27(5), pp.1385–1390.

Glinka, 1985a. Calculation of inelastic notch-tip strain-stress histories under cyclic loading. *Engineering Fracture Mechanics*.

Glinka, 1985b. Energy density approach to calculation of inelastic strain-stress near notches and cracks. *Engineering Fracture Mechanics*.

Glinka & Newport, 1987. Universal features of elastic notch-tip stress fields. *International Journal of Fatigue*, 9(3), pp.143–150.

Goldman & Pruitt, 1998. Comparison of the effects of gamma radiation and low temperature hydrogen peroxide gas plasma sterilization on the molecular structure, fatigue resistance, and wear behavior of UHMWPE. *Journal of biomedical materials research*, 40(3), pp.378–84.

Gomoll, A., Wanich & Bellare, 2002. J-integral fracture toughness and tearing modulus measurement of radiation cross-linked UHMWPE. *Journal of Orthopaedic Research*, 20, pp.1152–1156.

Gomoll, a, Wanich & Bellare, 2002. J-integral fracture toughness and tearing modulus measurement of radiation cross-linked UHMWPE. *Journal of orthopaedic research : official publication of the Orthopaedic Research Society*, 20(6), pp.1152–6.

González della Valle et al., 2001. Dislodgment of polyethylene liners in first and second-generation Harris-Galante acetabular components. A report of eighteen cases. *The Journal of bone and joint surgery. American volume*, 83-A(4), pp.553–9.

Gregory et al., 2009. Glenoid loosening after total shoulder arthroplasty: an in vitro CT-scan study. *Journal of orthopaedic research : official publication of the Orthopaedic Research Society*, 27(12), pp.1589–95.

Griffith, 1921. The Phenomena of Rupture and Flow in Solids. *Philosophical Transactions of the Royal Society A: Mathematical, Physical and Engineering Sciences*, 221(582-593), pp.163–198.

Grivas et al., 2007. Neck fracture of a cementless forged titanium alloy femoral stem following total hip arthroplasty: a case report and review of the literature. *Journal of medical case reports*, 1, p.174.

Gul et al., 2003. Effect of consolidation on adhesive and abrasive wear of ultra high molecular weight polyethylene. *Biomaterials*, 24(19), pp.3193–3199.

Gunther et al., 2002. Retrieved glenoid components: A classification system for surface damage analysis. *The Journal of Arthroplasty*, 17(1), pp.95–100.

Haddad & Dowling, 1980. J integral applications for short fatigue cracks at notches. *International Journal of* ….

El Haddad, Smith & Topper, 1979. Fatigue Crack Propagation of Short Cracks. *Journal of Engineering Materials and Technology*, 101(1), p.42.

Haddad, Smith & Topper, 1978. A strain based intensity factor solution for short fatigue cracks initiating from notches. *Fracture Mechanics*.

Hailer, Garellick & Kärrholm, 2010. Uncemented and cemented primary total hip arthroplasty in the Swedish Hip Arthroplasty Register. *Acta orthopaedica*, 81(1), pp.34–41.

Halley, Glassman & Crowninshield, 2004. Recurrent dislocation after revision total hip replacement with a large prosthetic femoral head. A case report. *The Journal of bone and joint surgery. American volume*, 86-A(4), pp.827–30.

Hamai et al., 2008. Evaluation of impingement of the anterior tibial post during gait in a posteriorly-stabilised total knee replacement. *The Journal of bone and joint surgery. British volume*, 90(9), pp.1180–5.

Hammouda & Miller, 1979. Elastic-plastic fracture mechanics analyses of notches. *ASTM special technical publication*.

Harman et al., 2011. A pictographic atlas for classifying damage modes on polyethylene bearings. *Journal of materials science. Materials in medicine*, 22(5), pp.1137–46.

Harris, 1995. The problem is osteolysis. *Clinical orthopaedics and related research*, (311), pp.46–53.

Harris & Jasty, 1985. Bone ingrowth into porous coated canine acetabular replacements: the effect of pore size, apposition, and dislocation. *The Hip*, pp.214–34.

Hendel, Garti & Weisbort, 2003. Fracture of the central polyethylene tibial spine in posterior stabilized total knee arthroplasty. *The Journal of Arthroplasty*, 18(5), pp.672–674.

Hertel & Ballmer, 2003. Observations on retrieved glenoid components. *The Journal of arthroplasty*, 18(3), pp.361–6.

Hertzberg & Manson, 1980. *Fatigue of engineering plastics*, Academic Press.

Hood, Wright & Burstein, 1983. Retrieval analysis of total knee prostheses: a method and its application to 48 total condylar prostheses. *Journal of biomedical materials research*, 17(5), pp.829–42.

Huang et al., 2006. Influence of post-cam design on stresses on posterior-stabilized tibial posts. *Clinical orthopaedics and related research*, 450, pp.150–6.

Huang et al., 2007. Stress Analysis of the Anterior Tibial Post in Posterior Stabilized Knee Prostheses. , (155), pp.442–449.

Huot et al., 2010. Evaluating the suitability of highly cross-linked and remelted materials for use in posterior stabilized knees. *Journal of biomedical materials research. Part B, Applied biomaterials*, 95(2), pp.298–307.

Hutchinson, 1968. Singular behaviour at the end of a tensile crack in a hardening material. *Journal of the Mechanics and Physics of Solids*, 16(1), pp.13–31.

Inglis, 1913. Stresses in a Plate Due to the Presence of Cracks and Sharp Corners. *Transactions of the Institute of Naval Architecst*, 55, pp.219–241.

Insall et al., 1976. Total condylar knee replacment: preliminary report. *Clinical orthopaedics and related research*, (120), pp.149–54.

Insall, Tria & Scott, 1979. The total condylar knee prosthesis: the first 5 years. *Clinical orthopaedics and related research*, (145), pp.68–77.

International Standards Organization, ISO 11542-1:2001 - Plastics -- Ultra-high-molecular-weight polyethylene (PE-UHMW) moulding and extrusion materials -- Part 1: Designation system and basis for specifications.

International Standards Organization, ISO 527-1:2012 - Plastics -- Determination of tensile properties -- Part 1: General principles.

International Standards Organization, *ISO 527-2:2012 - Plastics -- Determination of tensile properties -- Part 2: Test conditions for moulding and extrusion plastics*,

International Standards Organization, 2010. *ISO 7206-4:2010 - Implants for surgery—Partial and total hip joint prostheses—Part 4: Determination of endurance properties and performance of stemmed femoral components*,

Irwin, 1957. Analysis of stresses and strains near the end of a crack traversing a plate. *Journla of Applied Mechanics*, 24, pp.361–4.

Irwin, 1960. Plastic zone near a crack and fracture toughness. In *Proceedings of the Seventh Sagamore Ordnance Materials Conference*. New York: Syracuse University, pp. 63–78.

Jahan et al., 1991. Combined chemical and mechanical effects on free radicals in UHMWPE joints during implantation. *Journal of biomedical materials research*, 25(8), pp.1005–17.

Jarrett et al., 2009. The squeaking hip: a phenomenon of ceramic-on-ceramic total hip arthroplasty. *The Journal of bone and joint surgery. American volume*, 91(6), pp.1344–9.

Jung et al., 2008. Fracture of a second-generation highly cross-linked UHMWPE tibial post in a posterior-stabilized scorpio knee system. *Orthopedics*, 31(11), p.1137.

Karduna et al., 1998. Total Shoulder Arthroplasty Biomechanics: A Study of the Forces and Strains at the Glenoid Component. *Journal of Biomechanical Engineering*, 120(1), p.92.

Kennedy et al., 2000. Contact Fatigue Failure of Ultra-High Molecular Weight Polyethylene Bearing Components of Knee Prostheses. *Journal of Tribology*, 122(1), p.332.

Khan et al., 2005a. Analysis and evaluation of a biomedical polycarbonate urethane tested in an in vitro study and an ovine arthroplasty model. Part I: materials selection and evaluation. *Biomaterials*, 26(6), pp.621–31.

Khan et al., 2005b. Analysis and evaluation of a biomedical polycarbonate urethane tested in an in vitro study and an ovine arthroplasty model. Part II: in vivo investigation. *Biomaterials*, 26(6), pp.633–43.

Kim, Fine & Mura, 1979. Plastic yielding at the tip of a blunt notch during static and fatigue loading. *Engineering Fracture Mechanics*, 11(4), pp.653–660.

Klapperich, Komvopoulos & Pruitt, 1999. Tribological Properties and Microstructure Evolution of Ultra-High Molecular Weight Polyethylene. *Journal of Tribology*, 121(2), p.394.

Klesnil & Lukáš, 1992. *Fatigue of Metallic Materials*, Elsevier.

Krzypow & Rimnac, 2000. Cyclic steady state stress–strain behavior of UHMW polyethylene. *Biomaterials*, 21(20), pp.2081–7.

Kujawski, 1991. Estimations of stress intensity factors for small cracks at notches. *Fatigue & Fracture of Engineering Materials & …*.

Kurtz, 1999. Advances in the processing, sterilization, and crosslinking of ultra-high molecular weight polyethylene for total joint arthroplasty. *Biomaterials*, 20(18), pp.1659–1688.

Kurtz et al., 2006. Anisotropy and oxidative resistance of highly crosslinked UHMWPE after deformation processing by solid-state ram extrusion. *Biomaterials*, 27(1), pp.24–34.

Kurtz, Steven M et al., 1998. Backside nonconformity and locking restraints affect liner/shell load transfer mechanisms and relative motion in modular acetabular components for total hip replacement. *Journal of Biomechanics*, 31(5), pp.431–437.

Kurtz et al., 2009. Future young patient demand for primary and revision joint replacement: national projections from 2010 to 2030. *Clinical orthopaedics and related research*, 467(10), pp.2606–12.

Kurtz et al., 2005. Prevalence of primary and revision total hip and knee arthroplasty in the United States from 1990 through 2002. *The Journal of bone and joint surgery. American volume*, 87(7), pp.1487–97.

Kurtz et al., 2007. Projections of primary and revision hip and knee arthroplasty in the United States from 2005 to 2030. *The Journal of bone and joint surgery. American volume*, 89(4), pp.780–5.

Kurtz et al., 2000. The relationship between the clinical performance and large deformation mechanical behavior of retrieved UHMWPE tibial inserts. *Biomaterials*, 21(3), pp.283–291.

Kurtz, Steven M. et al., 1998. The yielding, plastic flow, and fracture behavior of ultra-high molecular weight polyethylene used in total joint replacements. *Biomaterials*, 19(21), pp.1989–2003.

Kurtz et al., 2002. Thermomechanical behavior of virgin and highly crosslinked ultra-high molecular weight polyethylene used in total joint replacements. *Biomaterials*, 23(17), pp.3681–3697.

Kurtz ed., 2009. *UHMWPE Biomaterials Handbook* 2nd ed., Academic Press.

Kurtz, Gawel & Patel, 2011. History and systematic review of wear and osteolysis outcomes for first-generation highly crosslinked polyethylene. *Clinical orthopaedics and related research*, 469(8), pp.2262–77.

Laird & Smith, 1962. Crack propagation in high stress fatigue. *Philosophical Magazine*, 7(77), pp.847–857.

Lam, Drew & Boscainos, 2013. Effect of acetabular orientation on stress distribution of highly cross-linked polyethylene liners. *Orthopedics*, 36(11), pp.e1346–52.

Lee et al., 2009. Early nontraumatic fracture of the polyethylene tibial post in a NexGen LPS-Flex posterior stabilized knee prosthesis. *The Journal of arthroplasty*, 24(8), pp.1292.e5–9.

Levy & Virani, 2007. Use of the reverse shoulder prosthesis for the treatment of failed hemiarthroplasty in patients with glenohumeral arthritis and rotator cuff deficiency. *Journal of Bone & Joint* ….

Li et al., 2005. Anterior tibial post impingement in a posterior stabilized total knee arthroplasty. *Journal of orthopaedic research : official publication of the Orthopaedic Research Society*, 23(3), pp.536–41.

Li et al., 2004. Knee kinematics with a high-flexion posterior stabilized total knee prosthesis: an in vitro robotic experimental investigation. *The Journal of bone and joint surgery. American volume*, 86-A(8), pp.1721–9.

Li & Burstein, 1994. Ultra-high molecular weight polyethylene. The material and its use in total joint implants. *The Journal of bone and joint surgery. American volume*, 76(7), pp.1080–90.

Lin & Argon, 1994. Structure and plastic deformation of polyethylene. *Journal of Materials Science*, 29(2), pp.294–323.

Livingston et al., 1997. Complications of total hip arthroplasty associated with the use of an acetabular component with a Hylamer liner. *The Journal of bone and joint surgery. American volume*, 79(10), pp.1529–38.

Lombardi et al., 1993. Dislocation following primary posterior-stabilized total knee arthroplasty. *The Journal of Arthroplasty*, 8(6), pp.633–639.

Lu, Qian & Brown, Notchology-the effect of the notching method on the slow crack growth failure in a tough polyethylene. *Journal of Materials Science*, 26(4), pp.881–888.

Lukáš, 1987. Stress intensity factor for small notch-emanated cracks. *Engineering Fracture Mechanics*, 26(3), pp.471–473.

Lukáš & Klesnil, 1978. Fatigue limit of notched bodies. *Materials Science and Engineering*, 34(1), pp.61–66.

Manson, 1954. Behavior of materials under conditions of thermal stress.

Mariconda, Lotti & Milano, 2000. Fracture of posterior-stabilized tibial insert in a genesis knee prosthesis. *The Journal of Arthroplasty*, 15(4), pp.529–530.

Massimini, Li & Warner, 2010. Glenohumeral contact kinematics in patients after total shoulder arthroplasty. *The Journal of bone and joint surgery. American volume*, 92(4), pp.916–26.

Matsen, Boileau & Walch, 2007. The reverse total shoulder arthroplasty. *The Journal of Bone & ….*

Mauerhan, 2003. Fracture of the polyethylene tibial post in a posterior cruciate-substituting total knee arthroplasty mimicking patellar clunk syndrome: a report of 5 cases. *The Journal of arthroplasty*, 18(7), pp.942–5.

McKellop, Shen, Lu, et al., 1999. Development of an extremely wear-resistant ultra high molecular weight polyethylene for total hip replacements. *Journal of orthopaedic research : official publication of the Orthopaedic Research Society*, 17(2), pp.157–67.

McKellop, 2007. The lexicon of polyethylene wear in artificial joints. *Biomaterials*, 28(34), pp.5049–57.

McKellop, Shen, DiMaio, et al., 1999. Wear of gamma-crosslinked polyethylene acetabular cups against roughened femoral balls. *Clinical orthopaedics and related research*, (369), pp.73–82.

McKelvey & Ritchie, 1999. Fatigue-crack propagation in Nitinol, a shape-memory and superelastic endovascular stent material.

Medel et al., 2007. Comparative fatigue behavior and toughness of remelted and annealed highly crosslinked polyethylenes. *Journal of biomedical materials research. Part B, Applied biomaterials*, 83, pp.380–390.

Medel, Kurtz, Parvizi, et al., 2011. In vivo oxidation contributes to delamination but not pitting in polyethylene components for total knee arthroplasty. *The Journal of arthroplasty*, 26(5), pp.802–10.

Medel et al., 2013. Microstructure, thermooxidation and mechanical behavior of a novel highly linear, vitamin E stabilized, UHMWPE. *Materials Science and Engineering: C*, 33(1), pp.182–188.

Medel, Kurtz, Sharkey, et al., 2011. Post damage in contemporary posterior-stabilized tibial inserts: influence of implant design and clinical relevance. *The Journal of arthroplasty*, 26(4), pp.606–14.

Melvin et al., 2014. Early failures in total hip arthroplasty -- a changing paradigm. *The Journal of arthroplasty*, 29(6), pp.1285–8.

Mestha, Shenava & D'Arcy, 2000. Fracture of the polyethylene tibial post in posterior stabilized (Insall Burstein II) total knee arthroplasty. *The Journal of arthroplasty*, 15(6), pp.814–5.

Meyer & Pruitt, 2001. The effect of cyclic true strain on the morphology, structure, and relaxation behavior of ultra high molecular weight polyethylene. *Polymer*, 42(12), pp.5293–5306.

Micheli et al., 2012. Knee simulator wear of vitamin E stabilized irradiated ultrahigh molecular weight polyethylene. *The Journal of arthroplasty*, 27(1), pp.95–104.

Mihalko & Papademetriou, 2001. Polyethylene liner dissociation with the Harris-Galante II acetabular component. *Clinical orthopaedics and related research*, (386), pp.166–72.

Mikulak et al., 2001. Loosening and osteolysis with the press-fit condylar posterior-cruciate-substituting total knee replacement. *The Journal of bone and joint surgery. American volume*, 83-A(3), pp.398–403.

Mitchell, 1979. *A Unified Predictive Technique for the Fatigue Resistance of Cast Ferrous-Based Metals and High Hardness Wrought Steels*,

Moore et al., 2008. Early failure of a cross-linked polyethylene acetabular liner. A case report. *The Journal of bone and joint surgery. American volume*, 90(11), pp.2499–504.

Morra & Greenwald, 2005. Polymer insert stress in total knee designs during high-flexion activities: a finite element study. *The Journal of bone and joint surgery. American volume*, 87 Suppl 2, pp.120–4.

Muratoglu et al., 2001. A novel method of cross-linking ultra-high-molecular-weight polyethylene to improve wear, reduce oxidation, and retain mechanical properties. Recipient of the 1999 HAP Paul Award. *The Journal of arthroplasty*, 16(2), pp.149–60.

Muratoglu et al., 2003. Optical analysis of surface changes on early retrievals of highly cross-linked and conventional polyethylene tibial inserts. *The Journal of arthroplasty*, 18(7 Suppl 1), pp.42–47.

Muratoglu et al., 1999. Unified wear model for highly crosslinked ultra-high molecular weight polyethylenes (UHMWPE). *Biomaterials*, 20(16), pp.1463–1470.

Nakayama et al., 2005. Contact stress at the post-cam mechanism in posterior-stabilised total knee arthroplasty. *The Journal of bone and joint surgery. British volume*, 87(4), pp.483–8.

Neuber, 1958. Kerbspannungslehre: Grundlagen für genaue Festigkeitsberechnung mit Berücksichtigung von Konstruktionsform und Werkstoff. *Springer*.

Neuber, 1946. *Theory of Notch Stresses* J. Edwards, ed.,

Newman, 1971. An improved method of collocation for the stress analysis of cracked plates with various shaped boundaries.

Newman, 1976. Predicting failure of specimens with either surface cracks or corner cracks at holes.

Ng & Chiu, 2003. Recurrent dislocation of total knee arthroplasty. *The Journal of Arthroplasty*, 18(8), pp.1067–1070.

Nho et al., 2008. Comparison of conforming and nonconforming retrieved glenoid components. *Journal of shoulder and elbow surgery / American Shoulder and Elbow Surgeons ... [et al.]*, 17(6), pp.914–20.

Nho et al., 2009. Observations on retrieved glenoid components from total shoulder arthroplasty. *Journal of shoulder and elbow surgery / American Shoulder and Elbow Surgeons ... [et al.]*, 18(3), pp.371–8.

Niinomi et al., 2001. Fatigue characteristics of ultra high molecular weight polyethylene with different molecular weight for implant material. *Journal of Materials Science: Materials in Medicine*, 12(3), pp.267–272.

Nisitani, 1978. Solutions of notch problems by body force method. *Stress analysis of notch problems.(A 79-40242 17-39) ….*

Norris & Lachiewicz, 1996. Modern cement technique and the survivorship of total shoulder arthroplasty. *Clinical orthopaedics and related research*, (328), pp.76–85.

Nusbaum & Rose, 1979. The effects of radiation sterilization on the properties of ultrahigh molecular weight polyethylene. *Journal of biomedical materials research*, 13(4), pp.557–76.

Oosterom et al., 2003. Translational stiffness of the replaced shoulder joint. *Journal of biomechanics*, 36(12), pp.1897–907.

Oral et al., 2012. A new mechanism of oxidation in ultrahigh molecular weight polyethylene caused by squalene absorption. *Journal of biomedical materials research. Part B, Applied biomaterials*, 100(3), pp.742–51.

Oral et al., 2004. Alpha-tocopherol-doped irradiated UHMWPE for high fatigue resistance and low wear. *Biomaterials*, 25(24), pp.5515–22.

Oral, Malhi, et al., 2008. Highly cross-linked ultrahigh molecular weight polyethylene with improved fatigue resistance for total joint arthroplasty: recipient of the 2006 Hap Paul Award. *The Journal of arthroplasty*, 23(7), pp.1037–44.

Oral et al., 2009. Improved resistance to wear and fatigue fracture in high pressure crystallized vitamin E-containing ultra-high molecular weight polyethylene. *Biomaterials*, 30(10), pp.1870–80.

Oral et al., 2013. Surface cross-linked UHMWPE can enable the use of larger femoral heads in total joints. *Journal of orthopaedic research : official publication of the Orthopaedic Research Society*, 31(1), pp.59–66.

Oral, Godleski Beckos, et al., 2008. The effects of high dose irradiation on the cross-linking of vitamin E-blended ultrahigh molecular weight polyethylene. *Biomaterials*, 29(26), pp.3557–60.

Oral, Ebru, Christensen, et al., 2006. Wear resistance and mechanical properties of highly cross-linked, ultrahigh-molecular weight polyethylene doped with vitamin E. *The Journal of arthroplasty*, 21(4), pp.580–91.

Oral, Ebru, Malhi & Muratoglu, 2006a. Mechanisms of decrease in fatigue crack propagation resistance in irradiated and melted UHMWPE. *Biomaterials*, 27(6), pp.917–25.

Oral, Ebru, Malhi & Muratoglu, 2006b. Mechanisms of decrease in fatigue crack propagation resistance in irradiated and melted UHMWPE. *Biomaterials*, 27(6), pp.917–25.

Oral, E, Rowell & Muratoglu, 2006. The effect of α-tocopherol on the oxidation and free radical decay in irradiated UHMWPE. *Biomaterials*.

Paris, Gomez & Anderson, 1961. A rationale analytic theory of fatigue. *The Trend in Engineering*, 13, pp.9–14.

Parvizi et al., 2004. Fifteen-year clinical survivorship of Harris-Galante total hip arthroplasty. *The Journal of arthroplasty*, 19(6), pp.672–7.

Pascual et al., 2012. Probabilistic assessment of fatigue initiation data on highly crosslinked ultrahigh molecular weight polyethylenes. *Journal of the mechanical behavior of biomedical materials*, 15, pp.190–8.

Paterson et al., 2012. Highly cross-linked vs conventional polyethylene: no differences in rim notching from micromotion on retrieved acetabular liners. *The Journal of arthroplasty*, 27(9), pp.1616–1621.e1.

Patten et al., 2014. Quantifying cross-shear under translation, rolling, and rotation, and its effect on UHMWPE wear. *Wear*, 313(1-2), pp.125–134.

Patten et al., 2013. Wear of UHMWPE from sliding, rolling, and rotation in a multidirectional tribo-system. *Wear*, 304(1-2), pp.60–66.

Pelton et al., 2008. Fatigue and durability of Nitinol stents. *Journal of the mechanical behavior of biomedical materials*, 1(2), pp.153–64.

Pelton, 2011. Nitinol Fatigue: A Review of Microstructures and Mechanisms. *Journal of Materials Engineering and Performance*, 20(4-5), pp.613–617.

Peterson, 1959. Notch Sensitivity. *Metal Fatigue*, pp.293–306.

Peterson & Sines, 1959. *Metal fatigue*, McGraw-hill.

Pierson, 1995. *Endurance: All-Poly Acetabular Cup System (Surgical Technique)*, Depuy Inc.

Pluvinage, 1998. Fatigue and fracture emanating from notch; the use of the notch stress intensity factor. *Nuclear Engineering and Design*, 185(2-3), pp.173–184.

Pluvinage, 2003. *Fracture and Fatigue Emanating from Stress Concentrators*, Springer Science & Business Media.

Pluvinage, 2001. Notch effects in fatigue and fracture. , (Figure I), pp.1–22.

Premnath et al., 1996. Gamma sterilization of UHMWPE articular implants: an analysis of the oxidation problem. Ultra High Molecular Weight Poly Ethylene. *Biomaterials*, 17(18), pp.1741–53.

Promsang, 2013. Stress analysis of a polyethylene acetabular component in the extreme flexion position—a finite element analysis. *Asian Biomed*, 7(6), p.881.

Pruitt et al., 2013. Clinical trade-offs in cross-linked ultrahigh-molecular-weight polyethylene used in total joint arthroplasty. *Journal of biomedical materials research. Part B, Applied biomaterials*, 101(3), pp.476–84.

Pruitt et al., 1995. Cyclic compressive loading results in fatigue cracks in ultra high molecular weight polyethylene. *Journal of orthopaedic research : official publication of the Orthopaedic Research Society*, 13(1), pp.143–6.

Pruitt, 2005. Deformation, yielding, fracture and fatigue behavior of conventional and highly cross-linked ultra high molecular weight polyethylene. *Biomaterials*, 26(8), pp.905–15.

Pruitt & Bailey, 1998a. Factors affecting near-threshold fatigue crack propagation behavior of orthopedic grade ultra high molecular weight polyethylene. *Polymer*, 39(8-9), pp.1545–1553.

Pruitt & Bailey, 1998b. Factors affecting near-threshold fatigue crack propagation behavior of orthopedic grade ultra high molecular weight polyethylene. *Polymer*, 39(8-9), pp.1545–1553.

Pruitt & Chakravartula, 2011. *Mechanics of Biomaterials: Fundamental Principles for Implant Design*, Cambridge University Press.

Pruitt, Hermann & Suresh, 1992. Fatigue crack growth in polymers subjected to fully compressive cyclic loads. *Journal of Materials Science*, 27(6), pp.1608–1616.

Pruitt & Ranganathan, 1995. Effect of sterilization on the structure and fatigue resistance of medical grade UHMWPE. *Materials Science and Engineering: C*, 3(2), pp.91–93.

Pruitt & Suresh, 1994. Cyclic stress fields ahead of tension fatigue cracks in amorphous polymers. *Polymer*, 35(15), pp.3221–3229.

Pruitt & Suresh, 1993. Cyclic stress fields for fatigue cracks in amorphous solids Experimental measurements and their implications. *Philosophical Magazine A*, 67(5), pp.1219–1245.

Pruitt, L, Simis, K, Bistolfi, 2003. The effect of high pressure crystallisation and cross-linking on the fatigue crack inception behavior of medical grade ultra high molecular weight polyethylene. In *12th International Conference on the Deformation, Yield and Fracture of Polymers*. London: IOM Communiciations, Ltd.

Puértolas et al., 2006. Influence of the remelting process on the fatigue behavior of electron beam irradiated UHMWPE. *Journal of biomedical materials research. Part B, Applied biomaterials*, 76(2), pp.346–53.

Puloski et al., 2001. Tibial post wear in posterior stabilized total knee arthroplasty. An unrecognized source of polyethylene debris. *The Journal of bone and joint surgery. American volume*, 83-A(3), pp.390–7.

Raiss et al., 2014. Longitudinal observational study of total shoulder replacements with cement: fifteen to twenty-year follow-up. *The Journal of bone and joint surgery. American volume*, 96(3), pp.198–205.

Reeves et al., 2000. Comparison of gas plasma and gamma irradiation in air sterilization on the delamination wear of the ultra-high molecular weight polyethylene used in knee replacements. *Proceedings of the Institution of Mechanical Engineers, Part H: Journal of Engineering in Medicine*, 214(3), pp.249–255.

Reinitz et al., 2014. Crosslink density, oxidation and chain scission in retrieved, highly cross-linked UHMWPE tibial bearings. *Biomaterials*, 35(15), pp.4436–40.

Rice, 1968. A Path Independent Integral and the Approximate Analysis of Strain Concentration by Notches and Cracks. *Journal of Applied Mechanics*, 35(2), p.379.

Rice & Rosengren, 1968. Plane strain deformation near a crack tip in a power-law hardening material. *Journal of the Mechanics and Physics of Solids*, 16(1), pp.1–12.

Ries et al., 1996. Fatigue strength of polyethylene after sterilization by gamma irradiation or ethylene oxide. *Clinical orthopaedics and related research*, (333), pp.87–95.

Ries & Pruitt, 2005. Effect of Cross-linking on the Microstructure and Mechanical Properties of Ultra-High Molecular Weight Polyethylene. *Clinical Orthopaedics and Related Research*, 440(&NA;), pp.149–156.

Rimnac et al., 1994. Post-irradiation aging of ultra-high molecular weight polyethylene. *The Journal of bone and joint surgery. American volume*, 76(7), pp.1052–6.

Rimnac, Wright & Klein, 1988. J integral measurements of ultra high molecular weight polyethylene. *Polymer Engineering & Science*, 28(24), pp.1586–89.

Ritchie et al., 1990. Cyclic fatigue-crack propagation, stress-corrosion, and fracture-toughness behavior in pyrolytic carbon-coated graphite for prosthetic heart valve applications. *Journal of biomedical materials research*, 24(2), pp.189–206.

Ritchie, 1996. Fatigue and fracture of pyrolytic carbon: a damage- tolerant approach to structural integrity and life prediction in “ceramic” heart valve prostheses. *The Journal of heart valve disease*, 5 Suppl 1, pp.S9–31.

Ritchie, 1977. Influence of microstructure on near-threshold fatigue-crack propagation in ultra-high strength steel. *Metal Science*.

Ritchie, 1988. Mechanisms of fatigue crack propagation in metals, ceramics and composites: role of crack tip shielding. *Materials Science and Engineering: A*.

Ritchie, 1999. Mechanisms of fatigue-crack propagation in ductile and brittle solids. *International Journal of Fracture*, 100(1), pp.55–83.

Ritter et al., 1990. Metal-backed acetabular cups in total hip arthroplasty. *The Journal of bone and joint surgery. American volume*, 72(5), pp.672–7.

Roberts, Ekelund & Renfree, 2007. Radiologic Assessment of Reverse Shoulder Arthroplasty 1. *Radiographics*.

Rockwood & Wirth, 2002. Observation on retrieved Hylamer glenoids in shoulder arthroplasty: Problems associated with sterilization by gamma irradiation in air. *Journal of Shoulder and Elbow Surgery*, 11(2), pp.191–197.

Rodriguez, Bhende & Ranawat, 2001. Total condylar knee replacement: a 20-year followup study. *Clinical orthopaedics and related research*, (388), pp.10–7.

Rooke, 1980. Asymptotic stress intensity factors for fatigue crack-growth calculations. *International Journal of Fatigue*.

Sands & Silver, 2005. Fracture of the polyethylene tibial post in a posterior stabilized PFC total knee arthroplasty. *Orthopedics*, 28(10), pp.1203–4.

Saxena et al., 1985. The behavior of small fatigue cracks at notches in corrosive environments. *International Journal of Fracture*, 28(2), pp.69–82.

Scarlat & Matsen, 2001. Observations on retrieved polyethylene glenoid components. *The Journal of arthroplasty*, 16(6), pp.795–801.

Schijve, 1980. Stress gradients around notches. *Fatigue & Fracture of Engineering Materials & Structures*, 3(4), pp.325–38.

Schijve, 1982. The stress intensity factor of small cracks at notches. *Fatigue & Fracture of Engineering Materials & Structures*, 5(1), pp.77–90.

Schroder et al., 2011. Retrieved highly crosslinked UHMWPE acetabular liners have similar wear damage as conventional UHMWPE. *Clinical orthopaedics and related research*, 469(2), pp.387–94.

Seebauer, 2007. Total reverse shoulder arthroplasty: European lessons and future trends. *AMERICAN JOURNAL OF ORTHOPEDICS-BELLE …*.

Severt et al., 1993. The influence of conformity and constraint on translational forces and frictional torque in total shoulder arthroplasty. *Clinical orthopaedics and related research*, (292), pp.151–8.

Shibata et al., 2003. Defect initiation at subsurface grain boundary as a precursor of delamination in ultrahigh molecular weight polyethylene. *Journal of biomedical materials research. Part A*, 67(1), pp.276–84.

Shibata & Tomita, 2005. The anti-oxidative properties of alpha-tocopherol in gamma-irradiated UHMWPE with respect to fatigue and oxidation resistance. *Biomaterials*, 26(29), pp.5755–62.

Shih & Chou, 2007. Fracture of the Polyethylene Tibial Spine in NexGen Posterior Stabilized Flex Knee Prosthesis: A Case Report. *Journal of Orthopedic Surgery Taiwan*, 24(1), pp.30–34.

Shin & Smith, 1988. Fatigue crack growth at stress concentrations—the role of notch plasticity and crack closure. *Engineering Fracture Mechanics*, 29(3), pp.301–315.

Siebel & Stieler, 1955. Dissimilar stress distributions and cyclic loading. *Z Ver Deutsch Ing*.

Simis et al., 2006. The combined effects of crosslinking and high crystallinity on the microstructural and mechanical properties of ultra high molecular weight polyethylene. *Biomaterials*, 27(9), pp.1688–94.

Sirimamilla, Furmanski & Rimnac, 2013. Application of viscoelastic fracture model and non-uniform crack initiation at clinically relevant notches in crosslinked UHMWPE. *Journal of the mechanical behavior of biomedical materials*, 17(null), pp.11–21.

Sirveaux & Mole, 2010. Failures of the reverse prosthesis: identifying the problems. *Revision and complex shoulder arthroplasty*.

Skwara et al., 2008. Damages of the tibial post in constrained total knee prostheses in the early postoperative course - a scanning electron microscopic study of polyethylene inlays. *BMC musculoskeletal disorders*, 9, p.83.

Smith & Nephew, 2014. R3 Acetabular System.

Smith & Miller, 1977. Fatigue cracks at notches. *International Journal of Mechanical Sciences*.

Smith & Miller, 1978. Prediction of fatigue regimes in notched components. *International Journal of Mechanical Sciences*.

Smithers, Young & Walch, 2011. Reverse shoulder arthroplasty. *Current reviews in musculoskeletal …*.

Sobieraj et al., 2013. Monotonic and fatigue behavior of five clinically relevant conventional and highly crosslinked UHMWPEs in the presence of stress concentrations. *Journal of the mechanical behavior of biomedical materials*, 28, pp.244–53.

Sobieraj et al., 2010. Notched fatigue behavior of PEEK. *Biomaterials*, 31(35), pp.9156–62.

Sobieraj et al., 2008a. Notched stress-strain behavior of a conventional and a sequentially annealed highly crosslinked UHMWPE. *Biomaterials*, 29(35), pp.4575–83.

Sobieraj et al., 2008b. Notched stress-strain behavior of a conventional and a sequentially annealed highly crosslinked UHMWPE. *Biomaterials*, 29(35), pp.4575–83.

Sobieraj, Kurtz & Rimnac, 2005a. Notch strengthening and hardening behavior of conventional and highly crosslinked UHMWPE under applied tensile loading. *Biomaterials*, 26(17), pp.3411–26.

Sobieraj, Kurtz & Rimnac, 2005b. Notch strengthening and hardening behavior of conventional and highly crosslinked UHMWPE under applied tensile loading. *Biomaterials*, 26(17), pp.3411–26.

Sobieraj & Rimnac, 2009a. Ultra high molecular weight polyethylene: mechanics, morphology, and clinical behavior. *Journal of the mechanical behavior of biomedical materials*, 2(5), pp.433–43.

Sobieraj & Rimnac, 2009b. Ultra high molecular weight polyethylene: mechanics, morphology, and clinical behavior. *Journal of the mechanical behavior of biomedical materials*, 2(5), pp.433–43.

Sonntag, Reinders & Kretzer, 2012. What’s next? Alternative materials for articulation in total joint replacement. *Acta biomaterialia*, 8(7), pp.2434–41.

Star et al., 1992. Dissociation of modular hip arthroplasty components after dislocation. A report of three cases at differing dissociation levels. *Clinical orthopaedics and related research*, (278), pp.111–5.

Stoller et al., 2011. Highly crosslinked polyethylene in posterior-stabilized total knee arthroplasty: in vitro performance evaluation of wear, delamination, and tibial post durability. *The Journal of arthroplasty*, 26(3), pp.483–91.

Strauss et al., 2009. The glenoid in shoulder arthroplasty. *Journal of shoulder and elbow surgery / American Shoulder and Elbow Surgeons ... [et al.]*, 18(5), pp.819–33.

Suresh, 1998. *Fatigue of Materials*, Cambridge University Press.

Suresh & Ritchie, 1984. Propagation of short fatigue cracks. *International Metals Reviews*, 29(1), pp.445–475.

Sutula et al., 1995. The Otto Aufranc Award. Impact of gamma sterilization on clinical performance of polyethylene in the hip. *Clinical orthopaedics and related research*, (319), pp.28–40.

Swieszkowski, Bednarz & Prendergast, 2003. Contact stresses in the glenoid component in total shoulder arthroplasty. *Proceedings of the Institution of Mechanical Engineers. Part H, Journal of engineering in medicine*, 217(1), pp.49–57.

Tada, Paris & Irwin, 1985. *The stress analysis of cracks handbook: by Hiroshi Tada, with the cooperation of Paul C. Paris and George R. Irwin*, Paris Productions & (Del Research Corp.).

Tanaka, 1983. Engineering formulae for fatigue strength reduction due to crack-like notches. *International Journal of Fracture*, 22(2), pp.R39–R46.

Tanaka et al., 2008. Influence of Environmental Degradation and Vitamin-E (α-Tocopherol) Addition on the Fatigue Crack Growth Property of Ultra High Molecular Weight Polyethylene. *Journal of the Society of Materials Science, Japan*, 57(9), pp.875–881.

Tanaka & Nakai, 1983. Propagation and non-propagation of short fatigue cracks at a sharp notch. *Fatigue & Fracture of Engineering Materials and Structures*, 6(4), pp.315–327.

Taylor, 1999. Geometrical effects in fatigue: a unifying theoretical model. *International Journal of Fatigue*.

Taylor, 2008. The theory of critical distances. *Engineering Fracture Mechanics*, 75(7), pp.1696–1705.

Taylor & O’Donnell, 1994. Notch geometry effects in fatigue: a conservative design approach. *Engineering Failure Analysis*.

Taylor & Wang, 2000. The validation of some methods of notch fatigue analysis. *Fatigue & fracture of engineering materials & structures*, 23(5), pp.387–394.

Terrier et al., 2009. Comparison of polyethylene wear in anatomical and reversed shoulder prostheses. *The Journal of bone and joint surgery. British volume*, 91(7), pp.977–82.

Terrier, Büchler & Farron, 2006. Influence of glenohumeral conformity on glenoid stresses after total shoulder arthroplasty. *Journal of shoulder and elbow surgery / American Shoulder and Elbow Surgeons ... [et al.]*, 15(4), pp.515–20.

Timoshenko & Goodier, 2014. Theory of elasticity. *… Journal of Bulk Solids Storage in Silos*.

Tomita et al., 1999. Prevention of fatigue cracks in ultrahigh molecular weight polyethylene joint components by the addition of vitamin E. *Journal of biomedical materials research*, 48(4), pp.474–8.

Tornier, 2004. *Aequalis Reversed Shoulder Prosthesis 510(k) Summary (K030941)*, Rockville, MD.

Tower et al., 2007. Rim cracking of the cross-linked longevity polyethylene acetabular liner after total hip arthroplasty. *The Journal of bone and joint surgery. American volume*, 89(10), pp.2212–7.

Unsworth, 1991. Tribology of human and artificial joints. *ARCHIVE: Proceedings of the Institution of Mechanical Engineers, Part H: Journal of Engineering in Medicine 1989-1996 (vols 203-210)*, 205(38), pp.163–172.

Urriés et al., 2004. Comparative cyclic stress-strain and fatigue resistance behavior of electron-beam- and gamma-irradiated ultrahigh molecular weight polyethylene. *Journal of biomedical materials research. Part B, Applied biomaterials*, 70(1), pp.152–60.

US Department of Commerce, 1983. The Economic Effects of Fracture in the United States. *National Bureau of Standards*, Special Pu.

Varadarajan, 2007. *On the Nature of Static and Cyclic Fracture Resistance of Ultra High Molecular Weight Polyethylenes used in Total Joint Replacements*. Case Western Reserve University.

Villarraga, M. L., Edidin, A., Herr, M., & Kurtz, 2004. Multiaxial fatigue behavior of oxidized and unoxidized UHMWPE during cyclic small punch testing at body temperature. *ASTM Special Technical Publication*, 1(1), p.1445.

Waewsawangwong & Goodman, 2012. Unexpected failure of highly cross-linked polyethylene acetabular liner. *The Journal of arthroplasty*, 27(2), pp.323.e1–4.

Wang et al., 1997. Orientation softening in the deformation and wear of ultra-high molecular weight polyethylene. *Wear*, 203-204, pp.230–241.

Wang et al., 2006. Wear, oxidation and mechanical properties of a sequentially irradiated and annealed UHMWPE in total joint replacement. *Journal of Physics D: Applied Physics*, 39(15), pp.3213–3219.

Wasielewski et al., 2005. The acetabular insert-metal backing interface: an additional source of polyethylene wear debris. *The Journal of arthroplasty,* 20(7), pp.914–22.

Werle et al., 2002. Polyethylene liner dissociation in Harris-Galante acetabular components: A report of 7 cases. *The Journal of Arthroplasty*, 17(1), pp.78–81.

Wilde & Walch, 2006. Humeral prosthetic failure of reversed total shoulder arthroplasty: a report of three cases. *Journal of shoulder and elbow surgery*.

Willert & Semlitsch, 1977. Reactions of the articular capsule to wear products of artificial joint prostheses. *Journal of biomedical materials research*, 11(2), pp.157–64.

Williams et al., 1997. Fixation of ultrahigh-molecular-weight polyethylene liners to metal-backed acetabular cups. *The Journal of arthroplasty*, 12(1), pp.25–31.

Williams, 1977. Fracture mechanics of polymers. *Polymer Engineering and Science*, 17(3), pp.144–149.

Williams et al., 2007. Highly Crosslinked Polyethylenes in Hip Replacements: Improved Wear Performance or Paradox? *Tribology Transactions*, 50(2), pp.277–290.

Williams, 1957. On the stress distribution at the base of a stationary crack. *Journal of Applied Mechanics*, 24, pp.109–14.

Williams, Mayor & Collier, 1998. The impact of sterilization method on wear in knee arthroplasty. *Clinical orthopaedics and related research*, (356), pp.170–80.

Wilson, 1974. Elastic-Plastic Analysis of Blunt Notched CT Specimens and Applications. *Journal of Pressure Vessel Technology*, 96(4), p.293.

Wolf, 1970. Fatigue crack closure under cyclic tension. *Engineering Fracture Mechanics*, 2(1), pp.37–45.

Wolf et al., 2006. Stabilisation of crosslinked ultra-high molecular weight polyethylene (UHMW-PE)-acetabular components with alpha-tocopherol. *Journal of materials science. Materials in medicine*, 17(12), pp.1323–31.

Wright & Bartel, 1986. The problem of surface damage in polyethylene total knee components. *Clinical orthopaedics and related research*, (205), pp.67–74.

Yates et al., 2008. Fractures of modern high nitrogen stainless steel cemented stems: cause, mechanism, and avoidance in 14 cases. *The Journal of arthroplasty*, 23(2), pp.188–96.

Young et al., 2000. Wear Testing of UHMWPE Tibial Components: Influence of Oxidation. *Journal of Tribology*, 122(1), p.323.

Zimmer, 2014a. Zimmer Longevity.

Zimmer, 2014b. Zimmer Trilogy Acetabular Hip System.

Zumstein et al., 2011. Problems, complications, reoperations, and revisions in reverse total shoulder arthroplasty: a systematic review. *Journal of Shoulder and Elbow* ….

# Appendix A – Supplemental Plots

This appendix provides additional plots produced for computational analysis of the notch plastic zone size for each notch root radii evaluated in **Chapter 5**.

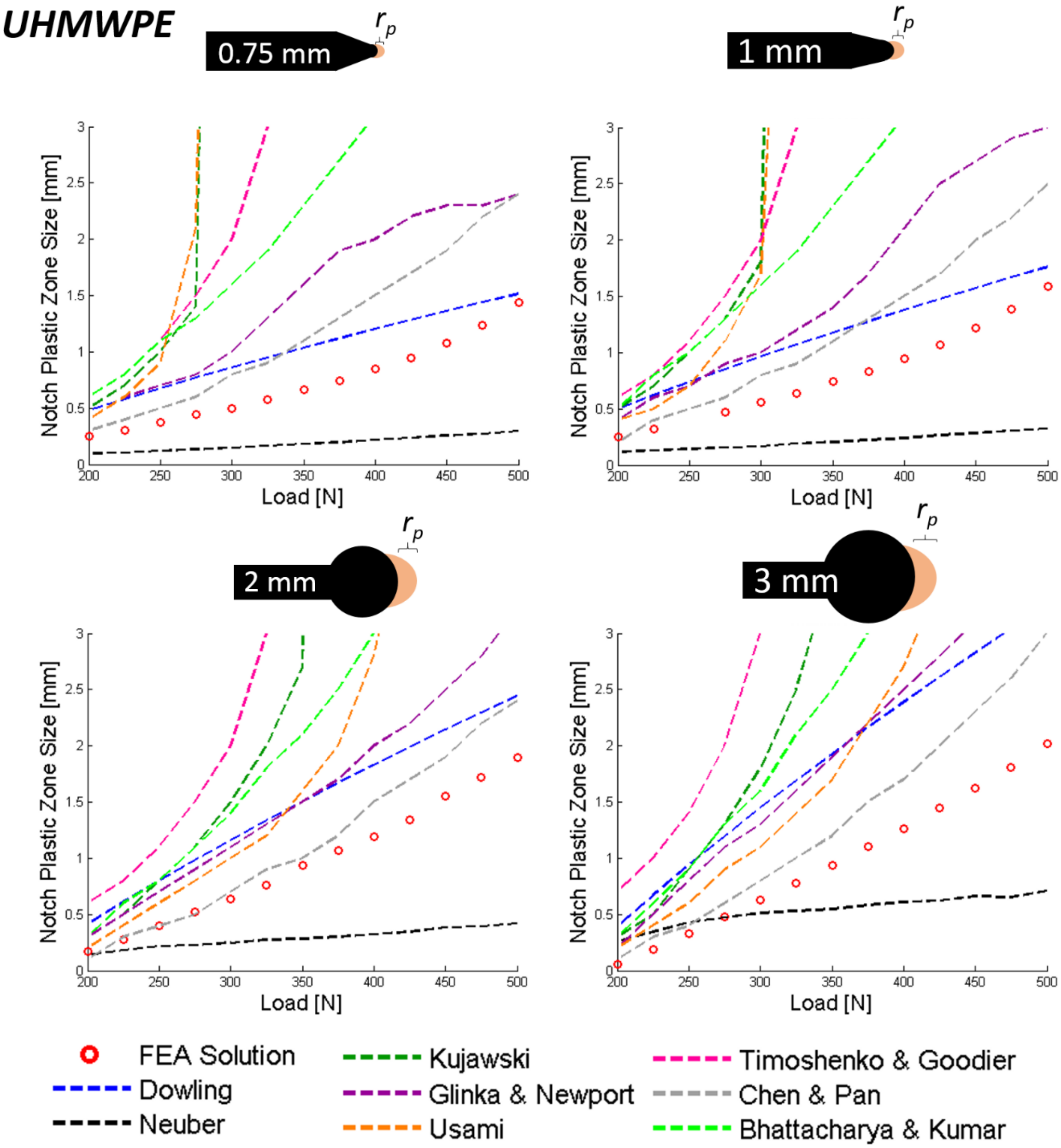

**Figure A.1 |** Reproduction of **Figure 5.6**, showing the notch plastic zone size in UHMWPE ahead of four notch root radii as a function of maximum tensile load for the CT specimens shown in **Figure 5.2**. Each plot compares the FEA solution (open red circles) with analytical solutions for the plastic zone size, the latter listed in **Table 5.3**. Chen & Pan (1978) provides a decent solution for 2 mm and 3mm notch root radii, but the expression deviates sharply for sharper crack-like notches.

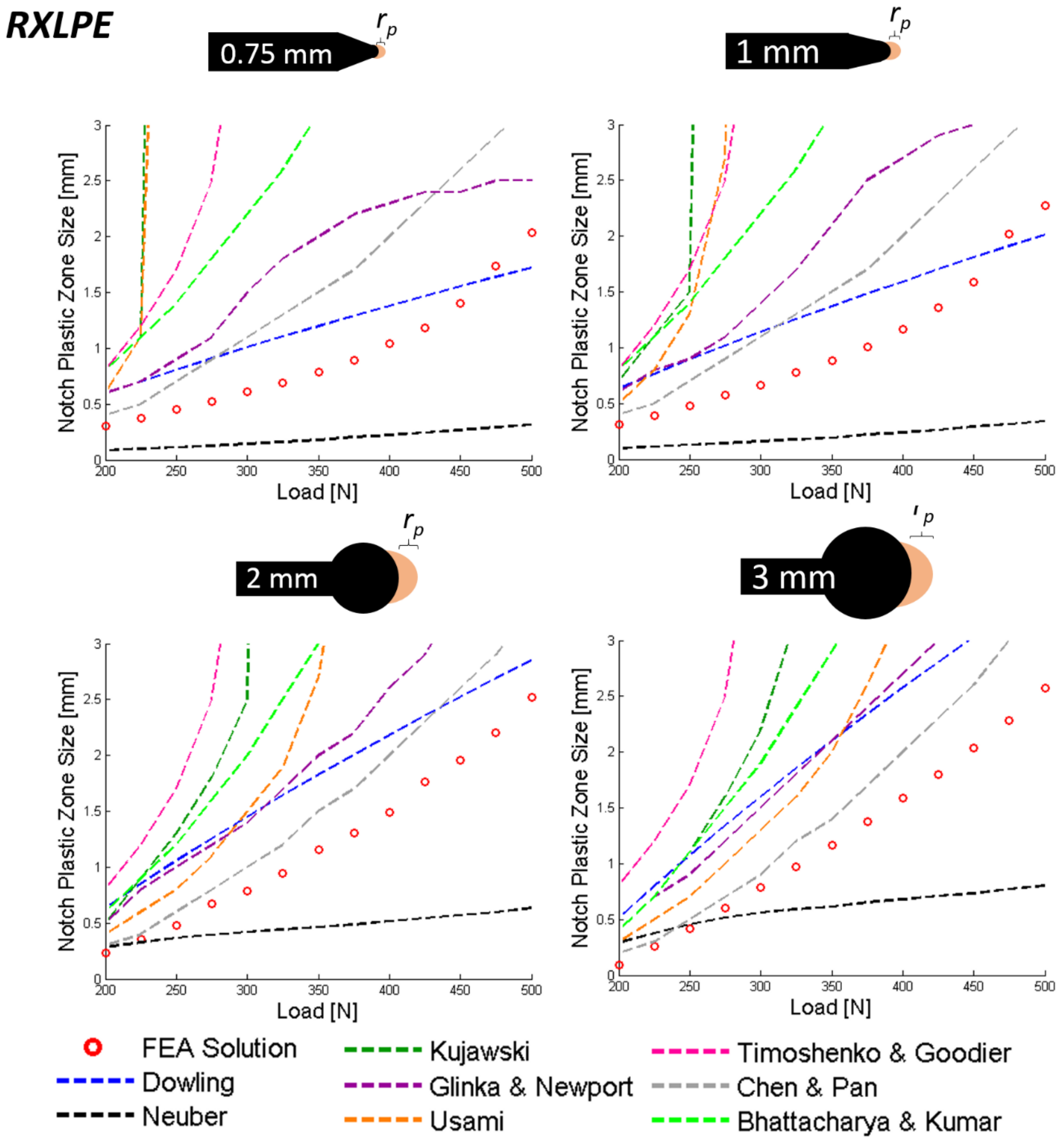

**Figure A.2 |** Notch plastic zone size ahead of four notch root radii as a function of maximum tensile load for RXLPE using the CT specimen dimensions shown in **Figure 5.2**. Each plot compares the FEA solution (open red circles) with analytical solutions for the plastic zone size, the latter listed in **Table 5.3**. Chen & Pan (1978) provides a decent solution for 2 mm and 3mm notch root radii, but the expression deviates sharply for sharper crack-like notches.

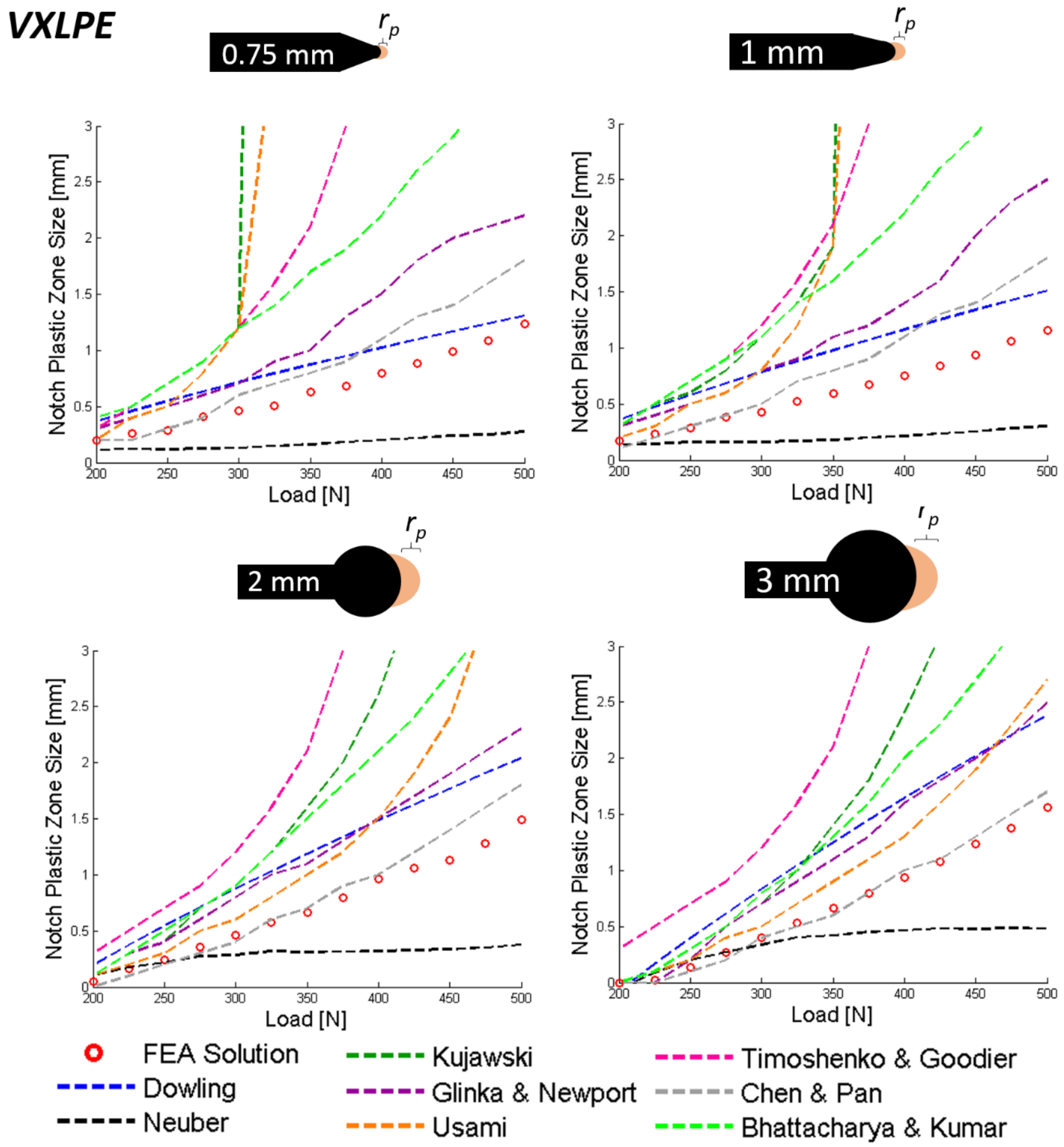

**Figure A.3 |** Notch plastic zone size ahead of four notch root radii as a function of maximum tensile load for VXLPE using the CT specimen dimensions shown in **Figure 5.2**. Each plot compares the FEA solution (open red circles) with analytical solutions for the plastic zone size, the latter listed in **Table 5.3**. The solution provided by Chen & Pan (1978) provides a good prediction for both 2mm and 3 mm notch root radii compared to all solutions, as well as compared to the same geometries for UHMWPE and RXPLE. However, deviations up to 50% for crack-like notches were seen for this prediction as well.

# Appendix B – Case Study: Unscrewing instability of modular reverse shoulder prosthesis increases propensity for in vivo fracture: a report of two cases

## INTRODUCTION

Reverse total shoulder arthroplasty (RSA) is an effective alternative to conventional total shoulder arthroplasty (TSA) for patients demonstrating shoulder instability (Seebauer 2007; Sirveaux & Mole 2010). RSA has especially improved stability for rotator cuff-deficient patients (Matsen et al. 2007; Seebauer 2007). Increased use of RSA over TSA for revision surgery, instability, and tumor and fracture sequelae has been reported (Drake et al. 2010). However, RSA complications have concurrently increased and include dislocations, infections, hematomas, instability, glenoid loosening, glenosphere unscrewing, scapular notching, polyethylene wear, and metallosis (Roberts et al. 2007; Seebauer 2007; Smithers et al. 2011).

RSA complications are frequently attributed to failure of the glenoid component. Nonetheless, humeral failure has been noted in several studies, and is more often associated with modular designs (K. I. Bohsali et al. 2006; Chuinard et al. 2006; Wilde & Walch 2006; Sirveaux & Mole 2010; Roberts et al. 2007). Dissociation of modular humeral components at the proximal metaphysis and distal diaphysis has been reported with only low frequency (1-2%) (K. I. Bohsali et al. 2006; Zumstein et al. 2011; Sirveaux & Mole 2010; Seebauer 2007; Favard et al. 2011). However, dissociation can lead to severe consequences including in vivo disassembly and device failure (Roberts et al. 2007). In this study, we examine two retrieved RSA modular devices from patients with proximal humeral bone loss:  both unscrewed in vivo and one fractured in vivo.

## CASE STUDY

### *Case I*

A modular cemented Tornier Aequalis RSA was retrieved from the left shoulder of a 79 year-old male patient after 9 years and 2 months in vivo (**Figure B.1a**). The patient initially fractured the proximal humerus during a ground level fall.  Surgery was then performed with open reduction and internal fixation using a proximal humeral locking plate. This fixation failed, and then a hemiarthroplasty surgery was performed. Since the tuberosity fixation failed, revision hemiarthroplasty surgery was performed.  Following the third surgical procedure, the tuberosities resorbed with subsequent anterior superior escape of the prosthesis. There was also a 5 cm area of proximal humeral bone loss.   Another revision surgery was then performed with conversion to a reverse prosthesis.

When this RSA was removed, preoperative radiographs revealed partial disassembly of the screw joint between the metaphysis and diaphysis on the humeral stem (**Figure B.1b**). The implant had not yet fractured or dissociated completely (**Figure B.1c**). Extensive metallosis was observed in the retrieved periprosthetic tissue (**Figure B.1d**).

Optical and metric analysis revealed a gap at the junction of the metaphysis and diaphysis. The two components were disassembled ex vivo and optical microscopy of the screw threads was conducted. Evidence of fretting wear was observed (**Figure B.2**). The screw was noted to have a 3 mm diameter transverse hole near the proximal end of the threads which was filled with a nylon bushing (**Figures B.1c & B.2**).

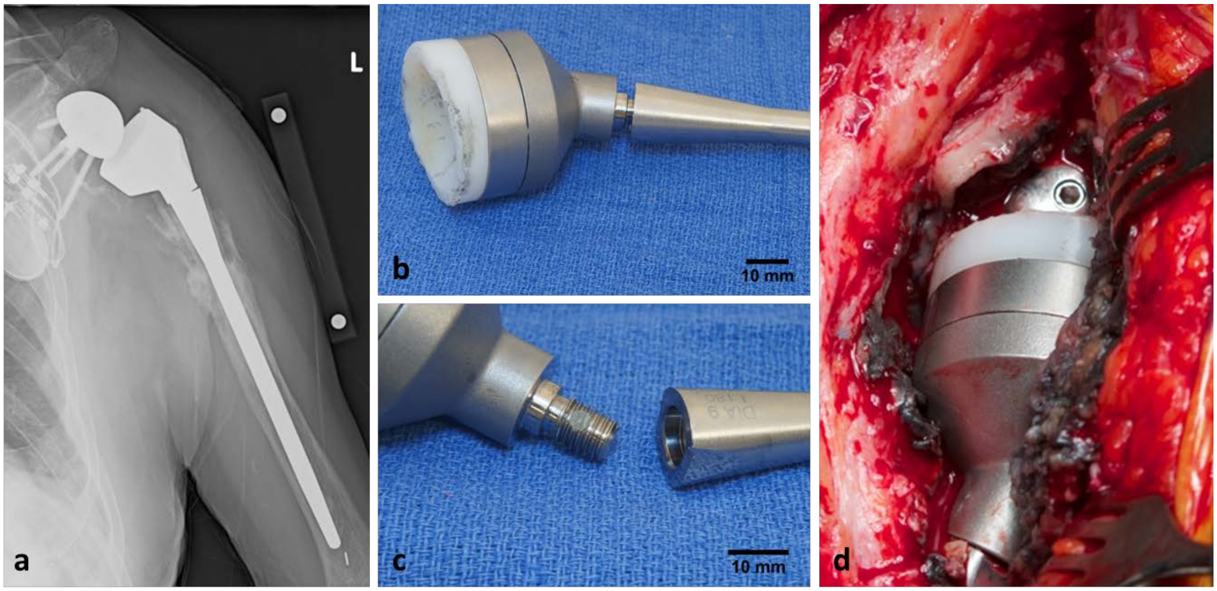

**Figure B.1 |** (a) Case I presented with in vivo unscrewing without dissociation or fracture. The implant as retrieved (b) and unscrewed (c) is shown. Note the screw has an approximate 3 mm diameter hole with a nylon bushing. Extensive metallosis (d) was present at the time of retrieval.

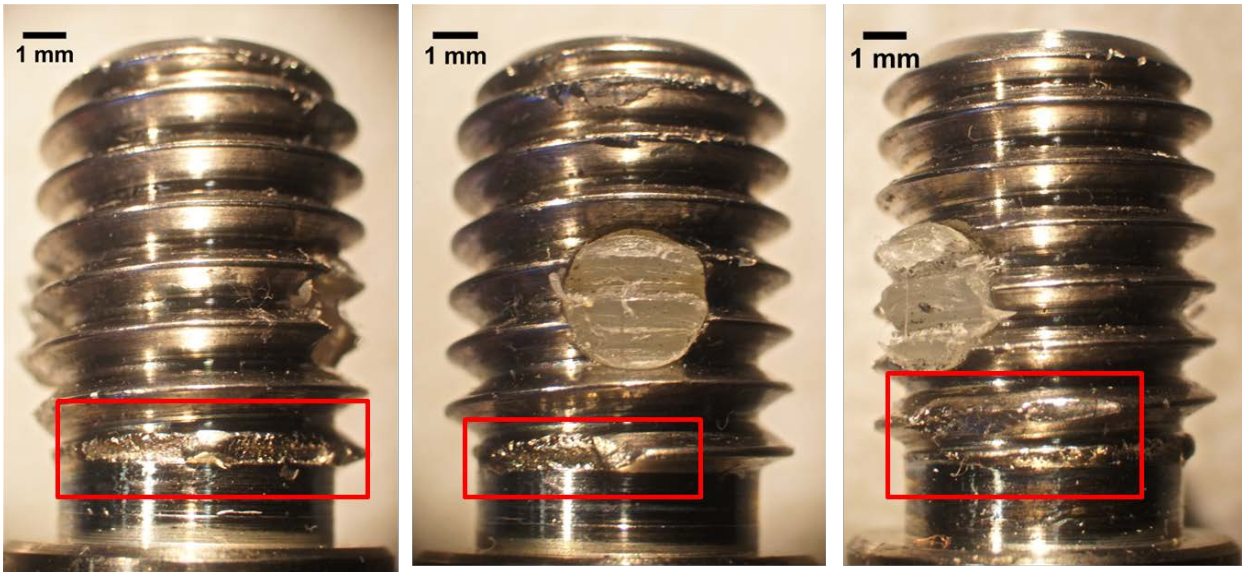

**Figure B.2 |** Threads from Case I displayed areas of damage consistent with fretting wear, highlighted in red.

*Case II*

A fractured modular Tornier Aequalis RSA was retrieved from the right shoulder of a 60-year-old male patient with rheumatoid arthritis after 4 years and 5 months in vivo (**Figures B.3a and B.3b**). Initially, multiple surgeries were performed for a massive rotator cuff tear including direct repair, latissimus dorsi transfer, and then pectoralis subcoracoid transfer. Finally, RSA was performed. The initial implant was in vivo for 17 months before undergoing revision due to humeral loosing. At the time of revision to the implant that is the subject of the current study, the greater tuberosity was fractured. This bony fragment was fixed to the implant with kinamed cables and the implant was secured with antibiotic impregnated methyl methacrylate cement. During follow up, he suffered progressive resorption of the greater tuberosity fragment leaving him with deficient bone in the metadiaphyseal region. Before the device fractured, the patient experienced episodes during which his shoulder was caught in external rotation and had to be manually rotated back in place to restore function.

The device failed at the junction of the metaphysis and diaphysis just above the remaining humeral bone while the patient was golfing. The implant was immediately retrieved. Extensive metallosis was observed in the periprosthetic tissue and down the humeral canal (**Figure B.3c**). Grade II scapular notching was noted.

Optical evaluation of the shoulder explant revealed that the fracture occurred through the metaphysis screw at the location of a 3 mm diameter through-hole that was plugged with an intact nylon bushing (**Figures B.3b and B.4**). Measurements of the remaining screw lodged in the diaphysis and the fractured screw fragment exposed a gap between the superior surface of the humeral stem and inferior mating surface of metaphyseal component. Furthermore, optical microscopy of the metaphysis screw revealed fretting wear of the threads that may have contributed to the extensive metallosis observed at retrieval (similar to the fretting wear seen in Case I).

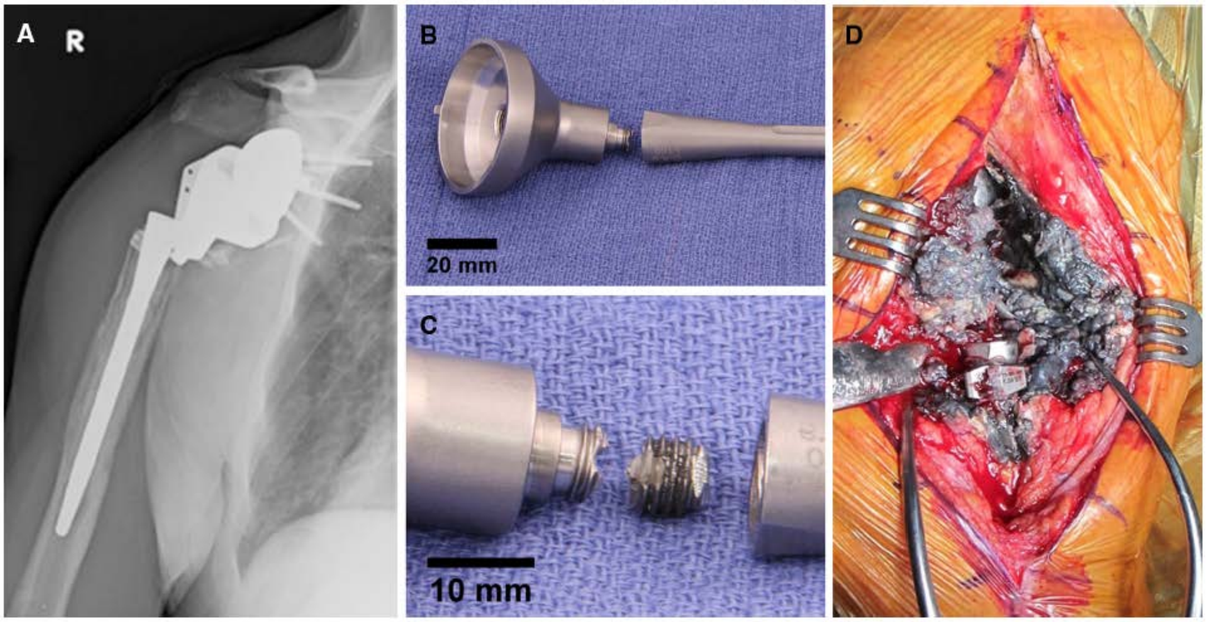

**Figure B.3 |** (a) Case II, in which fracture occurred in vivo at the metaphysis-diaphysis screw junction. The device is shown (b) at retrieval and (c) after removal of the remaining screw fragment from the housing, revealing that the component fractured at the through-hole, leaving a nearly intact nylon bushing. Extensive metallosis (d) was observed at retrieval.

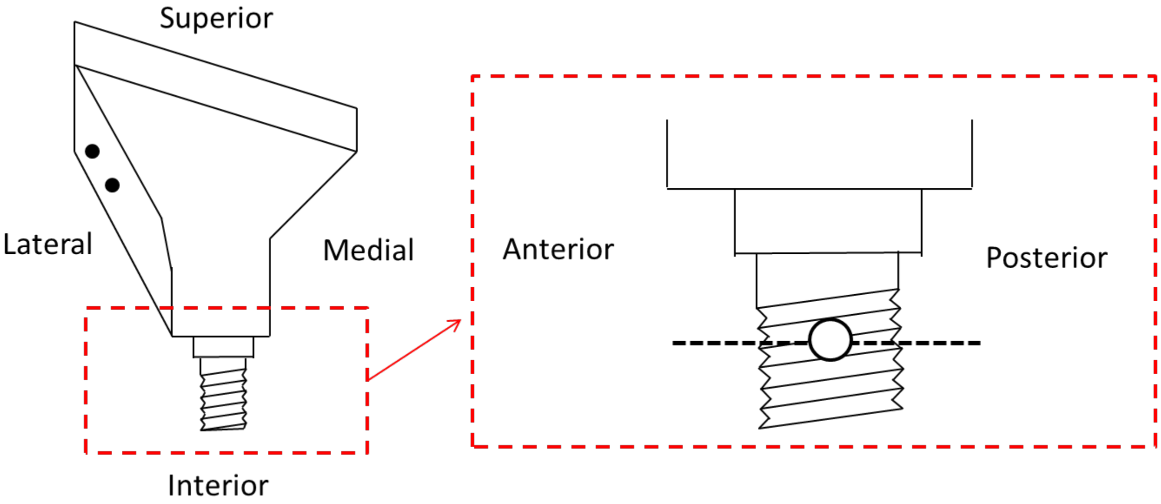

**Figure B.4 |** Illustration of the metaphyseal component. The fracture (dotted black line) occurred at a through-hole incorporated in the screw design.

Scanning electron microscopy (SEM) of the fracture surface did not show any evidence of fatigue damage (**Figure B.5**). Surface features were consistent with brittle fracture, suggesting breakage during an overload event while the patient was golfing. Failure analysis of the implant considering no proximal bone support was performed using composite beam theory under pure bending to evaluate the stresses at the screw joint and then compared to analysis of an implant with proximal bone support. An annulus cross section (**Figure B.6**) was used to model the composite beam. Stresses were calculated as:

$$\sigma_s = \frac{E_s M y}{\sum E_i I_i} \qquad \textbf{eq. B.1,}$$

where $\boldsymbol{\sigma_s}$ is the maximum normal stress in the metaphyseal screw and $\boldsymbol{E_s}$ is its elastic modulus; $\boldsymbol{M}$ is the bending moment applied about the neutral axis of the composite beam; y is the maximum distance from the neutral axis of the composite beam (the radius of the stem); $\boldsymbol{E}_\mathrm{i}$ is the elastic modulus of each contributing material; and $\boldsymbol{I_i}$ is the second moment of inertia for each material cross section, calculated as:

$$I_i = \frac{\pi}{64}(d_o^4 - d_i^4) \qquad \textbf{eq. B.2,}$$

where $\boldsymbol{d_o}$ is the outer diameter and $\boldsymbol{d_i}$ is the inner diameter. Geometries and material properties used in the analysis are shown in **Table B.1**.

**Table B.1 |** Summary of values used in composite beam analysis.

| **Material** | **E [GPa]** | **Diameter [mm]** |
|---|---|---|
| Corticol Bone [28] | 16 | 35 |
| Diaphysis – Phynox (ISO 5832-4 [19]) | 204 | 14 |
| Metaphysis – Alacrite (ISO 5832-7 [20]) | 248 | 8 |

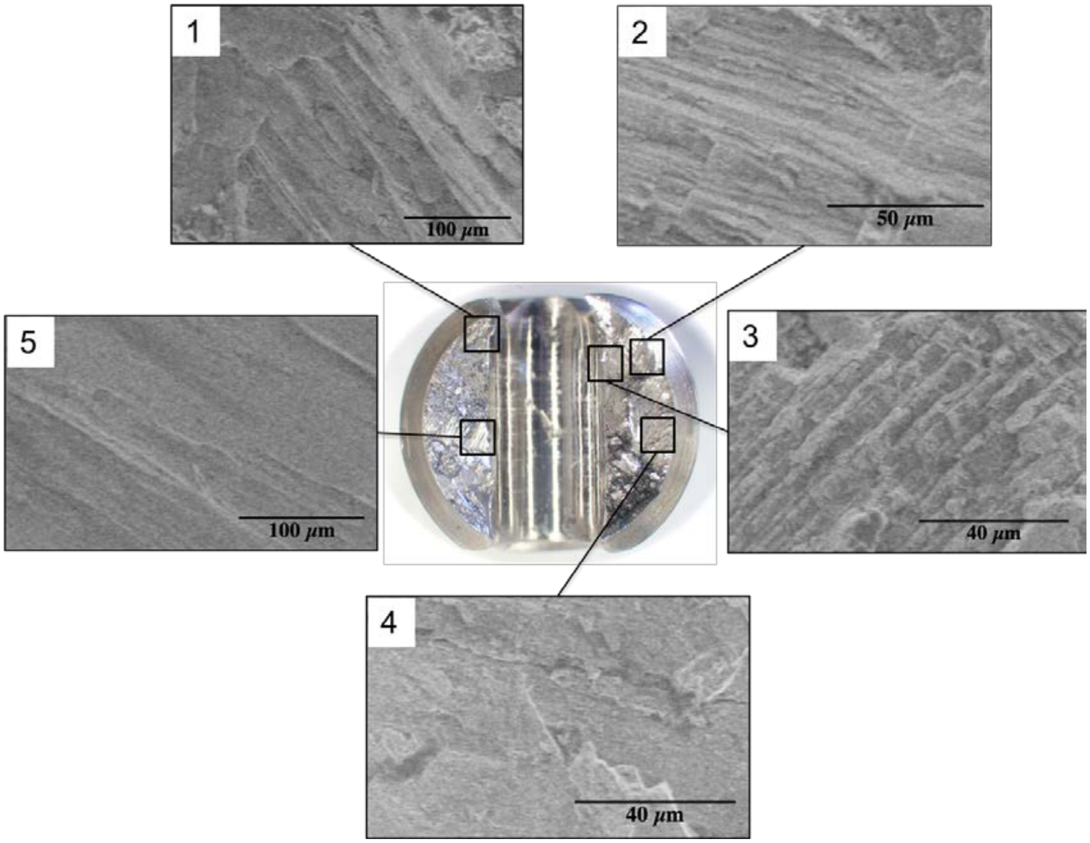

**Figure B.5 |** SEM images of fracture surface of metaphysis screw. No evidence of fatigue failure was present.

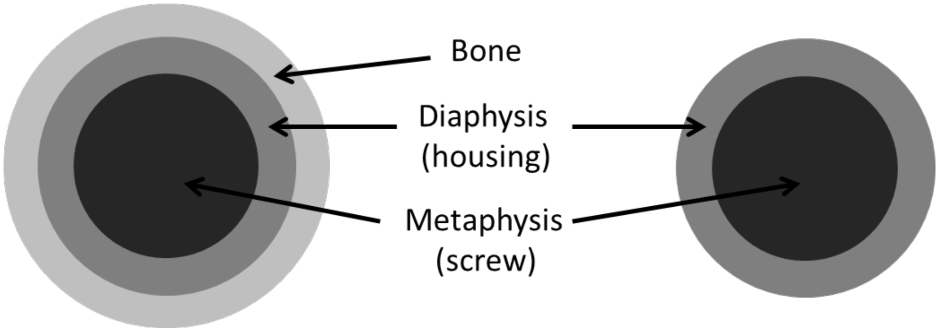

**Figure B.6 |** Cross-sectional geometry used in composite beam analysis.

Given the same dimensions and bending moment applied to the device, the proximal bone deficiency was shown to increase stresses in the implant by 60%. Unscrewing at the metaphysis-diaphysis joint further reduces the cross-sectional diameter, resulting in an exponential decrease in the moment of inertia of the humeral stem (**eq. B.2**) and exacerbation of implant stresses (**eq. B.1**) with loosening of the device. Furthermore, the addition of a through-hole in the implant could elevate stresses threefold in tension under elastic loading conditions.30

## DISCUSSION

Glenoid component failure is the primary reason for revision in RSA (Seebauer 2007; Smithers et al. 2011). Yet humeral complications can have devastating consequences including complete dissociation of modular components (Roberts et al. 2007). Unscrewing of the metaphysis-diaphysis joint in modular humeral stems has been reported (Roberts et al. 2007; Sirveaux & Mole 2010; K. Bohsali et al. 2006; Chuinard et al. 2006; Wilde & Walch 2006). Roberts et al. (2007) shows radiographs of two modular RSA implants that partially and completely unscrewed in vivo, claiming that modification of such early European designs have since eliminated this complication. Two of three humeral component failure cases reported by De Wilde and Walch included partial disassembly due to unscrewing (Wilde & Walch 2006). To our knowledge, this is the first study in which a case of metaphysis-diaphysis junction unscrewing was coupled with fracture of the component during an overload event.

Both cases of unscrewing examined in this study featured extensive metallosis in the patients at the time of removal, suggesting that even before fracture, fretting wear at the unstable screw joint can cause serious tissue damage due to metal debris release. Screw threads displayed evidence of low volume wear at higher magnifications, revealing that even minimal metal debris release can significantly compromise periprosthetic tissue. In addition to soft tissue damage, a more severe consequence of unscrewing can be seen with the fracture of Case II, which was influenced by three factors. First, composite beam analysis demonstrated that a lack of proximal bone support can lead to a 60% increase in stresses for a fully intact stem. Second, this stress is exponentially increased due to unscrewing, which reduces the cross-sectional diameter and thus increases the moment of inertia.   Finally, the addition of a through-hole provides a stress concentration. The hole was plugged with a nylon bushing presumably to prevent unscrewing; however, the location of fracture through this hole reflects the vulnerability of this design input.

All three of these factors – the lack of proximal bone support, the unscrewing mechanism, and the through-hole – contributed to a weaker metaphysis-diaphysis interface that predisposed the implant to failure during an overload event. The observations during retrieval and ex vivo optical analysis provided evidence for the failure mechanism presented in **Figure B.7**.

The suggested mechanism for in vivo unscrewing is attributed to several factors. De Wilde and Walch proposed that unscrewing can be attributed to the blockage of tuberosity movement against the anterior wall of the glenoid in maximal internal rotation during forearm flexion (Wilde & Walch 2006). Several authors recommend vigorous tightening of the screw junction during implantation to prevent such a mechanism for disassembly (Wilde & Walch 2006; Matsen et al. 2007; Sirveaux & Mole 2010). However, even with sufficient securement of the modular components, the absence of external proximal support has been frequently cited as a cause for unscrewing (Matsen et al. 2007; Sirveaux & Mole 2010; Cuff et al. 2011; Wilde & Walch 2006). Our cases as well as those in De Wilde and Walch's case report, involved patients with deficient humeral bone above the metaphysis-diaphysis junction. Cuff et al. demonstrated a higher rate of rotational micromotion and eventual failure under cyclic loading for modular stems in no-bone models compared to both modular and monoblock systems in fully intact bone models (Cuff et al. 2011). As demonstrated with our composite beam analysis, proximal bone loss not only contributes to unscrewing but also elevates stresses under bending conditions. Clinical evidence further supports the need for allograft support in place of a deficient proximal humeral bone with reports of higher patient satisfaction and lower complication rates (Chacon et al. 2009; Levy & Virani 2007).

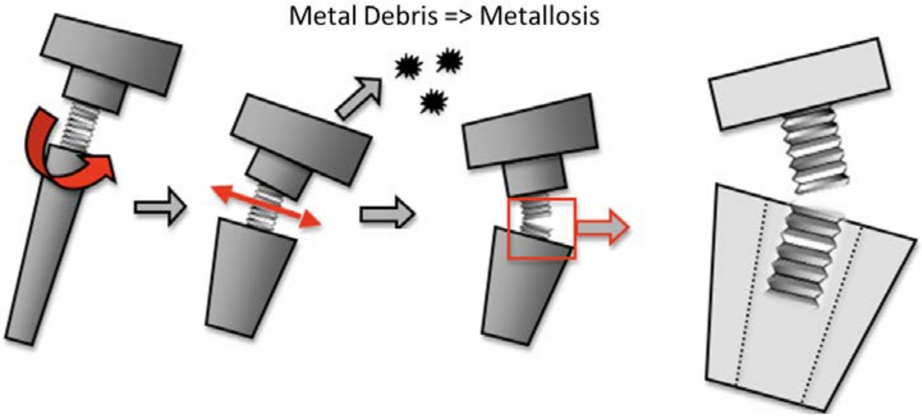

**Figure B.7 |** Optical analysis suggests the following failure mechanisms: unscrewing, fretting wear (metallosis), and fracture due to overload.

The consideration of monoblock versus modular humeral stem components highlights the role of implant design in contributing to catastrophic failure such as disassembly or fracture (Cuff et al. 2011). Levy et al. also allude to a 5 cm lateral bone deficiency as an appropriate threshold for allograft placement (Cuff et al. 2011; Levy & Virani 2007). This lies very close to the metaphysis-diaphysis junction, and can even lie below the mating surface for larger implants. To mitigate risk of unscrewing, either a lower cutoff is needed or that this limit only be applied with the use of monoblock systems (Seebauer 2007). The addition of a stress concentration in the implant for both cases in our study also questions the rigor of preclinical bench testing in assessing implant mechanical function under reduced stability (i.e. unscrewing). ASTM and ISO standards for cyclic fatigue and fretting corrosion of modular joints only exist for hip prostheses (International Standards Organization 2010; ASTM International 2013c; ASTM International 2009b; ASTM International 2011). No testing standards exist specifically for RSA, and current standards for shoulder prostheses only consider glenoid component dissociation (ASTM International 2010; ASTM International 2012b; ASTM International 2009a). ASTM F2028-08 for glenoid loosening or dissociation is currently being revised to include tests for reverse shoulder prostheses (ASTM International 2014b). However, there is no indication that this standard will address humeral stem testing. Our review of unscrewing events in RSA supports the need to extend current ASTM standards for fatigue and fretting assessments of modular hip stems to similar standards for reverse shoulder components. Ideally, these standards should account for overload events under varying degrees of dissociation of modular implants, especially if indicated for patients without allograft bone support.

In reports of unscrewing and/or disassembly of the humeral stems, the authors allude to improvements in design that have eliminated such complications (Chuinard et al. 2006; Roberts et al. 2007). Even with historical evidence presented in this and other case studies, the “lessons learned” from previous devices may have avoided these clinical complications. With the emergence of the reverse prosthesis in the late 1980s, a substantial foundation of knowledge regarding modular hips could have informed design decisions to prevent humeral stem failures. When tracing the evolution of the Tornier Aequalis Reverse Shoulder through FDA submissions, substantial equivalence can be traced back to the Delta III RSA – the implant that exhibited the unscrewing failures reported by De Wilde and Walch – which was first deemed equivalent to modular TSA designs that do not utilize screw fixation (Tornier 2004; Biomet Inc 1999b; Biomet Inc 1999a; Depuy Inc 1999; Depuy Inc 2003).

The introduction of a modular connection with a threaded interface over the more traditional Morse taper warrants implementation of more rigorous modular component testing to evaluate both fretting prevention and mechanical stability. Such testing should evaluate the degree of unscrewing that leads to instability, both with and without proximal bone support. In addition, laboratory studies should be combined with clinical know-how to understand the mechanisms of unscrewing in vivo and thoroughly vet designs that seek to prevent them (such as the nylon bushing in the Tornier Aqualis).

## CONCLUSION

Our work demonstrates that both clinical and design considerations contributed to the premature failure of two modular RSAs. Previous literature has suggested several clinical measures to prevent unscrewing of modular implants in vivo, including the use of an allograft composite to reduce torsional instability in patients with proximal humeral bone deficiency. While clinical actions can prevent unscrewing, our work shows that designs that include stress concentrations can significantly reduce mechanical integrity, especially during daily patient activity.